massachusetts institute of technology — artificial intelligence laboratory

Modeling, Estimation, and Control of Robot-Soil Interactions

Won Hong

AI Technical Report 2001-007 September 2001

Modeling, Estimation, and Control of Robot-Soil Interactions

by

Won Hong

B.S., Mechanical Engineering and Material Science
University of California, Berkeley (1993)

S.M., Mechanical Engineering
Massachusetts Institute of Technology (1995)

Submitted to the Department of Mechanical Engineering
in partial fulfillment of the requirements for the degree of

Doctor of Philosophy in Mechanical Engineering

at the

MASSACHUSETTS INSTITUTE OF TECHNOLOGY

September 2001

Certified by: J. Kenneth Salisbury, Thesis Co-Chairperson
Principal Research Scientist, Mechanical Engineering, MIT
Professor (Research) of Computer Science and Surgery, Stanford

Certified by: Jean-Jacques E. Slotine, Thesis Co-Chairperson
Professor of Mechanical Engineering and Information Sciences and
Professor of Brain and Cognitive Sciences, MIT

Accepted by: Ain A. Sonin
Chairman, Department Committee on Graduate Students

Modeling, Estimation, and Control of Robot-Soil Interactions

by

Won Hong

Submitted to the Department of Mechanical Engineering on July 12, 2001, in partial fulfillment of the requirements for the degree of Doctor of Philosophy in Mechanical Engineering

Abstract

This thesis presents the development of hardware, theory, and experimental methods to enable a robotic manipulator arm to interact with soils and estimate soil properties from interaction forces. Unlike the majority of robotic systems interacting with soil, our objective is parameter estimation, not excavation. To this end, we design our manipulator with a flat plate for easy modeling of interactions. By using a flat plate, we take advantage of the wealth of research on the similar problem of earth pressure on retaining walls.

There are a number of existing earth pressure models. These models typically provide estimates of force which are in uncertain relation to the true force. A recent technique, known as numerical limit analysis, provides upper and lower bounds on the true force. Predictions from the numerical limit analysis technique are shown to be in good agreement with other accepted models.

Experimental methods for plate insertion, soil-tool interface friction estimation, and control of applied forces on the soil are presented. In addition, a novel graphical technique for inverting the soil models is developed, which is an improvement over standard nonlinear optimization. This graphical technique utilizes the uncertainties associated with each set of force measurements to obtain all possible parameters which could have produced the measured forces.

The system is tested on three cohesionless soils, two in a loose state and one in a loose and dense state. The results are compared with friction angles obtained from direct shear tests. The results highlight a number of key points. Common assumptions are made in soil modeling. Most notably, the Mohr-Coulomb failure law and perfectly plastic behavior. In the direct shear tests, a marked dependence of friction angle on the normal stress at low stresses is found. This has ramifications for any study of friction done at low stresses. In addition, gradual failures are often observed for vertical tools and tools inclined away from the direction of motion. After accounting for the change in friction angle at low stresses, the results show good agreement with the direct shear values.

Thesis Committee:

J. Kenneth Salisbury, Co-Chairperson
Principal Research Scientist, Mechanical Engineering, MIT
Professor (Research) of Computer Science and Surgery, Stanford

Jean-Jacques E. Slotine, Co-Chairperson
Professor of Mechanical Engineering and Information Sciences and
Professor of Brain and Cognitive Sciences, MIT

Andrew J. Whittle
Professor of Civil and Environmental Engineering, MIT

Gill A. Pratt
Assistant Professor of Electrical Engineering and Computer Science, MIT

Acknowledgments

Thanks first to my committee. To Prof. Ken Salisbury and Prof. Jean-Jacques Slotine, for their support and encouragement throughout my entire stay at MIT. To Prof. Andrew Whittle, for his aid in the soil modeling aspects of this work and for helping me along at a critical point in my graduate studies. To Prof. Gill Pratt, for pushing me along at the close of this work.

I would also like to thank Dr. Jack Germaine, for the many helpful discussions and suggestions and for arranging for lab space and access to test apparatus. Also, thanks to Dr. Boonchai Ukritchon, for supplying source code for the UB/LB programs used in this work.

I would like to especially thank the many *jks-grads*, past and present, for the fun we have had through the years. I would like to especially thank Mark Ottensmeyer, Arrin Katz, Ela Ben-Ur, and Brian Anthony for their help and support in the completion of this thesis.

I would also like to thank the *labrats* in the Civil and Environmental Engineering Department, for welcoming me into their lab group meetings and for the free pizza. Thanks especially to Sanjay Pahuja, for fun talks across the barrier in 347.

Finally, I would like to thank my family, my mother and grandmother, and my father, who I know would be proud, and my brother. I would also like to thank Pat and Suh Yoon-Chen, who are practically family.

None of this would have been possible without the amazing grace of God. To God be the glory, Amen!

This research was conducted at the MIT Artificial Intelligence Laboratory under NASA/JPL Contract No. 959774. Thanks also go to the Civil and Environmental Engineering Department at MIT for the use of their facilities and materials.

Contents

List of Figures

List of Tables

Chapter 1

Introduction

Digging is done on an everyday basis with little understanding of the forces of interaction. This is acceptable in terrestrial systems where torque and power considerations do not play a role and where the only goal is simply to excavate a given region of soil. For power constrained systems or for systems which have additional sensing goals, a detailed analysis of interaction forces and a better understanding of the process can lead to more robust, efficient, and precise control and sensing strategies.

1.1 Motivation

Many people are interested in automating the digging/excavation process. In addition to earth-based digging applications, NASA has a need for well designed, small-scale, autonomous digging robots for Mars (and Lunar) exploration. NASA is interested in the collection of any geological information about the Martian surface. A sample return mission is not planned until 2014 (at the earliest, 2011, on an accelerated schedule). Therefore, any exploration of the soil must be conducted remotely.

Previous interactions with Martian soil have been conducted using a manipulator arm (Viking missions [71]) and also by spinning the wheels of a rover vehicle (Pathfinder/Sojourner mission [114]) to obtain measurements of physical soil properties. Specific results from these missions will be discussed in the next chapter.

Future landers and rovers are increasingly being equipped with manipulator arms in order to place instruments, collect samples, conduct experiments, and for all-purpose manipulation. An example of this

Photo courtesy of the Jet Propulsion Laboratory, California Institute of Technology.

Figure 1.1: The FIDO rover at the Jet Propulsion Laboratory is equipped with an instrument arm, to which we temporarily mounted a flat plate in order to interact with the soil to see how feasible the technology would be.

type of system is the ill-fated Polar Lander mission that was scheduled to land on Mars in December 1999. It was equipped with a three meter manipulator arm which was to conduct multiple tasks, one of which was to dig a half meter trench in the soil. Another example is the future 2003 dual-rover mission, in which two identical rovers each will use an instrumented robotic arm to conduct a variety of tasks, possibly including scraping, brushing, and close-proximity imaging of rock samples. In addition, other interactions with soil mediums are being examined, for geological purposes, excavation, sample collection, or for buried object retrieval.

The FIDO Rover at the Jet Propulsion Laboratory shown in Figure 1.1 is representative of what might be expected on future systems. The FIDO Rover is a test-bed/prototype for the rovers to be sent in the 2003 mission. I have had the privilege of working on this system for a brief time, during which I mounted a flat plate to the end of the instrument arm on the front of the rover. Preliminary stroking tests in simulated soil were conducted. While no precise directed studies were carried out, it is clear that it would be possible to use this arm to interact with soil in this manner.

With the existence of robotic arms on future rovers and landers (of greater dexterity and precision than the Viking missions [71]), it is logical to examine what geological information could be obtained through controlled interaction using these robotic arms. Thus, this motivates the study of robot-soil interactions presented in this thesis.

1.2 Background and Goals

From a survey of many papers on robotic excavation, there is surprisingly little study of soil-tool interaction modeling for the prediction of interaction forces and estimation of soil properties. Most researchers in this area have focused on obstacle avoidance, reactive stroke path planning to avoid torque limiting, and planning of excavation of specified volumes of soil. This work is typically done on large scale excavation systems. The goal of these systems is improved excavation, not estimation, and thus less focus has been given to the precise modeling of interactions and the feasibility of parameter estimation.

On the other hand, in the Civil Engineering community, there is an abundance of papers on the topic of active and passive earth pressure. Active earth pressure theory examines the pressure developed on a fixed retaining wall from the weight of a soil mass pushing against it. Passive earth pressure theory examines the forces required to move a wall pushing against a soil mass. Therefore, when using a flat plate embedded in a soil mass, the force required to move the plate will be a combination of the active and passive earth pressure components. By using a flat plate as the means of interaction, the wealth of existing research in this field can be applied to the analysis.

The research in robotic excavation could greatly benefit from a detailed study and application of the Civil Engineering work. This thesis proposes to serve as a bridge between the two communities, drawing from research in both robotics and Civil Engineering.

The ultimate goal of this research is to provide all necessary techniques to enable a robotic manipulator arm to accurately estimate soil properties through interactions alone. There are four intermediate goals which are necessary to achieve the ultimate goal: select suitable soil models for the prediction of interaction forces by examining existing models and exploring novel methods ; verify the validity of the selected models through experimentation ; develop new methods to invert these soil models to estimate soil parameters from interaction data ; and enhance the control of a manipulator arm for useful soil interactions.

1.3 Outline of Thesis

Chapter 2 discusses previous work on topics related to soil-tool interactions and discusses the proposed approach for this research. The results from the studies of Martian soils from the 1975 Viking Project and the 1997 Pathfinder/Sojourner Mission are summarized. Various models for earth pressure in Civil Engineering are discussed. A listing of prior work on robotic excavation is also presented.

Chapter 3 discusses the development of the manipulator arm used in this research. It also discusses the associated software for control of the manipulator. A number of improvements were made to the manipulator design to increase its strength and sensing capabilities. The system architecture for real-time control and data collection is also described.

Chapter 4 discusses existing soil models for the prediction of draft force[1] and also details the first extensive application of a numerical limit analysis technique to this prediction problem. In this chapter, it is shown that the numerical limit analysis technique produces predictions which are in good agreement with other commonly referenced models. In addition, the numerical limit analysis technique has the added benefits of providing upper *and* lower bounds on the failure force and increased versatility for modeling a variety of tool and soil configurations.

Chapter 5 presents the experimental procedure for data collection. The development of a number of techniques are discussed. The manipulator end-effector plate must be inserted into the soil with minimal disruption of the soil state. After insertion, the plate must be pulled through the soil in a controlled manner. An iterative method for the *in situ* determination of soil-interface friction is also developed.

Chapter 6 presents the experimental results from interactions with three different cohesionless soils: two in a loose state and one in both loose and dense states. The results are compared to measurements from direct shear tests. Discussions of the results and sources of error are presented.

Chapter 7 discusses the development of a new parameter space model inversion technique. The soil models are nonlinearly dependent on four parameters. In order to determine parameter estimates from force data, a nonlinear optimization would typically be done. Instead, this chapter presents the development of a graphical parameter estimation technique which uses both force measurements and associated uncertainties to determine *ranges* of parameters which are consistent with the observed measurements.

Finally, Chapter 8 discusses ideas for the future and applications of this work. Chapter 9 concludes with a summary of the recommendations and contributions of this thesis.

---

[1] "draft" force – the force to pull a tool, the force to pull the plate through the soil.

Chapter 2

Previous Work

This chapter begins with a discussion of the previous work done in the exploration of Martian soils. This is followed by a discussion of prior work in modeling of soil behavior and manipulator interactions with soil. Finally, the proposed approach used in this thesis for the development of our system is outlined.

2.1 Previous Exploration of Martian Soils

There have been two landmark missions to the Martian surface. The first mission had two identical landers which touched down at two geographically distinct locations. These were the Viking 1 and 2 landers, launched in 1975, which conducted surface sampling experiments from 1976 to 1978. The second mission was the Pathfinder lander, carrying the Sojourner rover, which landed on Mars in July of 1997 (fairly close to the Viking 1 landing site). Among their many tasks, these missions conducted studies of soil properties.

The Viking lander experiments [70, 71] were conducted with a surface sampler arm [23], which scraped the soil to dig shallow trenches (0.04-0.06 m deep). Investigators examined the record of arm forces, visually estimated failure wedges, and examined the slopes of the resulting trench walls. From this data, they extracted estimates of the cohesion and internal friction angles[1] using a model from McKyes and Ali [69]. The soil encountered was classified into three types: drift, crusty to cloddy, and blocky. Using a technique relating the geometry

---

[1] The internal friction angle is the angle of friction when soil is rubbing against soil. A friction angle, ϕ, is related to a friction coefficient, μ, by the relation: $\mu = \tan \phi$.

of the failure wedge to the internal friction angle, they obtained the following estimates for friction angles: for drift material, 14° to 21°, for crusty to cloddy material, 28° to 39°, and for blocky material, 27° to 33°. Cohesion estimates were also determined: for the drift material, 1.4 to 3.0 kPa, for the crusty to cloddy material, 0.5 to 5.8 kPa, and for the blocky material, 2.2 to 6.2 kPa.

From the Pathfinder/Sojourner mission, researchers have published data on the observed angles of repose and the friction angles of Martian soil [114, 113]. The angle of repose was measured using images from the lander camera and they reported values between 30° and 38°. Friction angles were obtained from simulated shear tests conducted by driving one of the wheels on the rover up to 1.5 turns, while keeping the other wheels stationary. The friction angles were found to be between 32° and 41°. The shear tests were conducted at normal stresses typically below 4 kPa. Two methods were used to estimate cohesion from the shear data. In the first, the angle of friction was assumed to be equal to the angle of repose[2], and for each measurement of normal and shear stress, a cohesion estimate was computed, resulting in values between 0.120 and 0.356 kPa. The second method uses a least squares fit to determine friction angles and cohesion estimates. In this case, the cohesion estimates were found to have a wider range and were sometimes negative. Overall, they conclude that the soil appears to show little or no cohesion.

A third mission to reach the Martian surface, which unfortunately did not land successfully, was the recent Polar Lander, scheduled to land in December 1999. It was equipped with a three meter long manipulator arm. This arm was designed to dig a half-meter to meter deep trench. As can be noted from the other missions, the greatest depth of soil probed has only been approximately 6 cm. Future missions will hopefully be able to uncover material at greater depth.

For the interested reader, there are also additional references about Martian soil. There is an article about considerations for cold temperature behavior of Martian and Lunar soil from Chua and Johnson [20]. This reference also provides general information about the Martian environment, summaries of the Viking and Pathfinder missions, and other soil mechanics considerations applicable to Mars. A white paper and large collection of references related to Mars soil from Haldemann [35]

---

[2] As noted by Terzaghi [112], the angle of repose for soils with cohesion is not a constant value and depends on the height of the slope. For cohesionless soils, he states that the angle of repose is approximately a constant, and independent of the height of the slope and fairly independent of the initial density of the soil. It is approximately equal to the angle of internal friction of the soil in its loosest state.

can be found online. In addition to Martian data, we also have data on Lunar Soil Simulants from Willman *et al.* [123, 124]. While lunar regolith is not expected to be identical to Martian soil, it is still of interest for any future missions to the Moon. Willman *et al.* compared experimental draft forces with those predicted using four different 3-D models of soil failure [39, 32, 69, 78], including the same model used in the Viking analysis, but found poor agreement.

2.2 Previous Work on Modeling and Manipulators

A significant body of work exists on the topic of robotic excavation. The work has primarily focused on planning, development and coordination of systems, or simple rule based control schemes to avoid stalling. This thesis is intended to fill a gap in the existing body of research. Researchers have primarily focused on high level planning and have not taken a close look at improving techniques for accurately predicting interaction forces, attempting to classify soils from interaction data, or developing control systems to use estimated soil parameters to enhance performance. The following survey of the existing body of work is divided into those related to the modeling of soil behavior and the control of manipulators interacting with soil.

2.2.1 Soil-Tool Interaction Models

When using a flat plate as the end-effector, the problem of predicting the draft force for the plate is equivalent to the classical case of the force on a retaining wall. The solution of this problem is commonly known as active and passive earth pressure theory. There are many papers on this topic. A few which are widely referenced or unique are mentioned here.

Study of this problem in Civil Engineering dates back to Coulomb (1776) [21]. It is also well known that there are limitations to the theory proposed by Coulomb. For instance, for soil-tool interfaces which exhibit friction, the larger the friction angle, the greater the prediction error. To account for such limitations, additional methods have been developed which use a logarithmic spiral failure surface near the soil-tool interface. These methods are discussed in soil mechanics texts like Terzaghi [112], Lambe and Whitman [62], or Jumikis [50]. These models, which pre-assume a failure surface and compute a force equilibrium based upon this failure surface, are commonly referred to as limit equilibrium methods.

In addition to limit equilibrium methods, there are methods which consider energy dissipation and stress equilibrium to determine upper and lower bounds on the failure force. These techniques are commonly referred to as limit analysis techniques. They are derived from the upper and lower bound theorems from Drucker [27]. Sokolovskii's slip line method [108] calculates a lower bound on the failure force from solving a set of stress equilibrium differential equations over discrete points in the soil mass using a finite difference method[3]. Caquot and Kerisel [17] provide a set of tables from the results of their calculations which are also based upon the solution of the governing equations of equilibrium[4]. Chen and Liu [18] provide an upper bound solution which assumes a failure mechanism composed of linear and logarithmic spiral components, but the calculation of failure force is based upon energy calculations rather than force balance, making this prediction a limit analysis upper bound, rather than a limit equilibrium technique. There is also another technique, which takes advantage of the ever increasing capability of computers, called numerical limit analysis. Sloan [107] develops finite-element numerical methods for the computation of upper and lower bound solutions. Together, we refer to upper and lower bound methods as the numerical limit analysis technique. Sloan provides examples for cases of bearing capacity of strip footings, active earth pressure, slope stability, and buried tunnel stability. Extensive work has also been done on the bearing capacity of foundations by Ukritchon [118, 117] using this technique.

There is also a final set of soil models which use finite element techniques to predict deflection and failure forces. Yong and Hanna [126] develop a two dimensional finite element model for soil cutting and verify their results using a 10 cm wide by 20 cm long blade at a variety of blade inclinations. Kushwaha and Shen [58, 93] and Chi and Kushwaha [19] develop 3-D finite element techniques using a stress-strain model from Duncan and Chang [29]. It is also interesting to note that Kushwaha and Zhang [60] have tried applying radial basis function neural networks to the modeling task.

In addition to the papers which develop theoretical models, there have been papers which study the agreement between theory and ex-

---

[3] Sloan [107] notes that Sokolovskii makes some assumptions in his calculations which make the results neither strict upper or strict lower bounds.

[4] Only sometimes viewed as a lower bound. Some references, such as Chen and Liu [18] refer to it as being, at times, viewed as a lower bound. Other references, such as Duncan and Mokwa [30] refer to it being based upon the logarithmic spiral theory, which would make it a limit equilibrium technique.

perimental data. Osman [75] tests a variety of inclined and curved blades 4" deep and 24" wide and compares the results with the predictions from the logarithmic spiral model. Rowe and Peaker [87] conduct studies with 1.5' deep and 6' wide wall and make interesting observations regarding progressive failure of loose and dense soils. James and Bransby [47] study the shape of the failure surface resulting from the rotation of a wall about its bottom tip and compare the results with the model from Sokolovskii [108]. And very recently, there has been a study from Duncan and Mokwa [30], who apply a load to a reinforced concrete anchor block of dimensions 3.5' high, 6.3' long, and 3' thick and study the load versus deflection curve and compare the measured failure force against the Coulomb and logarithmic spiral models.

All of the methods discussed above, except for the 3-D finite element method from Kushwaha *et al.*, have been 2-D. There were a number of 3-D models in existence which have already been mentioned briefly related to the testing of the Lunar Soil Simulant. These models were from Godwin and Spoor [32], Hettiaratchi and Reece [39], McKyes and Ali [69], and Perumpral, Grisso, and Desai [78]. These are typically more complex and not necessarily more accurate. The use of a plate with a large width to depth ratio can enable the use of the many 2-D models and avoid the complications and added uncertainty of the 3-D models. However, such ratios cannot always be obtained in practice, especially at larger depths, in which case the 3-D models would be required.

2.2.2 Control of Manipulators for Interaction with Soil

There has been extensive prior work in the area of robotic excavation. The majority of these systems incorporate some form of adaptation in the control scheme. The adaptation in these cases refers to the capability of altering the digging trajectory to avoid stalling or to avoid obstacles, not explicit adaption to soil properties. Each group of researchers in the area of robotic excavation are discussed briefly below.

Singh and others at CMU [68, 101, 102, 100] have done much work in the area of planning excavation and constructing complete systems capable of autonomously scooping and loading material. Originally they had used a linear failure surface model based upon the model from Reece [83], but they also developed a neural network learning scheme to predict resistive forces [16]. This group is probably the most advanced in this field. Their manipulator executes digging strokes in pre-planned trajectory motions after the high level planner tells them where to dig. Their primary focus is to successfully remove a selected volume of material through strategically planned strokes. They have implemented their system on a Caterpillar backhoe and combined it with laser range finders to measure the soil surface and locate dump trucks for autonomous truck loading [109].

Shi, Wang, and Lever [96, 95, 97, 122] used fuzzy logic rules derived from the knowledge of a skilled operator to adjust digging trajectories incrementally to avoid obstacles and stalling. They used force sensor measurements to trigger state changes and obstacle navigation was limited to in-plane 2-D navigation, either under or over objects. They also performed some basic study of neural network methods.

Bradley and Seward and a variety of colleagues [11, 10, 91, 92] have constructed a 1/5th scale hydraulic backhoe arm and have studied digging in a planar trench. Their system is not back-driveable, however, they implement a software-based force feedback measurement system using induced errors in desired trajectory tracking. They avoided the use of sensitive force sensors in an inherently rough environment. Their obstacle avoidance scheme is basically a trial and error method constrained to the plane of digging.

Huang and Bernold and colleagues [7, 44, 45] have studied impedance based methods for digging control, obstacle detection via discrete contacts, and made initial attempts at characterizing soil properties through digging resistance measurements. They discuss methods for handling obstacles by recording coordinates of impact with the obstacle, moving slightly and attempting to check for another impact. By repeating this procedure the spatial extent of the obstacle can be determined. Sampling of multiple points happens discretely and is a somewhat lengthy process. If the manipulator is back-driveable, a continuous method for obstacle mapping which we have developed can also be attempted [42].

A few other sets of researchers in the field of excavator control can also be mentioned. Koivo and Vähä and colleagues [8, 52, 56, 119] have done work on modeling the dynamics of excavators and for conducting simulations of excavator systems. Bullock *et al.* [12] studied planning techniques to excavate a given geometrical region of soil and conducted basic studies of varying digging depth based upon strain measurements on their robotic arm. Bodur *et al.* [8] conducted simulations of a backhoe, where the desired digging path is adjusted in increments when the force limit is reached so that the trajectory is a bit higher at each step until the force limit is satisfied. Forces in the simulations are based upon equations from Vähä's study [119]. And finally, one other interesting direction of research was from Ostoja-Starzewski *et al.* [76] who examined the use of force-feedback in a master-slave configuration to allow operators to have a better sense of the forces of interaction in excavation.

2.2.3 Specific Work on Parameter Estimation

As noted, most of the work on robot-soil interaction has been concerned with planning and obstacle negotiation. These have typically been large scale systems, where researchers are not interested in precise interactions. In contrast, the goal of this research is estimation, not excavation.

There has been a small amount of work from robotics researchers examining the topic of property estimation. Bernold [7] mentions how "measured forces can be used to create characteristic patterns or fingerprints for various soil conditions." Bernold's idea was to develop a means of classification of soils into similar categories rather than direct parameter estimation. Some very initial experimental results were provided which support his hypothesis, showing that different soils will produce different interaction forces. Further work on categorizing soil types from interaction data has not resulted.

There is also the work from Luengo, Singh, and Cannon [68] on interaction force estimation. Their system uses a large hydraulic backhoe with a bucket scooping up soil. Estimation is done concurrently with excavation. They estimate parameters for use in their selected soil model to obtain reasonable predictions of interaction forces. The accuracy of the force predictions are assessed, but the accuracy of the parameter estimates are not. As will be seen in this thesis, a wide variety of parameter values can produce the same forces. Interaction forces alone cannot be used for parameter estimation, additional information is required. Thus, while they obtain force estimates to within roughly 10-60%, there is no guarantee on the accuracy of their parameter estimates. However, since their goal is force prediction, not parameter estimation, they need not be concerned with this fact.

2.3 Proposed Approach

As stated throughout, the ultimate goal of this work is to develop techniques to accurately estimate soil properties through controlled interactions. For this purpose, we need to know how these properties relate to quantities which can be measured. For robotic manipulators, these quantities are typically force and displacement. If visual feedback is available, then we can also estimate the failure region.

In order to understand how the soil properties relate to the force and displacement, a study of the various soil models for predicting failure force is required. Since there are a variety of models in existence, and not all necessarily in agreement, a few models are examined and compared in Chapter 4.

These soil models will require certain conditions on the loading. In order to compare measured forces with these models, the manipulator must be controlled to obey the loading requirements. The development of suitable manipulator control techniques is presented in Chapter 5. Experimental interaction data is collected with sample soils and presented in Chapter 6.

Finally, in order to use the interaction data to obtain soil property estimates, the soil models must be inverted. A graphical technique for the inversion of the soil models is developed in Chapter 7 and applied to the experimental interaction data.

Before the above techniques are presented, the details of the development of the robotic manipulator arm used in this research are provided first in the following chapter.

Chapter 3

Hardware and Control

This chapter discusses the evolution of the manipulator from its initial bare-bones state to the final system for experimentation. The limitations of the manipulator resulting from design choices and how those limitations exhibit themselves in data collection are outlined. In addition to the manipulator itself, the development of the supporting hardware for sensing, computation and control is presented. Finally, the software architecture, manipulator control, and user interface are discussed. Material covered in this chapter is not essential for understanding the later chapters and may be bypassed for those more interested in soil modeling and interactions.

3.1 Manipulator Evolution

Very rarely is any piece of hardware perfected in its first incarnation, and our system is no exception. Design is an iterative process, where insights are gained through discovery of shortcomings. A significant amount of time was spent completing and redesigning our manipulator to achieve the levels of performance necessary to conduct the required experiments. In the process, a number of critical issues were uncovered which may be useful to future researchers.

The primary design of the manipulator used in this research was completed by two other researchers, Katz [51] and Curtis [24]. Originally, the manipulator was designed to be a platform for the study of nonlinear compliant transmissions. It was to be equipped with a hybrid of two rotary and two linear compliant elements on the four major joints. The study of the novel compliant elements themselves were completed within the framework of one degree-of-freedom (DOF) test-beds.

These compliant elements were not integrated into the final manipulator for a number of reasons. Due to time constraints, the other two researchers were not available to modify the designs of the elements to have the proper strength and sensing range. It was discovered that the typical loads experienced in our experiments would be greater than the strength and sensing range of the original designs. In addition, the compliant elements were not fundamentally necessary for this research. Although the compliant elements were originally envisioned as a means for obtaining force information, for the proof-of-concept nature of this research, an accurate force/torque sensor was used instead. This allows us to separate any issues associated with obtaining accurate force measurements through the compliant elements from issues directly related to the primary goal of property estimation through controlled interactions.

In addition to the incorporation of the force/torque sensor, other modifications were made to the manipulator design. In the next sections, the original design and the subsequent modifications are briefly outlined.

3.1.1 Initial Design

The original design sought to develop an arm which could achieve approximately 5 lbf at the end-point comfortably, had a workspace of approximately 30-40 inches, and had at least 4 DOF (6 DOF would have been ideal). The end-effector DOF(s) should not be back-driveable to ensure that the end-effector motor(s) do not have to work against the other arm motors during stroking. A planar design with a base azimuth DOF was chosen as a starting point.

The resulting manipulator design is shown in Figure 3.1. The design has a few notable features, including a differential in the elbow for increased torque capability in the most critical joint for stroking, and a very compact end-effector design with a worm gear transmission. The base and shoulder joint were intended to have rotary compliant elements. The two motors located to the far left were to drive the differential located in the elbow. The large space between the rear motors and the shoulder joint was to accommodate linear compliant elements which would be placed in-line with the cabling. As noted previously, the compliant elements were not incorporated in the final manipulator.

Figure 3.1: The original manipulator design, un-cabled, before the modifications and additions to make it fully functional. Rotary compliant elements were to be placed in the base and shoulder and linear compliant elements were to be placed in-line with the cabling in the open space above the horizontal base platform.

3.1.2 Design Revisions

This section briefly discusses the primary revisions to the original design. These highlight issues which may be of interest for future researchers designing manipulators. Figure 3.2 provides a graphic summary of the modifications.

- **Stronger Cables** Larger cable diameters (0.054", 240 lbf) than the ones originally selected (0.032", 120 lbf) were required to carry loads up to the desired 5 lbf. This required a redesign of the routing to accommodate the larger diameter cable.

- **"Gear" Reduction** A smaller capstan for the shoulder motor and larger elbow pulleys were required in order to increase the force capability. These modifications effectively doubled the force capability of the arm and also reduced the effect of the backlash in the motor gearheads. The new elbow pulleys also had cable terminations so that two lengths of cable can be used instead of one lengthy one which would be difficult to pre-tension to a reasonable level.

- **Stiffer Links** Reinforcement pieces were required to stiffen the open rectangular channel used for the upper arm link and also to stiffen the long base platform. Both of these would deflect under typical operating loads.

- **Counterweights** Counterweights made of Tungsten alloy ($\sim$ 17.6 g/cc) were added to statically balance the arm (elbow: $\sim$ 2 lbf @ 6.75", shoulder: $\sim$ 10 lbf @ 7.25"). All motions executed by the arm are expected to be low velocity maneuvers and so the increased inertia is of less concern than the force capability of the arm. In most soil interactions, the weight of the arm would actually be helpful (e.g. insertion and downward stroking). On the other hand, it would complicate free-space motions, lifting, and data processing. Also, unintended power shutdowns would result in the manipulator falling under its own weight.

- **Joint Stops** Joint stops were added to each joint for calibration of the relative (incremental) encoders. A homing procedure was implemented to locate these stops at start up.

- **External Encoders** The motors which had been selected were Maxon RE035 DC motors with 72.38:1 three-stage planetary gearheads. Each stage of the gearheads have a no-load backlash of $< 0.7°$, which results in approximately 2° of backlash at the motor shaft. Due to the large backlash in the motor gearheads, external encoders were essential on the major joints in order to have accurate end-point sensing. The external encoders are 3600 counts-per-turn (CPT). Prior to the addition of these encoders, the end-point sensing accuracy was approximately 0.5", after the addition, the accuracy is approximately 0.05" (typical insertion depths are 1"). This is still much larger than desired, but to achieve greater accuracy would require a substantial redesign.

- **Sensor Co-location** The end-effector was redesigned in order to place the force/torque sensor directly behind the plate instead of at the end of the forearm link before the end-effector motor. Figure 3.3 shows the design before and after the modification. This allows direct measurement of the force on the plate. A flat plate was chosen because of the resulting simplification in the soil interaction models. This is consistent with the goal of property estimation rather than excavation, which would be impractical with a manipulator of this size and strength.

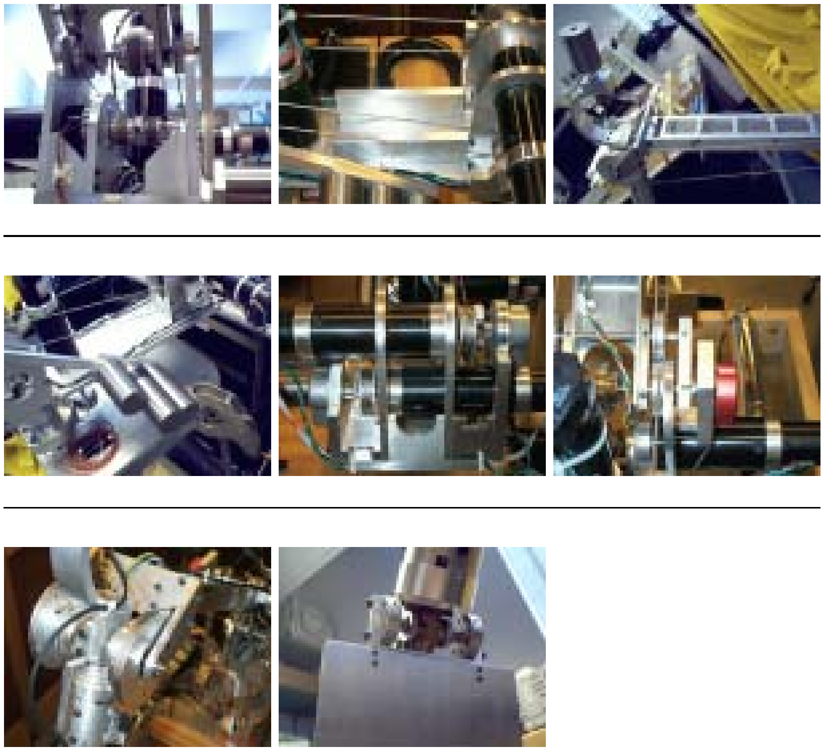

Figure 3.2: Summary of modifications from left to right, top to bottom: (row 1) redesigned smaller capstan for shoulder, base reinforcement, elbow counterweight and link 1 reinforcement, (row 2) shoulder counterweight, external encoders for elbow motors, external encoder for shoulder joint, (row 3) enlargement of elbow differential pulleys and forearm joint stop, and end effector design utilizing a worm gear.

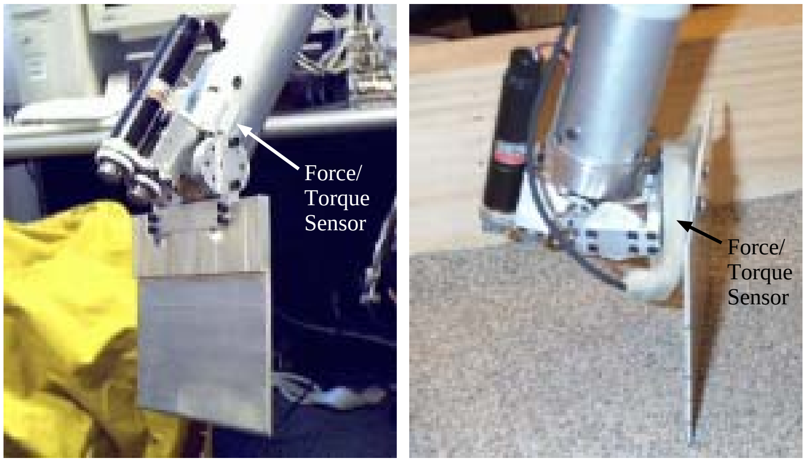

Figure 3.3: The previous end-effector design had the F/T sensor located between the end-effector and the arm (in place of the cylindrical piece at the end of the forearm shaft). The new end-effector places the F/T sensor directly behind the plate (wrapped in latex for protection from sand particles).

3.1.3 Limitations, Compensation, and Lessons

There are a number of limitations which still exist with the final manipulator used in experimentation. These limitations are in strength, position sensing accuracy, and arm flexibility.

At nominal arm extension, the arm can achieve 5 lbf at the end-point, but there is no safety factor beyond that limit as originally hoped. With the stronger shoulder cables, the shoulder motor becomes the limiting factor by a small margin[1]. This strength limitation translates into limits on the width and depth of insertion of the plate used in experimentation. Although greater strength would have been preferred, in actuality, an arm of this size being capable of exerting 5 lbf is very reasonable. Any rover-based manipulator arm would likely be in this range.

As mentioned previously, the resulting end-point sensing accuracy at nominal extension is approximately 0.05" and the backlash is approximately 0.5". The backlash is less of a factor than the sensing

---

[1] The motor can generate approximately 70 in lbf continuous torque at the shaft. The capstan is 0.75" in diameter, resulting in a force in the cable of 190 lbf. The new 0.054" cable has a strength of 240 lbf.

accuracy since during digging the motors will always be on one side of the deadzone. The sensing accuracy, on the other hand, creates difficulties in obtaining accurate insertion depths (typically 1") and smooth end-point displacement data. The uncertainty in insertion depth can be compensated for with external measurements during experimentation. The end-point displacement will contain discontinuous jumps as a result of the resolution of the external encoders. Although this is evident in the resulting data, the control compensates for the jumps and settles fairly rapidly. The resulting force measurement is often unaffected by the discontinuities. Thus, the resulting poor sensing accuracy can be overcome. Future designs can easily avoid these problems by selecting motors with minimal backlash.

Another limitation, tied to both the strength and sensing accuracy, is the flexibility in the arm. There exists a small amount flexibility in the actual arm links, but the main source of flexibility lies in the cabling. Typically, one would pre-tension the cables to at least half the expected load. Due to the space limitations and the long runs of cable for the elbow joint, the design does not incorporate enough space to properly pre-tension the cables. This results in a very evident stretch in the elbow transmission which is not sensable with the external encoders. The stretch is typically up to 1-2 degrees at the elbow at nominal loads. In order to compensate for this stretch, the apparent stiffness of the arm can be measured and approximately compensated for. Appendix A documents the flexibility compensation.

In summary, there are a number of limitations that still remain in the system. Design revisions have been completed to compensate for these limitations so that useful data can be obtained. In the control and experimentation, this work has endeavored to remove any special characteristics of this particular manipulator so that no special artifacts can be attributed to this system. Ideally, all the data is independent of the specific system from which it has been obtained. Experiments conducted with another system under the same conditions are expected to produce the same results.

3.2 Final Hardware System

Figure 3.4 shows the final manipulator, workstation, power rack, and sandbox. The final manipulator is a five DOF arm whose evolution has just been discussed. The first four DOF (base, shoulder, elbow, forearm twist) are all cable-driven. The wrist uses spur gears which drive a final worm gear. The arm has a reach of approximately 36

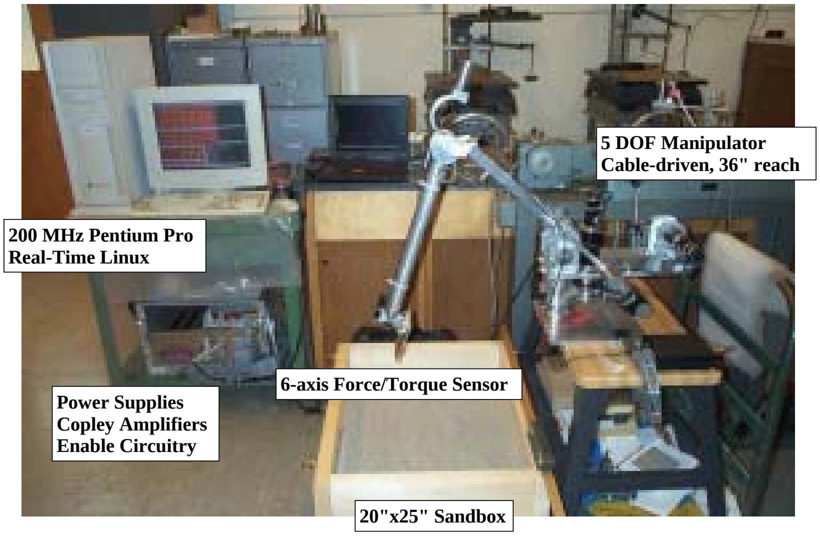

Figure 3.4: Final hardware system showing the manipulator arm, workstation, power rack, and sandbox.

inches fully extended. It can lift approximately 5 lbf at 80% extension (the typical operating extension).

The arm is equipped with a Mini-40 6-axis force/torque (F/T) sensor from ATI Industrial Automation shown in Figure 3.5. The F/T sensor is 40 mm in diameter and 12.3 mm thick. It uses silicon strain gauges for greater signal strength and overload protection compared to foil gauges. The calibrated sensing range is 100 N shear force, 300 N normal force, and 5 N-m torque with 16 bit resolution. The overload protection has a maximum allowable shear of 1300 N, normal of 2900 N, and torque of 25 N-m. It interfaces using an ISA card in the PC which can produce readings at rates up to 4 kHz.

This sensor was selected based upon the original manipulator design with the sensor placed after the end-effector motor (Figure 3.3, left image). The driving consideration was the torque sensing range. The calibrated sensing range is quoted for loading along individual axes, combined loading situations have reduced limits. Loads of up to 22 N (5 lbf) at 0.2 meters were expected, resulting in 4.4 N-m at the sensor – near the limit for combined shear/torque loading. With the new placement of the sensor directly behind the plate, the sensor has a larger range than necessary. Typical interactions will only use less

Figure 3.5: The Mini-40 6-axis force/torque sensor is shown above, where we have used small standard brass masses to test the Z-axis calibration.

than 1/10th of the full sensing range (up to 20 N). The calibration was tested over the typical loading range and found to be within 1% of the actual force.

The manipulator arm is controlled by a 200 MHz Pentium Pro computer equipped with an 8-axis ServoToGo I/O card running Real-Time Linux [5]. The I/O card provides 8 encoder input channels, 8 analog-to-digital (A/D), 8 digital-to-analog (D/A) channels, and a number of digital input-output (I/O) channels. The D/A channels are used to provide inputs to the amplifiers which power the motors and the A/D channels are used to monitor the current and voltage output of the amplifiers. The servo loop is programmed as an interrupt service routine (ISR) triggered via the interrupt generated by the I/O card which can be programmed for different rates. Currently the system is run at 500 Hz. All computations are done by the Pentium Pro processor.

The manipulator arm is powered using five Copley Controls Model 412 DC Brush Servo Amplifiers which are powered by two 48V DC power supplies. These are all mounted within a compact custom built rack (18" x 19" x 12") shown in Figure 3.4. The rack also contains basic logic circuitry for the enable lines, kill button, and break-out wiring for the ribbon cables from the I/O card.

3.3 System Architecture

Much of the initial inspiration for the style of the architecture was drawn from that of the Whole Arm Manipulator (WAM) system [72,

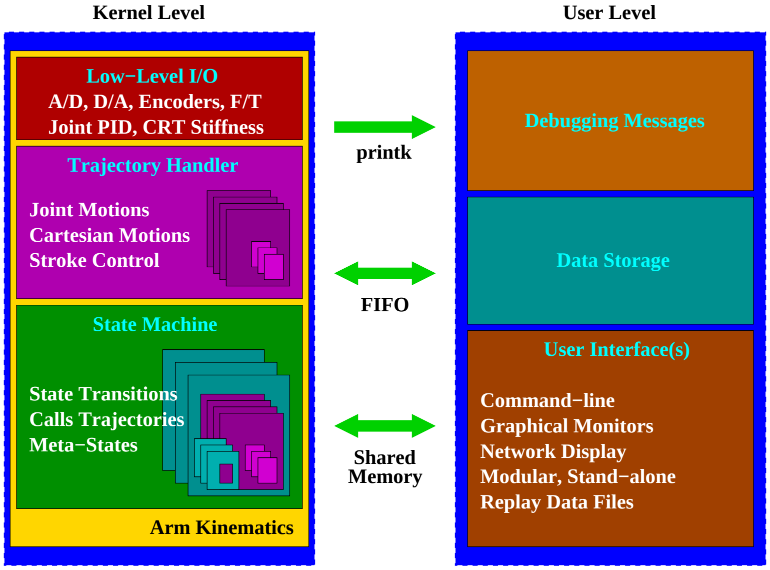

Figure 3.6: The illustration above shows the system architecture for manipulator control. On the left, the servo loop is run as a kernel level process which operates in hard real-time with guaranteed bounds on latencies. On the right, the user-level processes have lower priority, no guarantees on timing, and are run in the time left over from the kernel-level processes.

41]. The architecture allows for multiple control laws, trajectories, and state sequences in a very modular fashion. This modularity facilitates the addition of new components in a structured manner, allows for independent testing of individual components, and facilitates rapid construction of new behaviors by combining existing behaviors. The complete system is programmed in C.

Figure 3.6 shows an illustration of the system architecture. Using the Real-Time Linux framework, the controller (servo loop) is run as a kernel-level process having the highest priority on the system. The terms “servo loop” and “controller” will be used interchangeably in the following discussions and refer to the kernel-level process which controls the manipulator. The user interface and data storage routines are run as user-level processes (along with the rest of the standard Linux kernel and programs). These user-level processes are run in the time left between periodic calls of the kernel-level process.

The controller (kernel-level process) communicates to the user-level processes via kernel print statements (for debugging messages), shared memory (for connecting to the user interface), and first-in-first-out pipes (FIFOs) (for data storage). The user interface is completely independent from the controller. This independence allows for the implementation of different user interfaces which can be used interchangeably or simultaneously, tailored for specific purposes.

This section presents general details about each of the components of the system and manipulator control. A more detailed presentation of the specific control of the manipulator for digging will be given in Chapter 5.

3.3.1 Manipulator Control

The components of the servo loop are shown in the left box of the Figure 3.6. The components are called sequentially within the servo loop. The servo loop is run in hard real-time with a guaranteed frequency of 500 Hz based upon interrupts generated by the I/O card.

The servo loop can be divided into multiple conceptual units. The lowest level handles the basic input and output routines, such as reading encoders, reading the F/T sensor data, and computing the torque output. The next unit is the trajectory generator which produces the sequence of desired positions to move the arm. There are multiple possible trajectories, including Cartesian and joint space motions. The next unit is the state machine. In the state machine, more complex logic can be programmed to execute a sequence of states (each of which can be trajectories or other state sequences) based upon various state transition conditions.

Underlying the trajectory generator and state machine, and tied to the low-level control, is the arm kinematics. Before discussing each of the units of the servo loop in turn, the derivation of the arm kinematics is presented.

3.3.1.1 Kinematics

The full arm 5-DOF forward and inverse kinematics and Jacobian computation are provided in Appendix B. Fortunately, the inverse kinematics can be computed directly, instead of resorting to an iterative approach. The kinematics routines convert from the five joint values to Cartesian x, y, z coordinates and two orientation angles n_1 and n_2 which represent the angle of the end-effector relative to vertical and the plane formed from the first two links of the manipulator (the vertical plane rotated through the base azimuth angle) respectively.

Figure 3.7 shows the coordinate frame for the arm and the orientation vectors. The end-point of the arm is located at the center bottom tip of the plate. For the orientation vectors, the rotation is first done about the Y axis by amount n_1 and then about the Z axis by amount n_2. These orientation angles were chosen so that the inverse kinematics could be computed directly using these angles.

These kinematics routines are fundamental to the control of the manipulator and are used extensively in the post-processing conversion of data. The forward kinematics, Jacobian, and inverse Jacobian are computed during each pass through the servo loop immediately following the low-level input routines and prior to the trajectory generation routines. If the trajectory generator is operating in Cartesian mode, then the inverse kinematics routines are called immediately after the trajectory generator in order to convert the desired Cartesian position into a desired joint position to feed to the low-level output routines. Finally, the low-level output routines use the Jacobian matrices to compute the proper torque output if operating in a Cartesian based control.

3.3.1.2 Low-Level Control

The low-level control can be divided into input and output routines. The input routines consist of reading the encoders, A/D channels, and F/T sensor data and performing the appropriate conversions. Basic filtering is done on the encoder inputs to smooth the signal. In addition, due to the differential in the elbow and the coupling of the shoulder and elbow joints, a motor/joint transformation (Appendix B) is applied to the encoder input to convert from motor space to joint space.

For the output, there are two basic types of low-level control. A number of other controllers are implemented as variations on these two basic types, but are not used frequently (such as velocity control). The two basic types are joint proportional-integral-derivative (PID) control and Cartesian Stiffness Control (Salisbury [89]).

The joint PID control is made slightly more interesting than a standard joint PID due to the presence of the motor encoders *and* the external encoders. Using the external encoders alone, a high stiffness cannot be obtained due to the backlash. Using the motor encoders alone, the sensing accuracy is unacceptable. Therefore, a PID loop is closed around the motor encoders to obtain high stiffness, and the external encoders are used with an integral gain for absolute positioning accuracy. Due to the differential and the coupling, joint gain matrices

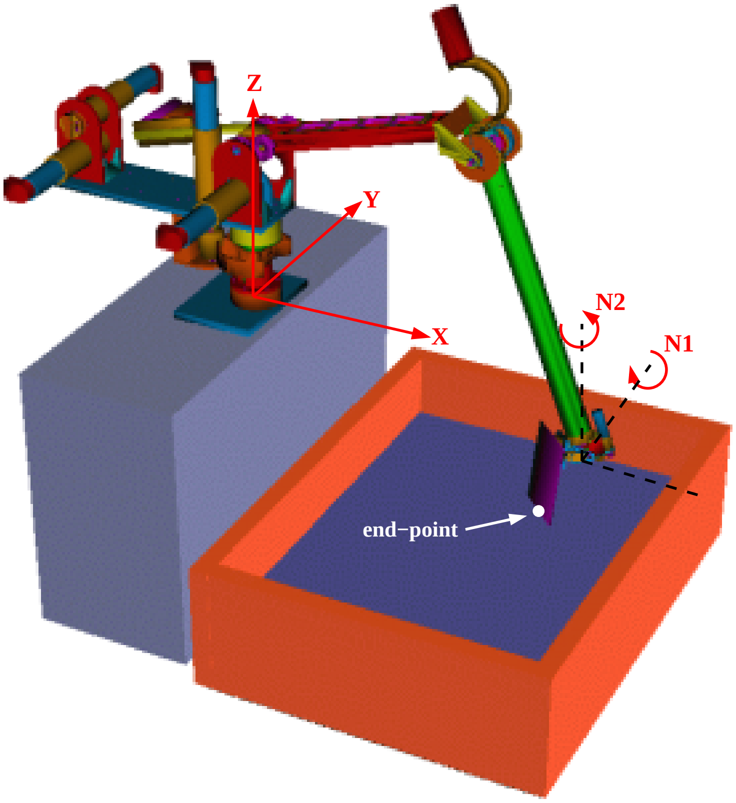

Figure 3.7: An illustration showing the Cartesian axes for the arm kinematics. The XYZ coordinates are relative to the base of the mounting plate, and N1 and N2 are orientation vectors for the end-effector. The end-point of the arm is located at the center of the bottom of the plate.

are used instead of gain vectors. The gain matrices are computed using diagonal joint gain matrices multiplied by the joint/motor transformation matrix.

$$\begin{aligned}\boldsymbol{\tau}_{mtr} &= \mathbf{T}_{jnt}^{mtr}\left[\left(\mathbf{K}_{P_{mtr}}\tilde{\mathbf{q}}_{mtr}+\mathbf{K}_{D_{mtr}}\dot{\tilde{\mathbf{q}}}_{mtr}\right)\right.\\ &\qquad\left.+\left(\mathbf{K}_{P_{ext}}\tilde{\mathbf{q}}_{ext}+\mathbf{K}_{I_{ext}}\int\tilde{\mathbf{q}}_{ext}\,dt\right)\right] \qquad (3.1)\end{aligned}$$

where $\tilde{\mathbf{q}}_{mtr} = \mathbf{q}_{des} - \mathbf{q}_{mtr}$ and $\tilde{\mathbf{q}}_{ext} = \mathbf{q}_{des} - \mathbf{q}_{ext}$.

Cartesian Stiffness Control is also implemented to allow specification of a desired stiffness which is independent of arm configuration. This is the primary control which is used during most of the experimentation, for reasons explained in Section 5.3.1. The position dependent Jacobian matrix is used to convert a Cartesian stiffness matrix into a position dependent joint stiffness matrix. Since the arm is essentially planar with a base rotation, a cylindrical stiffness is specified instead of a Cartesian stiffness. A cylindrical stiffness matrix is obtained by rotating a Cartesian stiffness matrix by the angle of rotation of the arm base joint.

$$\begin{aligned}\boldsymbol{\tau}_{mtr} &= \mathbf{T}_{jnt}^{mtr}\left[\mathbf{J}(\mathbf{q}_{ext})^{-1}\mathbf{R}(q_0)^{-1}\;\mathbf{K}_{crt}\;\mathbf{R}(q_0)\mathbf{J}(\mathbf{q}_{ext})\;\tilde{\mathbf{q}}_{mtr}\right.\\ &\qquad\left.+\;\mathbf{K}_{D_{mtr}}\dot{\tilde{\mathbf{q}}}_{mtr}\right] \qquad (3.2)\end{aligned}$$

The gain on the velocity term is the same as in the joint PID control. It is unnecessary to convert this into a Cartesian frame since most of the motions will be of low velocity and the primary force will be a result of position error rather than damping terms. An integral term is not used in this control mode since its presence would alter the desired stiffness. When using the stiffness control, the external encoders are used for accurate position sensing and to drive the desired position in the trajectory generation, but they do not directly enter into the control law. They are only indirectly used in the final low-level control law through the desired position and the Jacobian matrices.

The gains of the above controllers were tuned empirically to obtain high stiffness with smooth motions. More sophisticated adaptive control was not found to be necessary for a number of reasons. The typical motions of the arm are fairly slow. The arm is counterbalanced for gravity compensation. The arm has high inertia, high gearing, low stiffness, and large backlash, making fast maneuvers problematic.

3.3.1.3 Trajectory Handler

There are multiple trajectories which are programmed to provide desired position and velocity values for the arm every servo loop. These trajectories can be classified as joint space or Cartesian space trajectories. Some examples of these trajectories would be joint space moves, Cartesian space moves, insertion trajectories, and various digging stroke methods. More details about the insertion and digging trajectories will be provided in Chapter 5.

Only a single trajectory is active at any given moment, but a listing of future trajectories to be executed is continuously maintained. This trajectory list takes the form of a circular ring of pointers to trajectory structures. As one trajectory completes, the next trajectory on the ring is initialized and run. When a sequence of trajectories is completed and the rest of the ring is empty, a joint or Cartesian hold is executed according to the type of the last trajectory.

Each trajectory is self-contained in its own file and relevant variables are passed as function arguments. Trajectories each have initialization and exit routines. They are time based, so that they are called every servo loop and must produce desired position coordinates for each time step. They are either finite duration, ending automatically after completion, or infinite duration, requiring a command to end execution.

The tracking of the current active trajectory, maintenance of the circular ring of future trajectories, and handling of trajectory transitions is all done by a trajectory handler. The modularity of the individual trajectories and the implementation of the trajectory handler allow for easy construction of complex sequential behaviors. In order to have non-sequential and event-driven behaviors, a finite state machine architecture was implemented which interfaces with the trajectory handler.

3.3.1.4 Finite State Machine

The finite state machine (FSM) allows for the programming of a set of states which can be moved between in an arbitrary order, depending upon various transition conditions. Typically, it is used to control the flow of a linear sequence of event-driven behaviors. However, it is capable of implementing a more complex set of state dependent transitions.

In this system, a state machine “sequence” is a set of independent states, each of which can execute a set of simple variable assignments, start or stop data storage, or call a trajectory or even another sequence of states. There are specific entry and exit functions which can be programmed for each state transition. In contrast to a trajectory, where the driving variable is always the time, the state sequences are time-independent and transitions are executed based upon programmed transition conditions which must be satisfied.

An example of a state sequence is the homing routine used to initialize the arm upon start up. For each joint, this sequence calls a joint-space "touch" trajectory that moves a specific joint incrementally until contact with a joint stop is detected via a large position tracking error. Once the joint stop is detected, the trajectory ends. This triggers a state transition and the "touch" trajectory is called for the next joint. When all stops have been contacted, the home position for the encoders is reset in the low-level input routines.

Another similar example is the wall sensing routine used to detect the edges of a sandbox. This routine calls a sequence of Cartesian "touch" trajectories which use the force/torque sensor to detect wall contacts. Each contact triggers a state transition which starts the next "touch" trajectory.

A widely used sequence, which is the primary means for data collection, is the "insert-stroke-pullout" sequence. This sequence assumes the arm is located above the soil at the desired point for stroking. The first step in the sequence uses a Cartesian "touch" trajectory to locate the soil surface. Next, it inserts the plate to a specified depth using an "insert" trajectory. Then a "stroke" trajectory is called. Finally, a Cartesian "moveto" is used to pull the plate out of the sand. Data storage is also optionally triggered at both the "insert" and "stroke" stages of the sequence.

A final example is the multiple-stroke sequence. This is an example of a "meta-sequence" – a state sequence that calls other state sequences. This meta-sequence positions the arm in multiple locations above the soil using Cartesian "moveto" trajectories and at each location it calls the "insert-stroke-pullout" state sequence. Using this meta-sequence, a single command can be entered into the user interface that will cause the arm to autonomously execute six strokes at various locations with associated data collection to time stamped data files.

This combination of a trajectory handler and a state machine architecture greatly simplifies the programming of the manipulator. It allows for easy reuse of trajectory and state sequence components and provides a simple framework for constructing complex sequences of behaviors.

3.3.2 User Interface

The final portion of the system architecture is the user interface. As mentioned previously the user interface is completely independent of the servo loop. The servo loop runs as a kernel-level interrupt service routine. There are only three methods by which the servo loop can communicate with the rest of the operating system. These three methods are via kernel print statements, shared memory, and FIFOs. All three methods are used to define an interface through which user-level programs can monitor and control the behavior of the servo loop and collect data.

The characteristics of each of the methods make them best suited for certain functions. The kernel print statement method is used primarily for debugging purposes since it is a one-way communication. While both the FIFO and shared memory methods can be used for two-way communication, shared memory is much more versatile. Therefore, the user interface communicates with the servo loop through the shared memory method. FIFOs are good for communicating streams of data and are therefore used as a means for data collection.

When data storage is triggered in the servo loop (by a trajectory, state sequence, or user command), a predefined structure composed of variables of interest are output via a FIFO. Whenever the arm is in operation, a user-level process is run which continuously checks for data in the FIFO. When data is found, it is decoded by the user-level process and stored to time-stamped text files. A special character sequence is output by the servo loop to signal the start of a new data file. Thus, data storage is done automatically and is independent of the primary user interface.

The primary user interface operates via a command-line interface combined with multiple graphical displays. Figure 3.8 shows the typical user interface comprised of multiple text monitor windows and a graphical 3D monitor window. The monitor windows can be individually enabled or disabled as needed. The command line interface has various features such as command completion and scripting capabilities. Inputted commands are communicated via shared memory to the kernel-level servo loop to start trajectories or state sequences, enable storage, or set various parameter values.

The text monitors are programmed using simple Xlib routines. When enabled, each monitor forks off as a separate process that obtains the data to be displayed via user-level shared memory. A distinction is made here between the shared memory used to communicate between the kernel-level controller and the user-level processes and the shared memory used to communicate between various user-level processes. The user-level shared memory is a copy of the contents of the kernel-level shared memory that is updated at a slower rate.

The graphical 3D monitor is a stand-alone program created using

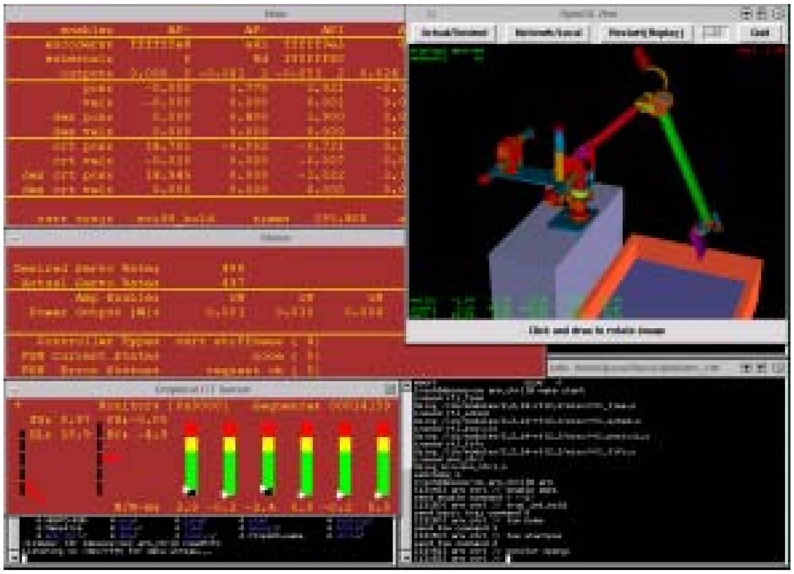

Figure 3.8: The user interface for manipulator control is comprised of multiple text monitor windows, a graphical 3D monitor window, and a command-line interface.

a combination of C and Tcl/Tk using Togl (an OpenGL widget for Tcl/Tk). The graphical monitor is typically run on a separate computer from the arm controller to off-load the computationally intensive rendering. The monitor is composed of two processes which communicate with each other via user-level shared memory; one renders the arm and the other handles the network communications over TCP/IP to the arm control computer. The rendering of the arm is generated by exporting assemblies from I-DEAS, our CAD package, into VRML. Since the arm was designed using I-DEAS, the rendering is identical to the actual manipulator (to very fine detail in fact, missing only the bolts and cabling).

The format conversion from VRML to OpenGL was accomplished with various tools to convert to 3D Studio (I have used AccuTrans 3D[2] and AC3D[3]). The 3D Studio files were then converted to C source code

---

[2] Commercial program with limited time trial, available at http://www.micromouse.ca/, other free alternatives may be available, such as AC3D or another program called 3Dto3D.

[3] A feature limited trial is available for both Windows and various UNIX oper-

containing OpenGL display lists for each of the joint assemblies (using VIEW3DS[4]).

As mentioned previously, the independence of the user interface from the servo loop control allows us to operate multiple user interface programs interchangeably or simultaneously. In addition, because all communication between the user interface(s) and the servo loop is through shared memory, I have also added a feature which simulates the servo loop shared memory using stored data files. The user interface can then serve as a stand-alone data file playback device.

3.4 Summary

This chapter has discussed the evolution of the manipulator used in this research and the lessons learned in the process. Designing with low backlash, stiff transmissions, adequate end-point sensing precision, and co-located sensors is recommended. This chapter has also discussed the design of the system architecture for control of the manipulator. An emphasis has been placed on the modularity of the system, which has greatly increased the ease with which complex behaviors can be implemented.

---

ating systems at http://www.comp.lancs.ac.uk/computing/users/andy/ac3d.html.

[4] A free 3D Studio to OpenGL converter written by David Farrell, which has since disappeared from the internet, but can be found inside of another program called GnOpenGL3ds at http://www.ifrance.com/yburgevin/.

Chapter 4

Soil Modeling

This chapter examines the different methods for the prediction of the force required to move a flat plate embedded in soil. In order for the plate to move, the soil must be displaced. This typically occurs with a failure surface developing between the moving soil directly in front of the plate and the stationary soil beyond. Therefore, the expression, "failing" the soil, is often used. The force required for failure is also sometimes referred to as the "draft" force – the force required to pull a tool.

This work is solely concerned with the force required to fail the soil, problems with elasticity or more detailed stress-strain relationships for soil are not considered. Instead, this work focuses on the strength of the soil, i.e. stress conditions which lead to failure. Consideration is also limited to dry soil, since it is expected that Martian soil will be dry and have little or no cohesion. The assumption of plane strain is also made in all the methods considered since they are 2-D methods.

Note that this problem is identical to the classic problem of passive and active earth pressure studied in Civil Engineering for hundreds of years, e.g. Coulomb (1776) [21]. Therefore the classical methods from Civil Engineering, as well as the more recent developments, will be examined. In this work, a number of methods have been selected which are representative of different methods popular today. These models are two-dimensional and do not consider pre-failure stress or deformations in the soil mass. The analyses consider soil as a continuum medium, in contrast to a few recent developments that explicitly treat the particulate nature of soil.

In this chapter, a total of five different methods are considered. These include two limit equilibrium methods, another method with predictions provided in tabular format, and two limit analysis methods – one providing an upper bound and the other providing both an upper and lower bound. The basics of the development of each of the models is presented. The limitations and sensitivity of the models are discussed and the resulting predictions are compared.

4.1 Background on Methods

The various methods which are presented here were chosen to reflect different approaches to the draft force prediction problem. These methods come in two varieties; methods based upon limit equilibrium, and methods based upon limit analysis (Drucker [26]). There are many other possible methods or tables which could also be included in this comparison. The following collection is believed to be representative of the various methods in use today and we believe they constitute a sufficient basis for comparison.

The most basic limit equilibrium method was developed by Coulomb (1776) [21] and assumes a planar failure surface. This model is known to be inadequate for cases where friction develops at the soil-tool interface. The next method, from Ohde (1938) [74], assumes a failure surface composed of a logarithmic spiral section plus a planar section. In contrast to Coulomb's Theory, this method accounts for soil-tool friction. These methods are typically used as ground truths for verifying more recently developed models – Coulomb's Theory for its historical usage and the logarithmic spiral due to its greater accuracy in predicting forces for frictional wall interfaces.

Another method that is commonly used as a basis for comparison is Caquot and Kerisel's earth pressure tables [17]. These tables are sometimes viewed as a lower bound on the draft force. Some references state that the computation is based upon the logarithmic spiral method and other references state that they are computed from equations of equilibrium. These predictions are most easily found in tabular form. It is clear from examination of the predictions from these tables, that they are neither strict upper or lower bounds.

Finally, two methods are discussed for limit analysis, yielding three predictions, two upper and one lower bound. The method proposed by Chen and Liu [18] is an upper bound based on velocity characteristics. The second method, using a technique from Ukritchon, Whittle, and Sloan [118], is a numerical, finite-element-like, approach which provides both upper and lower bounds. Examples of application of this technique to a variety of typical soil problems is given by Sloan [104]. This thesis extends the application of this numerical technique, providing the first extensive set of predictions for the passive and active earth pressure problem.

The goal of this section is to introduce the numerical limit analysis technique and show the added benefits from application of this technique. It will be shown that the predictions from the numerical technique compare favorably with the other accepted models which are presented. In addition, it will be shown that the numerical technique provides additional capabilities which make it the most versatile of all the methods.

In the following sections, each of the methods is discussed in more detail. Much of the discussion is drawn from three primary sources. For a complete presentation of the limit equilibrium techniques, see Terzaghi [112]. For a complete and rigorous presentation on the application of limit analysis to soils, see Chen and Liu [18]. For a complete presentation of the numerical limit analysis technique, see Sloan [104].

4.1.1 Basic Assumptions and Notation for Models

A number of assumptions are made in the following models. As stated before, the models are two-dimensional and assume plane strain behavior. The soil is assumed to be isotropic and homogeneous. The properties are assumed to be constant during loading. At failure, the behavior is assumed to be perfectly plastic. Lastly, the shear strength of the soil is assumed to be given by the Mohr-Coulomb Failure Law, presented next.

4.1.1.1 Mohr-Coulomb Failure Law

The Mohr-Coulomb failure law provides an expression for the shear strength of soil. It is given by the following equation,

$$s = c + \sigma \tan \phi \tag{4.1}$$

where s is the shearing resistance of the soil, c is the cohesion, σ is the normal stress applied on the shear surface (positive in compression), and ϕ is the angle of shearing resistance[1]. There exists a similar equation for the shear along the soil-tool interface[2].

---

[1] Readers may be more familiar with the concept of a coefficient of friction, μ, rather than a friction angle, ϕ. The friction angle is related to the coefficient of friction by $\mu = \tan \phi$. It represents the angle of the resultant force relative to the vector normal to the shearing plane.

[2] The cohesion, c, is replaced with c_a, and ϕ is replaced with δ. In this case, c_a is the adhesion and δ is referred to as the angle of wall friction.

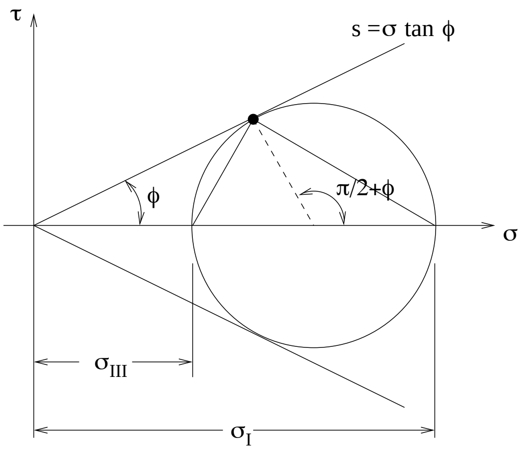

Figure 4.1: Illustration of the Mohr-Coulomb failure law for cohesionless soil.

The failure law can be visualized using a Mohr circle construction. It is noted that the soils in this research are expected to be cohesionless. Therefore, c is zero, and the shearing resistance given by $s = \sigma \tan \phi$. Figure 4.1 shows an illustration of a state of stress at failure. In this construction, the shearing resistance given by the Mohr-Coulomb failure law can be represented as a straight line inclined at an angle of ϕ. Failure will occur when the circle of stress is tangent to the inclined line representing the shearing resistance (as shown). A state of stress below the inclined line will not fail.

4.1.1.2 Notation for Models

All of the models have the following common parameters.

α	tool angle measured relative to horizontal
β	soil surface angle measured relative to horizontal
H	vertical insertion depth of tool
ϕ	internal friction angle of soil against soil
δ	interface friction angle between soil and tool
γ	unit weight of the soil

The parameters can be separated into two groups. The upper three are geometric parameters which can be controlled and the lower three

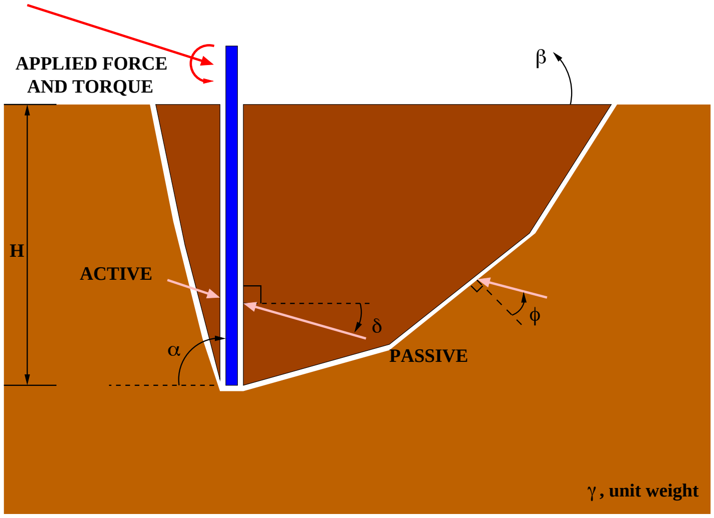

Figure 4.2: Illustration showing the various parameters of the soil models. The draft force on the embedded plate is a combination of the the contributions from the active and passive earth pressures.

parameters are inherent properties of the soil. These parameters are illustrated in Figure 4.2.

4.1.1.3 Active and Passive Earth Pressure

The draft force for an embedded plate can be computed from two contributions, as shown in Figure 4.2. Force is applied to the back of the plate by the soil wanting to fall in to fill the area vacated as the plate moves forward. Force is also applied by the plate onto the soil ahead of the plate in order to fail the soil. The pressure the soil applies to the back of the plate is referred to as the *active earth pressure*. The pressure required to fail the soil ahead of the plate is referred to as the *passive earth pressure*. The net force on the plate at failure can then be expressed as $F = F_P - F_A$, the resulting passive force minus the active force. Because the dependence upon density and depth are well known, the forces are often expressed in terms of *earth pressure coefficients*. These earth pressure coefficients are dimensionless numbers that depend upon the other geometric and soil parameters.

$$F = F_P - F_A = \frac{1}{2}\gamma H^2 \left(K_P(\alpha, \beta, \phi, \delta) - K_A(\alpha, \beta, \phi, \delta)\right) \tag{4.2}$$

Thus, in the following discussions, both the active and passive earth pressure equations will be presented.

4.1.2 Limit Equilibrium Methods

The limit equilibrium models pre-assume a shape of the failure surface (linear, logarithmic spiral). Using this shape, they compute a force equilibrium and optimize for the minimum force to fail the soil. Before discussing the two limit equilibrium models, the concept of a Rankine state of stress, which is used by both models, is presented.

4.1.2.1 Rankine State

Consider the state of stress shown in the Mohr circle diagram in Figure 4.1. A relation for the stress required for failure can be determined for the special case when the principal stresses are vertical and horizontal. This problem was solved for the active and passive case by Rankine (1857) [82] (independent of Coulomb's Theory, which preceded it) and the solution is often termed the active and passive Rankine states. This derivation can be found in most soil mechanics texts.

In the Mohr circle representation, assume that the vertical stress is kept constant and the horizontal stress is varied until failure. Again, the case where the principal stresses are vertical and horizontal is considered. The notation of σ_I simply denotes the largest principal stress and σ_{III} the smallest, which could be either vertical or horizontal. For the active case, σ_{III} would be decreased until failure, and for the passive case, σ_I would be increased until failure.

From this construction, using the properties of the Mohr circle, it can be deduced that the plane along which failure will occur will be oriented at $\frac{1}{2}(\pi/2-\phi)$ from horizontal in the passive case, and $\frac{1}{2}(\pi/2+\phi)$ from horizontal in the active case. Also, a relation between the horizontal stress, σ_h, and vertical stress, σ_v, at failure can be determined (from Lambe and Whitman [62]). Considering the triangle formed by the origin, center of the circle of stress, and the point of tangency, then

$$\sin\phi = \frac{(\sigma_I - \sigma_{III})/2}{(\sigma_I + \sigma_{III})/2} = \frac{\sigma_I/\sigma_{III} - 1}{\sigma_I/\sigma_{III} + 1} \tag{4.3}$$

$$\frac{\sigma_I}{\sigma_{III}} = \frac{1+\sin\phi}{1-\sin\phi} = \tan^2\left(\frac{\pi}{4}+\frac{\phi}{2}\right) = N_\phi \tag{4.4}$$

For the active case, $\sigma_I = \sigma_v$ and $\sigma_{III} = \sigma_h$, and so

$$\frac{\sigma_h}{\sigma_v} = \tan^2\left(\frac{\pi}{4}-\frac{\phi}{2}\right) = \frac{1}{N_\phi} \tag{4.5}$$

and for the passive case, $\sigma_I = \sigma_h$ and $\sigma_{III} = \sigma_v$, giving

$$\frac{\sigma_h}{\sigma_v} = \tan^2\left(\frac{\pi}{4} + \frac{\phi}{2}\right) = N_\phi \tag{4.6}$$

As noted above, both of these relations can be expressed in terms of N_ϕ, which is referred to as the *flow value* or *flow factor*. The flow value and the terminology of a Rankine zone (or Rankine state) is used in the simplest case of Coulomb's Theory, as a part of the logarithmic spiral solution, and as a part of Chen and Liu's upper bound solution.

4.1.2.2 Coulomb's Theory of Earth Pressure

Coulomb's Theory (1776) [21] of passive earth pressure of ideal sand (Terzaghi [112], p. 105) computes the horizontal force required to fail a soil mass and then projects this force into the proper direction given values of α and δ. The method can be used for both positive and negative values of β and δ, though it is known to be increasingly incorrect as δ deviates from zero.

If the simple case of a vertical wall, horizontal soil surface, and no wall friction is considered, the soil will be in an active and passive Rankine state. The vertical stress at depth z is given by the geostatic stress, $\sigma_v = \gamma z$. The solution for the active and passive force can then be computed as

$$F_A = \int_0^H \sigma_h dz = \int_0^H \gamma z \frac{1}{N_\phi} dz = \frac{1}{2}\gamma H^2 \frac{1}{N_\phi} \tag{4.7}$$

$$F_P = \int_0^H \sigma_h dz = \int_0^H \gamma z N_\phi dz = \frac{1}{2}\gamma H^2 N_\phi \tag{4.8}$$

In this simple case, it is found that $K_A = 1/N_\phi$ and $K_P = N_\phi$. This solution is also useful for the other models, for example, it will be used in the logarithmic spiral model.

The solution shown above is extended to handle inclined tools and surfaces and non-zero wall friction. Figure 4.3 shows an illustration of the planar failure surface assumed by Coulomb's Theory. The passive force F_P can be computed from minimizing the value of P_1 given various locations for the point c_1. Given the point c_1 and the assumption of a planar failure surface, by enforcing the constraint of no net moment in the soil (the line of action of all three forces shown must intersect at a point) the value of P_1 can be determined. Then, the optimal passive force is given by $F_P = \min|P_1|$.

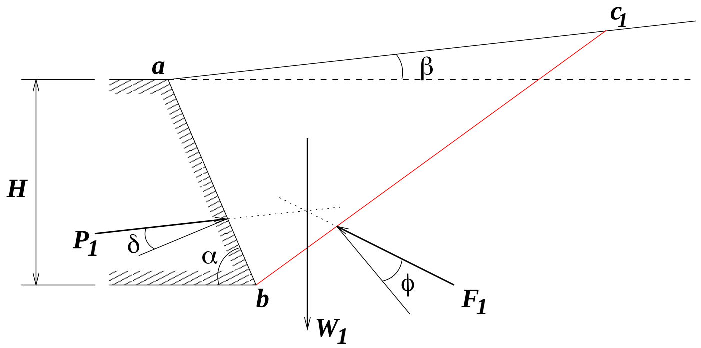

Figure 4.3: Coulomb's Theory assumes a planar failure surface to greatly simplify the problem. The above illustration is for the passive case. The active case is similar, but with opposite signs for ϕ and δ, resulting in forces oriented on the other side of the respective normals. The draft force is then given by $F_P = \min|P_1|$.

The solution can be obtained graphically, as demonstrated above, or algebraically, as Coulomb has done, resulting in the following equation for determining the minimum draft force,

$$F_P = \frac{1}{2}\gamma H^2 \frac{K'_P}{\sin\alpha\cos\delta} \tag{4.9}$$

where K'_P is given by

$$K'_P = \frac{\sin^2(\alpha-\phi)\ \cos\delta}{\sin\alpha\sin(\alpha+\delta)\left[1-\sqrt{\frac{\sin(\phi+\delta)\sin(\phi+\beta)}{\sin(\alpha+\delta)\sin(\alpha+\beta)}}\right]^2} \tag{4.10}$$

To place it in the common form stated previously, the $\sin\alpha\cos\delta$ term in Equation 4.9 should be incorporated into the coefficient.

The active earth pressure derivation is similar and results in the following closed form equation,

$$F_A = \frac{1}{2}\gamma H^2 \frac{K'_A}{\sin\alpha_A\cos\delta} \tag{4.11}$$

where K'_A is the coefficient of active earth pressure given by

$$K'_A = \frac{\sin^2(\alpha_A+\phi)\ \cos\delta}{\sin\alpha_A\sin(\alpha_A-\delta)\left[1+\sqrt{\frac{\sin(\phi+\delta)\sin(\phi-\beta_A)}{\sin(\alpha_A-\delta)\sin(\alpha_A+\beta_A)}}\right]^2} \tag{4.12}$$

Care must be taken to properly handle the sign and angle changes for the active case from the passive case. For a plate inserted at angle α into a soil with a constant β inclination, the active equations should use $\alpha_A = \pi - \alpha$ and $\beta_A = -\beta$. Also note, in the graphical construction, the positive direction of δ and ϕ are reversed from the passive case.

Before moving on, a few comments should be made regarding the validity of this model. Although this model is commonly used as a basis for comparison, it is primarily for its historical nature, rather than its wide applicability. There range of applicability of this model is fairly well known, and care should be used not to apply it to situations for which it is known to be a poor predictor. The underlying equation of this model is Rankine's equation. The addition of wall friction invalidates the assumptions and changes the shape of the failure surface away from linear. Terzaghi states that if the wall friction δ is smaller than $\phi/3$, then the difference in the failure surfaces is very small, and this model can be used.

4.1.2.3 Ohde's Logarithmic Spiral Method

Ohde's (1938) [74] method, as described in Terzaghi [112], improves upon Coulomb's theory by incorporating a more complex failure surface. It is known that for simple cases the soil failure surface will either be planar, circular (for zero internal friction angle), or logarithmic (for non-zero friction angle). The logarithmic spiral produces a curve such that the normal to the curve is at a constant angle relative to the line from the origin of the spiral. When this angle is zero, then the curve is a circle. Ohde's method uses this property and assumes a failure surface composed of a logarithmic portion and a planar portion.

Figure 4.4 shows an example of the failure surface assumed by Ohde's method. The method uses a graphical technique to obtain a solution for P_1 given a value of l_0, the distance from point a to the origin of the logarithmic spiral, O_1. An analytical solution for this model was not found. Thus, in order to place this in a more useful form, I have taken the graphical method and transformed the steps into sequences of equations, whose derivation is outlined below. The theory and graphical construction is directly from Terzaghi, the implementation in equation form described here is original.

The first step in the solution of the problem requires the determination of the orientation of the planes of failure in the soil, assuming Rankine's theory is applicable. The state of stress at a point in the soil, b, corresponding with the tip of the tool, as shown in Figure 4.5, is known. Figure 4.6 shows the Mohr circle of stress for this state. The

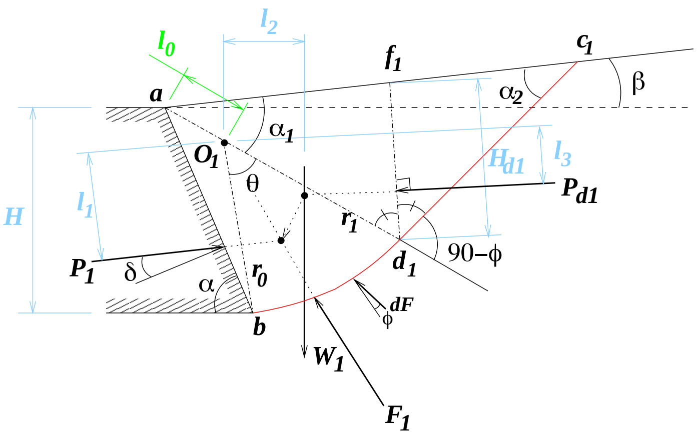

Figure 4.4: Later steps determine the shape of the failure surface given the input value of l_0.

angles α_1 and α_2 must be determined. In order to compute these angles, the center of the circle and the coordinates of the pole, P_P, must be determined.

The state of stress at the bottom tip of the tool (point b) on a plane oriented parallel to the surface of the soil, inclined at angle β, is known. This point is denoted $\mathbf{x}_1 = (x_1, y_1)$ on the Mohr circle. It is assumed that the strength of the soil obeys the Mohr-Coulomb failure law, $s = \sigma \tan\phi$ (assuming no cohesion). This failure envelope will intersect with the circle of stress at a point where the soil fails, at point $\mathbf{x}_2 = (x_2, y_2)$. The center of the circle must lie on the horizontal axis, so it can be given coordinates $(h, 0)$. The value of x_2 can be obtained from the following quadratic equation

$$x_2^2 - 2x_1x_2 - \frac{x_1^2 + y_1^2}{1 + \tan^2\phi} = 0 \tag{4.13}$$

and then $y_2 = x_2 \tan\phi$ and $h = x_2(1 + \tan^2\phi)$. Next the coordinates of $P_P = (x_P, y_P)$ are found by solving another quadratic equation

$$x_P^2 - \frac{2h}{1 + \tan^2\beta} + \frac{h^2 - r^2}{1 + \tan^2\beta} = 0 \tag{4.14}$$

and then $y_P = x_P \tan\beta$. Since the coordinates of $\mathbf{x}_2$ and P_P are known, the angles α_1 and α_2 can be found.

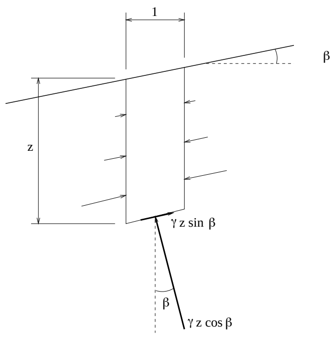

Figure 4.5: Stress state on a plane oriented at angle β at a depth of z for an element in an infinite medium.

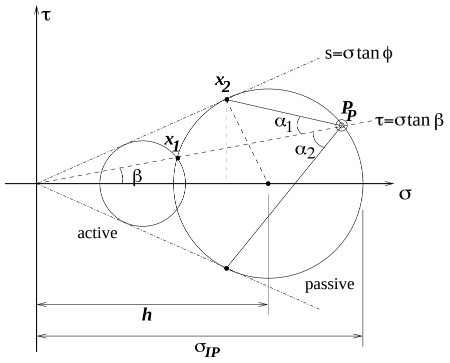

Figure 4.6: The first step in Ohde's method requires us to compute the orientations of the planes of failure using Mohr's circle of stress.

The second step in the graphical method requires the determination of the parameters of the logarithmic spiral. The value of l_0 is known, it is given to us as our free variable in the optimization. The value of α_1 was obtained in the first step, and so the coordinates of O_1 can be computed. From there, r_0 and θ can be computed. The equation for the logarithmic spiral gives us r_1 from

$$r_1 = r_0 e^{\theta \tan \phi} \tag{4.15}$$

Note that if $\phi = 0$ then $r_1 = r_0$. From r_1, the coordinates of d_1 can be found.

In the third step, the point of application and direction of the force from the planar wedge of soil formed by $c_1 d_1 f_1$ is computed. Figure 4.7 provides an illustration for this portion of the problem. It can be seen that $\theta_i = \pi - \alpha_1 - (\pi/4 + \phi/2)$ and using the law of sines, H_{d1} can be found to be

$$H_{d1} = \frac{(l_0 + r_1)\sin \alpha_1}{\sin \theta_i} \tag{4.16}$$

The point k is located 1/3 of the distance from d_1 to f_1. Note that $\theta_{d1} = \pi/2 - (\alpha_1 + \pi/4 + \phi/2 - \beta)$. From this, the length l_3 can be found. The magnitude of the force P_{d1} is also needed. For the special case when $d_1 f_1$ is vertical, as in the case of a horizontal surface (which

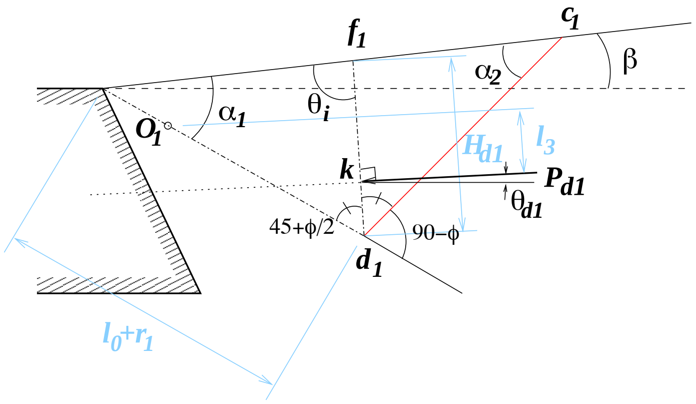

Figure 4.7: The third step of the graphical solution for Ohde's method requires us to find the point k and angle θ_{d1}.

is the situation for all of the testing in this research) then the force would be the same as that discussed from Rankine's theory.

$$P_{d1} = \frac{1}{2}\gamma H_{d1}^2 N_\phi = \frac{1}{2}\gamma H_{d1}^2 \tan^2(\pi/4 + \phi/2) \tag{4.17}$$

For the case of a non-vertical section $d_1 f_1$, the wedge $c_1 d_1 f_1$ can be treated like the failure wedge from Coulomb's theory with the assumption of zero wall friction.

Next, the fourth step, the area and center of gravity for the region $abd_1 f_1$ is computed. This gives the location and magnitude of the weight vector W_1, from which the value of l_2 can be found. Finally, if the moments are summed about point O_1, the moment of force F_1 is zero since it passes through O_1, and the following relation is found for the candidate draft force P_1

$$P_1 = \frac{1}{l_1}(W_1 l_2 + P_{d1} l_3) \tag{4.18}$$

Optimize over l_0 to find the minimum P_1 and this will be the final draft force, F_P. Note that l_0 can also be negative. In fact, as l_0 approaches $-\infty$ the curve bd_1 approaches a straight line, and the whole solution approaches that predicted from Coulomb's theory.

The logarithmic spiral passive model does not have a direct active counterpart. For this model, the active force from one of the other models is used to determine the complete passive minus active force for failure.

4.1.2.4 Caquot and Kerisel's Earth Pressure Tables

The work from Caquot and Kerisel (1948) [17] are said to be "computed from the integration of differential equations governing the conditions of limiting equilibrium". In this respect, it is likely similar to Sokolovskii's slip line method [108] which also solves the differential equations of limiting equilibrium. Although they are grouped with the limit equilibrium techniques, they are sometimes viewed as being lower bounds. Sloan [104] states that as a result of assumptions made in their calculations, the values cannot be considered as strict lower bounds. Regardless, while not representing strict upper or lower bounds, the predictions are believed to be trustworthy and are often used as a basis for comparison. Their results are most easily found in tabular format [17]. These values have been input and interpolation is used to determine intermediate values.

For the passive case, the tables provide coefficients assuming a perfectly rough tool interface. For surfaces with friction less than the soil internal friction, a reduction factor, given via a second table, is multiplied with the rough coefficient to obtain a corrected passive earth pressure coefficient. For the active case, the tables provide coefficients for various ratios of β/ϕ and δ/ϕ. The force applied on the wall can then be calculated from the coefficient simply by

$$F = \frac{1}{2}\gamma H^2 b \tag{4.19}$$

where b is the adjusted passive earth pressure coefficient or the active earth pressure coefficient.

4.1.3 Limit Analysis Methods

Limit analysis techniques applied to soils was introduced by Drucker *et al.* (1952-1953) [27, 28, 26]. A very cursory examination of the fundamentals of limit analysis is presented below. For a very rigorous examination of all facets of the application of limit analysis techniques to soils, including discussions of the assumptions, ramifications, and applicability, the reader is directed to Chen and Liu (1990) [18].

4.1.3.1 Cursory Discussion of Limit Analysis Applied to Soils

Limit analysis techniques can be used to define upper and lower bounds on the true failure force by applying the upper and lower bound theorems from Drucker. These techniques are limited to rigid-perfectly plastic or elastic-perfectly plastic materials (i.e. no plastic hardening/softening). In fact, all of the models discussed here make the assumption of perfectly plastic behavior.

The upper bound theorem states that if a velocity field can be found which satisfies the velocity boundary conditions and the strain and velocity compatibility conditions, then the loads associated with this velocity field will be greater than those required for failure. The loads are computed by equating the external rate of work to the internal rate of energy dissipation. Such a velocity field is termed a kinematically admissible velocity field. The velocity boundary conditions are self-explanatory. The strain and velocity compatibility conditions are defined by a concept known as normality, or the associated flow rule. Basically, this condition requires that the vector representing the direction of the plastic strain rate be normal to the failure surface. This condition is the basis for the computation of the internal energy dissipation for a given velocity field. A discussion of the associated flow rule is beyond the scope of this work (see Chen and Liu [18]).

The lower bound theorem states that if a stress field can be found that satisfies the equilibrium equations, the stress boundary conditions, and no where violates the yield criterion, then the loads associated with this stress distribution are lower than those required for failure. Such a stress field is termed a statically admissible stress field.

The upper bound computation is concerned only with velocity conditions and energy dissipation. The lower bound computation is only concerned with equilibrium and yield conditions. There is no requirement for a stress-strain relationship for the soil, only a yield criterion and the assumption of normality (which is an idealized stress-strain relationship). In addition, the material is idealized as perfectly plastic, i.e. infinite strains will occur at constant stress at failure.

There are issues related to the applicability of these theorems to soils, primarily because soils are known to be frictional, non-associated flow materials. Chen and Liu prove the following theorem for the upper bound case

> Theorem V (Upper Bound) - Any set of loads which produces collapse for the material with associated flow rule will produce collapse for the same material with non-associated flow rules.

This theorem allows us to compute the upper bound solution as if the material obeyed the associated flow rule, and the result will still be an upper bound on the collapse load.

For the lower bound counterpart, the theorem is more involved and the result not as clear. This theorem requires knowledge of the yield surface and the directions of the plastic strain rate on this yield surface, which may not be normal to the yield surface. From this knowledge, a new yield surface is constructed which would satisfy the normality condition. If this new yield surface lies completely within the original yield surface, then the lower bound theorem can be applied. If normality is obeyed, then these yield surfaces are identical. Clearly, this result is not as compelling, nor assured, as that from Theorem V. In actuality, the computations for considering candidate stress fields for the lower bound case makes no use of the normality condition. While there may be deeper dependencies on normality in the basis of the lower bound theorem, the numerical lower bound computations used here are independent of the normality condition.

One final assumption is made, related to the deformation of the soil prior to failure. These limit analysis techniques assume that changes in geometry of a soil mass at the instant of collapse is small. As a result, the virtual work equation is applicable.

4.1.3.2 Chen and Liu's Upper Bound

While the limit theorems provide the basis for the conclusions, creativity must be exercised to create candidate velocity and stress fields. Chen and Liu derive equations for an upper bound solution to the earth pressure problems assuming a three part failure mechanism from James and Bransby (1970) [47]. The equations developed by Chen and Liu are based on energy equilibrium rather than on force equilibrium as employed in the limit equilibrium method.

The three zones of the failure mechanism are shown in Figure 4.8. The first zone, Region I, is a triangular region and is assumed to be a Rankine zone which is not influenced by the interface friction at the wall. This is similar to the logarithmic spiral method. The second zone, Region II, is also triangular, and is governed by the interface friction. The third zone, Region III, is a transition zone or mixed zone, and takes the form of a logarithmic spiral.

Using equations based upon energy dissipation using the above mechanism, Chen and Liu derived the following coefficient of passive earth pressure as an upper bound

$$K_P = \frac{\cos(\rho_f - \phi)\sin(\alpha + v_w)}{\sin^2\alpha\cos\phi\,[\sin(\alpha+\delta)\cos(\rho_f + v_w) - \cos\delta(\tan\delta - \tan v_w)\cos(\alpha - \rho_f)\cos v_w]}$$

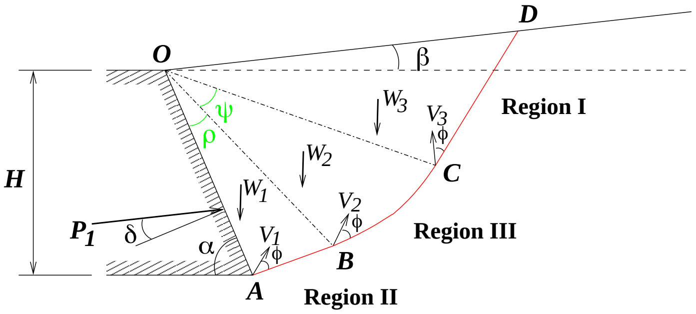

Figure 4.8: Chen's method has three sections and uses velocity admissibility conditions to determine the shape of the failure surface.

$$\Bigg[\sin\rho_f\ \cos(\alpha-\rho_f)+\frac{\cos(\rho_f-\phi)}{(b^2+1)\cos\phi}$$
$$\Big(\cos(\alpha-\rho_f)\left[e^{b\psi_f}(b\cos\psi_f+\sin\psi_f)-b\right]+$$
$$\sin(\alpha-\rho_f)\left[e^{b\psi_f}(b\sin\psi_f-\cos\psi_f)+1\right]\Big)+$$
$$\frac{\cos(\rho_f-\phi)\sin(\alpha+\beta-\rho_f-\psi_f)\cos(\alpha-\rho_f-\psi_f)e^{b\psi_f}}{\cos(\alpha+\beta+\phi-\rho_f-\psi_f)}\Bigg] \quad (4.20)$$

where $b = 3\tan\phi$ and v_w is a value which can vary from 0 to ϕ and relates to the normality condition, the details of which are omitted for simplicity. For the purposes of this research, $v_w = 0$ is used.

In order to find the critical values of ρ and ψ, an optimization is conducted in these two variables until the minimum K_P is found. The corresponding critical values are denoted by ρ_f and ψ_f. Once the critical K_P is found, the draft force is computed from $F_P = \frac{1}{2}\gamma H^2 K_P$.

The equation for the active earth pressure follows the same lines. The active earth pressure coefficient is the same as the passive coefficient with ϕ replaced with $-\phi$, v_w with $-v_w$, δ with $-\delta$, and b with $-b$. Similar modifications to α and β need to be made as stated in the section on Coulomb's Theory, $\alpha_A = \pi - \alpha$ and $\beta_A = -\beta$.

$$K_A = \frac{\cos(\rho_f+\phi)\sin(\alpha_A-v_w)}{\sin^2\alpha_A\cos\phi\left[\sin(\alpha_A-\delta)\cos(\rho_f-v_w)+\cos\delta(\tan\delta-\tan v_w)\cos(\alpha_A-\rho_f)\cos v_w\right]}$$

$$\Bigg[\sin\rho_f\ \cos(\alpha_A-\rho_f)+\frac{\cos(\rho_f+\phi)}{(b^2+1)\cos\phi}$$
$$\Big(\cos(\alpha_A-\rho_f)\left[e^{-b\psi_f}(-b\cos\psi_f+\sin\psi_f)+b\right]+$$

$$\sin(\alpha_A - \rho_f)\left[e^{-b\psi_f}(-b\sin\psi_f - \cos\psi_f) + 1\right]\big) + \\ \left.\frac{\cos(\rho_f + \phi)\sin(\alpha_A + \beta_A - \rho_f - \psi_f)\cos(\alpha_A - \rho_f - \psi_f)e^{-b\psi_f}}{\cos(\alpha_A + \beta_A - \phi - \rho_f - \psi_f)}\right] \tag{4.21}$$

An optimization is done over ρ and ψ to find the critical K_A. Then the active force is given by $F_A = \frac{1}{2}\gamma H^2 K_A$.

Chen and Liu conduct comparisons of this model with the zero-extension line theory of Habibagahi and Ghahramani (1979) [34] and with the slip-line method of Sokolovskii (1965) [108]. These all have similar three part failure zones. The solutions were found to be in good agreement.

4.1.3.3 Numerical Limit Analysis

While limit analysis has been applied to soil problems over the last few decades; recently, there has been work to develop numerical methods which use finite element meshes to compute lower and upper bound solutions. This work was originally done by Sloan [104, 106, 107] and further developed by Ukritchon, Whittle, and Sloan [118]. One of the difficulties in applying limit analysis techniques has been the construction of velocity and stress fields. This method eliminates the need for making assumptions about failure mechanisms and stress fields. By using a numerical mesh based approach, no assumptions of failure mechanism need be made.

This method has been applied to numerous other problems such as bearing capacity of foundations, stability of slopes, and retaining walls with tie-backs [116, 117]. The prior work primarily focused on cohesive, non-frictional ($c \neq 0, \phi = 0$) materials, such as clays. The technique had not been extensively applied to passive earth pressure problems until this work.

Using programs developed by Ukritchon, Whittle, and Sloan, upper and lower bounds for the passive and active earth pressure coefficients can be computed. The programs combine constraints on all the nodes of the generated meshes to form a very large linear programming problem (for our typical problem, the number of variables is near 20,000 and the number of constraints can be over 200,000). Most constraints are linear, except for the Mohr-Coulomb yield criterion. If plotted with the axes of $\sigma_x - \sigma_y$ and $2\tau_{xy}$, the yield criterion would plot as a circle of a radius dependent upon c, σ_x, σ_y and ϕ. This circle is linearized using p segments. For our meshes, we have used $p = 36$. The programs also allow for velocity discontinuities between triangles in the upper bound case and stress discontinuities the lower bound case. The solution of the resulting large linear programming problem is carried out through an active set method (Sloan [105]).

The programs themselves are compiled from Fortran sources. I have written programs for mesh generation in Matlab. The meshing relies heavily upon Delaunay triangulation for the elements near inclined tools and for the non-square lower bound meshes. I provide a bit of detail regarding the upper and lower bound meshes below.

In order to use these methods, a set of nodes and a triangular mesh connecting these nodes must be constructed. In addition, structural elements (such as our plate) which interact with the mesh must be added. Properties of the soil medium and properties of the structure (which is also allowed to fail, but it is typically set to very high strengths) are input. The properties of the soil need not be homogeneous. For the upper bound mesh, velocity boundary conditions and a displacement direction for the structure are specified. Special properties for the nodes at the structure-soil interface are specified to simulate different soil-tool friction values. For the lower bound mesh, stress boundary conditions around the boundary and a direction of loading for the structure must be specified. Special properties of the soil-tool interface are also specified. For the lower bound meshes, extension elements are also incorporated to allow the stress field to extend beyond the finite mesh.

Sample upper and lower bound meshes are shown in Figure 4.9 for an inclined tool. The dots around the boundary indicate fixed boundary conditions. The upper surface of the mesh is allowed to move freely. The repeated square arrangement of four triangles is the recommended form, though not required in the presence of the velocity discontinuities between each of the element faces. The velocity discontinuities between the soil elements and the structural elements are used to specify the interface friction angle. For the lower bound mesh, two different mesh forms are used. One form is identical to the square meshing in topology, and the second is the radial arrangement shown with a concentration near the point of loading. There are extension elements around the side and bottom boundaries to extend the stress field. The nodes at the soil surface are constrained to have zero normal and shear stress. The structural element in the lower bound mesh is hidden by the overlapping stress constraints which are required to specify a given interface friction angle.

The passive and active cases independently can be solved independently and then combined. To save computation time, the combined meshes incorporating both the active and passive earth pressures on an embedded plate simultaneously are solved. Figure 4.10 shows some of the resulting data from the numerical computations for $\alpha = 80°$,

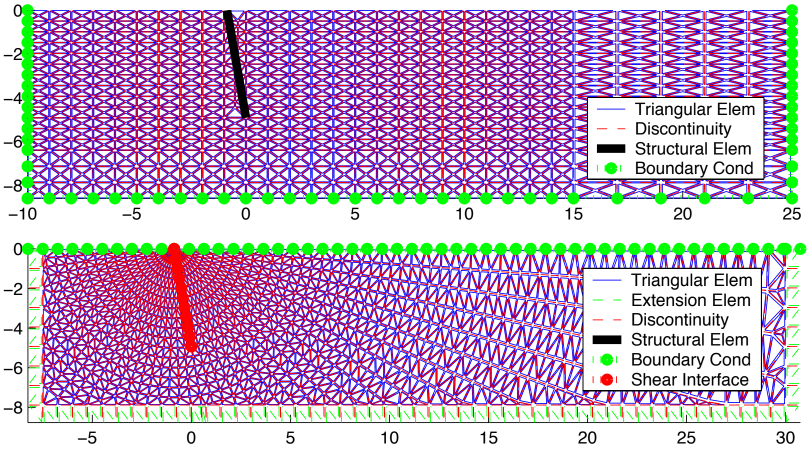

Figure 4.9: Upper and lower bound meshes prior to computation.

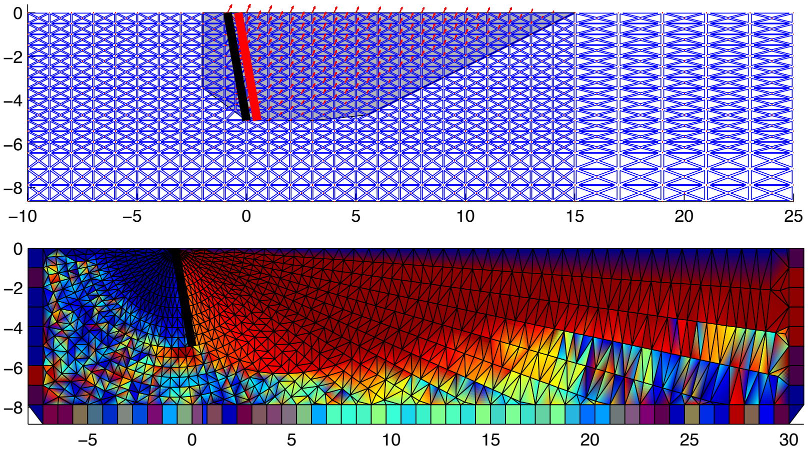

Figure 4.10: Sample upper and lower bound meshes after solution.

$\phi = 40°$, and $\delta = 25°$. The upper plot shows the kinematically admissible velocity field computed by the upper bound program. The shading is included to highlight the regions where the velocity exceeds a certain value (shown here with 1e-5). Both the active and passive failure regions can be seen. The lower plot shows one aspect of the resulting statically admissible stress field computed by the lower bound program. The figure shows the orientations of the principal stresses relative to vertical. Dark regions indicate orientations close to vertical, and the red (or lighter) regions indicate orientations close to horizontal. Note that the orientations are near horizontal for the passive region and near vertical for the active region. The programs return the loads which correspond to the velocity field and the stress field shown.

These upper and lower bound solutions are not guaranteed to form tight bounds on the predicted force. Refining of meshes is often needed to obtain tighter bounds on the solution. This is where the primary work is involved, selectively refining the granularity and topology of the meshes to obtain tighter bounds on solutions. A number of changes are made to the mesh to try to obtain tighter bounds. Note that the mesh size is much finer near the plate in both cases. Tight upper bound solutions are typically easier to obtain. The lower bound solutions are more difficult. Both square and radial meshes were generated, and in some cases the square mesh produces better results, while in other cases, the radial mesh produces better results. The square and radial predictions are compared and the tightest bounds are used in each case.

In this work, the failure force predictions are the only results used from the models. There are additional results from these computations which may be of interest. The shape of the failure surface may be estimated from the upper bound solution and compared with experimentally observed results. The stress distribution across the plate computed by the lower bound solution can also be examined.

4.1.4 Summary of Models

Table 4.1 presents a summary of all the methods discussed in this chapter. The equations in the table take into account the α_A and β_A changes for the active cases, so a single α and β value can be used throughout. In addition to this summary table, a table of the resulting predictions for each of the models for the complete range of parameters of interest can be found in Appendix C.

Model	Active and Passive Equations	Notes	Figures - Passive
Coulomb (1776) [112]	$F_P = \frac{1}{2}\gamma H^2 K_P$ and $F_A = \frac{1}{2}\gamma H^2 K_A$ $K_P = \dfrac{\sin^2(\alpha-\phi)}{\sin^2\alpha\sin(\alpha+\delta)\left[1-\sqrt{\frac{\sin(\phi+\delta)\sin(\phi+\beta)}{\sin(\alpha+\delta)\sin(\alpha+\beta)}}\right]^2}$ $K_A = \dfrac{\sin^2(\alpha-\phi)}{\sin^2\alpha\sin(\alpha+\delta)\left[1+\sqrt{\frac{\sin(\phi+\delta)\sin(\phi+\beta)}{\sin(\alpha+\delta)\sin(\alpha+\beta)}}\right]^2}$	Assumed linear failure surface. Analytical equation for optimal values. Known to be poor predictor as δ increases.	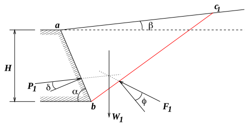
Ohde (1938) [112]	Graphical method converted to series of equations for the computation of lengths l_1, l_2 and l_3 and weight W_1 and force P_{d1}. See relevant section of paper for full derivation. $F_P = \frac{1}{l_1}(W_1 l_2 + P_{d1} l_3)$ [no active equation, using Caquot and Kerisel's]	Assumed mixed failure surface with logarithmic spiral portion and linear portion. Minimize F_P by varying l_0.	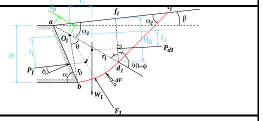
Chen and Liu (1990) [18]	$F_P = \frac{1}{2}\gamma H^2 K_P$ and $F_A = \frac{1}{2}\gamma H^2 K_A$ $K_P = \dfrac{\cos(\rho_f-\phi)\sin(\alpha+v_w)}{\sin^2\alpha\cos\phi\left[\sin(\alpha+\delta)\cos(\rho_f+v_w)-\cos\delta(\tan\delta-\tan v_w)\cos(\alpha-\rho_f)\cos v_w\right]}$ $\left[\sin\rho_f\ \cos(\alpha-\rho_f)+\dfrac{\cos(\rho_f-\phi)}{(b^2+1)\cos\phi}\right.$ $\left(\cos(\alpha-\rho_f)\left[e^{b\psi_f}(b\cos\psi_f+\sin\psi_f)-b\right]+\right.$ $\left.\sin(\alpha-\rho_f)\left[e^{b\psi_f}(b\sin\psi_f-\cos\psi_f)+1\right]\right)+$ $\left.\dfrac{\cos(\rho_f-\phi)\sin(\alpha+\beta-\rho_f-\psi_f)\cos(\alpha-\rho_f-\psi_f)e^{b\psi_f}}{\cos(\alpha+\beta+\phi-\rho_f-\psi_f)}\right]$ where $b = 3\tan\phi$. The active coefficient is nearly identical with ϕ replaced with $-\phi$, v_w with $-v_w$, δ with $-\delta$, and b with $-b$. Also use $\alpha_A = \pi - \alpha$ and $\beta_A = -\beta$.	Assumed mixed failure surface with linear portion, logarithmic spiral portion, and linear portion. Derived using limit analysis ideas based on velocity characteristics. Minimize F_P and maximize F_A by varying ψ and ρ.	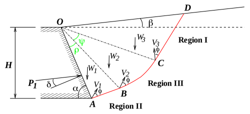
Caquot and Kerisel (1948) [17]	Computed from solving the differential equations of limiting equilibrium. [tabular data for active and passive coefficients]	Table lookup for the proper coefficients. Sometimes viewed as a lower bound.	
Numerical Limit Analysis (1988-1998)	Sample upper and lower bound meshes prior to computation. 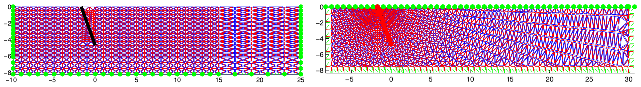	Computes upper and lower bounds by solving large sparse linear programming problems. Uses code from Sloan [104, 106, 107] and Ukritchon [117, 118].	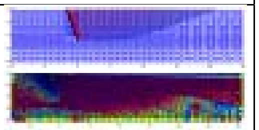

Table 4.1: Summary of models for draft force prediction.

Symbol	Description	Base Value	Variation
α	Tool Angle	$70° - 100°$	1°-5°
β	Surface Angle	0°	1°-5°
ϕ	Internal Friction Angle	40°	1°-5°
δ	External Friction Angle	25°	1°-5°
γ	Soil Density	1.5 g/cc	n/a
z	Tool Depth	$1''$	n/a

Table 4.2: Definition of symbols and base configuration values and variations used in the sensitivity analysis are listed. No variations are done with the density and depth since their dependence is well known and common to all models ($\propto \gamma$ and $\propto z^2$).

4.2 Comparison of Models

In this section, the sensitivity of each of the models to small variations in parameters is examined. Next, a comparison of the the failure surfaces used in each model is shown. Then, the predictions of each of the methods for various geometrical configurations of tool and soil are compared. Finally, a discussion of the benefits and disadvantages of the novel numerical limit analysis techniques is presented.

4.2.1 Sensitivity to Parameters

The sensitivity of the various models to variations in the parameters is computed from a baseline configuration. Each of the parameters is varied while keeping the other parameters constant. The resulting percentage change in the draft force prediction is then compared.

The parameters for each of the models, the base configuration value, and the symbols used in the models are shown in Table 4.2. It is expected that this case will be fairly representative of the soils to be encountered. The dependence of the draft force on the soil density and the tool depth is well known and consistent across all the models, hence the relative sensitivity to these two parameters need not be examined. (The force is proportional to the density and proportional to the square of the depth of the tool.) For the other four parameters, each are varied in turn, while holding the other three parameters constant. The percentage change of the resulting prediction is computed. The results are shown in Table 4.3. Results for only horizontal surfaces have been computed for the upper bound (UB) solutions. Similarly, only the horizontal tables have been input from Caquot and Kerisel. For these cases, variations in the surface inclination are not computed.

		$\alpha+\Delta$					$\beta+\Delta$					$\phi+\Delta$					$\delta+\Delta$				
Δ	α	Coul	Log	Caq	Chen	UB	Coul	Log	Caq	Chen	UB	Coul	Log	Caq	Chen	UB	Coul	Log	Caq	Chen	UB
1°	70°	4.5	4.6	4.1	4.0	4.5	5.7	5.6	xx^1	5.1	xx^1	5.1	5.0	5.0	5.2	6.1	3.9	4.1	3.6	3.3	3.2
	80°	5.4	4.3	3.9	4.1	4.7	6.8	4.9	xx^1	5.2	xx^1	6.7	6.4	6.5	6.5	7.8	5.4	4.2	3.6	3.7	3.6
	90°	7.5	4.1	3.8	4.2	5.0	9.0	4.5	xx^1	5.3	xx^1	9.5	7.8	8.0	8.0	9.8	7.9	4.3	3.6	4.0	3.8
	100°	13.2	4.0	3.8	4.3	xx^2	15.1	4.3	xx^1	5.4	xx^1	16.1	9.5	9.5	9.6	12.6	14.2	4.4	3.6	4.3	4.1
2°	70°	9.3	9.3	8.4	8.2	9.1	11.7	11.2	xx^1	10.4	xx^1	10.5	10.4	9.6	10.7	12.3	8.1	8.5	7.2	6.7	6.4
	80°	11.3	8.7	7.9	8.3	9.5	14.1	9.9	xx^1	10.6	xx^1	14.0	13.3	12.5	13.5	15.6	11.2	8.5	7.3	7.5	7.1
	90°	15.9	8.3	7.8	8.5	10.0	19.3	9.2	xx^1	10.9	xx^1	20.3	16.5	15.4	16.8	19.7	16.9	8.7	7.2	8.2	7.5
	100°	29.4	8.2	7.7	8.7	xx^2	33.7	8.7	xx^1	11.1	xx^1	36.1	20.1	18.1	20.4	25.2	31.7	8.9	7.2	8.7	8.3
3°	70°	14.3	14.3	12.9	12.6	13.7	18.1	17.0	xx^1	15.9	xx^1	16.3	16.1	14.9	16.5	18.4	12.6	12.9	10.9	10.2	9.7
	80°	17.6	13.2	12.1	12.8	14.2	22.1	15.0	xx^1	16.3	xx^1	22.1	20.8	19.6	21.1	23.4	17.6	13.0	10.9	11.4	10.7
	90°	25.4	12.8	11.9	13.1	14.9	30.8	13.9	xx^1	16.7	xx^1	32.6	26.1	24.3	26.5	29.5	27.1	13.3	10.9	12.4	11.3
	100°	49.6	12.5	11.8	13.4	xx^2	57.1	13.3	xx^1	17.0	xx^1	61.4	32.1	28.8	32.6	37.8	53.7	13.6	10.9	13.2	12.4
4°	70°	19.7	19.3	17.4	17.1	18.3	24.9	22.8	xx^1	21.7	xx^1	22.6	22.3	21.4	22.8	24.6	17.4	17.5	14.6	13.9	12.9
	80°	24.5	18.0	16.4	17.4	18.8	30.8	20.2	xx^1	22.2	xx^1	30.9	28.9	28.4	29.4	31.2	24.5	17.6	14.6	15.5	14.3
	90°	36.1	17.3	16.2	17.8	19.7	44.0	18.8	xx^1	22.8	xx^1	46.7	36.7	36.0	37.3	39.4	38.7	18.0	14.6	16.8	15.1
	100°	75.3	17.1	16.0	18.2	xx^2	87.1	18.0	xx^1	23.2	xx^1	94.1	45.6	43.6	46.4	50.4	81.9	18.4	14.5	17.9	16.5
5°	70°	25.4	24.6	22.2	21.8	22.9	32.3	28.8	xx^1	27.7	xx^1	29.2	28.9	29.4	29.5	30.7	22.5	22.3	18.3	17.6	16.1
	80°	32.1	22.9	20.8	22.2	23.4	40.4	25.6	xx^1	28.4	xx^1	40.5	37.9	39.8	38.5	39.1	32.2	22.4	18.3	19.6	17.8
	90°	48.4	22.1	20.6	22.8	24.4	59.2	23.9	xx^1	29.1	xx^1	63.1	48.6	51.5	49.4	49.2	52.0	22.8	18.3	21.4	18.9
	100°	108.7	21.7	20.5	23.3	xx^2	126.3	22.9	xx^1	29.7	xx^1	137.3	61.0	64.1	62.0	63.0	118.8	23.3	18.2	22.7	20.6

[1] Since our experiments are conducted for horizontal cases only, the Caquot and Kerisel tables were only input for the horizontal case and the numerical limit analysis solutions were also only computed for horizontal case.

[2] The numerical limit analysis solutions are only computed up to 100°, so interpolations cannot be done beyond that.

Table 4.3: Approximate sensitivity (percentage change of prediction from the baseline value) of each of the models to variations of each of the four parameters with the other three held constant. The order of the columns in each parameter section is Coulomb, Logarithmic Spiral, Caquot and Kerisel, Chen, and the numerical Upper Bound. The first batch is for a 1° change, second for 2°, and so on. Note that the Caquot and Kerisel and the UB values are interpolated between discrete points and so may be slightly inexact, whereas the other values are computed directly for each specific case.

In actuality, better resolution in the tool angle and surface angle can be achieved, since these are geometric parameters which we control. The model sensitivity to these parameters provides an idea of what effect inaccuracies in positioning and leveling will have on the resulting measurement. The sensitivity to friction angle variations provides a measure of how easy it will be to distinguish variations in actual soil parameters.

It can be noted from the percentage variations that the models are most sensitive to changes of equal magnitude in the internal friction angle. In addition, the sensitivity increases as the tool angle increases. This indicates that higher angle configurations may be more useful in distinguishing soil friction angle properties.

4.2.2 Failure Surfaces

Figure 4.11 shows the computed failure surfaces for three of the models for the passive case, with $\phi = 40°$ and $\delta = 25°$. The Coulomb and logarithmic spiral failure forces are actually computed from these failure surfaces while the Chen and Liu model is not. The Chen and Liu model computes the failure force using energy equilibrium using the failure mechanism shown, but a direct force balance is not computed. It is interesting to note that while the Chen and Liu failure surface is greater in extent than the logarithmic spiral model, the Chen and Liu force is less. Figure 4.12 shows each of the failure surfaces plotted on top of one another. It is also interesting to note that the angle of the Rankine zone in both the logarithmic spiral and Chen and Liu models agree, though they are computed by very different means.

4.2.3 Comparison of Predictions

This section compares the numerical UB and LB predictions with the other models presented. For simplicity, consideration is limited to cases with a horizontal soil surface. A range of tool angles of 70°-100° relative to horizontal is considered. Plots of the passive minus active earth pressure coefficients versus internal friction angles are shown in Figures 4.13, 4.14, and 4.15. Plots of the coefficients versus interface friction angle are shown in Figures 4.16, 4.17, and 4.18.

In each of the plots, the percentage difference between the upper and lower bounds are shown. It can be observed that it is much more difficult to obtain tight bounds for high friction angles. In the future, additional mesh refinement may be done to try to obtain tighter lower bounds.

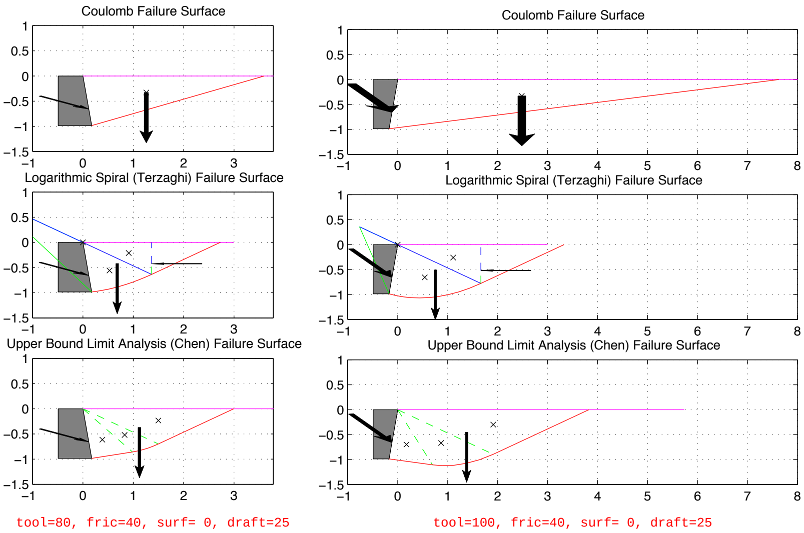

Figure 4.11: Comparison of the passive failure surfaces from three of the models for 80° and 100° tools with $\phi = 40°$ and $\delta = 25°$.

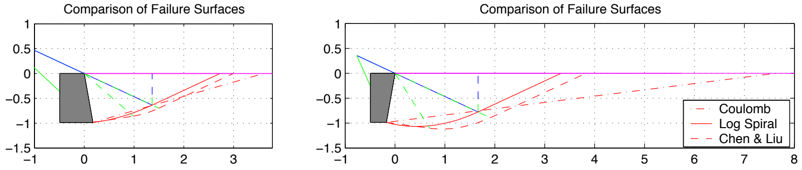

Figure 4.12: View of the overlapped failure surfaces from the three models. Clearly Coulomb's model predicts too large a failure wedge for walls with high interface friction, especially at larger tool angles.

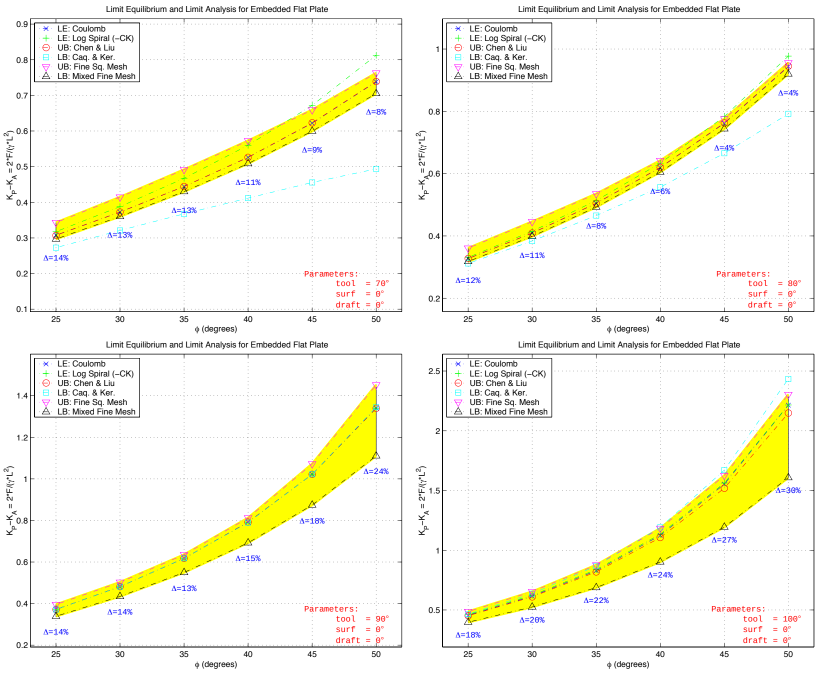

Figure 4.13: Limit equilibrium and limit analysis results for tool angles of 70, 80, 90, and 100 degrees with a smooth tool interface, $\delta = 0°$.

For a simple case of a 90° (vertical) tool and a smooth interface (Figure 4.13, lower left plot), all of the other model predictions overlap, with the numerical upper and lower bounds bracketing the other predictions. This shows that for simple configurations, all the models are in exact agreement.

In a few instances, there is a rather large variation between the methods. For instance, for a tool at 70° with a smooth tool interface (Figure 4.13, upper left plot), Caquot and Kerisel's predictions are much lower than the other predictions. This is an unexplained odd behavior. Since these coefficients were provided via a table, rather than the equations used to derive the coefficients, comments cannot be made regarding the source of the discrepancies. The other models are more closely grouped, so it is believed that the Caquot and Kerisel predictions are in error in this case.

In all cases, the numerical UB predictions are either nearly identi-

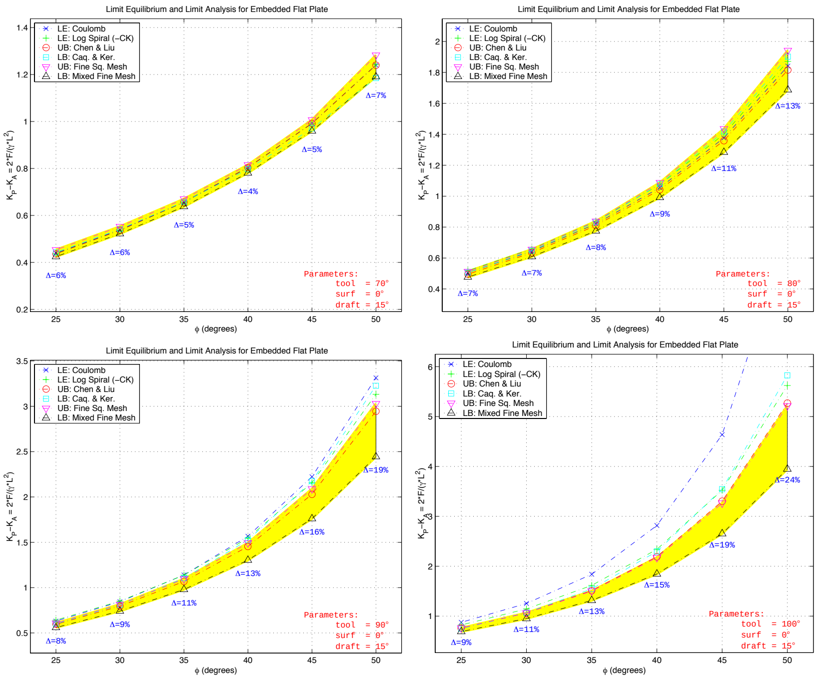

Figure 4.14: Limit equilibrium and limit analysis results for tool angles of 70, 80, 90, and 100 degrees with $\delta = 15°$.

cal to Chen and Liu's upper bound predictions, or the numerical UB and LB predictions bound Chen and Liu's predictions. Chen and Liu have compared their model to two additional methods which were not considered in this work, the slip-line and zero-extension line models. They have shown good agreement with these models.

As expected, Coulomb's model deviates from the other predictions at large interface friction angles. This is a direct consequence of the linear failure surface assumed by Coulomb's Theory. The logarithmic spiral model also tends to have this trend, but to a lesser degree. Overall, the logarithmic spiral either matches well or tends to over-predict compared to the other models. There is an odd down-turn in the Caquot and Kerisel predictions as δ approaches ϕ. Chen and Liu also show this trend in their comparisons as well. The source of this effect is uncertain, but perhaps this results from approximations in their secondary table used to compensate for non-rough interfaces.

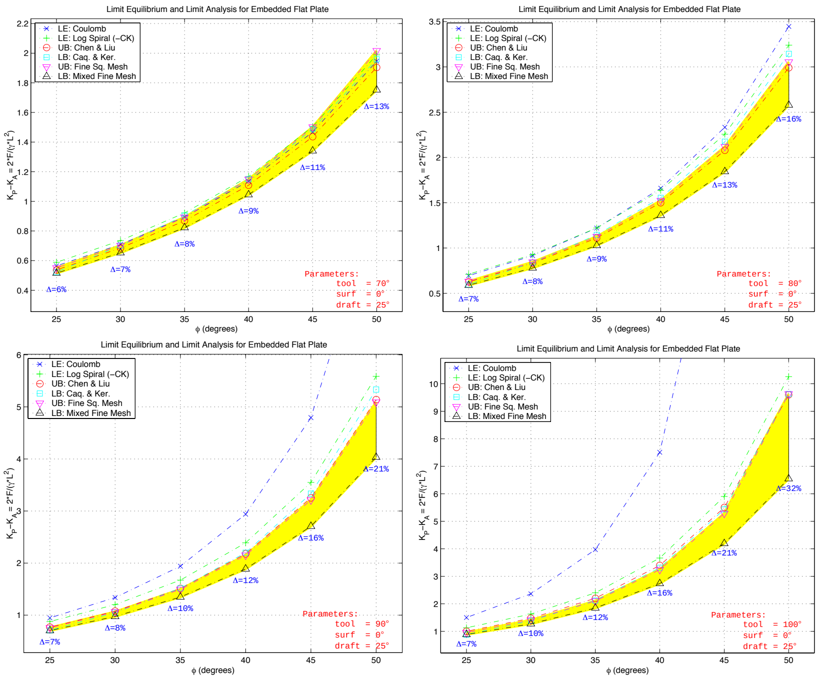

Figure 4.15: Limit equilibrium and limit analysis results for tool angles of 70, 80, 90, and 100 degrees with $\delta = 25°$.

In summary, apart from the case of a smooth interface, the numerical UB and LB predictions compare well with Chen and Liu's upper bound and with Caquot and Kerisel's predictions. Coulomb's predictions deviate at larger interface frictions as expected. The logarithmic spiral method is typically close to the numerical UB. The limit equilibrium models are expected to be closer to the numerical UB predictions. This is consistent with the fact that limit equilibrium models are considered rough upper bounds. Large discrepancies, aside from those noted, are not observed.

4.2.4 Benefits of the Numerical Limit Analysis Technique

It has been shown that the results from the numerical limit analyses are in good agreement with the currently accepted models for the pre-

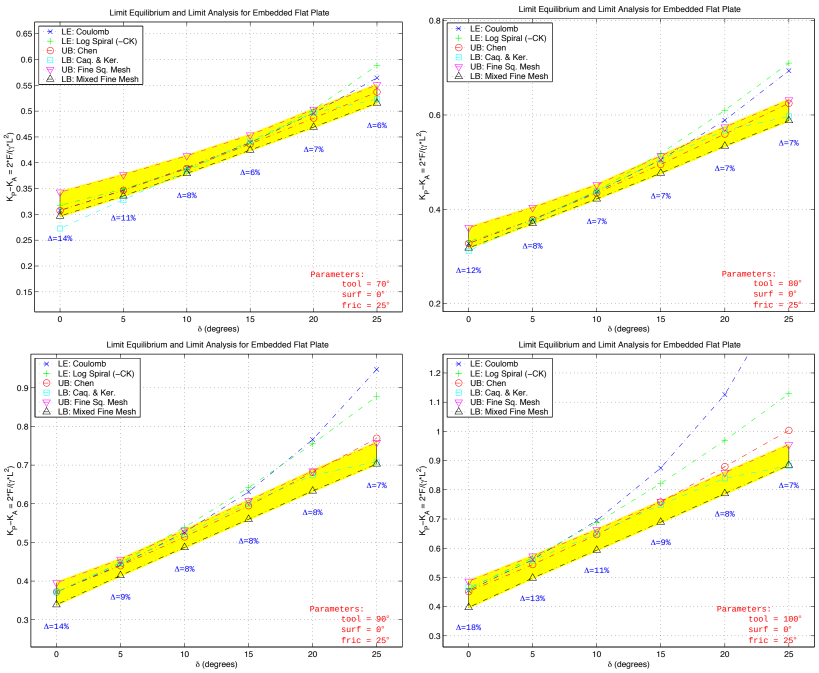

Figure 4.16: Limit equilibrium and limit analysis results for tool angles of 70, 80, 90, and 100 degrees with $\phi = 25°$.

diction of earth pressures. When introducing a new prediction model, good agreement with currently accepted models or experimental phenomena should be shown and the models should provide additional features or capabilities not found in the existing models. Therefore, the advantages and disadvantages of the numerical limit analysis technique are discussed here.

The main advantages of the numerical limit analysis technique are the versatility in the modeling and the provision of *both* upper and lower bounds. It does not assume a pre-defined failure surface and thus is less constrained. In addition, this method allows for the incorporation of variations in soil parameters across the mesh unlike any of the other methods. Rigid boundary conditions simulating buried obstacles can be included. Complex structural elements such as curved blades or piecewise linear blades can be constructed. Overall, this method provides the most versatile solution for this problem. The predictions are in good

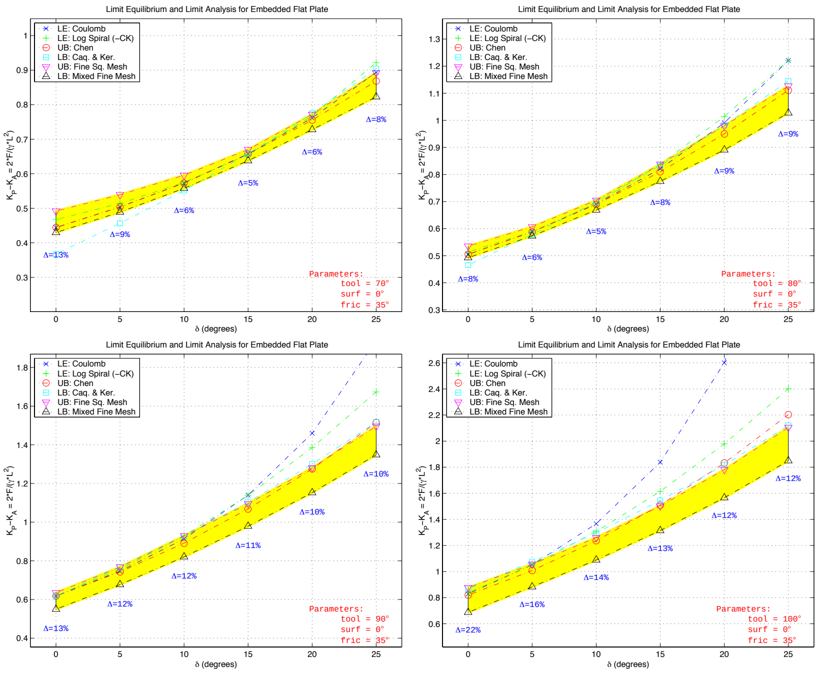

Figure 4.17: Limit equilibrium and limit analysis results for tool angles of 70, 80, 90, and 100 degrees with $\phi = 35°$.

agreement with currently accepted models. And it provides a lower bound solution, in addition to the commonly available upper bound solution.

For the disadvantages, there are a number of difficulties in implementing the numerical limit analysis method. Meshing can be complex. For the upper bound case, typically the square mesh produces very good results and a finer mesh will produce better results. The path to obtaining tighter bounds is clear. For the lower bound, there is no obvious path for altering the topology of a mesh to obtain tighter bounds. Simply making the mesh finer produces only small incremental improvements. The lower bound is much more sensitive to the arrangement of the mesh. Now, with finer and more complex meshes, comes another caveat, computation time. With simpler meshes, and computations would take on the order of minutes. The finer meshes which were used in the final computation (with thousands of nodes), compu-

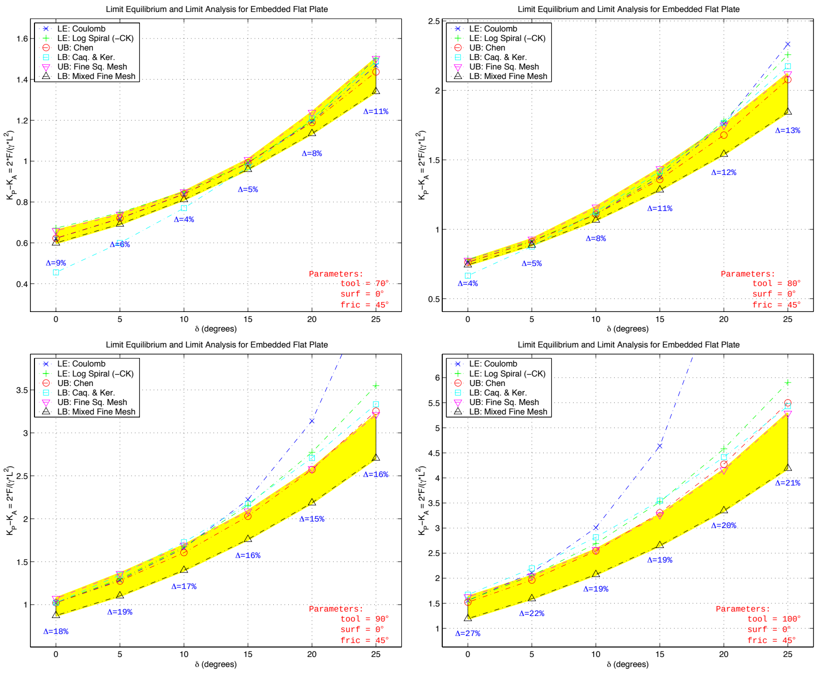

Figure 4.18: Limit equilibrium and limit analysis results for tool angles of 70, 80, 90, and 100 degrees with $\phi = 45°$.

tation times would be on the order of two hours on an AMD 1.2GHz for *each* mesh. For this work, approximately 300 meshes were solved for the UB case and 600 meshes were solved for the lower bound case (300 square, 300 radial). This equates to roughly 2.5 months of solid computation.

A recent development from Sloan addresses the computation time issue. A new solution technique using nonlinear programming has been developed, which results in an order of magnitude improvement in computational efficiency. This development, in combination with the ever increasing speed of computer processors, essentially removes any concerns about the computation time. This should enable researchers to obtain tighter bounds, explore more complex meshes, and solve a greater number of cases, reducing the need for interpolation.

4.3 Conclusions

Four existing models have been presented in this chapter. These existing models have been compared with the results from numerical limit analysis technique for computing upper and lower bounds. The numerical technique has previously been applied to a number of other problems, however, this is the first presentation of comprehensive results specifically for the passive and active earth pressure problem. It has been shown that there is good agreement with currently favored solutions to this problem, and in addition, the numerical technique provides additional versatility for modeling more complex problems and has the benefit of providing both upper *and* lower bounds on expected forces.

Chapter 5

Experimental Methods

This chapter discusses the experimental procedure which was developed for collecting failure force data in soils. The chapter begins with a discussion of a basic technique for plate insertion with minimal disturbance of the nearby soil. Next, the control techniques implemented to perform controlled stroking in the soil are outlined. Finally, the processing of the resulting data to obtain meaningful failure force measurements is shown.

5.1 Platform for Data Collection

The development of the manipulator for this research was discussed in Chapter 3. In addition to the manipulator, a sandbox was constructed, with dimensions of approximately 23"x25"x10". These dimensions were selected to be compatible with the raining assembly developed in the Civil and Environmental Engineering Department (Larson [63]) for the creation of uniform soil samples. Figure 5.1 shows the raining assembly placed above the sandbox. The resulting rained sand has a depth of 5-6 inches. This is more than sufficient depth for our experiments (the typical depth of insertion is one inch). The sandbox is placed on a cart to simplify positioning underneath the raining assembly. The manipulator arm is also affixed to the same cart to prevent relative motion between the sandbox and manipulator.

The raining assembly is only used for one of the soils tested, Ticino sand. The assembly was previously designed and validated using this sand. The other soils have too fine of a grain size to be rained. Instead, these soils are manually re-mixed between stroking experiments. This will introduce some variation in density between the samples in

Figure 5.1: The raining assembly placed on top of sandbox for the deposition of uniform soil samples. The sandbox and manipulator are both mounted on a rolling cart for easy transport. The images to the right show the holes in the upper assembly and the screens in the lower assembly.

the experiments. Care is taken to obtain approximately identical soil conditions from stroke to stroke. The resulting variation in sample density can be estimated by repeated measurements to obtain a rough uncertainty value.

The configuration of the arm during a typical digging sequence is shown in Figure 5.2. The full forward reach of the manipulator is approximately 36” and the downward reach is approximately -23” from the origin of the manipulator frame of reference (center of the mounting base). The soil surface in the sandbox will then be at a depth of -13” in the manipulator frame. As can be seen in the images, the typical arm configuration during digging places the upper link of the manipulator below or near horizontal. The majority of the stroking force is generated by the elbow joint driven by two motors through the elbow differential. The majority of the insertion force is generated by the shoulder joint. The insertion force reaches up to 5 lbf for our depths and soils and the stroking force reaches up to 3 lbf. The next sections

Figure 5.2: Front and side view of the manipulator arm executing and completing a digging sequence in the sandbox. The origin of the manipulator coordinate frame is located directly below the shoulder joint at the level of the table surface. The soil surface is typically located at z = -13” in the manipulator frame. Insertion forces are primarily generated by the shoulder joint, and stroking forces are primarily generated by the elbow joint.

describe the specific techniques for insertion and stroking.

5.2 Plate Insertion

The first step that must be taken in order to collect data is to insert the plate into the soil. This must be done carefully so that the state of the soil around the plate is minimally disturbed. Initial tests inserting the plate into the sand show a large build up of lateral forces on the plate and large deformation of the nearby soil. As a result, some form of accommodation is necessary in order to account for small inaccuracies in positioning and orientation of the manipulator and the resulting response by the soil.

In order to address the lateral force build up issue, a simplified remote center-of-compliance technique is implemented (Peshkin [79]). Figure 5.3 shows an illustration of the end-effector plate being inserted into soil at a given inclination. Coordinate frames are labeled and forces acting on the plate are illustrated.

Examining the planar forces on the plate during insertion, the following logic to compensate for the forces and torques can be devised:

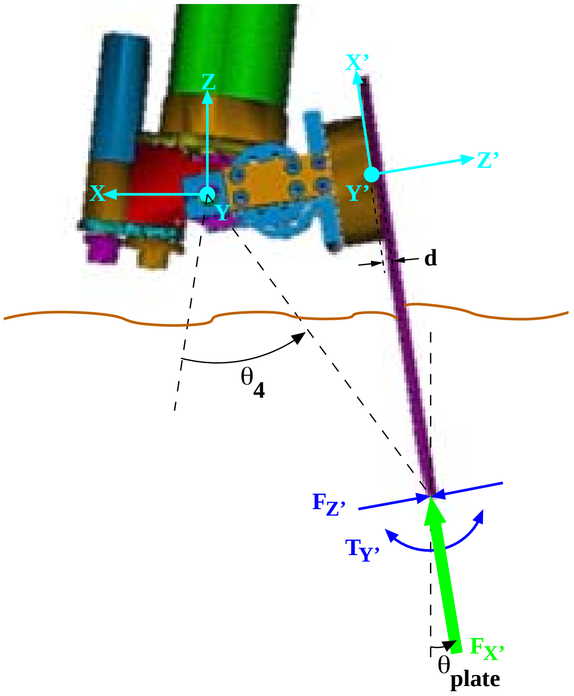

Figure 5.3: Cartesian coordinate frame and F/T sensor coordinate frame and forces acting on the end-effector plate during insertion. The desired insertion velocity is adjusted in order to accommodate for the buildup of lateral forces.

$+T_{Y'} \rightarrow +Z', \pm X$ (+ for $\theta_{plate} > 0$), $-\theta_4$
$-T_{Y'} \rightarrow -Z', \mp X$ (− for $\theta_{plate} > 0$), $+\theta_4$
$+F_{Z'} \rightarrow +Z'$
$-F_{Z'} \rightarrow -Z'$
$+T_{Z'} \rightarrow$ not enough DOF
$-T_{Z'} \rightarrow$ not enough DOF

As noted, compensation can be done for forces in the Z' direction and torques about the Y' axis. The manipulator does not have sufficient degrees of freedom to compensate for possible torques about the Z' axis. These torques are expected to be inconsequential.

The logic can be reduced further. Since the force in the vertical direction of the plate is controlled to drive the insertion, both position and force in this direction cannot both be specified. The only adjustments possible are in the direction perpendicular to the plate, Z', and the wrist joint, θ_4, which controls the plate orientation.

The logic thus far can be written in equation form. Cylindrical notation is more convenient, and so r' is used in place of Z'. The accommodation is accomplished by using θ_4 adjustments to correct for $T_{Y'}$ and r' adjustments to correct for $F_{Z'}$. The following relation is obtained

$$\frac{d}{dt}\begin{bmatrix} r' \\ \theta_4 \end{bmatrix} = \begin{bmatrix} k_F & 0 \\ 0 & k_T \end{bmatrix} \begin{bmatrix} F_{Z'} \\ T_{Y'} - F_{X'}d \end{bmatrix} \tag{5.1}$$

where k_F and k_T are accommodation gains.

The plate orientation should not be allowed to change arbitrarily (the goal is to run controlled experiments with tool angles at fixed values). Therefore, θ_4 should not be modified during insertion. In future scenarios, where the tool angle need not be a fixed value, the final plate angle may be allowed to vary to obtain better insertions. In such cases, the θ_4 portion of the accommodation relation may be enabled. However, for the experiments presented here, the θ_4 portion is left disabled. This then leaves only the first half of Equation 5.1, or simply $\dot{r}' = k_F\ F_{Z'}$. Thus, for any lateral force on the plate, the desired end-point location of the arm is adjusted to relieve that lateral force by moving in a direction perpendicular to the insertion direction.

To complete the derivation, the equation must be converted into the cylindrical world frame from the end-effector frame. The orientation of the plate in the world frame is at an angle, $\theta' = \theta_1 + \theta_2 + \theta_4 - \pi$, where θ_1, θ_2, and θ_4 are the shoulder, elbow, and wrist angles respectively. The derivative is $\dot{\theta}' = \dot{\theta}_1 + \dot{\theta}_2$ (with $\dot{\theta}_4 = 0$). The accommodation in the world frame is then

$$\begin{bmatrix} \dot{r} \\ \dot{z} \end{bmatrix} = \begin{bmatrix} \cos\theta' & -r'\sin\theta' \\ -\sin\theta' & -r'\cos\theta' \end{bmatrix} \begin{bmatrix} \dot{r}' \\ \dot{\theta}' \end{bmatrix} \tag{5.2}$$

The final desired insertion velocity for the manipulator end-point becomes

$$\mathbf{v}_{des} = \mathbf{v}_0 + \begin{bmatrix} \dot{r}\cos\theta_0 & \dot{r}\sin\theta_0 & \dot{z} & 0 & 0 \end{bmatrix}^T \tag{5.3}$$

where $\mathbf{v}_0$ is the unmodified insertion velocity and θ_0 is the base joint angle used to convert from the cylindrical to Cartesian frame.

Results for the force and torque measured at the plate for insertion with accommodation and without accommodation show the effectiveness of this technique. Figure 5.4 and 5.5 show the results for both

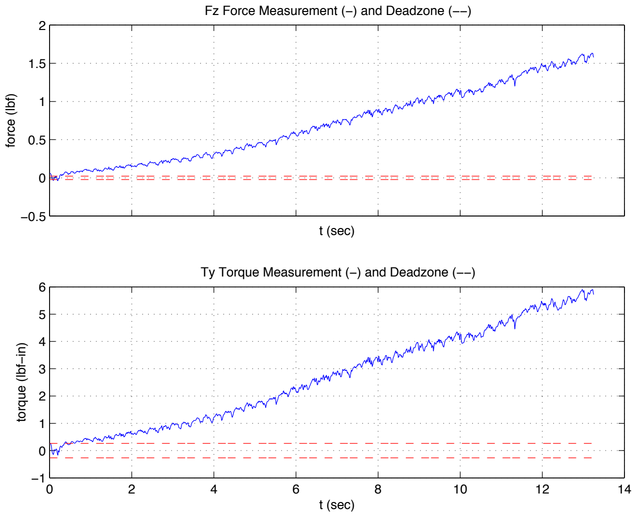

Figure 5.4: Plate insertion with lateral force accommodation disabled. The dashed horizontal lines represent the desired dead-zone for insertion.

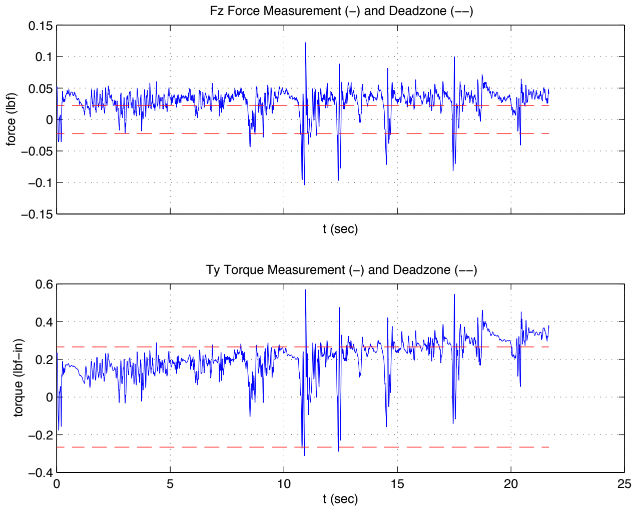

Figure 5.5: Plate insertion with lateral force accommodation enabled. The dashed horizontal lines represent the desired dead-zone for insertion.

cases. The dashed horizontal lines, which represent the force and torque dead-zones, are at the same values in both plots. Note that the force is slightly outside the dead-zone in the accommodation plots. This is because no correction occurs until the force moves outside of the dead-zone. Thus the force is expected to be slightly outside of this band, as is the case. Note that without accommodation, the force builds up to approximately 1.5 lbf, and with accommodation, the force remains around 0.05 lbf. The disturbance to the nearby soil is observed to be much less for the insertion with accommodation.

5.3 Stroke Controller Design

As previously discussed in Chapter 3, the manipulator can be controlled using joint proportional-integral-derivative (PID) control or Cartesian Stiffness control. First, the performance of these two control methods are examined in the context of stroking. Next, the development of a high-level position feedback control and force feedback control are examined. The suitability of each of these approaches is considered.

5.3.1 Effective Cartesian Stiffness of Position Controllers

This section examines the effectiveness of two different position control schemes, joint PID and Cartesian Stiffness, on the resulting stroke control. Assuming quasi-static motions, so that effects of the derivative (velocity/damping) terms can be ignored, the effective force output of the control methods to a given position error is examined. Although a higher level closed-loop feedback control will be present on top of these low-level controllers (so that eventually, the correct force output will be achieved), it would be beneficial to have an open-loop force output which reasonably matches the direction of the Cartesian error. A poorly performing low-level controller will require greater correction from the high-level controller.

Given a Cartesian position error, the computed output force from each of the two low-level controllers can be skewed from the direction of the position error. For the joint PID, the output force vector is computed as

$$\mathbf{F}_{PID} = \mathbf{J}^{-T}\,\boldsymbol{\tau} = \mathbf{J}^{-T}\,\mathbf{K}_{PID}\,\Delta\mathbf{q} = \mathbf{J}^{-T}\,\mathbf{K}_{PID}\,\mathbf{J}^{-1}\,\Delta\mathbf{x} \quad (5.4)$$

For the Cartesian Stiffness control, the resulting force vector is computed as

$$\begin{aligned}
\mathbf{F}_{CRT} &= \mathbf{J}^{-T}\,\boldsymbol{\tau} && (5.5)\\
&= \mathbf{J}^{-T}\,\mathbf{J}^{T}\,\mathbf{K}_{PX}\,\mathbf{J}\,\Delta\mathbf{q} && (5.6)\\
&= \mathbf{J}^{-T}\,\mathbf{J}^{T}\,\mathbf{R}^{T}\,\mathbf{K}_{CRT}\,\mathbf{R}\,\mathbf{J}\,\mathbf{J}^{-1}\,\Delta\mathbf{x} && (5.7)
\end{aligned}$$

The Jacobian is non-square because the wrist is turned off during stroking, resulting in a 5x4 matrix. Rather than complicate the notation, where inverses have been indicated in the above equations, pseudo-inverses are intended, but for cleanness, the more convenient inverse notation has been used. Since the Jacobian is non-square, the Jacobian multiplied by its pseudo-inverse may not be exactly the identity matrix, therefore these terms are left in the equation and computation. The **R** matrices are rotation matrices of the base joint angle, θ_0, which are used to make the stiffness matrix cylindrical instead of Cartesian.

Using Equations 5.4 and 5.7, the resulting skewing can be examined. The Cartesian error, $\Delta\mathbf{x}$, is specified to be a unit vector first in the radial direction and second in the vertical direction at various arm configurations. For each Cartesian error, the resulting directions of the output forces are computed. The controllers will each produce an open-loop force which may be skewed from the Cartesian error direction.

Figure 5.6 shows the results for three different arm configurations: radial extensions of 8", 12", and 17" at a height of -12.5". As can be seen, the joint PID control results in widely skewed force vectors which are highly configuration dependent. This does not make the PID control unusable, since the high-level controller will adjust the desired position until the desired output force direction is achieved. However, this configuration dependent skewing causes difficulties in the selection of correction gains for the high-level feedback loop. This results in a poor solution requiring large changes in desired position to obtain the desired force direction. Instead, the Cartesian Stiffness control does as it is expected to and compensates for arm configuration changes and maintains good orientation of open-loop force vectors. For this reason, the Cartesian Stiffness control is used as the low-level controller for stroking.

5.3.2 Position Feedback versus Force Feedback Control

As just discussed, both of the low-level controllers are position-based. In order to maintain the modularity of the system architecture and

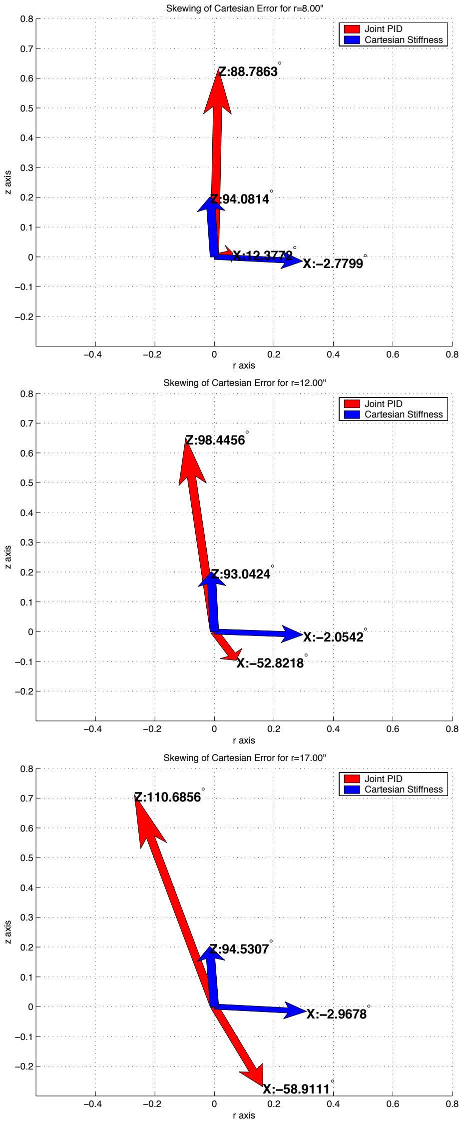

Figure 5.6: These figures show the resulting direction of the end-point force output by the arm controller for a unit error in the radial and vertical directions. The joint PID control results in a position dependent skewing of the end-point force, whereas the Cartesian Stiffness Control maintains the output force direction close to the error direction.

reduce the overall complexity, both high-level controllers are designed to provide position set-points for the low-level controllers. This is not a restriction for the force feedback based control. It is always possible for us to recast the force feedback law into a position feedback law to obtain numerically identical output torques at the motors. Neglecting derivative terms, a position-based control will compute torques based upon

$$\boldsymbol{\tau} = \mathbf{K}_P \ (\mathbf{q}_{des} - \mathbf{q}) \tag{5.8}$$

A force based control will compute the output torque from the desired force using

$$\boldsymbol{\tau} = \mathbf{J}^T \ \mathbf{F} \tag{5.9}$$

With some mathematical manipulation, an equivalent desired position to obtain the numerically identical torques can be computed as

$$\mathbf{q}_{des} = \mathbf{K}_P^{-1} \ \mathbf{J}^T \ \mathbf{F} + \mathbf{q} \tag{5.10}$$

This assumes the joint gain matrix is invertible. Typically joint gain matrices are required to be positive definite for stability. This ensures that the gain matrix is invertible. For this manipulator, the gain matrix is diagonal (before multiplying by the joint-motor transformation matrices) with strictly positive elements, and therefore invertible.

Therefore, in this implementation, both the position feedback and the force feedback control provide a desired set-point position to drive the low-level position control schemes. How the desired set-point is computed distinguishes the two control methods, as will be shown next.

5.3.2.1 Goals of Control Schemes

Once the plate is inserted into the sand, forces must be built up on the plate until failure occurs. How these forces are built up is critical to the quality and usefulness of the resulting data. The numerical limit analysis models assume a perfectly horizontal instantaneous motion for the plate. The limit equilibrium models are more general and simply require knowledge of the interface friction angle between the soil and the plate. In order to be consistent with all the models, the initial plate motion should be perfectly horizontal with a steady interface friction angle.

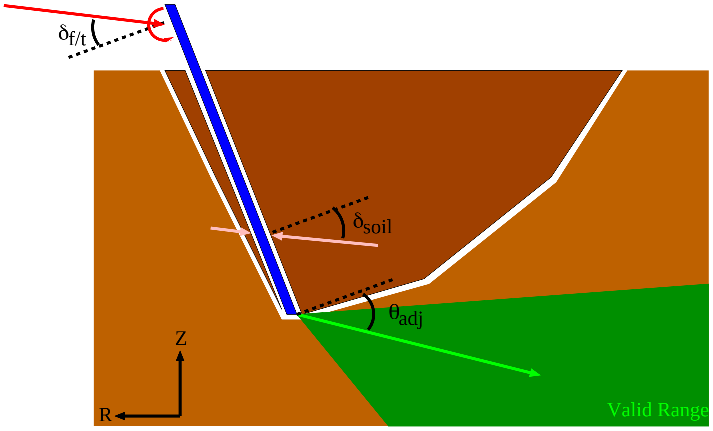

Figure 5.7: The control during a stroke is accomplished by varying the leading and orientation of a vector within acceptable bounds (shown in green).

5.3.2.2 Position Feedback Control

The control during a stroke is accomplished by adjusting the desired position to lie along a vector oriented at angle θ_{adj} as shown in Figure 5.7. The magnitude of the difference between the desired position and the actual position of the arm end-point is called the *lead*. The lead is increased steadily until failure occurs. As the lead is increased, the orientation, θ_{adj}, is controlled using a proportional-integral (PI) controller on the Z error of the plate.

$$\begin{aligned} \theta_{adj}(t) &= \theta_{des} + k_{p_{stroke}} \left(z(0) - z(t)\right) \\ &\quad + k_{i_{stroke}} \int \left(z(0) - z(t)\right)\, dt \end{aligned} \tag{5.11}$$

where θ_{des} is the desired initial inclination angle. The integral term corrects for large scale and steady state errors and brings the system into the correct region. The proportional term then does the fine corrections to regulate the output.

The angle of orientation is constrained to remain within reasonable bounds. These bounds are only of importance during the first fraction of a second of the stroke in order to keep the plate from lifting or sinking before any appreciable force is applied on the soil. Typical bounds are $[\theta_{plate} - \delta_{soil} + 10°, 60°]$ from horizontal, where θ_{plate} is the angle of the plate relative to vertical and δ_{soil} is an estimate of the soil-tool friction angle.

There are a number of problems with this position feedback approach. The first is that it relies upon the position measurements from the external encoders, which are at the limit of their resolution, providing poor feedback. Also, in order to compensate for a Z error, motion must have already occurred to create the error. Taking into account the low position sensing resolution of our manipulator, a large motion must have occurred. In contrast, the goal of the control is to increase the force applied by the plate with little or no vertical motion of the plate.

Vertical motion may not necessarily indicate relative motion between the soil and the plate. The environment has some stiffness, and so, a vertical deflection may occur without interface sliding. In order to sense such motion, much more precise sensing accuracy is required. For the manipulator in this work, any detected vertical motion will indicate that the configuration of plate and soil has changed. In the absence of an accurate force measurement, the position scheme will only be viable if a high level of position sensing is available.

Figure 5.8 shows the data from a stroke using position feedback. In the upper plot, the discontinuous steps in the solid line are a result of the encoder resolution. The gap between the actual and motor position is a result of compliance and backlash in the shoulder joint. In the lower plot, the resulting variation in interface friction angle is shown. The measured interface friction angle between the soil and plate, $\delta_{f/t}$, is not regulated and varies considerably up to the point of failure.

The uncontrolled force direction leads to an unreliable failure force measurement. The failure force is highly dependent upon the angle of the applied force. If the angle of force momentarily becomes smaller than the true interface friction at a given force magnitude (which would not typically fail the soil at the proper interface friction angle), then the soil will prematurely fail, resulting in a low reading. If the angle of force is excessively large for a period of time while the force magnitude continues to increase, then when the force angle reaches a more reasonable value, the force magnitude is already great enough to fail the soil, resulting in a high reading. Therefore, any readings taken with large variations in angle of force are unusable.

5.3.2.3 Force Feedback Control

Given that position feedback control is not possible for our system, and the arm is equipped with force sensing capability, a force feedback

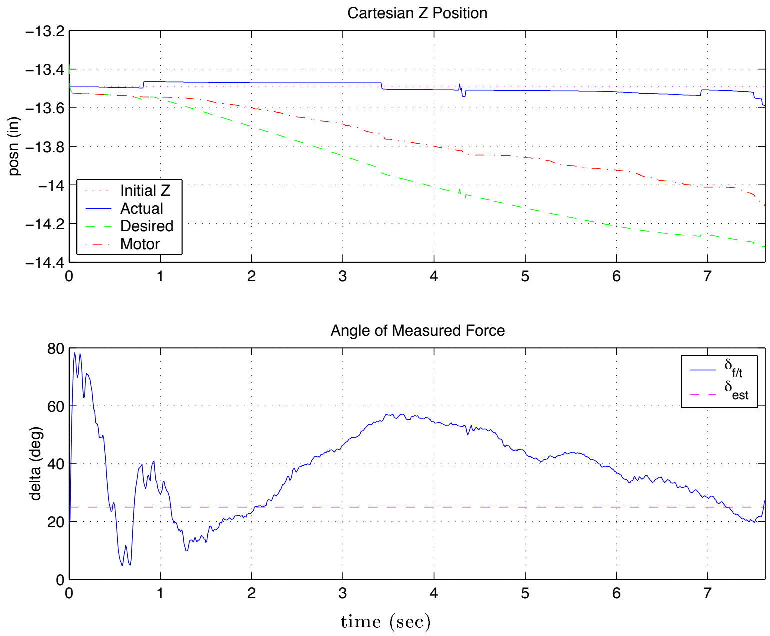

Figure 5.8: Results from a stroke using position feedback. The upper plot shows the desired and actual Z coordinates and the lower shows the angle of the measured force.

control law is developed to solve the problem. Examining the forces in Figure 5.7, if the net vertical force on the plate is zero, then no vertical motion should occur. This is the premise behind the force control method. No explicit feedback of the Z error is used. Instead, it is assumed that the interface friction between the plate and soil can be estimated, and that this estimate can be used as a set-point for the force control. If the interface friction estimate is correct, and the control can maintain the angle of force at the estimated friction angle, then the plate should move horizontally. If the estimate is incorrect, then there are no guarantees on the horizontal motion.

Assuming we have an accurate estimate of the true interface friction angle, a force control law must be developed which can accurately track this desired angle. The development of such a control law is described in this section.

The initial basis for the stroke control comes from a basic proportional force control law. For a desired force output from the arm, $\mathbf{F}_{des}$,

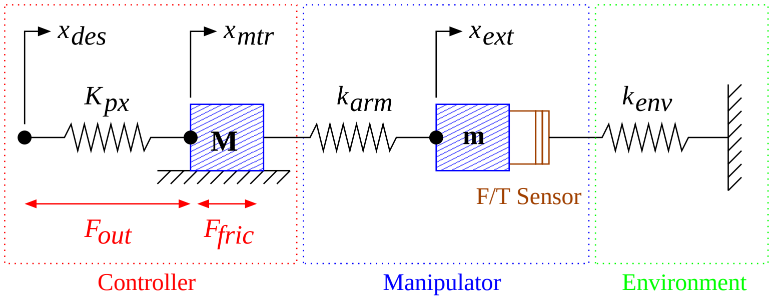

Figure 5.9: One-dimensional conceptual model of arm flexibility and backdrive friction for force control.

joint torques, $\boldsymbol{\tau}$, are output using a proportional control law given by

$$\boldsymbol{\tau} = \mathbf{J}^T\ \mathbf{F}_{ctrl} = \mathbf{J}^T\ [\mathbf{K}_{pf}\ (\mathbf{F}_{des} - \mathbf{F}_{env}) + \mathbf{F}_{des}] \tag{5.12}$$

where $\mathbf{K}_{pf}$ is the force gain and $\mathbf{F}_{env}$ is the measured end-point force. The development begins with this equation and adds modifications to address issues which are specific to this manipulator and problem. First, the arm is flexible and highly geared. This will change the design of the controller in a subtle way. Second, while the above system will regulate force, the goal in stroking is to control orientation, and to a lesser extent magnitude. For the magnitude, it is sufficient to simply have it increase in a steady monotonic fashion. The controller should be able to handle orientation and magnitude separately.

The issue of arm flexibility and gearing is considered first. Figure 5.9 shows a simple one-dimensional model to help formulate a conceptual understanding of the problem. The control force, F_{out}, is applied to a mass, M, resting on a frictional ground to simulate backdrive friction. Attached to the mass is a spring representing the arm flexibility, with stiffness k_{arm}. The other end of the spring is connected to the arm mass, m, and the force/torque sensor, which in turn is connected to the environment, with stiffness k_{env}. The point where the force is applied to the motor mass is labeled as x_{mtr} and the position of the arm measured by the external encoders is labeled as x_{ext}.

The controller must regulate the force on the environment, as measured by the force/torque sensor. Starting with a standard proportional force control law of a mass-spring system (Craig [22]), a force f_{ctrl} is applied to the mass m given by

$$f_{ctrl} = m\ k_{env}^{-1}\ k_{pf}\ (f_{des} - f_{env}) + f_{des} \tag{5.13}$$

where f_{env} is the force measurement from the force/torque sensor and f_{des} is the desired force on the environment.

Now, f_{ctrl} is the force to be applied to mass m. In order to apply this force, we must specify an input to the low-level arm controller. The low-level control is the Cartesian Stiffness previously presented. It computes an output force according to

$$F_{out} = K_{px}\left(x_{des} - x_{mtr}\right) \tag{5.14}$$

where K_{px} is the controller stiffness gain and x_{des} is the desired position of the motor. Let us examine how to specify x_{des} in this control law.

Two different cases can be considered, depending on the arm stiffness. Most manipulators tend to be very stiff, however, there is an increasing trend towards the design of compliant manipulators (Pratt [80]).

If the manipulator stiffness is high, then k_{arm} can be ignored. The desired set-point can be computed as

$$\begin{aligned} x_{des} &= K_{px}^{-1} f_{ctrl} + x_{mtr} && (5.15)\\ &= K_{px}^{-1}\left(m\ k_{env}^{-1}\ k_{pf}\left(f_{des} - f_{env}\right) + f_{des}\right) + x_{mtr} && (5.16)\end{aligned}$$

The x_{mtr} terms will cancel in the low-level control, and the resulting output will be exactly the desired control force.

If, on the other hand, the manipulator is flexible, the force applied to the mass m can be controlled by adjusting the deflection of the spring k_{arm}. The desired motor position to achieve the control force can be computed according to

$$\begin{aligned} k_{arm}\left(x_{des} - x_{ext}\right) &= m\ k_{env}^{-1}\ k_{pf}\left(f_{des} - f_{env}\right) + f_{des} && (5.17)\\ x_{des} &= m\ k_{arm}^{-1}\ k_{env}^{-1}\ k_{pf}\left(f_{des} - f_{env}\right)\\ &\qquad + k_{arm}^{-1}\ f_{des} + x_{ext} && (5.18)\end{aligned}$$

In the above equation, m, k_{env}, and k_{arm} are unknown. The first terms can be grouped with the force control gain k_{pf} which is empirically tuned. This still leaves k_{arm} in the second term.

Through the use of the force/torque sensor, it should be possible to estimate k_{arm} using the force/torque sensor measurement, f_{env}, and the motor-external displacement. One item to note when approximating k_{arm}, the one dimensional model helps us gain a conceptual understanding, but there is another component that occurs when moving to two dimensions. In addition to the magnitude scaling, there is a possible rotation resulting from the arm stiffness matrix. For this arm, this effect will be fairly drastic. The external encoder for the shoulder is mounted directly at the joint, with a large compliance between the motor and the joint. The elbow encoders, on the other hand, are mounted to the output shafts of the motors, before the long cable transmission. These will have a small detected compliance, and a large unmeasured compliance in the cable transmission. The external encoders were a later addition and were not originally intended to be used for force control through measured compliance. As a result, between the motor and the external positions, a very flexible shoulder and stiff elbow would be perceived (usually translating to a flexible vertical axis and stiff radial). However, since the elbow is indeed flexible, this works to undo the rotation that would be perceived in the motor-external deflection. For simplicity, it is assumed that k_{arm} is diagonal. It is also assumed that the stiffness is constant over the region we are stroking.

Using the desired position from Equation 5.18 in the low-level control law, the following output force is obtained

$$\begin{align}
F_{out} &= K_{px}\left(x_{des} - x_{mtr}\right) \tag{5.19} \\
&= K_{px}\; m\; k_{arm}^{-1}\; k_{env}^{-1}\; k_{pf}\left(f_{des} - f_{env}\right) \nonumber \\
&\quad + K_{px}\; k_{arm}^{-1}\; f_{des} + K_{px}\left(x_{ext} - x_{mtr}\right) \tag{5.20} \\
&= K_{px}\; m\; k_{arm}^{-1}\; k_{env}^{-1}\; k_{pf}\left(f_{des} - f_{env}\right) \nonumber \\
&\quad + K_{px}\; k_{arm}^{-1}\; f_{des} + K_{px}\; k_{arm}^{-1} k_{arm}\left(x_{ext} - x_{mtr}\right) \tag{5.21} \\
&= K_{px}\; m\; k_{arm}^{-1}\; k_{env}^{-1}\; k_{pf}\left(f_{des} - f_{env}\right) \nonumber \\
&\quad + K_{px}\; k_{arm}^{-1}\;\left(f_{des} - f_{env}\right) \tag{5.22}
\end{align}$$

It is interesting to note that if $K_{px} = \alpha\; k_{arm}$, then this results in an output force given by

$$F_{out} = \alpha\left(m\; k_{env}^{-1}\; k_{pf} + 1\right)\left(f_{des} - f_{env}\right) \tag{5.23}$$

Effectively, this is simply just a single gain multiplying the force error and does not require direct estimation of k_{arm}. This equation was originally derived from the premise that the arm was flexible and the controller stiff. In the steady state case, this control implies that to maintain a given force on the environment, no additional force from the motor needs to be applied. The control adjusts the position of x_{mtr}, not the force. The motor positioning at x_{mtr} would automatically contribute the additional force, $f_{env} = f_{des}$, at steady-state, through the stored force in the spring, k_{arm}. In order to keep the motor positioned at x_{mtr}, there must be some force holding it there. This is an idealization in the derivation (i.e. assuming that the system is a perfect position source).

There is another factor which makes the idealization of the arm as a perfect position source valid: the presence of backdrive friction. The backdrive friction for this arm is large enough to require end-point forces approximately 0.25 lbf to backdrive the shoulder motor and 0.6 lbf to backdrive the elbow motors in a typical digging configuration. This is a significant fraction of the total forces experienced during digging. This friction would act to maintain the arm position at x_{mtr}.

Two alternatives have been discussed: a stiff manipulator acting as a force source, and a compliant manipulator with backdrive friction acting as a position source. These alternatives translate into two equations: to specify the desired position to the low-level control as $x_{des} = K_{px}^{-1} f_{ctrl} + x_{mtr}$, or as $x_{des} = K_{px}^{-1} f_{ctrl} + x_{ext}$. Both versions of the control law are tested on our system for stroking. In each case, the gains were tuned independently. The performance is found to be poor when specifying the desired position relative to the motor position. The controller performs very well when specifying the desired relative to the external position. There is one minor difficulty with this approach. The external encoders are known to have a low sensing resolution. Since the control law uses the external position explicitly, it produces a discontinuity in the desired position whose effect is noticeable in the data, but the controller is sufficiently capable that the disturbance is quickly rejected. Clearly the combination of $K_{px} > k_{arm}$, low arm stiffness, and the presence of the backdrive friction call for the use of x_{ext} in the desired position of the controller.

In summary, the force control law, up to this point, specifies the desired set-point for the low-level Cartesian Stiffness control according to (reverting to vector notation)

$$\mathbf{x}_{des} = \mathbf{K}_{px}^{-1} \left[\mathbf{K}_{pf} \left(\mathbf{F}_{des} - \mathbf{F}_{env} \right) + \mathbf{F}_{des} \right] + \mathbf{x}_{ext} \tag{5.24}$$

In the absence of arm flexibility and backdrive friction, $\mathbf{x}_{ext}$ can be replaced with $\mathbf{x}_{mtr}$.

The second issue with our force controller relates to the impact of the control law on orientation and magnitude. Figure 5.10 gives an illustration of the controller correction for a desired force $\mathbf{F}_{des}$ and a measured force $\mathbf{F}_{env}$. The existing control structure does not allow for separate gains on the orientation and magnitude. To obtain fast orientation correction, a large gain must be used, but by doing so, the magnitude varies greatly. In addition, the incorporation of an integral correction term in a vector context may introduce unexpected orientation changes. Orientation correction is more critical than magnitude correction. So, the control is separated into orientation and magnitude

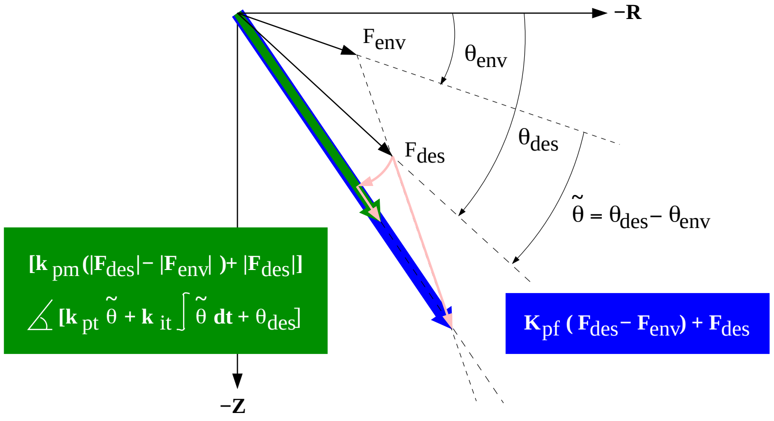

Figure 5.10: The direction and magnitude of the correction vectors of the standard force control law and the orientation based control.

components. Following along the lines of the position control scheme previously discussed, two independent PI control laws are implemented:

$$\begin{aligned}
\mathbf{F}_{ctrl} &= \mathbf{K}_{pf}\left(\mathbf{F}_{des} - \mathbf{F}_{env}\right) + \mathbf{F}_{des} && (5.25)\\
&= \Big(k_{pm}\left(|\mathbf{F}_{des}| - |\mathbf{F}_{env}|\right) + |\mathbf{F}_{des}|\Big) \\
&\qquad \begin{bmatrix} \cos\left(k_{pt}\tilde{\theta} + k_{it}\int\tilde{\theta}dt + \theta_{des}\right) \\ \sin\left(k_{pt}\tilde{\theta} + k_{it}\int\tilde{\theta}dt + \theta_{des}\right) \end{bmatrix} && (5.26)
\end{aligned}$$

where $\tilde{\theta} = \theta_{des} - \theta_{env}$, the desired inclination angle minus the force/torque sensor measured inclination. Only the radial and vertical components are shown.

The magnitude is not of great concern, except that it should monotonically increase, so the magnitude proportional control can be replaced with an open-loop increasing lead given by $(l_0 + l_{rate}t)$, where l_0 is the initial lead and l_{rate} is the rate of increase. The initial lead is often small, but is necessary so that the stroke begins with a non-zero force applied to the soil. This provides some initial interface friction to keep the plate from moving in the early stages of the stroke.

The rate of increase of the leading is an important variable in controlling the duration of the stroke, allowing for sufficient time for the orientation controller to operate. It also affects how drastic the final soil failure will be. If the force build up is fast enough at failure to overcome the increase in resistance due to the soil build up, then the plate will continue its forward motion more rapidly.

After this lengthy development, the force feedback control is found to be the same form as the position feedback control. The only difference is the error measure in the PI control is the force inclination error instead of the Z position error. There are a number of reasons why this method is a better approach than the previous Z error method. By controlling the force angle directly, if the angle of the applied force is maintained to be smaller than the true interface friction angle, then slip cannot occur. Therefore, the plate is not moving relative to the soil. Unlike the previous method, this approach does not require motion to occur in order to perform correction. While the force builds up, the controller can safely regulate the friction angle. However, this method will be susceptible to the same quality problem as the previous approach if the applied angle of force cannot be controlled within suitable bounds prior to failure.

Through experimentation, the gains of the control loop are tuned so that good tracking (within 1°-3°) of the desired interface friction angle for most of the duration of the stroke can be achieved. In the resulting data, large variations in the friction angle at early stages of the stroke can be ignored. This portion reflects the initial convergence of the system at very low forces and care is made to ensure that this variation is often in the downward direction (into the soil), where small forces will have little or no effect on the greater resistance of the underlying soil.

Figure 5.11 shows sample data from a force control stroke. As mentioned before, the force control relies upon a good estimate of the interface friction angle to be used as a set-point. In this case, from the minimal Z motion, it is noted that a good estimate of the interface friction angle has indeed been obtained. In the lower plot, it can be seen that the force control tracks the desired set-point to within a few degrees. It can also be noted that there is almost no perceptible Z motion.

5.3.3 Safe Orientations and Magnitudes

Figure 5.12 gives an illustration of safe orientations and magnitudes of force which do not cause relative motion between the plate and soil. The boundary can be computed using the soil models to estimate the force required to fail the soil at various angles of applied force. There is the added resistance to insertion when forces are applied in the downward direction. The downward insertion force combined with the other

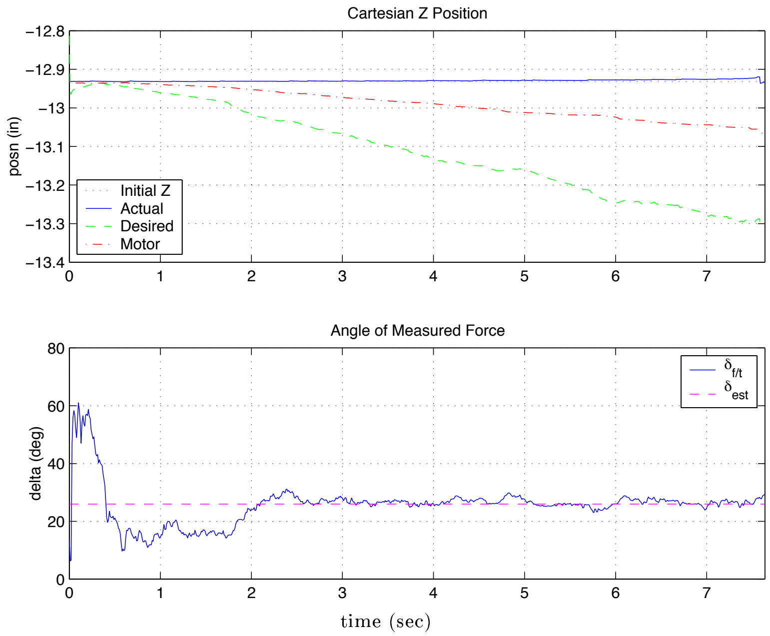

Figure 5.11: Results from a stroke using force control. The upper plot shows the desired and actual Z coordinates and the lower shows the angle of the measured force.

force predictions construct a boundary for safe angles and magnitudes. Note that with a force magnitude of $F_{\theta_{adj}=\delta_{soil}}$, an orientation angle greater than δ_{soil} will not cause motion. Thus if there are transients in the stroke control, for small magnitudes, the orientation can safely vary significantly, with larger magnitudes, it is better to err towards a greater downward orientation to avoid premature failure.

A more detailed study and experimental verification of the dependence of the failure force on angle of applied load would be quite interesting. Such data could be used to plan optimal digging trajectories through soil for a torque limited manipulator. This topic is not explored in this work and is left as a possibility for future research.

5.4 Interface Friction Angle Estimation

The position and force feedback controller development assumed a desired inclination for the applied force during stroking. This inclination

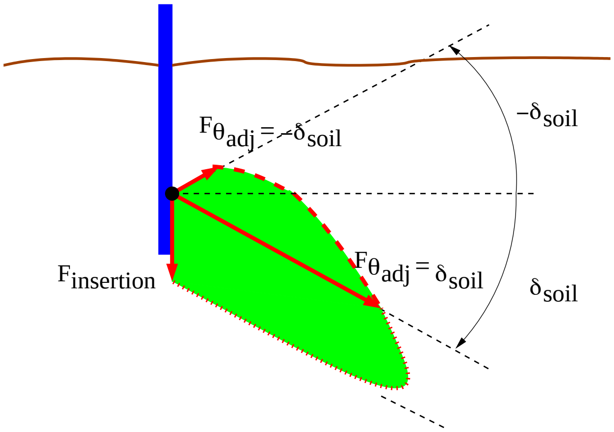

Figure 5.12: There exists a range of force vectors which can be applied to the soil without causing relative motion. Below δ_{soil}, the actual magnitude is uncertain, but is likely to be a combination of insertion and earth pressure predictions up to $\delta = \phi$.

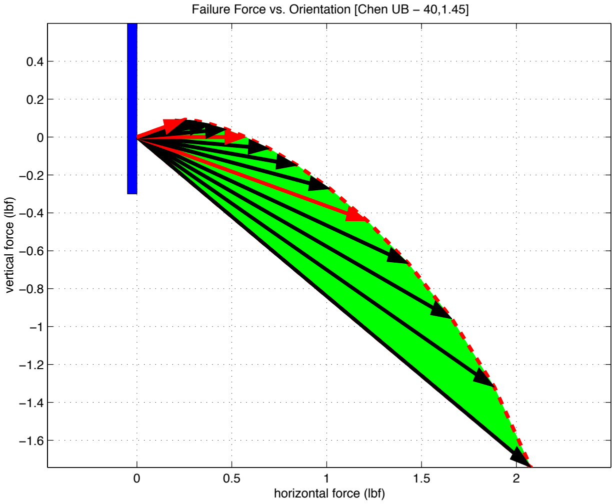

Figure 5.13: Actual results using Chen and Liu's upper bound model to illustrate the dependence of the failure force on interface friction angle. The predictions are shown for up to $\delta = \phi$, using $\phi = 40°$ and γ=1.45 g/cc, with highlighted vectors at 0° and ±20°.

is the interface friction angle, δ_{soil}. A method must be developed for estimation of the true soil-tool interface friction angle for the test soils.

Considering the stroke control once again, forces are built up on the plate with a given orientation until the force is sufficient to fail the soil. At this point, failure will occur (hopefully in a drastic fashion) with a large horizontal motion of the plate. When the force is large enough to initiate motion, the soil adjacent to the plate rises relative to the plate, causing a force on the plate which is at the true friction angle between the plate and soil. If the estimated friction angle used in the force controller is different from the true value, an error in the measured force will be observed. The force controller will not respond instantaneously to this error. Therefore, this provides a mechanism to verify if the friction angle estimate used for a stroke is incorrect.

This approach is expected to work if the estimated value is lower than the true friction angle. If, instead, the estimate is too large, then the plate drives into the soil. During failure in this case, a larger downward force angle may be maintained (no error will be observed) since the underlying soil will resist the force. A drop in the Z coordinate of the plate may perhaps be observed, but this requires precise sensing. It is likely that the deflection will not be noticeable unless there is a large error in the estimated friction angle.

Therefore, the experimental procedure for determining the interface friction angle is to attempt multiple strokes in the soil starting with a known lower friction estimate and building up until a rise in the angle of force is not seen in the data at failure. By this method the true interface friction angle is bracketed through a few strokes.

Figure 5.14 shows the results from strokes in Ticino sand, using friction angle estimates from 18° to 28°. Failure occurs in the last fraction of a second of the stroke. The earlier portion of the data is the force buildup stage. The $18° - 22°$ strokes show lifting, while the $24° - 28°$ strokes do not. From this, it is inferred that the true friction angle is near 23°. As shown, the tracking of the estimated friction angle is very good using the PI force controller. The jumps that occurs midway through the strokes are an artifact of the shoulder encoder resolution. The disturbances are rejected quickly and do not affect the final critical portion of the stroke.

In order to verify the accuracy of this approach, sand was glued to a flat plate. The plate was rubbed over the arm end-effector plate and data on the maximum interface friction angle was observed. This test is used only for ballpark verification, since the glued sand surface may be irregular and may not accurately simulate the configuration of soil adjacent to an inserted plate. The actual angle may be near or greater

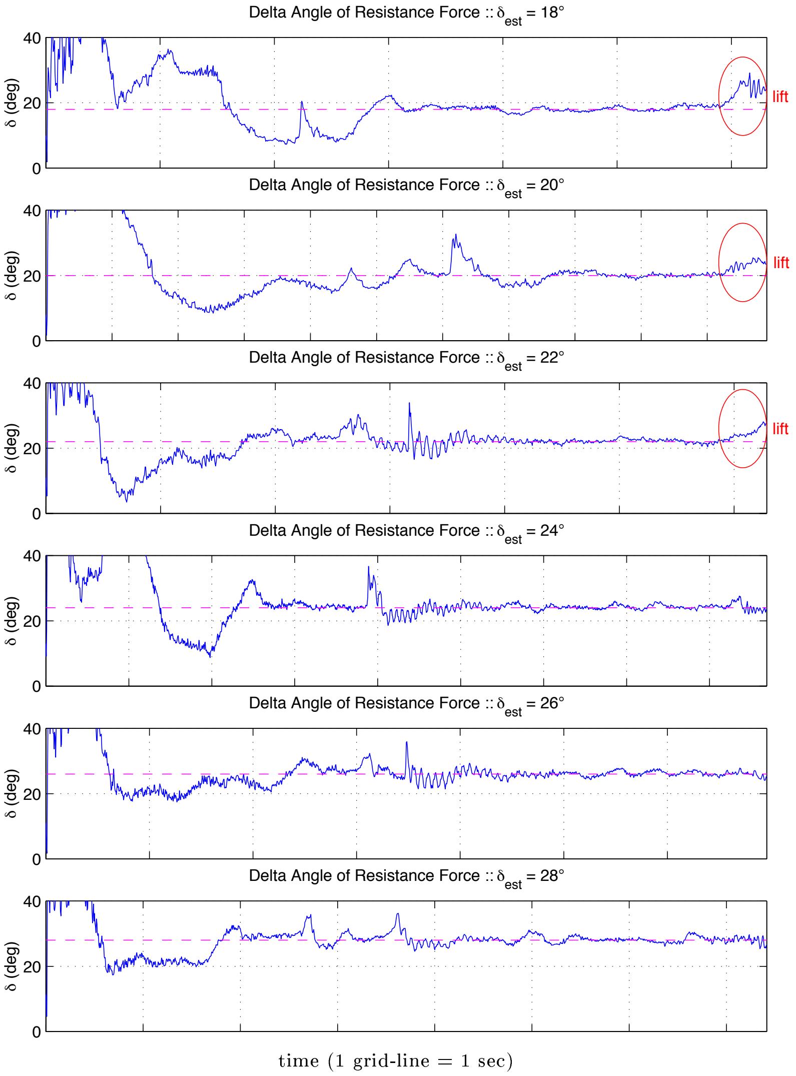

Figure 5.14: Data plots for the friction angle from the F/T sensor at various desired delta angles. The first three plots show lifting at the end, while the rest do not.

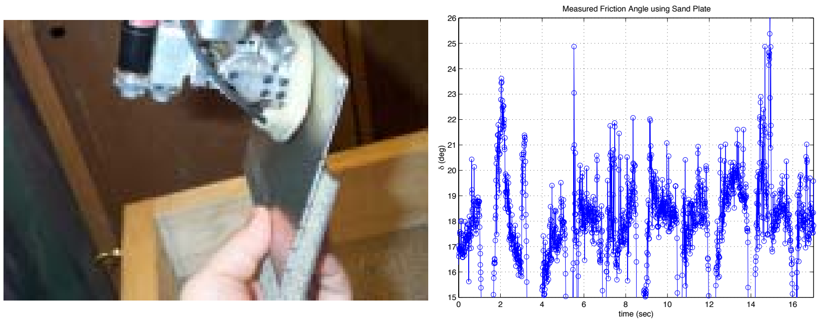

Figure 5.15: Ticino sand was glued to a plate and rubbed on the end-effector plate to validate the friction angle estimate. The plot on the right shows a portion of the data showing peaks in the $23° - 25°$ range.

than the peaks observed in these tests, rather than near the mean. This has been conducted with each of the soils used. The agreement between this method and the experimental iterative technique has proven to be good. Thus, it is concluded that this approach to interface friction estimation produces valid estimates typically within $1° - 2°$ of the true angle.

One final practical note about this approach: the delta estimation should only be implemented with tool angles in the $80° - 90°$ range. If a 70° tool is used, for instance, it is possible that tip effects (from the inclined width of the bottom of the plate) will come into play, increasing the apparent interface friction angle. Using a 100° degree tool is also problematic, primarily because these strokes are more difficult to conduct, and the motion of the soil relative to the plate is not observed as readily.

5.5 Data Processing

Once a stroke is completed, the resulting data must be analyzed to determine failure force. Force data from the F/T sensor (measuring forces directly on the plate) and joint data from the arm (used to determine the Cartesian motion of the plate) are collected for each stroke. These are combined into a force versus displacement plot, which is the primary means to estimate failure force.

There are some difficulties in the data processing. These arise from two primary sources. The first is the low position sensing resolution of

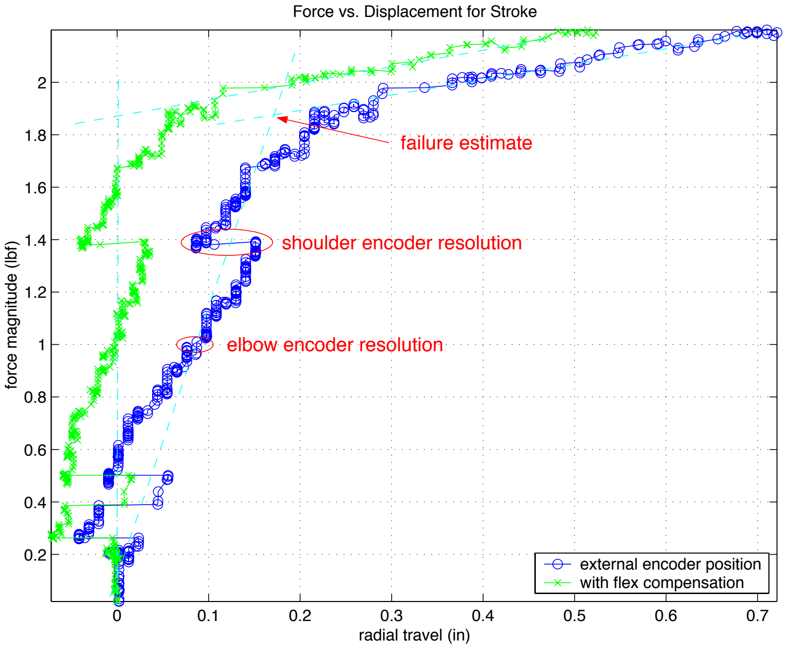

Figure 5.16: A force versus displacement plot for a 90° tool in Ticino sand, shown with and without flexion compensation, showing a gradual failure. The discontinuities are from the limited external encoder resolution.

the arm, due the large backlash of the motors, combined with the unsensed flexibility in cable transmission of the arm. The second difficulty is from the possibility of gradual failure of the soil. Figure 5.16 shows a force versus displacement plot for a sample stroke which illustrates each of these difficulties. The figure also illustrates the elbow flexion compensation discussed in Appendix A.

The encoder resolution limit, in actuality, does not create great difficulties in experimentation. The discontinuities are easily detected in the resulting data plots and can be ignored, since the resulting disturbances are quickly rejected. It should be emphasized that this sensing limitation is a shortcoming of this particular manipulator and does not affect the validity of the techniques used.

The gradual failure of the soil is another difficulty, which is not related to the manipulator. Ideally all strokes would exhibit drastic

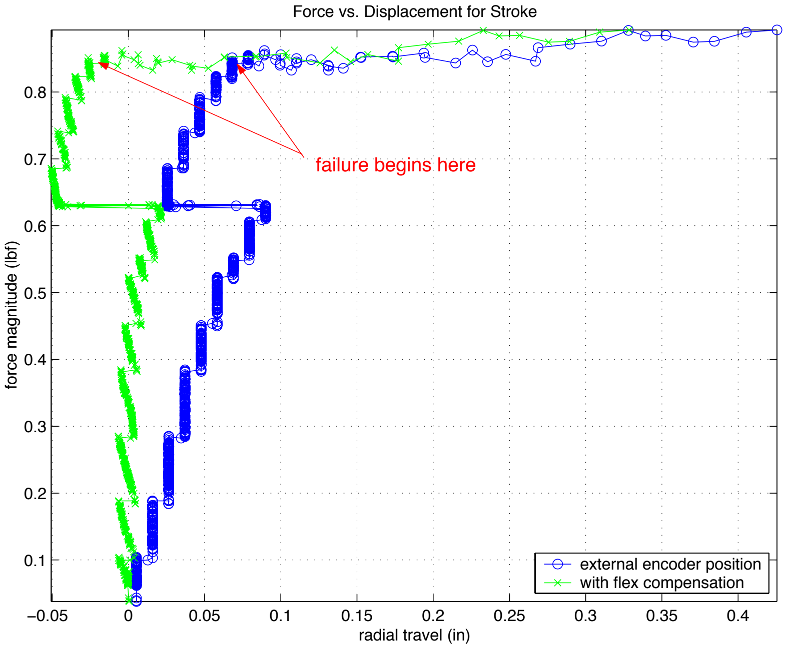

Figure 5.17: A force versus displacement plot for a 70° tool in Ticino sand, shown with and without flexion compensation, illustrating a more drastic definite failure.

failures, with large scale motions. This would make the failure force clearly discernible in the resulting data plots. Figure 5.17 shows an example of a drastic failure. The flex compensation in this plot is slightly excessive, but the compensation is known to be an approximation and not required or expected to be exact. The drastic failures are often characteristic of strokes at lower tool angles.

For the larger tool angles, in which the forces are greater and the build up of soil during motion is greater, the failure can often be gradual in nature and therefore difficult to pick out a single point of definite failure. In these situations, a consistent guideline in picking points of failure is used. Two lines are fit to the early portion and later portion of the force versus displacement curve. The breakpoint is located from the intersection of these lines (as shown in Figure 5.16).

There are additional sources of information that can aid in the determination of the onset of motion. These include a change in the Y coordinate of the point of application of the force on the plate, a change in the measured friction angle of the soil, or a change in the Z end-point coordinate. These were occasionally used as supplemental sources in the data analysis; however, the primary and best source for estimating the failure force is the force versus displacement plot.

5.6 Verification of Depth Dependence

As an additional verification of the methods outlined in this chapter, tests to verify known dependencies of the force have been conducted. The draft force required to fail soil should be linearly dependent on the density of the soil and quadratically dependent upon the depth of the plate. The density of our samples cannot be precisely controlled over a range of values; however, the depth of insertion can be controlled. A study of the dependence of the failure force on the depth of insertion can be conducted. This is especially of concern because of the shallow depths of insertion. If this dependence cannot be verified, then scaling the results to larger depths of insertion is questionable. Vice versa, the application of soil prediction models to these small insertion depths would be questionable.

Depths from 0.5" to 1.0" at 0.1" intervals are used. Smaller insertion depths are not useful and much deeper depths would be near the maximum strength capabilities of the manipulator. Strokes at each of the depths are conducted three times. Figure 5.18 shows the combined median results for the three test sets. The upper plot shows failure force versus depth of insertion and a quadratic least squares fit. The lower plot shows the normalized force, F/H^2, versus depth, H, which ideally would result in a horizontal line.

Each of the individual test sets produced essentially the same results, with only small variations. Each set showed the proper dependence within the error bounds shown. The error bounds in the figure result from the estimated accuracy of the insertion depth. The sensing accuracy of the manipulator end-point is approximately 0.05", and thus the insertion depth may be off by plus or minus this amount. In the stroking experiments, manual verification of the insertion depth is conducted. Small adjustments to the commanded depth of insertion are made to obtain the correct depth, or the resultant force values are scaled to the appropriate depth.

This depth verification test has also been repeated multiple times in the other soils used, with similar results. It can be concluded that the H^2 dependence on the depth holds true even at these small insertion

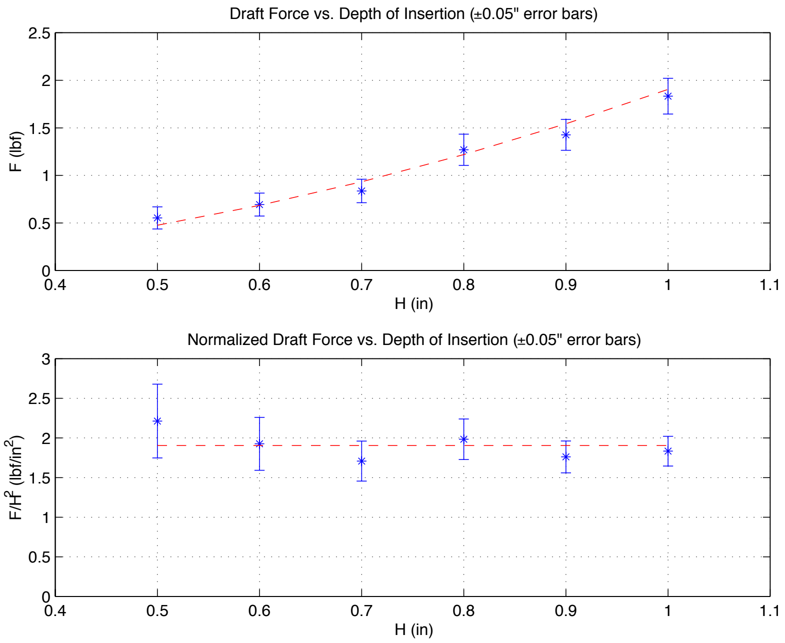

Figure 5.18: Tests were conducted to measure failure force at various depths of insertion. The upper plot shows force versus depth and a quadratic fit. The lower plot shows the normalized force, F/H^2, versus depth, H.

depths. This serves as a partial validation of the methods described, showing that this particular dependence can be observed using this system. In the next chapter, further interaction results using the techniques described in this chapter are presented.

Chapter 6

Experimental Results

This chapter presents results from interactions between the manipulator and various sample soils. The chapter begins with a discussion of soil selection and data collection procedures. Next, the data from interactions with each of the sample soils is presented. The chapter concludes with a presentation of independent tests for verification and a discussion of the sources of errors.

6.1 Selection of Soils

Three different soils were selected for testing. The goal in material selection was to span a range of friction angles and densities. As a secondary consideration, a variety of grain sizes was sought. An exhaustive collection of soils was not gathered, but rather a few soils were selected to verify our system and methods. The selected soils are all cohesionless sands. The three soils selected were Ticino sand, Nevada Fine sand, and glass beads (to simulate a low friction soil).

In order to obtain a dense, high friction angle sample, a raining assembly was used in combination with the Ticino sand. The other sands could not be rained because their particle size was too fine. Raining of these other sands would create a large amount of airborne particles and would result in separation of the finer particles from the test samples with repeated raining. In order to obtain a lower friction angle sample, fine rounded glass impact beads were obtained to simulate sand. The Nevada Fine sand was chosen with the expectation that it would provide an intermediate friction angle sample.

In the following discussions, loose or unrained soil will be indicated to distinguish it from the dense rained soil. No particular effort has

Soil	Density (g/cc)	Particle Size (μm)	Desired Friction Angle
Rained Ticino	1.60 (1.43-1.69)	350-700	$50°+$
Ticino	1.43 (1.43-1.69)	350-700	$40° - 50°$
Nevada Fine	1.44 (1.35-1.57)	180^1-280	$30° - 40°$
Glass Beads	1.46 (1.45-1.55)	90-150	$20° - 30°$

[1] 30% particles by weight instead of 10%.

Table 6.1: Measured density of the test cases and the rough measured loose-dense range in parentheses, 10-90% particle size ranges, and the desired friction angles of the soils used in our experiments. The loose-dense ranges are approximate and were acquired through simple pouring and raining preparations. The true ranges likely extend outward in both directions.

been made to make the soil especially loose. These soils were in a simply poured and shifted state, which typically placed them in the lower portion of their density ranges. Approximate density measurements of the soils in the same state used in each stroking experiment were done for verification. It is expected that there will be variation in these sands due to the lack of special preparation, but the impact is believed to be minimal. In addition, some variation in soil density should be expected in the real world, so it is of interest to see the impact of such variation in testing. From our experience, repeated testing of samples prepared in this way resulted in a maximum density variation of about 4%, with most being within 2% of the mean.

Table 6.1 shows the range of densities, particle size distribution, and desired friction angles for the soils selected. The range of densities are approximate and were determined with basic procedures. The loose case was prepared through depositing the soil into a cylinder of known volume at low velocity using a funnel. The dense case was prepared through gradual raining of the soil into the cylinder from a height of approximately 6 inches. The true range of loose-dense is likely to extend outward in both directions. The friction angles in the table are values that were anticipated for each soil type. The Ticino sand was expected to provide samples in the $40° - 50°+$ range as quoted from Larson [63]. The glass beads, with a majority of fine round particles, were known to have a much lower friction angle. The Nevada Fine sand was expected to provide an intermediate value. Thus, a range of friction angles from the twenties to the fifties would be spanned.

Radius	17”	12”
Set 1	90°	70°
Set 2	80°	70°
Set 3	100°	90°
Set 4	100°	80°
Set 5	90°	100°
Set 6	80°	90°
Set 7	80°	70°
Set 8	100°	70°

Table 6.2: Arrangement of tool angles for six-stroke batches (unrained).

6.2 Organization of Data Collection

The stroking tests in the sample soils were conducted in sets of six strokes per batch, except for the rained cases, in which only four strokes were completed per batch. The soil was prepared to have a surface within one degree of horizontal, using a digital level as verification. Care was taken in the rained cases to carefully level the soil without disturbing or piling loose soil in regions where stroking was to be conducted. As a result, only four strokes per rained batch, rather than the typical six, were conducted. In the unrained cases, the soil was manually remixed to obtain approximately constant conditions over multiple batches.

To verify that there is no dependence on arm configuration, multiple batches were run with a staggered arrangement of tool angles. For the unrained soils, the strokes were done with three strokes at one tool angle at radius near 17” and another three strokes at another tool angle at radius near 12”. The 70° tool angle can only occur at the 12” radius due to the limited range of motion of the wrist joint. With this limitation, in order to have every possible combination and an equal number of data points for every tool angle, there are a total of eight possible combinations, as shown in Table 6.2. At each radius, three strokes were completed (with base angles of $\{-25°, 0°, 25°\}$ at 17” and $\{-35°, 0°, 35°\}$ at 12”). Therefore, eight batches of three+three strokes produce a total of 48 strokes per collection.

For the rained soil, a different staggered arrangement of tool angles was used. Since there were four strokes per batch and there were four tool angles of interest, strokes were conducted at each of the four tool angles in every batch. There were three combinations of stroke arrangements, and repeating each batch four times, the same 48 strokes per collection were obtained.

Radius	17”		12”	
Base Angle	15°	−15°	20°	−20°
Set 1	100°	90°	80°	70°
Set 2	100°	80°	90°	70°
Set 3	90°	80°	100°	90°

Table 6.3: Arrangement of tool angles for four-stroke batches (rained).

The radial variation and the angular variation ensured that the stress fields of the strokes did not interact with each other. At depths of 1”, it was expected that a 5” gap was more than sufficient to leave the soil undisturbed for the subsequent strokes.

With the staggered arrangement of stroke configurations, it was found in our experimentation that there was no significant or consistent variation in failure force as a result of arm configuration. This is to be expected, yet this was achieved only as a result of the staggered arrangement highlighting controller issues which had to be addressed. A specific example was the skewing of forces by the joint PID control, and the solution resulting from the analysis of the effective Cartesian stiffness described in Section 5.3.1.

One final manipulator-dependent issue that was addressed was insertion accuracy. As discussed, the arm sensing resolution is approximately 0.05”. An insertion error of up to 0.05” for a 1” insertion would result in a maximum $(1.05^2 - 1) * 100 \approx 10\%$ error in failure force. Ideally, greater insertion depths would be used to reduce the impact of this error. However, greater insertion depths would likely exceed the strength capabilities of the arm. To mitigate this effect, manual verification of insertion depth was done during testing. Adjustments were made to the commanded insertion depth or to the resulting force estimate based on external measurements of insertion depth. It is expected that with another manipulator, greater precision can be obtained without resorting to manual external measurement, or that other means of automated verification can be utilized, such as using machine vision[1].

6.3 Interface Friction Estimation

In order to conduct controlled strokes in each of the soils, the interface friction angle must be known. For each of the soils, the iterative estimation technique for interface friction determination described in Section

---

[1] The NASA/JPL Mars rovers, which are equipped with instrument arms, are also equipped with stereo cameras (used primarily for navigation), but which can easily be used for visual feedback of insertion depth.

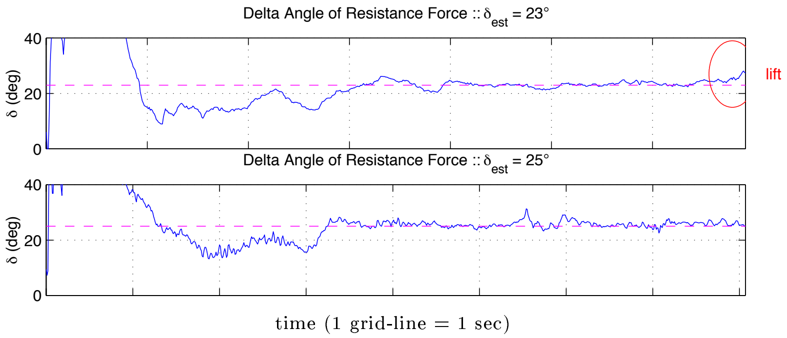

Figure 6.1: A couple strokes were conducted in the rained Ticino as verification of the interface friction angle. There is only a mild lift at 23°, but none at 25°. Each vertical grid-line represents one second.

5.4 was conducted. The results for the Ticino sand were presented in Figure 5.14. The interface friction was not expected to change as a result of raining. As verification, a few additional strokes in the rained samples were conducted. As a reminder, in these data plots, no motion of the plate is occurring for the majority of the time shown. The force exerted by the arm is increasing gradually until failure, which occurs in the last fraction of a second of the stroke. Each vertical grid-line represents one second. Figure 6.1 shows two cases at 23° and 25°. The friction angle was previously estimated to be between 22° and 24°. The lower plot shows that 25° was clearly high. The lifting at 23° was mild, and therefore, for consistency, 23° was used for the rained Ticino.

The stroke results for Nevada Fine sand is shown in Figure 6.2. The resulting estimate is approximately 27° (additional iterations placed it in the $26° - 28°$ range). This result was also verified by creating another plate with the fine sand glued to the face.

Finally, for the glass beads, the interface friction was estimated to be approximately 19°. Figure 6.3 shows four strokes in the glass beads. The lifting effect is fairly mild at $17° - 18°$ and the small lifting observed in the 19° data at 1.5 seconds from the end is an encoder disturbance.

6.4 Stroke Results

The failure force data collected for each of the soils is presented in this section in the order that the soils were tested: unrained Ticino, Nevada

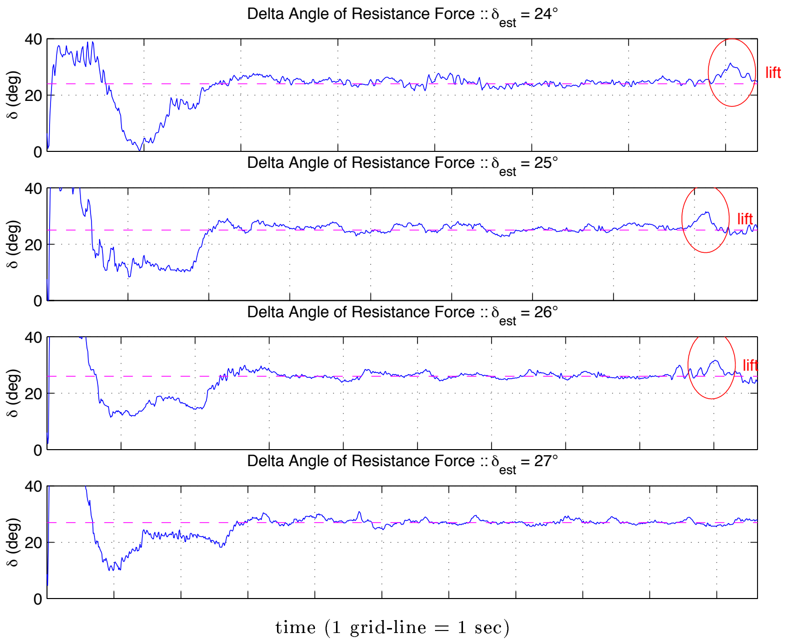

Figure 6.2: The friction angle estimation for the Nevada Fine sand produces an estimate of approximately 27°. Each vertical grid-line represents one second.

Fine, rained Ticino, and the glass beads. Comparisons of the resulting experimental data with the model predictions are given in the section following the results from all the soils.

6.4.1 Unrained Ticino Sand

The first sample tested was the unrained Ticino sand. Multiple collections were conducted in the unrained Ticino, working towards improving the data collection method, primarily for tool angles of 90° and 100°. The quality of some of the 90° and 100° strokes made it difficult to determine a failure force. The unusable strokes resulted primarily from gradual failure, with large-scale arm flexion triggering the end of the stroke prior to true failure (the stroke is ended when the arm has traveled a given distance). In cases with larger tool angles, a larger wedge of soil must be mobilized and more soil accumulates in front of the plate as it moves; thus, failure requires greater forces and greater

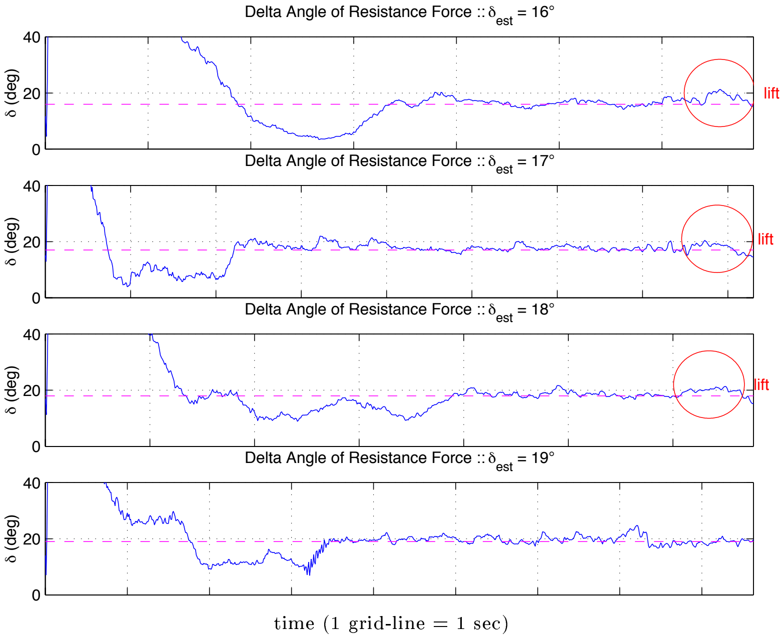

Figure 6.3: The friction angle estimation for the glass beads produces an estimate of approximately 19°. Each vertical grid-line represents one second.

rate of increase in order to make the failure more discernible. A lesson learned from these experiments was to use more shallow insertion depths for the 100° cases, so that lower forces are required for failure. The 100° cases in these data sets were taken at depths of 0.5”, 0.85”, and 1”. The later strokes were all conducted at a depth of 0.85”. A depth of 0.5” was deemed too shallow, creating greater uncertainty.

The results for two collections of 48 strokes are shown in Table 6.4 and 6.5. The data is shown graphically above each of the tables. The agreement for the 70° and 80° cases is fairly good. These failures are typically easily discernible, having drastic failures similar to that shown in Figure 5.17. The 90° and 100° show larger variation. Combined results for the two collections are shown in Table 6.6.

As noted previously, the interface friction was estimated to be 23°. The density, in the state in which these strokes were conducted, was measured and found to be 1.43 g/cc, with a coefficient of variation[2] of approximately ±2% over multiple trials.

The mean and standard deviation of the force measurements have been used in the data reduction. This implicitly assumes that the data is expected to fall in a Gaussian normal distribution, so that the best prediction is the mean. This is a simplification. A greater number of measurements would need to be compiled in order to find the true distribution. The actual distribution is uncertain due to the many contributing sources of error. These sources for error will be discussed in more depth in the subsequent discussion section.

---

[2] The coefficient of variation is the standard deviation divided by the mean, expressed as a percentage.

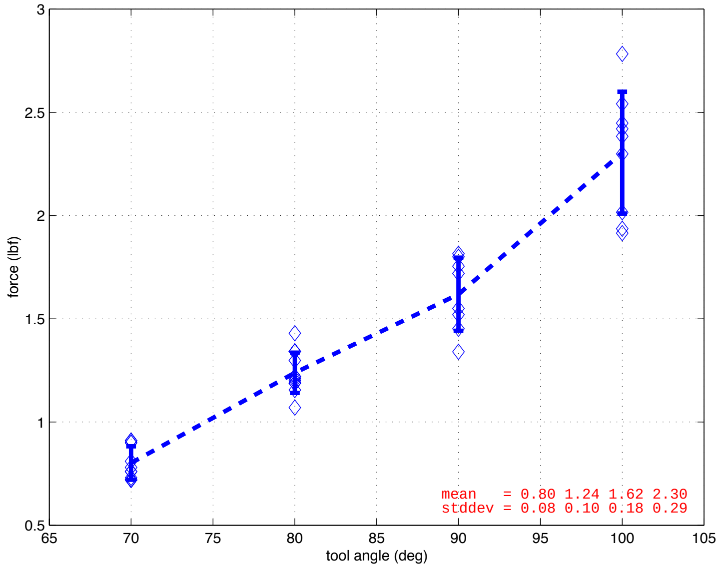

Unrained Ticino – Set 1

Tool Angle	70°	80°	90°	100°
Failure Force	0.76	1.30	1.52	2.38
	0.72	1.22	1.55	xxx[1]
	0.72	1.16	1.34	2.42
	0.72	1.20	xxx[1]	1.94
	0.76	1.22	xxx[1]	2.54
	0.73	1.07	1.45	xxx[1]
	0.90	1.21	xxx[1]	1.92
	0.90	1.19	1.80	2.02
	0.81	1.43	1.72	2.45
	0.78	1.34	1.75	xxx[1]
	0.91	1.19	xxx[1]	2.78
	0.91	1.34	1.81	2.30
Mean	0.80	1.24	1.62	2.30
Standard Dev.	0.08	0.10	0.18	0.29
Coef. of Var.	10.1%	7.9%	11.0%	12.8%

Units are in lbf.

[1] Either incomplete stroke or indiscernible failure force.

Table 6.4: Failure force results for tests in the unrained Ticino sand – Set 1.

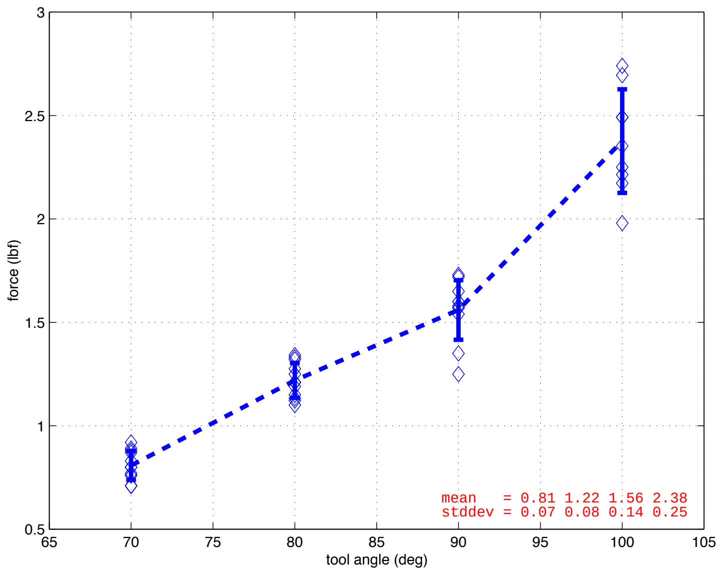

Unrained Ticino – Set 2

Tool Angle	70°	80°	90°	100°
Failure Force	0.71	1.33	xxx[1]	2.74
	0.88	1.21	1.54	2.35
	0.71	1.34	1.65	2.49
	0.80	1.12	1.57	2.70
	0.87	1.21	1.57	1.98
	0.76	1.10	1.60	xxx[1]
	0.80	1.28	1.35	2.49
	0.83	1.32	1.60	2.17
	0.76	1.13	1.25	2.21
	0.92	1.25	1.58	2.25
	0.77	1.15	1.73	xxx[1]
	0.89	1.19	1.72	xxx[1]
Mean	0.81	1.22	1.56	2.38
Standard Dev.	0.07	0.08	0.14	0.25
Coef. of Var.	8.7%	6.9%	9.2%	10.5%

Units are in lbf.

[1] Either incomplete stroke or indiscernible failure force.

Table 6.5: Failure force results for tests in the unrained Ticino sand – Set 2.

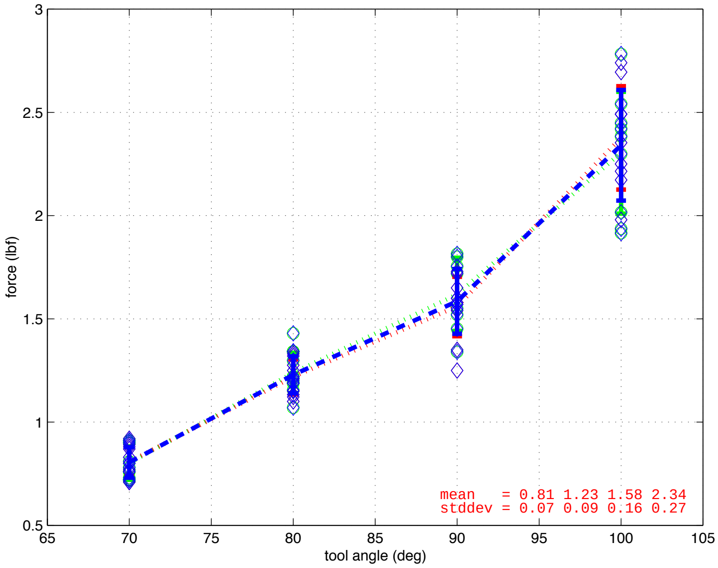

Tool Angle	70°	80°	90°	100°
Mean	0.81	1.23	1.58	2.34
Standard Dev.	0.07	0.09	0.16	0.27
Coef. of Var.	9.2%	7.3%	9.9%	11.4%

Table 6.6: Combined results from the two sets in the unrained Ticino sand.

6.4.2 Nevada Fine Sand

The next sample tested was the Nevada Fine sand. The same arrangement of strokes completed in the Ticino sand were completed in the Nevada Fine sand. Data was collected for two sets of 48 strokes. An interface friction value of 27° was used. The density of the Nevada Fine sand was measured to be 1.44 g/cc with a variation of approximately ±2%. The shallow insertion depths were used for the 100° case, and the resulting force data scaled to 1" depth.

The agreement between the two sets is fairly good. There remained a few strokes with indiscernible failures. The criteria for assessing the acceptability of the data was fairly stringent. If an easily discernible failure estimate could not be determined, that stroke was omitted. To fill in some of the incomplete strokes from the first set, the second set was completed. The combined results from both sets are shown in Table 6.9.

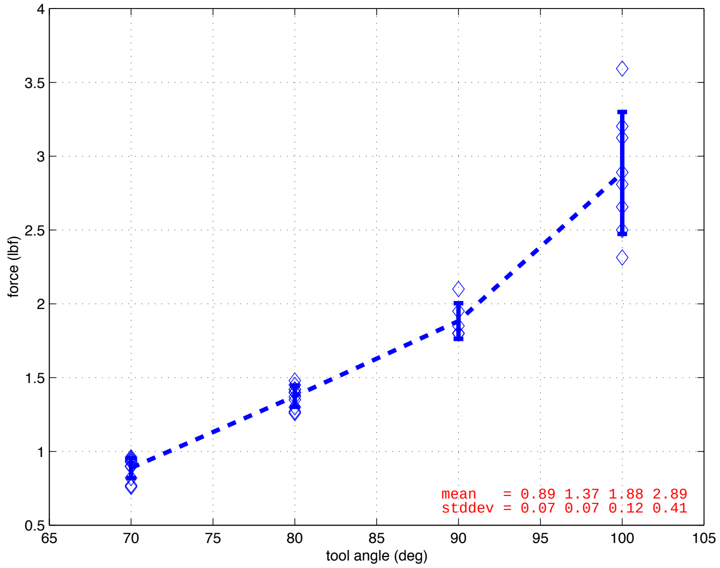

Nevada Fine – Set 1

Tool Angle	70°	80°	90°	100°
Failure Force	0.76	xxx[1]	1.80	xxx[1]
	0.93	1.42	1.80	xxx[1]
	0.77	1.45	1.95	xxx[1]
	0.95	1.26	xxx[1]	xxx[1]
	0.82	1.40	xxx[1]	2.81
	0.90	1.40	xxx[1]	2.31
	0.90	1.48	1.85	3.59
	0.96	1.37	2.10	3.20
	0.93	1.35	1.80	2.66
	0.90	1.42	xxx[1]	3.12
	0.94	1.30	xxx[1]	2.89
	0.90	1.27	xxx[1]	2.50
Mean	0.89	1.37	1.88	2.89
Standard Dev.	0.07	0.07	0.12	0.41
Coef. of Var.	7.6%	5.3%	6.4%	14.3%

Units are in lbf.

[1] Either incomplete stroke or indiscernible failure force.

Table 6.7: Failure force results for tests in the Nevada Fine sand – Set 1.

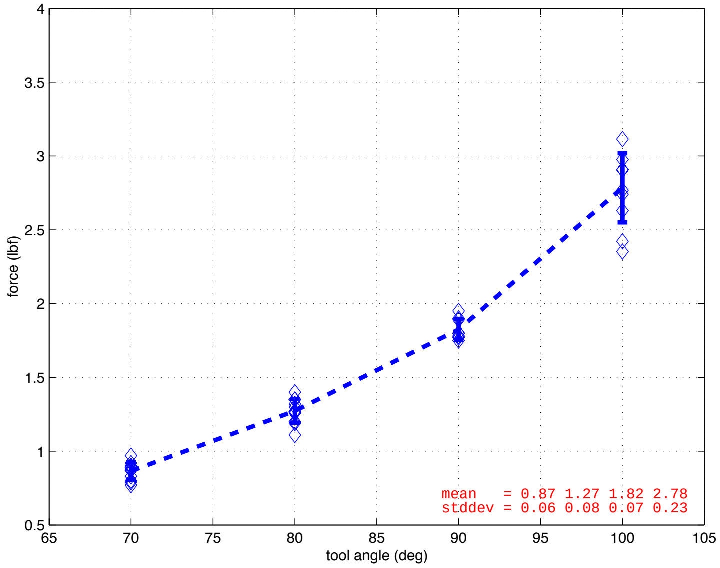

Nevada Fine – Set 2

Tool Angle	70°	80°	90°	100°
Failure Force	0.83	1.32	1.89	2.42
	0.79	1.11	1.80	2.35
	0.89	1.27	1.77	2.63
	0.80	1.30	1.78	2.98
	0.77	1.40	1.80	2.91
	0.87	1.35	1.90	2.77
	0.90	1.35	1.75	xxx[1]
	0.87	1.27	1.78	2.74
	0.97	1.19	1.95	2.91
	0.92	1.26	xxx[1]	3.11
	0.90	1.26	xxx[1]	2.91
	0.88	1.20	xxx[1]	2.91
Mean	0.87	1.27	1.82	2.78
Standard Dev.	0.06	0.08	0.07	0.23
Coef. of Var.	6.7%	6.3%	3.8%	8.4%

Units are in lbf.

[1] Either incomplete stroke or indiscernible failure force.

Table 6.8: Failure force results for tests in the Nevada Fine sand – Set 2.

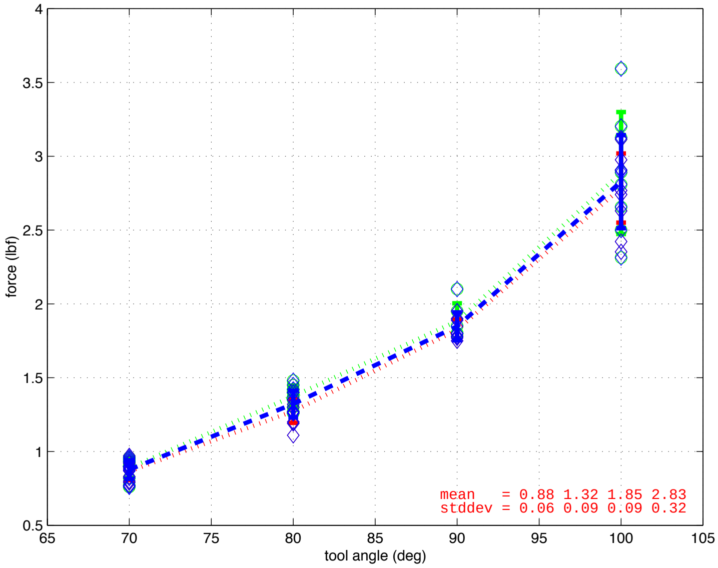

Tool Angle	70°	80°	90°	100°
Mean	0.88	1.32	1.85	2.83
Standard Dev.	0.06	0.09	0.09	0.32
Coef. of Var.	7.2%	6.9%	5.1%	11.2%

Table 6.9: Combined results from the two sets in the Nevada Fine sand.

6.4.3 Rained Ticino Sand

Having established a viable procedure for data collection with the two unrained samples, the next sample tested was the more involved rained Ticino sand. The Ticino sand was rained using the raining assembly shown in Figure 5.1. The density of the rained sand was measured to be 1.60 g/cc with less than ±0.5% coefficient of variation. Thanks to experience gained through the multiple trials in the unrained Ticino and Nevada Fine sand, only a single collection was necessary in the rained Ticino. All the 100° strokes for this sample were conducted at an insertion depth of 0.85".

Typically, during insertion in the loose samples, the adjacent soil is minimally disturbed. However, for these dense rained samples, a small (but noticeable) motion of the grains of sand up to 1.5" away from the plate can be observed. The large grain size of this soil (up to 0.7 mm), especially relative to the width of the plate (2 mm), is likely to produce greater shifting of the grains, loosening the rained soil in the neighborhood of the plate. This topic will be explored more in the subsequent discussion section.

In the data for this sand, there appear to be a few apparent outliers, more so than in the test batches from the other sands. If these outliers are removed, the following results are obtained:

Tool Angle	70°	80°	90°	100°
Mean	0.85	1.29	2.01	2.95
Standard Dev.	0.07	0.12	0.14	0.07
Coef. of Var.	7.9%	9.4%	6.8%	2.5%

The removal of these outliers does not significantly affect the mean, but decreases the standard deviation significantly. The reduced standard deviations are comparable to (or better than) those from the other soils. It was expected that there would be less variation in the measurements if the primary cause was density variation in sample preparation. The rained samples should be more uniform than the manually re-mixed samples. It would appear that either the plate insertion disturbs the repeatability of sample preparation, or the variations result from other factors, such as inclination of the soil surface or inaccuracies of the manipulator.

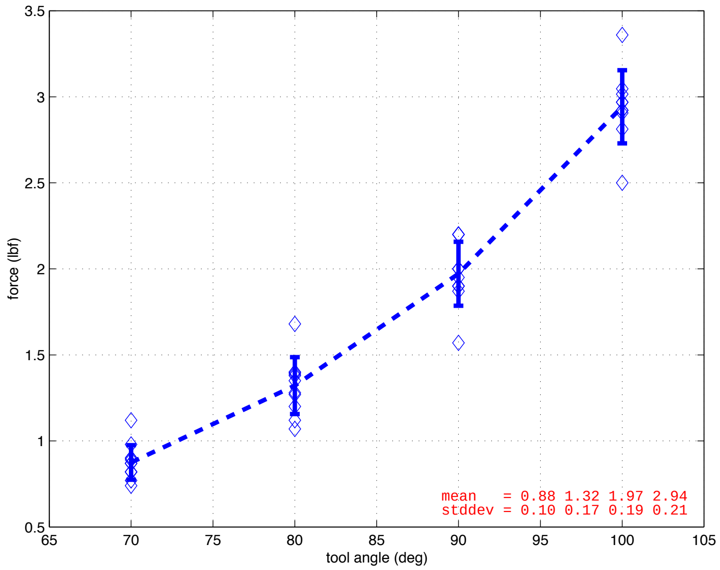

Rained Ticino

Tool Angle	70°	80°	90°	100°
Failure Force	0.87	1.12	1.90	xxx[1]
	1.12	1.20	1.90	2.92
	0.98	1.27	1.87	2.92
	0.87	1.07	1.95	2.81
	0.82	1.40	2.20	3.05
	0.82	xxx[1]	xxx[1]	3.36
	0.74	1.28	2.20	3.02
	0.90	1.39	2.20	2.97
	0.77	1.35	2.00	xxx[1]
	0.90	1.38	1.57	2.50
	0.89	1.68	2.00	2.91
	0.82	1.40	1.90	2.97
Mean	0.88	1.32	1.97	2.94
Standard Dev.	0.10	0.17	0.19	0.21
Coef. of Var.	11.5%	12.5%	9.4%	7.2%

Units are in lbf.

[1] Either incomplete stroke or indiscernible failure force.

Table 6.10: Failure force results for tests in the rained Ticino sand.

6.4.4 Glass Beads

Finally, in order to test a material with a much lower friction angle, fine glass impact beads from Potters Industries Inc.[3] were obtained. The specification from the supplier states that the beads are composed of a minimum of 85% rounds. The density of the beads, in the state stroked, was measured to be 1.46 g/cc with a coefficient of variation of approximately ±1%.

A single collection was completed for this sample. The failure forces were all less than one pound. The full one inch insertion depth for all tool angles was used. Greater depths of insertion were also tested. However, for depths greater than 1.5", with lower tool angles, the spur gears of the end-effector contact the soil surface. So, while the magnitude of forces do not preclude testing at greater depths, the end-effector design limits the depth of insertion. Future designs should carefully consider both the range of tool angles and depths of insertion which can be achieved with a given end-effector design.

---

[3] These are Ballotini Impact Beads, Potters Spec. AE, US Sieve 100-170. More information can be found at http://www.pottersbeads.com/.

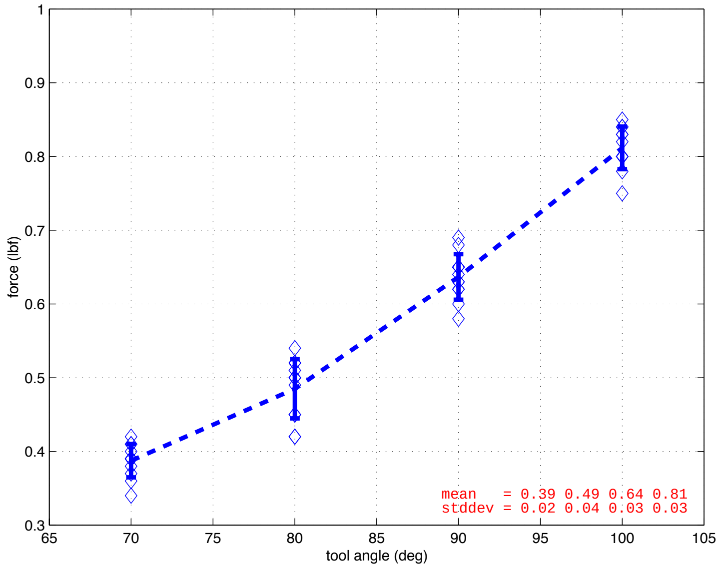

Glass Beads

Tool Angle	70°	80°	90°	100°
Failure Force	0.39	0.51	0.65	0.84
	0.38	0.49	0.68	0.80
	0.37	0.54	0.63	0.83
	0.36	0.50	0.62	0.75
	0.41	0.45	0.69	0.80
	0.34	0.42	0.58	0.80
	0.39	0.45	0.64	0.82
	0.39	0.42	0.62	0.84
	0.40	0.52	0.60	0.78
	0.41	0.52	0.65	0.85
	0.39	0.50	0.65	0.80
	0.42	0.50	0.63	0.83
Mean	0.39	0.49	0.64	0.81
Standard Dev.	0.02	0.04	0.03	0.03
Coef. of Var.	5.8%	8.3%	4.8%	3.6%

Units are in lbf.

Table 6.11: Failure force results for tests in the glass beads.

6.5 Comparison with Model Predictions

At this point, mean and standard deviation values for each of the soils have been collected. Density has been independently measured. The interface friction angles have been determined using the iterative technique. The following plots show the experimental mean and standard deviations superimposed on the model predictions using the interface friction and density values (Figures 6.4, 6.5, 6.6, 6.7, 6.8, and 6.9). The only unknown parameter for the models is the internal friction angle. This angle is varied in the models to obtain overlap between the experimental mean measurements and the model predictions. For comparison, both the upper and lower bound numerical predictions are matched in order to illustrate the effect of small friction angle variations and provide upper and lower bounds on the friction angle prediction (when fitting to the experimental means). It is noted that the change in internal friction angle required to match the upper bound to the lower bound, keeping the other parameters constant, is $1.4° - 2.4°$ (5%-6%). The upper to lower bound range is typically larger than the magnitude of the standard deviation, which would indicate that the upper/lower bound separation from the numerical limit analysis technique is of a reasonable magnitude for this application.

An interesting effect is observed for the loose Ticino and the Nevada Fine sand. The 70° and 80° cases typically match well with one friction angle (Figures 6.4 and 6.6), while the 90° and 100° cases match a lower friction angle (Figures 6.5 and 6.7) . A change of 2.4° and 0.7° is observed for the two soils respectively. Two possible explanations for this effect may be proposed. The first is the dependence of friction angle on normal stress at low stress values. The stress for the 70° cases can typically be half the stress of the 90° and 100° (which both have nearly the same stress when the 100° data is collected at ∼0.85" depths, as we have done). This effect is observed on a smaller scale in the glass bead results, where the 70° result is a fraction of a degree higher than the other angles. The second possible explanation is the progressive failure that typically occurs in these sands with higher tool angles. Both of these effects will be discussed in more detail in the discussion section.

The results from the model comparisons shown in the following figures are compiled in Table 6.12. Contrary to the anticipated soil characteristics from the soil selection, the Nevada Fine sand proved to be very similar in nature to the Ticino sand. Another anomaly from the anticipated values is the low friction angle estimates from the rained Ticino. The rained Ticino was too easily disturbed to maintain a 50°+

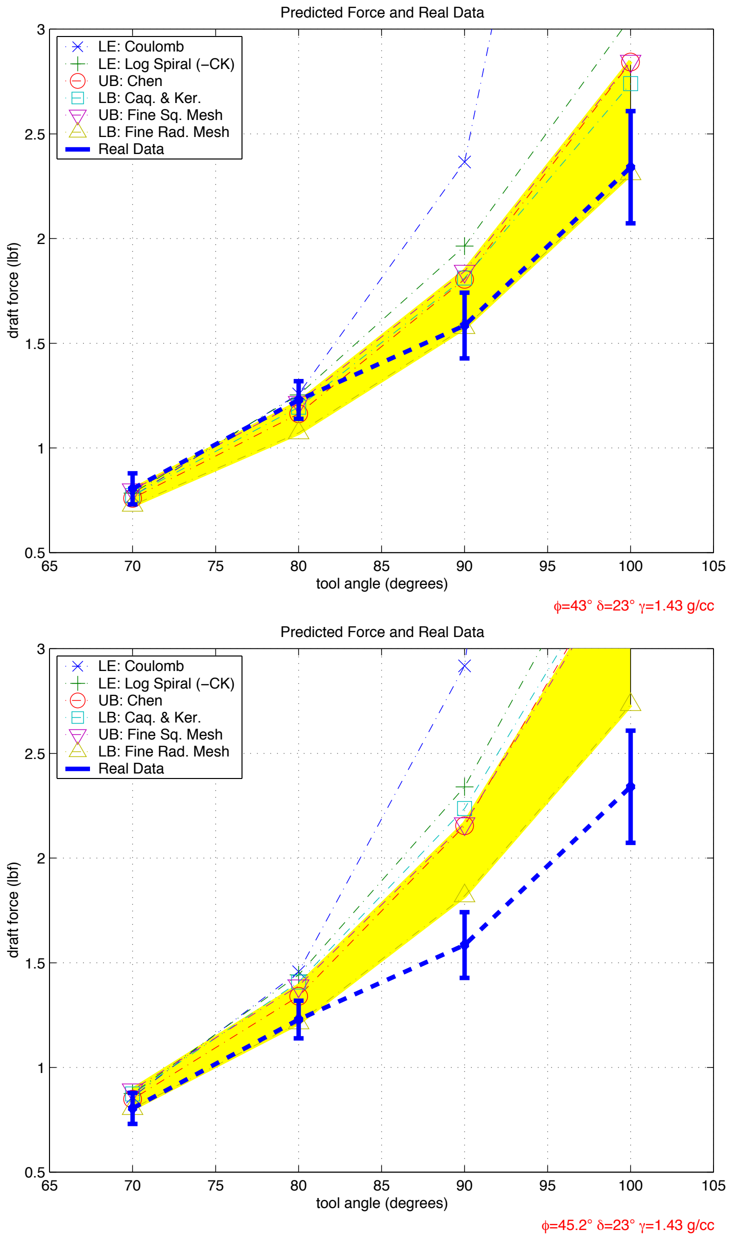

Figure 6.4: Comparison of model predictions and experimental results for the 70° and 80° strokes in unrained Ticino sand.

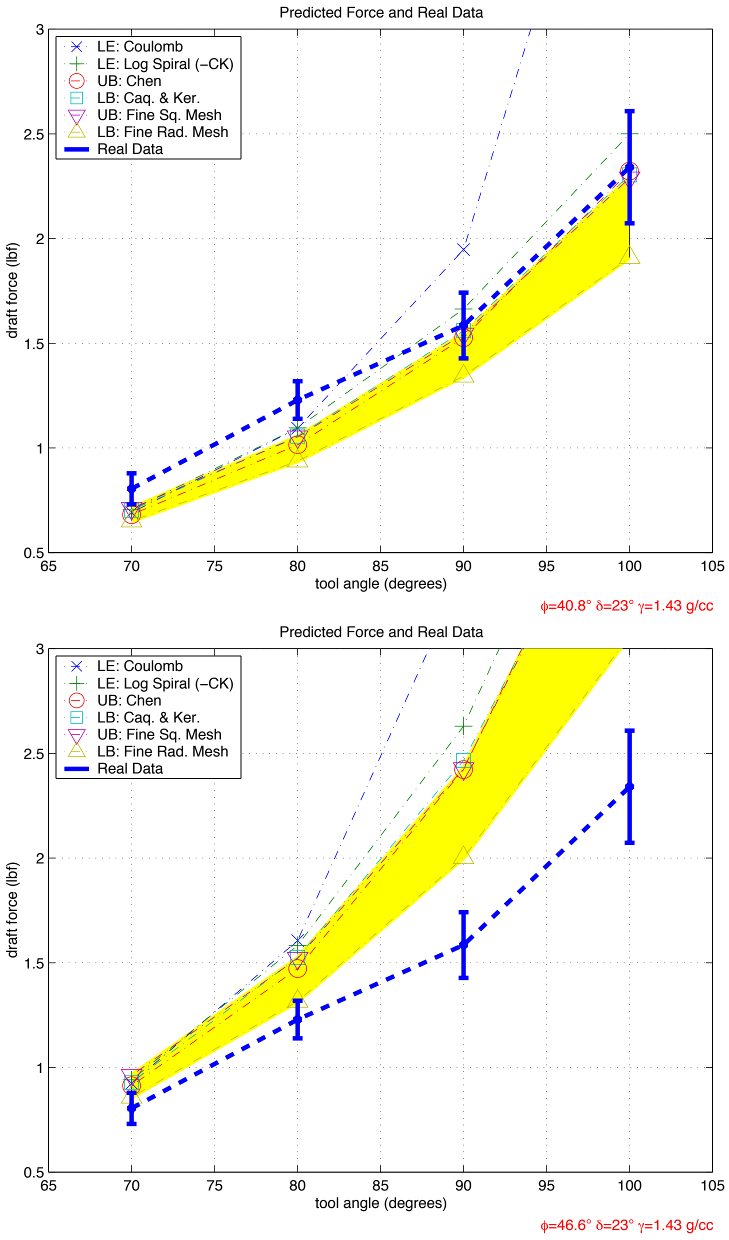

Figure 6.5: Comparison of model predictions and experimental results for the 90° and 100° strokes in unrained Ticino sand.

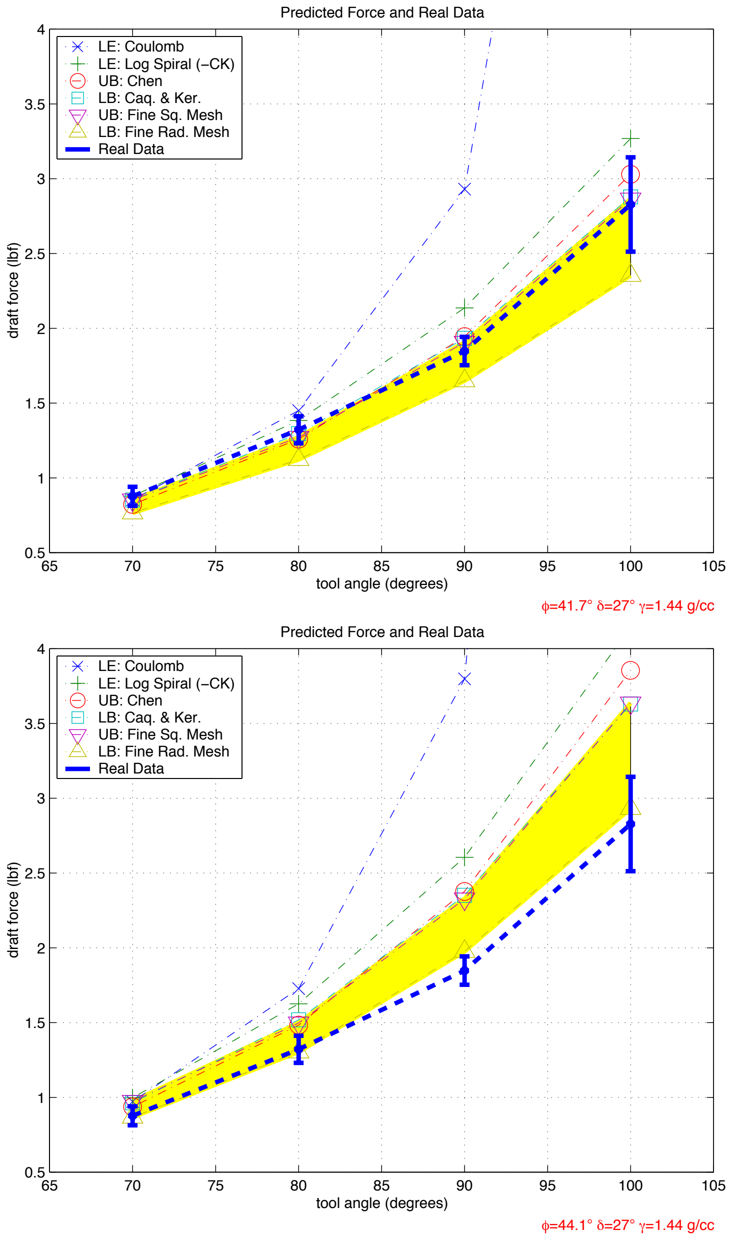

Figure 6.6: Comparison of model predictions and experimental results for the 70° and 80° strokes in Nevada Fine sand.

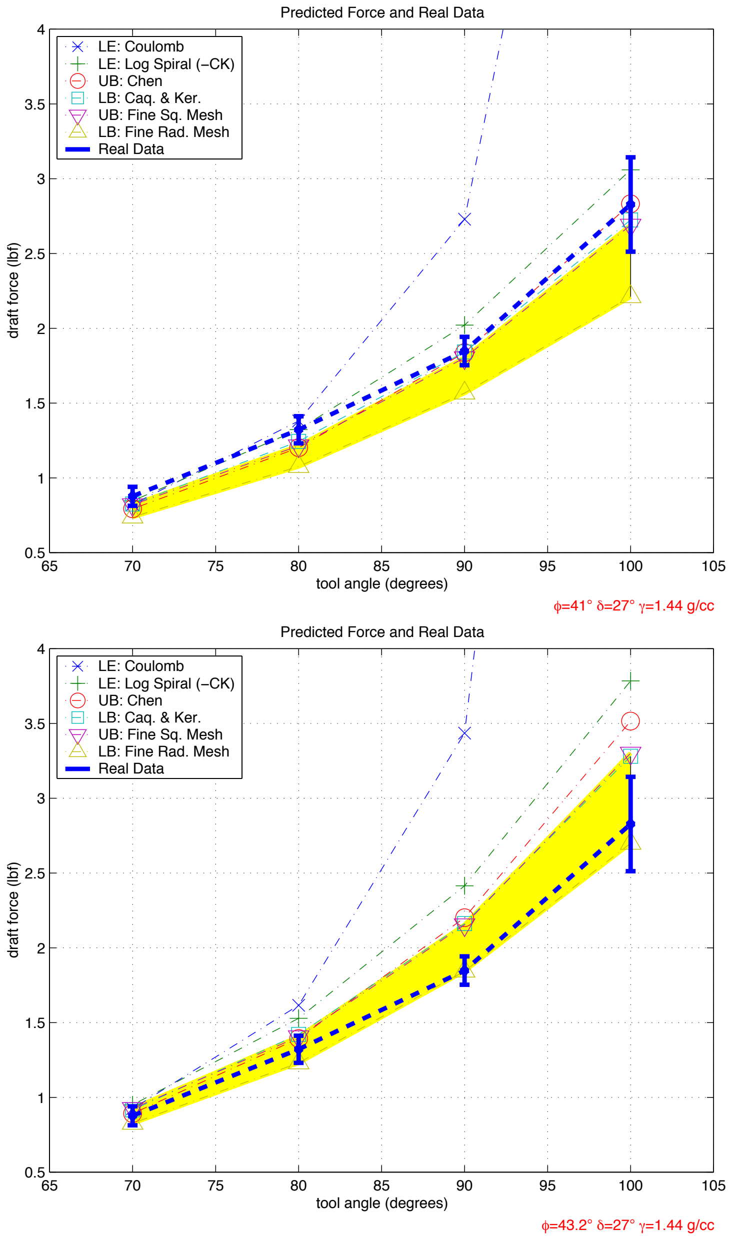

Figure 6.7: Comparison of model predictions and experimental results for the 90° and 100° strokes in Nevada Fine sand.

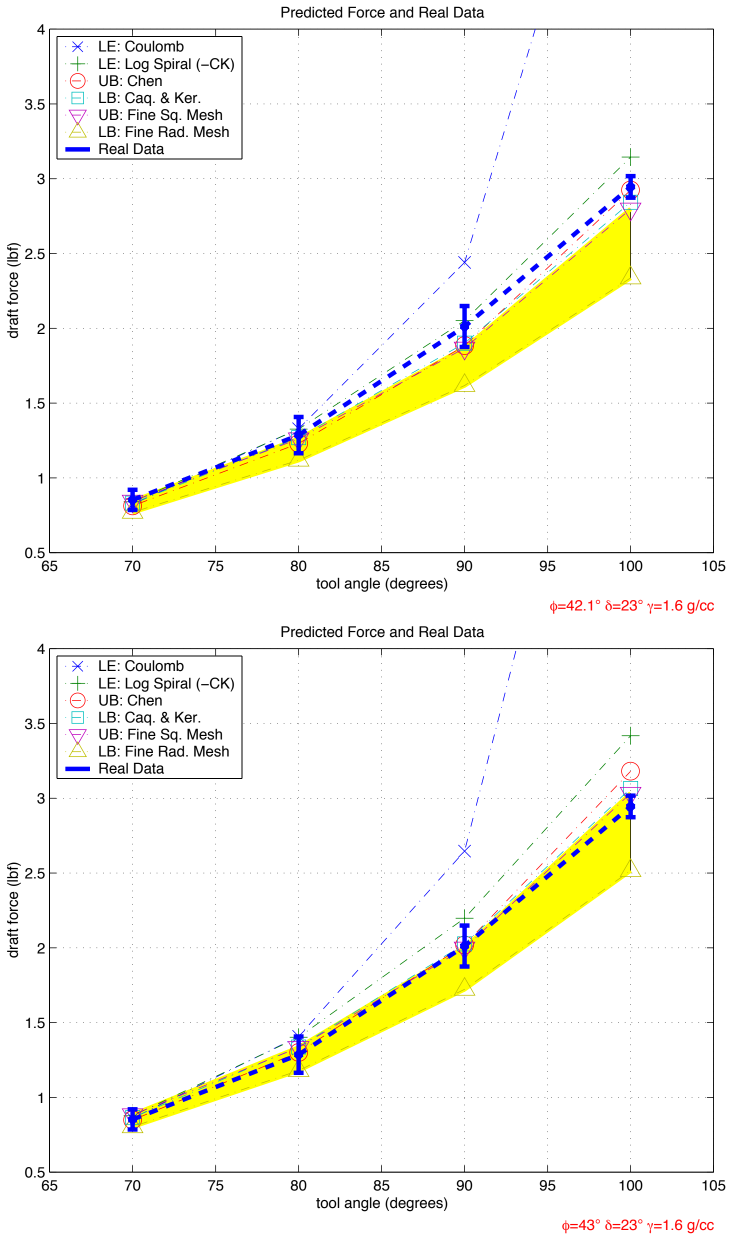

Figure 6.8: Comparison of model predictions and experimental results for strokes in rained Ticino sand.

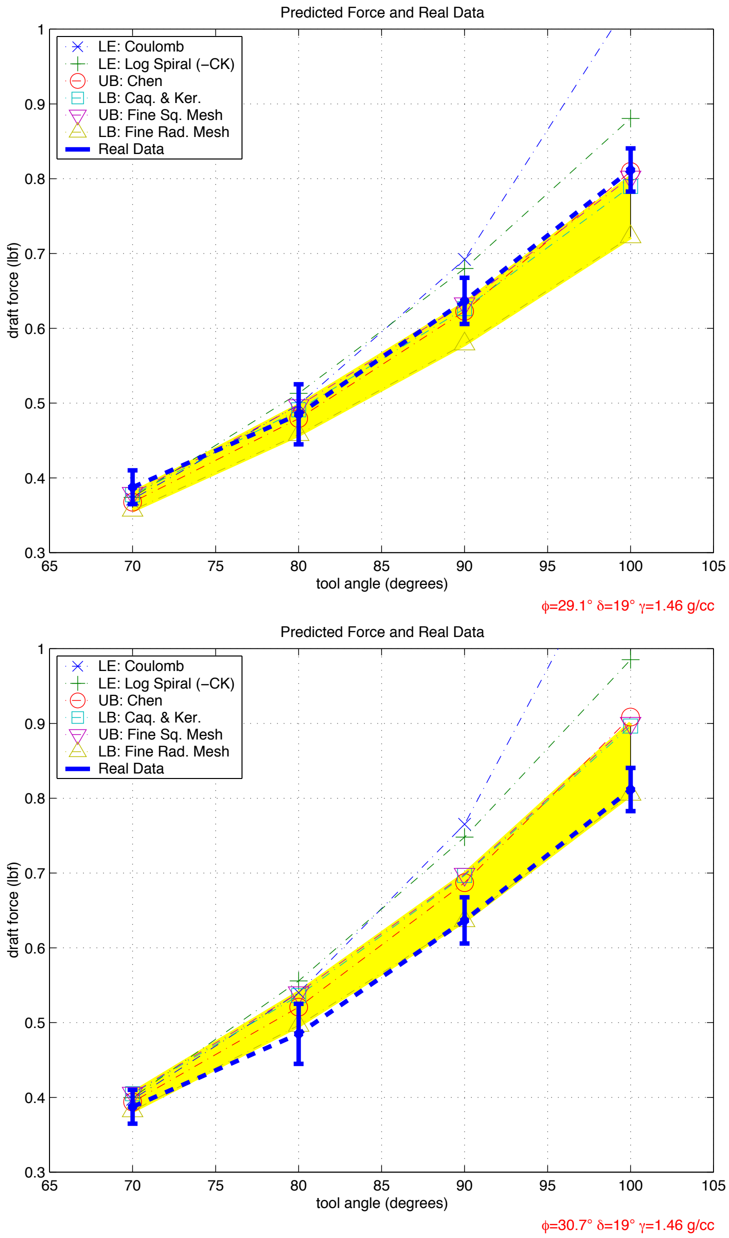

Figure 6.9: Comparison of model predictions and experimental results for strokes in the glass beads.

	Fit - UB		Fit - LB	
	70°, 80°	90°, 100°	70°, 80°	90°, 100°
Ticino	43.0°	40.6°	45.2°	43.0°
Nevada Fine	41.7°	41.0°	44.1°	43.2°
Rained Ticino	42.1°		44.6°	
Glass Beads	30.0°[1]		31.4°[1]	

[1] The 70° data fits 30.6° upper - 31.9° lower, but the 80° data fits 29.5° upper - 31.2° lower. The table values fit the average of all.

Table 6.12: Results from the comparison of experimental data with numerical upper and lower bound predictions. The table lists the matching internal friction angles for the various mediums and tool angles.

friction angle as expected. For the dense rained Ticino sand, during insertion, there was a noticeable shifting of the sand up to 1.5" away from the plate. This reduced the density and tight packing of the sand. It is difficult to maintain a local arrangement of particles in a very dense state, especially when experimenting on small scales with such a large grain size. The experimental forces account for the change in density (since the forces are elevated relative to the unrained case), but yet reflect no real substantial change in friction angle.

6.6 Direct Shear Tests

In order to have a basis for comparison for the internal friction angle estimates, standard direct shear tests have been conducted on the soils, with one critical modification. Figure 6.10 shows an illustration of a shear box apparatus. The standard direct shear apparatus requires a normal load on the order of 10 psi to be applied to the top of the soil sample so that the friction between the soil and the walls of the upper half of the shear box assembly is sufficient to suspend the upper half of the shear box above the shear plane (the upper half of the shear box weighs roughly three pounds).

In order to compare results from the stroking experiments to the direct shear tests, direct shear estimates should be obtained for pressures similar to those experienced when using the manipulator arm. The pressure on the embedded plate is not constant, but increases from the surface of the soil to the bottom tip of the plate. The normal stress along the failure surface will also vary. As a first approximation, the measured failure force can be divided by the area of the embedded portion of the plate (typically 5 in.^{2}) to obtain a simplified pressure

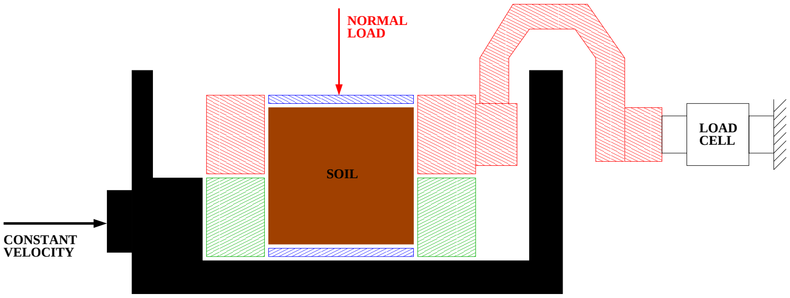

Figure 6.10: The unmodified shear box is shown here. The upper half of the assembly weights roughly three pounds. This weight must be supported by the soil-wall friction, requiring a large vertical load to be applied.

value. If a linear increase in pressure from zero to the maximum at the tip of the plate is assumed, then the pressure at the tip of the plate will be twice that computed from this simplification. Half of the plate would experience a higher pressure and half a lower pressure. It is clearly difficult to draw a direct comparison between the normal stress applied in the direct shear test and the varied stress experienced in the embedded plate tests. However, by simply using the approximation of uniform stress over the inserted plate as an initial guideline for comparison purposes only, some ballpark deductions can be made.

In the stroking configuration, the inserted plate area is 5 in.^{2} (except for the shallow 100° cases) and the range of forces on the plate is 0.4-2.0 lbf. Assuming a uniform distribution, a guideline stress range of 0.08-0.40 psi is obtained. This is more than an order of magnitude lower than typically used in direct shear tests. A pressure of this magnitude would not be sufficient to support the weight of the upper half of the shear box. Therefore, a special attachment to the upper half of the shear box was used to suspend it from above so that lower confining pressures could be used. Figure 6.11 shows the modified shear box and test assembly. The upper half was suspended by rubber bands from a horizontal rod placed above the assembly. Using these modifications, the load on the soil sample was reduced to as low as 0.98 lbf over an area of 5.57 in.^{2}, resulting in a pressure on the shear surface of 0.18 psi.

Using the modified assembly, tests were conducted at loads of 0.18, 0.36, 1.16, and 2.33 psi. For these low values, four tests were conducted at each load and three were kept. Single tests were conducted at each of

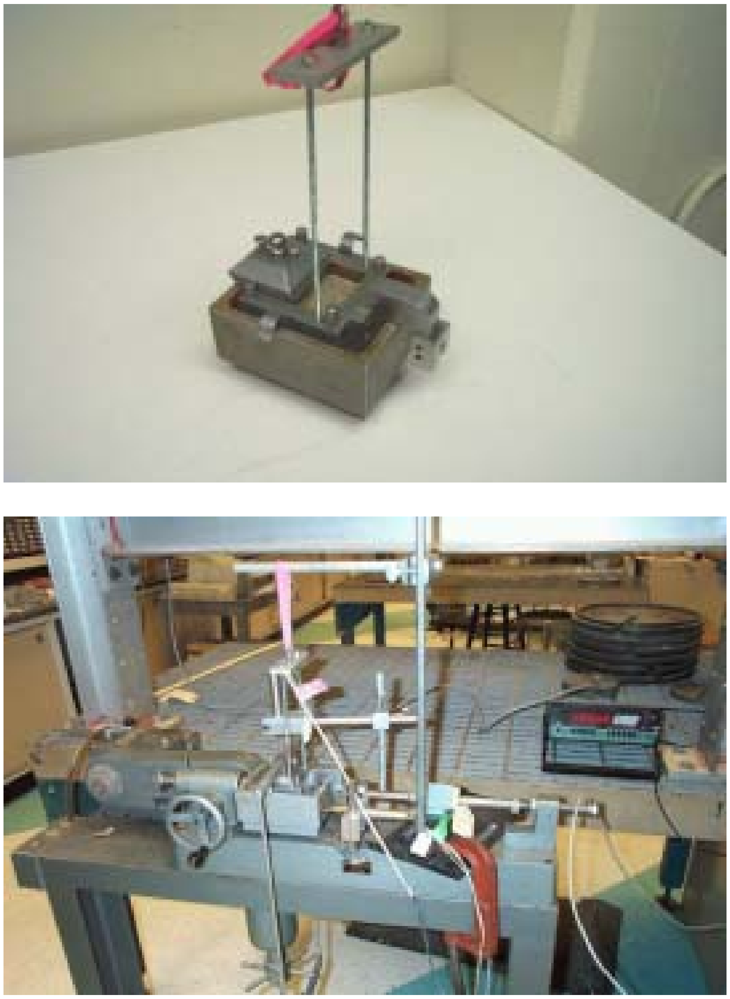

Figure 6.11: Direct shear box and test assembly used for measuring the soil internal friction angle. This system has been modified so that the mass of the upper half of the shear box can be suspended from above. This allows us to test with much lower normal loads.

	Direct Shear at Various Normal Pressures (psi)						
	0.18	0.36	1.16	2.33	6.95	10.91	18.82
Ticino	41.3°	39.3°	38.5°	35.3°	31.6°	31.6°	32.0°
Nevada Fine	38.7°	36.1°	33.5°	32.3°	32.0°	31.2°	31.6°
Rained Ticino	47.9°	43.8°	43.0°	41.7°	39.9°	40.9°	40.8°
Glass Beads	29.9°	28.1°	26.4°	24.9°	25.2°	24.7°	24.2°

Table 6.13: Average friction angles measured with the low-stress direct shear box apparatus.

the larger stresses of 6.95, 10.91, and 18.82 psi to estimate the friction angle at more typical higher loads. The specific results from each of these tests are compiled in Appendix D. The tests show a variation of up to 2° in estimated friction angle. This agrees with Lambe and Whitman [62] who state that the measurement of the peak friction angle from the standard direct shear test can give rise to an error of as much as 2°.

Table 6.13 shows the average results from the low-stress direct shear tests. Figure 6.12 plots all the measured angles up to 6.95 psi. The high stress values were all found to be within 1° of each other. Thus, over the range of 7-19 psi, the assumption of a constant friction angle in direct shear is reasonable. Comparing the measured friction angles at high stresses to those at the lowest stress, increases of 5.2° to 9.7° are found. Limiting our attention to the lowest two test loads, one roughly one half of the other, a variation of measured friction angles of 1.8° to 4.0° is found. Clearly, the measured friction angle is much larger at lower stresses, a fact which has been known for some time and demonstrated here experimentally.

6.6.1 Estimating Comparable Loading

In order to compare results from the direct shear tests to the stroke results, a method must be devised to find comparable load values. Figure 6.13 shows an illustration of the upper half of the Mohr circle diagrams for three different loading paths.

Let us consider the loading paths for direct shear and passive earth pressure scenarios. The loading in direct shear maintains a constant vertical pressure. The motor driving the two halves of the shear box increases the shear on the horizontal plane between the two halves of the box until failure. Thus, the loading path is shown (top-most Mohr circle diagram) as an arrow in the vertical direction at stress σ_v until failure.

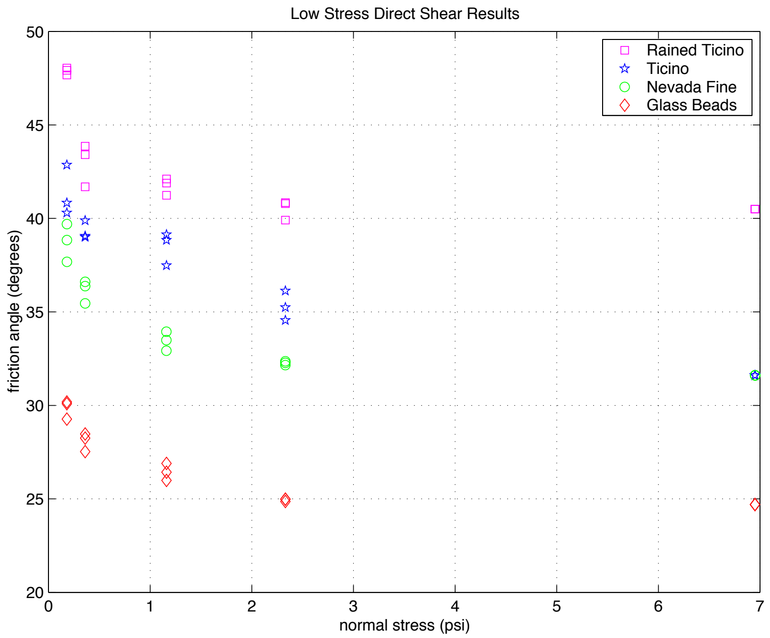

Figure 6.12: Low-stress direct shear results for the tested soils, showing clear increases at lower stresses.

For comparison with the stroking data, comparable pressures must be computed for the failure surface in the earth pressure scenario. Since the forces are dominated by the passive earth pressure component, the computation focuses on the passive case.

The soil models all incorporate the assumption of a Rankine zone in the failure wedges away from the tool. This portion of the soil will not be affected by the interface friction at the tool. Therefore, as a low estimate of the equivalent normal pressure on the failure surface, the case for $\delta = 0$ (no interface friction) is considered. The vertical stress in the soil is simply the geostatic stress, γz. This remains constant during loading, while the horizontal stress is increased until failure. Using σ_v and the estimated friction angle, an equivalent low estimate of pressure can be computed, denoted σ_L (shown in the middle Mohr circle diagram).

For the region of the soil near the tool that does experience the interface friction, a point adjacent to the plate is considered. A vertical

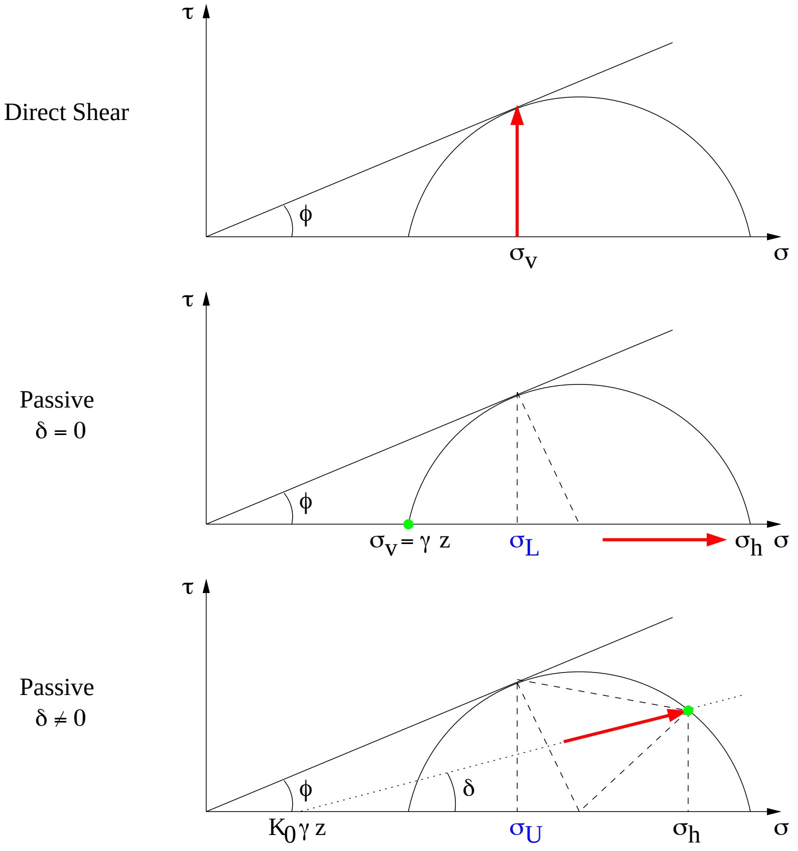

Figure 6.13: The upper half of the Mohr circle diagrams are shown for three different loading paths. The cases for direct shear and passive earth pressure with and without interface friction are shown.

	UB/LB	at $z = 1/2''$ (psi)			at $z = 2/3''$ (psi)		
	avg. ϕ	σ_L	$\sigma_{U,70}$	$\sigma_{U,90}$	σ_L	$\sigma_{U,70}$	$\sigma_{U,90}$
Ticino	42.9°	0.032	0.062	0.118	0.042	0.083	0.157
Nevada Fine	42.6°	0.032	0.072	0.148	0.043	0.096	0.197
Rained Ticino	43.4°	0.032	0.066	0.144	0.047	0.088	0.191
Glass Beads	30.7°	0.034	0.051	0.097	0.046	0.068	0.129

Table 6.14: Estimated equivalent pressures for passive loading, computed using the average UB/LB ϕ estimates, are shown for each of the test cases. The low estimates depend only on depth and estimated friction angle. The high estimates also depend on failure force, so values for 70° and 90° tools are shown.

plate is assumed in the following; for a non-vertical plate, the derivation is the same, with the direction normal to the plate being thought of as horizontal. Since the interface friction, δ, is known, the orientation of the force on the plate is directed at an angle of δ from the normal of the plate. Before the stroke begins, the initial horizontal stress in the soil at rest is given by the coefficient of lateral earth pressure at rest, K_0, times the vertical stress, γz. As the plate is loaded, the horizontal stress is increased, and the interface friction introduces shear on the vertical face of the element. The loading path is drawn as a line inclined at angle δ in the bottom-most Mohr circle diagram. Using the horizontal pressure and shear on the element at failure and the estimated friction angle, an equivalent high estimate of pressure can be computed, denoted σ_U.

One final item is required for obtaining the estimated pressures. A value for z must be selected. To use the full depth of the plate would result in high estimates which would likely only be true very close to the tip of the plate. An approximate average value is preferred. Using $z = 1/2''$ or $z = 2/3''$ would likely provide suitable average values. Table 6.14 shows the results from computations at both depths using the average estimated UB/LB friction angles. It should be noted that the lowest direct shear measurement was taken at 0.18 psi. Therefore, except for two of the cases, extrapolation of the direct shear data is required.

6.6.2 Comparisons

Once the low and high estimates of equivalent pressure are computed, the values from the direct shear tests must be interpolated or extrapolated to obtain estimates of friction angles for comparison. For the sets of data from the four low-stress cases, an exponential curve can be fit.

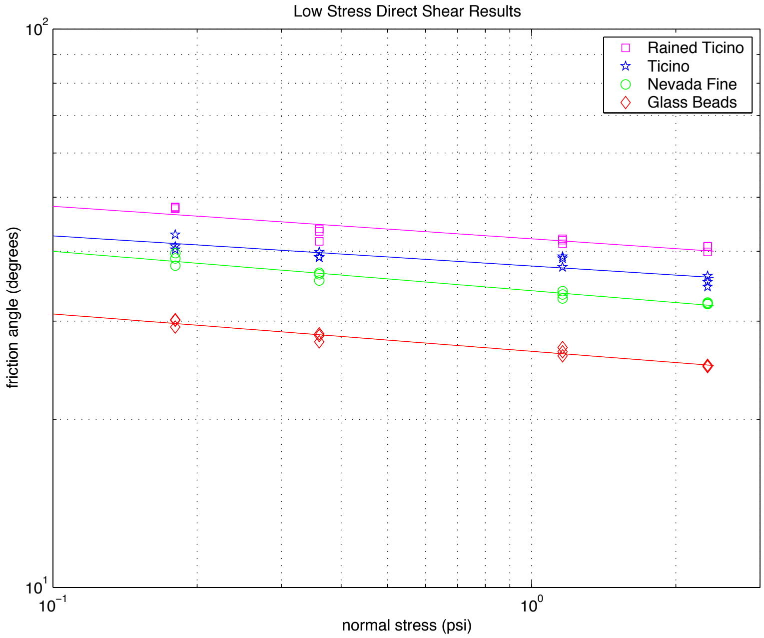

Figure 6.14: A straight line is fit to the direct shear data when plotted on a log-log scale.

Figure 6.14 shows the direct shear data plotted on a log-log scale, with a linear fit superimposed on the data. Figure 6.15 shows the direct shear data and the resulting fits plotted with normal axes.

As noted, the majority of the equivalent pressures are found to be outside of the range which could be measured in direct shear. Thus extrapolation, rather than interpolation, is being done. Extrapolation is less trustworthy, and therefore the resulting friction angle estimates must be taken with a grain of salt. Nevertheless, the resulting values are likely in the correct ballpark[4].

Another item of note, the average UB/LB estimated friction angles are used in the calculations of equivalent pressure. These are estimates with associated uncertainties which would impact the pressures computed by small amounts, however, the direct shear friction angle curves are steep in this region. Nevertheless, some approximations must be

---

[4] Although the fit is shown to increase exponentially at low pressures, it is expected that the curve will level off at some low value.

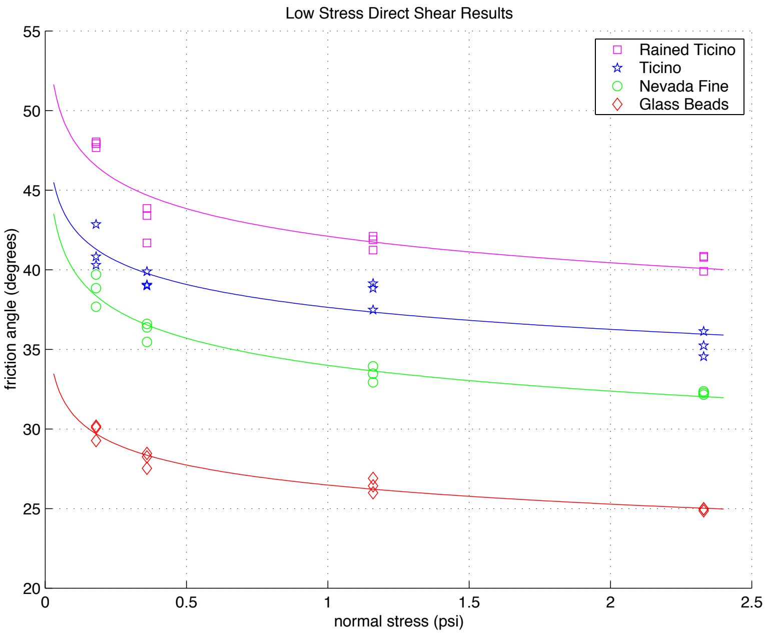

Figure 6.15: The direct shear data in the low-stress range is fit using an exponential curve.

done in order to obtain values for comparison. The sources of variation discussed in this paragraph should be kept in mind when examining the final results.

Table 6.15 shows the resulting friction angle estimates using the computed equivalent pressures. The mean UB and LB friction angle fits are shown for comparison. The agreement is good, except for the dense Ticino, which will be discussed in more detail in the following discussion section. A more complete comparison of the direct shear and stroke results is given in the next chapter, where the model inversion technique for parameter estimation is discussed.

6.7 Discussion

In this closing section, the difficulty in obtaining verification of the friction angles estimated through our experiments with friction angles obtained by other means is discussed first. A few anomalies in our

	Mean	Mean	$z = 1/2''$			$z = 2/3''$		
	ϕ_{LB}	ϕ_{UB}	ϕ_L	$\phi_{U,70}$	$\phi_{U,90}$	ϕ_L	$\phi_{U,70}$	$\phi_{U,90}$
Ticino	44.1°	41.8°	45.4°	43.7°	42.3°	44.7°	43.1°	41.6°
Nevada Fine	43.7°	41.4°	43.3°	40.9°	38.9°	42.5°	40.1°	38.1°
Rained Ticino	44.6°	42.1°	51.2°	49.3°	47.1°	50.3°	48.5°	46.4°
Glass Beads	31.4°	30.0°	33.2°	32.3°	31.0°	32.6°	31.7°	30.4°

Table 6.15: Friction angles obtained from the fits to the direct shear data using the estimated equivalent pressures.

data are discussed. Issues to note when applying the estimated friction angles from this work to other loading scenarios are also presented. Finally, the various sources of error in the measurements and the conclusions reached from these experiments are presented.

6.7.1 On the Great Variety of Friction Angles

The linear approximation of shear strength, known as the Mohr-Coulomb failure law, given as $s = c + \sigma \tan \phi$, is known to apply only over regions of normal stress, σ. A single friction angle, ϕ, is not sufficient to capture the variations over a wide range of stress, particularly at very low stress, for which the friction angle required for this equation to match the observations varies considerably. In order for us to compare the estimated friction angles to any other measured angles, there are a number of considerations which must be made regarding the magnitude of stress, loading conditions, and soil conditions. Therefore, the theories on the shear strengths of soils must be examined.

Lee and Seed [64] quantify the measured shear strength of cohesionless soils as the contribution of three components

$$\begin{aligned} \text{Measured shear strength} \quad &= \quad \text{strength due to sliding friction} \\ &\quad + \text{dilatancy effects} \\ &\quad + \text{crushing and rearranging effects} \end{aligned}$$

Figure 6.16 is a reproduction of the schematic illustration from Lee and Seed. The strength due to sliding friction is assumed to be constant over various confining pressures. This friction angle is typically denoted ϕ_μ and represents the sliding friction between individual particles. It depends on the composition of the particles and the roughness (and as shown by Rowe, on the load per particle, though Lee and Seed propose that this effect cancels in typical loading). At larger stresses,

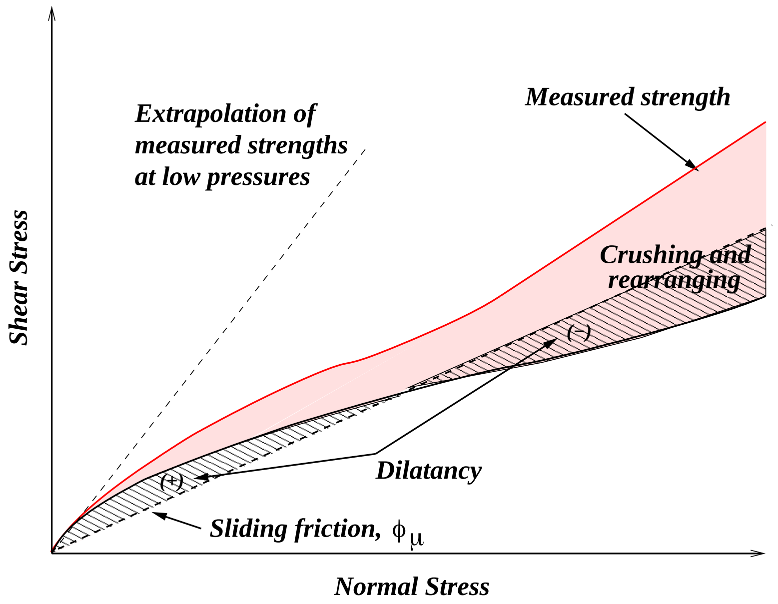

Figure 6.16: Schematic illustration of factors contributing to the measured shear strength of cohesionless soils. Reproduced from Lee and Seed, 1967 [64].

the relative significance of the dilatancy and the crushing and rearranging are dependent upon the type of sand, particle size, and initial void ratio. At low stresses, the crushing and rearranging effects will be minimal and the primary increase in apparent friction angle is a result of the dilatancy effects. The dilatancy effect is clearly seen in the direct shear results in Appendix D. The samples were approximately the same height. As expected, the magnitude of the dilation is more pronounced for the large grain size sands (Ticino) and smallest for the finest material (glass beads) and it is more pronounced for the dense sand (dense Ticino).

Given the dependence of friction angle on a number of factors, it would seem best to conduct tests with identical loading conditions using another apparatus for verification. Our use of direct shear tests required the computation of equivalent friction angles that were rough and fraught with approximations. Future researchers may prefer to conduct independent passive plane strain tests at similar stress levels. No other plane strain apparatus was available for this work. Triaxial tests would be of no benefit since they exhibit a wide variety of measured friction angles depending upon loading path. In addition, no apparatus was available to conduct tests at such low confining pressures. Another possible solution would be to have a manipulator which can exert greater forces at greater depths and span a range of stresses. Using measurements over a range of stresses, work can be done to relate the observed trends directly to the observed trends in direct shear or triaxial tests for verification and construct a specialized dilatancy correction directly for earth pressure scenarios.

6.7.2 Low Forces and Dense Samples

For the loose Ticino and Nevada sands, lower forces than expected were found for the 90° and 100° tool angles. One possible cause for the variation is the change in the dependence of the friction angle on normal stress. A change of almost 2° is seen to result from the friction angles using the estimated equivalent pressures from the 70° to the 90° case. This effect is clearly possible, as seen in our direct shear tests, but it may not be the only cause.

Another highly likely cause results from the gradual nature of failure more typical in the 90° and 100° strokes in the higher friction angle soils. As noted by Rowe and Peaker [87], the full mobilization of internal friction in the passive case does not occur until after significant deformation has occurred (up to 16-26% of the insertion depth for loose sands). They give the following example to illustrate this concept: if the failure region in the soil is imagined to be composed of wedges on a frictional surface with springs between the wedges, in order for the force from the wall to be fully transmitted to all the blocks representing the full failure region, the springs must be compressed in turn. In these cases, it is likely that our break-point computation used to estimate the failure force will produce failure force estimates before the internal friction has been fully mobilized, resulting in lower estimated friction angles.

Another anomaly in our data was the low friction angle estimates for the rained Ticino. Another insight from Rowe and Peaker relates to this issue as well. In their experiments, the typical failure for dense sands exhibit a peak in the failure force at horizontal displacements within the first 4-5% of the wall height. The data then shows a measurable decrease. The failures for the dense soil tested here do not exhibit this behavior. In the direct shear tests, a peak is also observed; however, after dilation has occurred, the measured shear strength is reduced significantly from the peak. Given the observed motions at the surface of the soil, it is likely that the region affected by insertion extends over 1" away from the plate. Thus, the additional strength attributed to dilation is gone after insertion, resulting in a condition in the soil similar to the loose configuration. This would agree with our observations.

6.7.3 Application of Estimated Friction Angle

There is an extensive amount of literature examining the dependence of apparent friction angle on loading path, relative density (void ratio) of the soil, magnitude of confining pressure, magnitude of the dilatancy, and other factors. In light of the amount of work compiled on computing friction angles that would fit within the framework of the Mohr-Coulomb failure law, a friction angle cannot be stated without specifying many accompanying factors to qualify it. One thing that can be said with confidence as a result of this investigation is that the Mohr-Coulomb failure law is a simplified approximation to the true behavior at low stress. A particulate model of soil behavior, instead of the continuum model used here, may produce better results, but would be very complex to implement, and is left for future researchers.

If the results from this work are to be applied for high stress scenarios, such as bearing capacity (e.g. lander stability) or retaining wall stability (e.g. building Martian or Lunar structures), then the relationship between the friction angles at low stresses, which can be measured with our system, and the friction angles at high stresses must be known. Currently, a shift of roughly $5^\circ - 9^\circ$ from high stress friction angles to the low-stress friction angles in direct shear is observed. As it currently stands, additional testing in either direct shear or triaxial tests would be required to use the above equations to extrapolate the manipulator results to other loading conditions. If the manipulator could span a greater range of forces, it is likely that an independent correction equation can be developed to extrapolate the results to other loading conditions.

Regardless of the means of compensation, it is clear that the dependence of friction angle on the various factors (normal stress, loading path, etc.) must be kept in mind. Otherwise, blind application of estimated friction angles from this work (at low stress, passive plane strain loading) may lead to gross over-estimation of the failure forces in other loading scenarios.

6.7.4 Sources of Error

In this section, the variance in the individual measurements are examined. There are sources of error, sources of variability, and procedural sources. The sources of error are manipulator dependent and result from imperfect control and sensing. The sources of variability are soil dependent effects and result from soil variations from stroke to stroke. The impact of each of these sources on the measured force are interpreted based upon the sensitivity analysis presented in Table 4.3 using Chen and Liu's upper bound model as an example. Comparisons are done relative to a baseline reference case: 40° friction angle, 25° interface friction angle, 1.5 g/cc density, and a horizontal soil surface.

The manipulator dependent effects relate to the interface friction angle, tool angle, and insertion depth. The arm can track the desired interface friction angle to within 1-2 degrees. A 1-2 degree error in tracking of the desired interface friction angle will result in 3%-9% error in force from the baseline case. An error in the tool angle of one degree will result in approximately 4% error in force. As previously mentioned, the insertion depth accuracy using the external encoders alone would contribute up to 10% error, but with the manual verification of insertion depth, this is likely reduced to within 5%. One final item, the independent tests on the force/torque sensor yielded an uncertainty of 1% in the range of forces encountered. The combination of these manipulator dependent effects could produce errors of 7-11%.

The soil dependent effects relate to the sample preparation and are independent of the specific limitations of the manipulator. An error of one degree in soil surface angle (to which each of the samples was prepared) can result in approximately 5% error. A variation in density of the soil across strokes will result in an equal percentage variation in force. Repeated preparation of samples resulted in a maximum 4% variation in density. Thus, the soil dependent variability alone could cause up to 6% error.

Combining the sources of error and variability, errors of 10-13% are possible. This agrees with the largest coefficients of variation which were observed for any set of measurements.

Apart from the manipulator and soil dependent sources, there are also errors introduced as a result of the procedure and assumptions. These are more difficult to quantify. The procedure for the estimation of failure force for gradual failures introduces a bias into the measurements. The magnitude of the bias may be in the 5-10% range. This number is estimated from the slope of the failure portion of the force versus displacement plot. Rowe and Peaker [87] have studied progressive failure for a vertical wall and state that for loose soils, the internal friction is fully mobilized after displacements of 16-26% of the height of the wall. Their experiments are different from this work in that the interface friction is also not mobilized initially, whereas we reach and track the interface friction angle early in the stroke. Using a 16-26% guideline, a rough estimate of the impact on the estimated failure force gives the 5-10% bias. The consideration of progressive failure applies only to roughly half of the 90° and most of the 100° tool angle strokes. The lower tool angles have more definite failures. Assumptions have also been made that the material is homogeneous and that the properties do not vary during a stroke. These assumptions break down in the presence of gradual failures, where compaction must occur prior to failure. In addition, since the friction angle is known to vary depending upon normal stress, and the normal stress varies along the failure surface, the friction angle cannot be a single constant value for a given failure. Therefore, it is an approximation to assign a single friction angle value to a given stroke. This is necessary until a more accurate model is developed.

The above percentages reflect the maximum possible error. None of these sources have a definite known bias, except the estimation technique used for gradual failures. In the absence of further knowledge regarding the distribution of the other sources of error, a simple Gaussian distribution is assumed[5]. Thus, the mean and standard deviation measures were used in the data reduction. Corrections to the gradual failure cases can be applied independently. To reduce the impact of these sources of error, repeated tests were conducted at each tool angle to obtain an average over a collection of measurements. The magnitude of the resulting standard deviations indicate that these individual sources are not consistently additive.

The sources of error from the manipulator can be reduced with greater sensing precision, reduced backlash in the motors, and greater force capabilities. The sources of error from the procedure can be reduced after more experience has been gained and the methods improved. The sources of variance in the soils are to be expected in soils that will be encountered in the field and cannot be reduced. Variations in measurements as a result of these sources of sample variability are a positive indication that the manipulator is sensitive to such variations in the soil. Data which reflects these variations are desirable.

---

[5] Initial examination of the collected data has been done. While the quantity is insufficient to make a definite conclusion, the data often appears to be approaching a Gaussian distribution.

6.8 Conclusions

This chapter has presented the results from measurements using the manipulator arm to interact with three different soils. The measurements typically showed a standard deviation of 10%. The maximum variance as a result of variations in soil conditions alone, independent of the manipulator and procedure, was shown to be about 6%. The results have shown that this system is sufficiently accurate for measuring interaction forces in loose soils. For dense soils, disruption of the soil resulting from insertion prohibits interactions with the soil in an undisturbed state. Greater insertion depths may overcome this barrier.

The comparisons of the estimated friction angles with independently measured direct shear values have shown good agreement. Additional testing on a greater variety of soils is necessary to fully validate the system. Many of the issues raised in the analysis of the resulting data do not undermine the method, but rather raise additional questions about the details of modeling soil behavior at low stress and for gradual failures.

Chapter 7

Parameter Estimation

In the previous chapter, knowledge of the interface friction and density of the samples was used to estimate the internal friction angle by manually matching the force versus tool angle curve to those predicted from the models. In this chapter, a general technique that automatically computes the valid regions of parameter space that could have possibly generated the observed measurements within the measured uncertainties is presented. This technique is applied to the experimental data from the previous chapter to produce complete bounds on the corresponding parameter estimates.

7.1 Defining the Problem

From the experimental interactions with soil using the manipulator arm, it is possible to collect a set of forces required to fail the soil in different configurations. The depth of insertion and the angle of the tool can be directly controlled. Of these two, the angle of the tool is more useful. The depth of insertion is not critical (aside from affecting the uncertainty associated with the measurement) for tests in cohesionless soils. The H^2 dependence on insertion depth is well known, and so, all the force data is normalized by dividing by the square of the insertion depth. Therefore, the primary control variable in the collection of data is the tool angle. The surface angle of the soil can also be controlled, however, the process would be complicated (not to mention unrealistic for tests on Mars) and approximate. In the interests of simplicity and speed of data collection, a horizontal soil surface was used throughout these tests.

Thus, each set of manipulator strokes produces a set of forces required to fail the soil for different tool angles, normalized to a unit depth of insertion. The problem statement then becomes: find estimates of the physical soil properties given these failure force measurements. This chapter examines if this problem is solvable, and if so, what is involved in the solution of the problem.

The soil models under consideration all have the same set of variables. These variables can be grouped into soil parameters and geometric parameters. The soil parameters are internal friction (ϕ), interface friction (δ), density (γ), and cohesion (c). The geometric parameters are tool angle (α), tool depth (H), surface angle (β), and surcharge pressure (q). In our tests, the soils are cohesionless, $c = 0$, and there is no surcharge, $q = 0$.

As described above, only the tool angle is varied for a set of measurements, and the resulting resistance forces are collected. This produces sets of data pairs $\{\alpha_n, F_n\}$ where α_n is the tool angle for the nth measurement and F_n is the force required to move the embedded plate and fail the soil, normalized to unit depth. Using these data pairs, the goal is then to invert the soil models to determine the estimates $\hat{\phi}$, $\hat{\delta}$, and $\hat{\gamma}$ which would account for these measurements.

7.2 Difficulties in Model Inversion

A standard method for determining estimates for parameters in a model that best fit measured data would be to use a nonlinear optimization technique that searches the parameter space to find the solution with the minimum sum-squared error (SSE) (or other error measure) between predictions and measurements. There are two issues which may complicate the implementation of a standard nonlinear optimization technique to this problem.

The first issue is a result of the nature of each of the soil models. Nearly all the models require optimizations in one or two variables to obtain solutions, or, they are tabular in nature. Both of these types of models, in actuality, present small barriers to implementation in a standard optimization framework. Since each function evaluation will itself require an optimization, this will increase the computation time. However, this is not a significant barrier. Nonlinear optimization techniques have been implemented in C (rather than Matlab) for speed, and typical runs require a fraction of a minute. The tabulated models will require an interpolation scheme, however, the models are locally smooth and interpolation schemes are easy to implement.

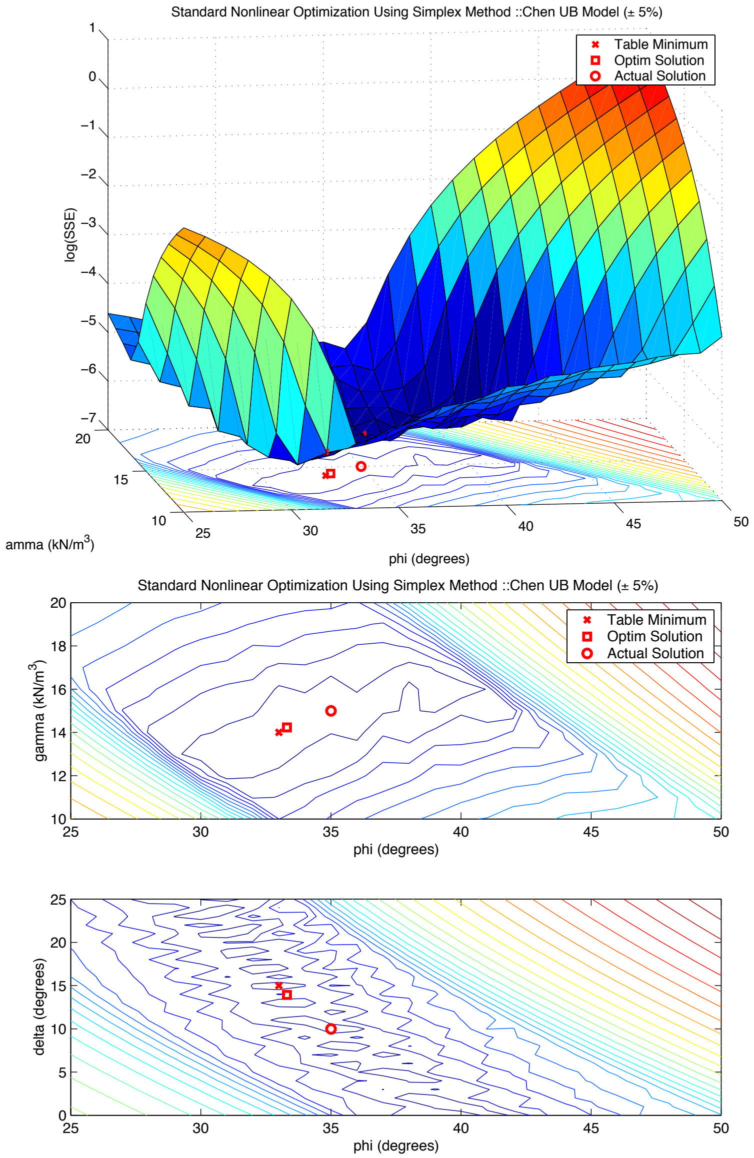

Figure 7.1: Example of the low sensitivity to parameter variation. Note the flat region in the SSE surface shown in the upper plot. The resulting contour plots for the SSE surface are shown in the lower plot with solutions marked.

The second issue is the non-unique mapping of parameters to forces. In the soil models, an infinite combination of parameters may produce the same force. In a standard nonlinear optimization, this would likely result in many local minima, or flat regions in the error surfaces. Consequently, solutions obtained from standard optimization techniques may lie far from the actual solution. Figure 7.1 shows the error surface and contour curves for an example case. Here, a set of measurements with random noise of ±5% has been used. The error surface is generated by computing a table of the sum-squared error at discrete points in the parameter space. In the lower portion of the figure, the contour curves for the computed SSE surface are plotted. The minimum value from the computed SSE table (used to generate the surface), the solution found from the nonlinear optimization, and the actual solution are marked. In this case, the nonlinear optimization has done a good job in locating the minimum of the error surface. However, neither computed solutions are close to the actual solution. This is a characteristic shortcoming of the nonlinear optimization method: it yields only a single point solution and does not utilize the uncertainty information in the measurements.

To address these difficulties, a novel parameter space intersection method is developed in this chapter. This method uses pre-computed tabulated model predictions and determines regions in parameter space which are consistent with a given set of measurements *with* associated uncertainties. The intersection of these regions for multiple measurements represents the collection of all possible parameters which could have possibly generated the given set of measurements.

7.3 Parameter Space Intersection Method

The development of the new parameter space intersection method for model inversion begins with an illustration of the tabulated data resulting from a typical soil model. Figure 7.2 shows a cube of the prediction values for a 70° tool, where the axes are the internal friction (ϕ), density (γ), and interface friction (δ). The shading of each block represents the magnitude of the predicted failure force. Similar cubes can be generated for other tool angles. The empty blocks in the upper left corner reflect the fact that the interface friction angle cannot be greater than the internal friction angle. Again, note that there are many different possible combinations of parameters which produce the same force value (imagine a surface connecting all blocks with the same shading – this surface would span a wide range in each of the axes). The model

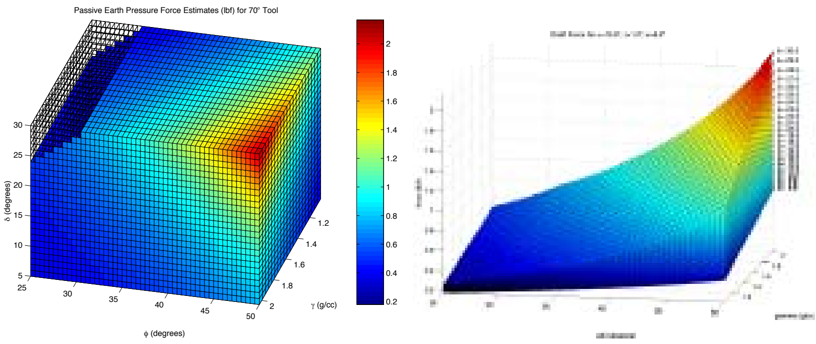

Figure 7.2: Sample force prediction data for a 70° tool shown in two formats, a colored cube (left) and a collection of surfaces at discrete δ values (right).

prediction values can also be depicted in another more useful form. Consider horizontal slices of the cube at constant δ values. If each of these slices are plotted with failure force on the vertical axis, the figure on the right is obtained, which plots F vs. ϕ and γ for constant δ.

7.3.1 Computing Contour Line Intersections

Let us assume that we have perfect measurement data. Figure 7.3 graphically illustrates the next steps in the development. A force measurement from the manipulator arm can be depicted as a horizontal surface intersecting all the F vs. ϕ and γ surfaces (1). This produces a set of contour curves, each curve associated with a different δ value (2). If this process is repeated for a second measurement at another tool angle, another set of contour curves is obtained, shown superimposed in (3). And again for a third (4) and fourth (5) measurement. Examining the intersections between these sets of contour curves, a trend can be observed. Each of the intersection points represents the agreement between two of the measurements. If multiple measurements are consistent with each other, then the locus of the intersections between the sets of contour curves will converge on the correct parameters (5). Ellipses are used to enclose the points of intersection. If the measurements are noisy or mildly inconsistent, then the ellipses will remain large (6). Appropriate parameter estimates may still be deduced by finding the smallest ellipse; however, this method is approximate and does not utilize the uncertainty information associated with the mea-

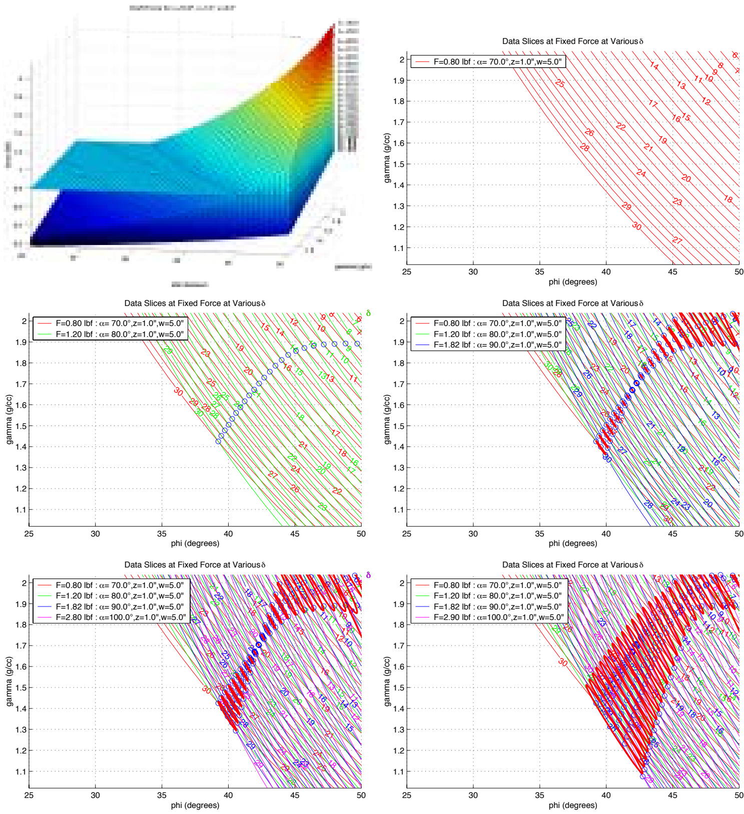

(1) (2) (3) (4) (5) (6)

Figure 7.3: Initial steps in the graphical method for computing contour curves for each measurement and the resulting intersections. The development flows from (1)-(5) assuming ideal data. (6) shows the results with noisy data.

surement data.

7.3.2 Computing Contour Band Intersections

To further develop this method in the presence of noisy measurements, let us consider how to incorporate the uncertainty information available with each measurement. Figure 7.4 graphically illustrates the next steps. An arbitrary random ±2% noise is added to the measurement data in this example. For each measurement, two sets of contour curves are computed, one for the upper limit (measurement+uncertainty) and another for the lower limit (measurement-uncertainty). This produces a set of contour *bands* (the regions between the two sets of contour curves). Repeating the process for a second measurement, two sets of bands are obtained (1). The intersection between these two sets of bands represents regions of the parameter space that are consistent with both measurements. Next, adding a third measurement, another set of bands is obtained, and the resulting computation of the intersecting regions produces a smaller consistent space (2). Adding a fourth measurements again decreases the final intersection regions (3). These final highlighted intersections denote regions of parameter space which could have generated the observed measurements within the given uncertainty bounds.

7.3.3 Utilizing Interface Friction Estimates

Now, from the stroking experiments, the interface friction can be independently determined. This information can be utilized in the inversion method developed here. In the contour band example, for a given measurement, the sets of bands represent sets of intersections with the multiple constant δ surfaces. In the case where the interface friction value is known, only the band corresponding to the known δ surface need be plotted, as shown in (4). Zooming in on the resulting intersection region (5), the resulting region of consistent parameters is seen to be greatly reduced.

7.3.4 Additional Notes

The parameter space intersection method produces the full range of parameters that are consistent with the measurements and associated uncertainties. If a single estimate of parameters is required, different techniques can be used to select such an estimate. Once the final intersection region is obtained, in the simplest case, the center of the region

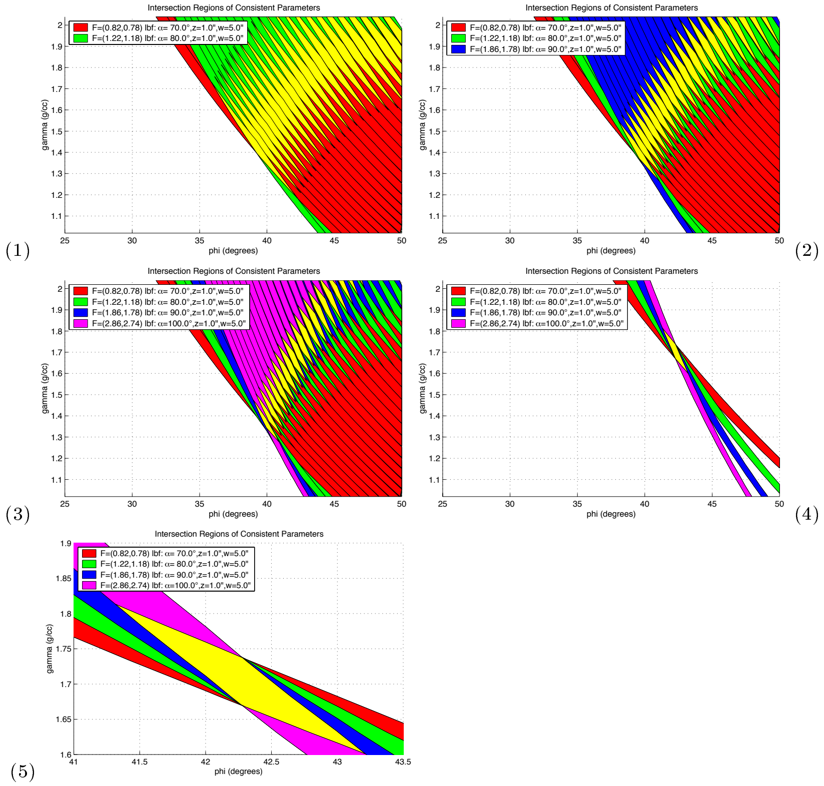

Figure 7.4: Next steps in the graphical method, utilizing measurements with uncertainty information. (1)-(3) show the superimposed contour bands from multiple measurements. (4) incorporates knowledge of δ to isolate one set of bands. (5) zooms in on the final consistent region.

can be selected as the estimate and uncertainty bands in ϕ and γ can be specified to encompass the whole consistent region. Another alternative is to compute the SSE over the final consistent region (which is a small subset of the whole parameter space) and select the minimum.

Obviously, the final intersection region should be as small as possible in order to get very precise parameter estimates. There are two mechanisms by which additional measurements can reduce the intersection region. Additional measurements at the same tool angle can reduce the uncertainty in a given measurement, which in turn thins each of the bands. Additional measurements at different tool angles are often more effective, as they generate a new set of bands that can potentially significantly reduce the final intersection region.

Note that the method outlined so far uses plots of ϕ versus γ. The same operations have also been done using plots of γ versus δ or ϕ versus δ. The plots of ϕ versus γ were used as a illustration so that knowledge of δ could be easily integrated. There is no barrier to using the other plots as well. The true consistent region of parameters is a 3-D volume in parameter space. These 2-D plots are projections of the 3-D volume. They each simply provide another view of the data. Which one is used depends on the goals of the parameter estimation. The variable that is not chosen as one of the axes will be represented in a discretized form (by the sets of bands), while the other variables on the axes will be continuous.

7.4 Comparison with Nonlinear Optimization

Now that the parameter space intersection method has been presented, it is of interest to see how it compares with a standard nonlinear optimization technique. Simulations have shown that the solution resulting from the graphical parameter space intersection method produces consistent intersection regions which typically enclose the local minima of the weighted sum-squared-error surface (Figure 7.5). The weighted sum-squared error is defined as

$$WSSE(\phi,\gamma,\delta) = \sum_n \left(\frac{F_n - F_{pred}(\alpha_n,\phi,\gamma,\delta)}{F_n} \right)^2 \tag{7.1}$$

This weighted form is used since it is expected that the errors would be larger in magnitude for the larger measurements. It can be seen from the left hand plots that there are multiple local minima. The

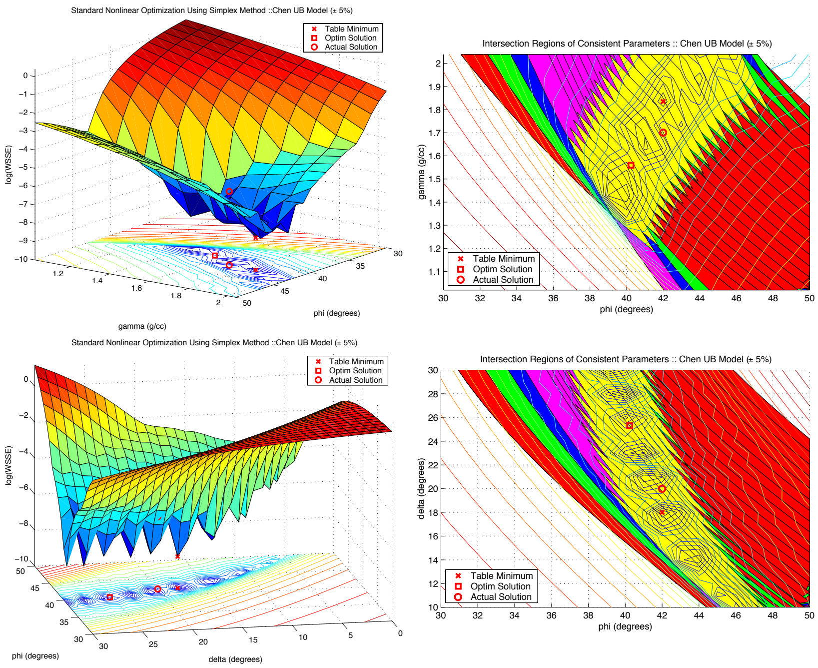

Figure 7.5: The left plots show the error surface computed at discrete points in parameter space. The contour curves from these surfaces are overlaid onto the results from our graphical method in the plots on the right. The graphical intersection regions are found to typically overlap the minimum error regions.

nonlinear optimization, based upon the WSSE, produces parameter estimates which fall into one of these minima and yield a single point solution. From the error surfaces, it is clear that the actual solution in this case is fairly distant from the minimum found using this error measure. On the other hand, the graphical procedure does not rely upon the selection of error measure for its construction. Some error measure may be utilized in the final stage to select a point from within the consistent intersection region, but the region itself is based solely on the measurements and the associated errors. As long as the given uncertainties fully represent the associated measurement errors, the actual solution is guaranteed to be found within the final intersection region. Instead of yielding a single point in parameter space, which is in uncertain relation to the actual parameters, sets of all parameters which are consistent with the measurements are obtained, enclosing the actual solution.

Time required for the two methods are comparable and are on the order of seconds. The graphical method is currently coded within Matlab, and takes fractionally longer. The nonlinear optimization is programmed in C using the downhill simplex method as described in Numerical Recipes [81]. The graphical method relies heavily upon Matlab functions for computing contours and polygon intersections and would be difficult to port to C. If this is done, the graphical method should be able to run an order of magnitude faster. Since we have no need for speed in these analyses, a difference of a second or two is not significant.

A key insight can be drawn from the results shown in Figure 7.5. The resulting region of consistent parameters shown in the plots on the right is extremely large. Only ±5% uncertainty in the measurements was used in this example (typical real measurements from the previous chapter had ±10% uncertainty), yet the range of consistent parameters is so large as to be nearly useless. This indicates that parameter estimation *cannot* be done using failure force measurements alone. Another independent source of information is required to reduce the problem. Application of a standard nonlinear optimization technique would give no indication of this grave difficulty. Fortunately, independent measurements of the interface friction, δ, are indeed available. These measurements will be shown to enable us to obtain reasonably good parameter estimates.

7.5 Results from Experimentation

Using the mean and standard deviation values from the experimental results in the previous chapter, parameter estimation has been accomplished using the estimated interface friction values for each soil. The following figures show estimation results using the upper bound (UB) and lower bound (LB) numerical soil models. In order to be absolutely thorough, the full range of uncertainty in the interface friction estimates and the density measurements must be incorporated into the parameter estimation.

The iterative technique for the estimation of interface friction angle (Section 5.4) produces estimates with an uncertainty of $\pm 1^\circ$. This information is used to limit the graphical method to the construction of three sets of contour bands, at δ and $\delta \pm 1^\circ$. Although only three discrete sets of bands are drawn in the figures, δ is a continuous variable, and the intermediate values would lie between the bands drawn.

Thus, the complete consistent region would include the small triangular regions between the tips of the intersection polygons in the figures, corresponding to non-integer δ values.

It can be seen that even with the use of the interface friction estimates, the final consistent region remains large. Thinning of the bands would not be helpful. Thus, the other means of reducing the final consistent region would be to add additional measurements at different tool angles. The current manipulator is limited to a lowest tool angle of 70°. In the subsequent discussion, it will be shown that additional strokes at low tool angles would provide the necessary information to reduce the final consistent region. However, in place of such information, we have used the available independent density measurements which were obtained in the previous chapter. The density measurements over repeated sample preparations was found to have a maximum variation of up to 4%. Therefore, a horizontal band of width ±4% of the density measurement is drawn in each figure (dash-dot lines). The final consistent region of parameter space would be the intersection of the contour bands (the light-shaded region) with the horizontal band resulting from the independent density measurement ± the density uncertainty.

Table 7.1 provides a listing of the full density and friction angle ranges predicted from the graphical method using the UB and LB models without the independent density measurements. In practice, these direct densities measurements would not be available. It can be seen that the range of estimates are fairly large if the density measurements are not used. It is clear that strokes at low tool angles would be necessary to reduce the final consistent region. Alternatively, independent sensing means might also be developed to estimate density (either from determining the composition from spectroscopy and estimating the void ratio, or using a vision system to estimate volume and the manipulator to weigh samples).

Table 7.2 provides a listing of the friction angle ranges from the graphical method utilizing the externally measured density values. The ranges using the Chen and Caquot and Kerisel models are shown for comparison. The Chen model does not predict a valid set of friction angles for the Ticino sand data at the specified density and interface friction. These measurements exhibited the most drastic change from low tool angles to higher tool angles. It was conjectured that this effect was a result of the stress-dependence of the friction angle combined with the progressive failure of the soil. The parameter estimate results in this case indicate that, at least for this particular model, no single friction angle could have generated the measurements with the associated uncertainties. The other models have valid intersections, but

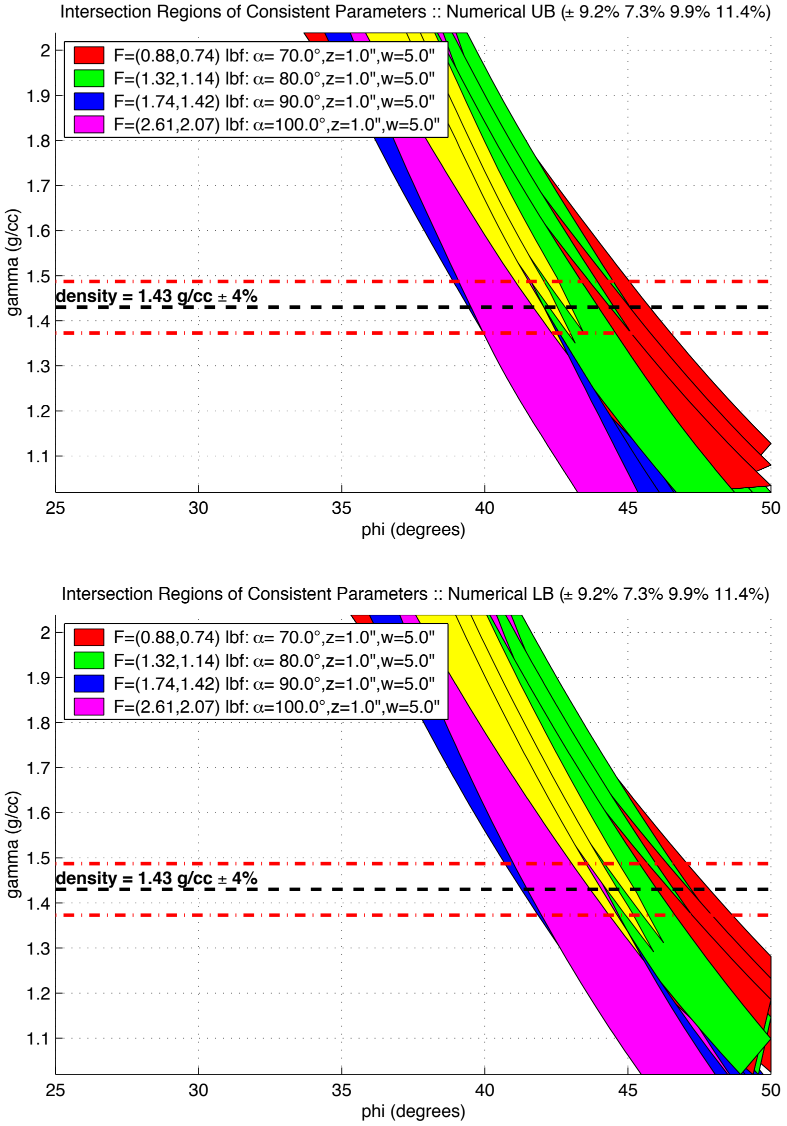

Figure 7.6: Parameter estimation for unrained Ticino results with a 23° interface friction angle using the UB (top) and LB (bottom) models.

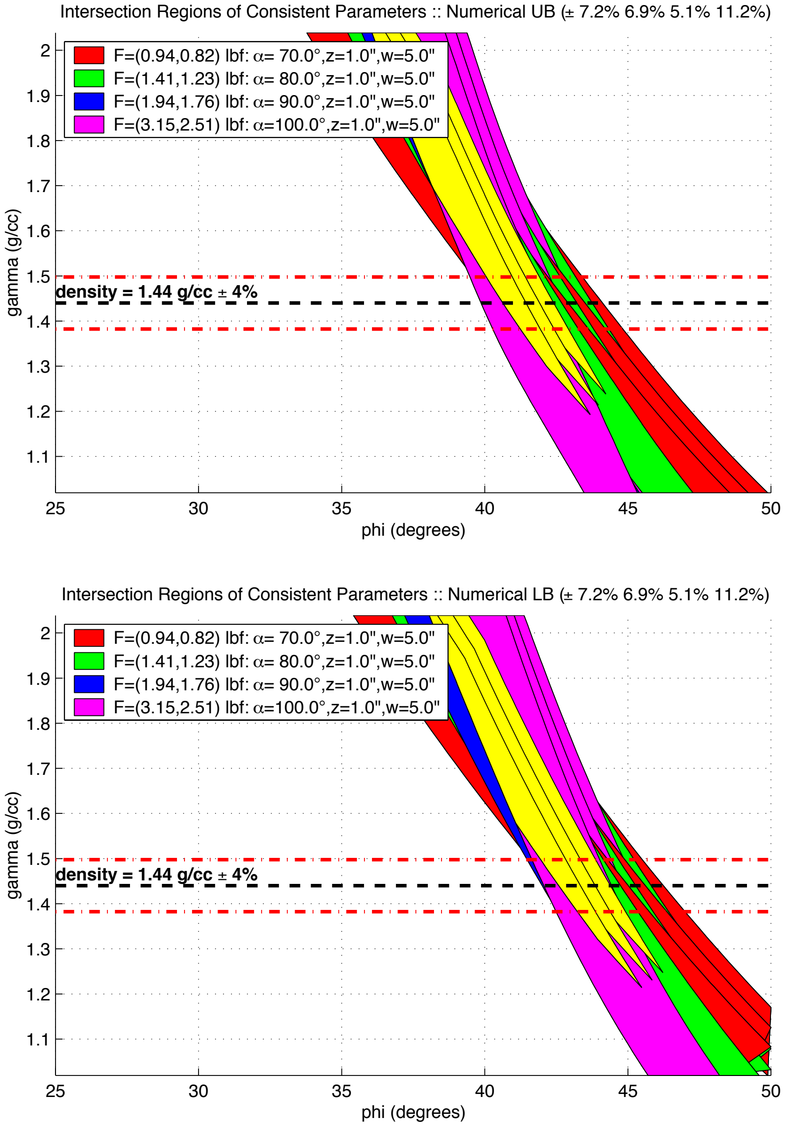

Figure 7.7: Parameter estimation for Nevada Fine sand results with a 27° interface friction angle using the UB (top) and LB (bottom) models.

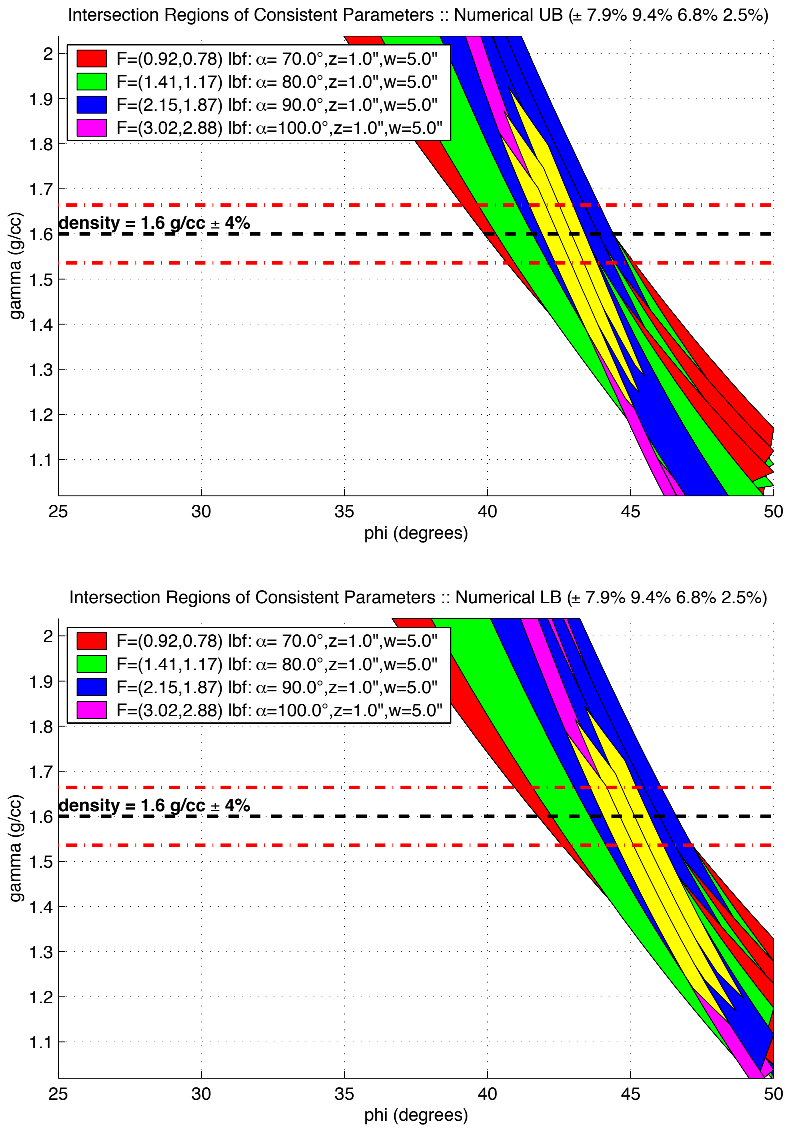

Figure 7.8: Parameter estimation for dense Ticino results with a 23° interface friction angle using the UB (top) and LB (bottom) models.

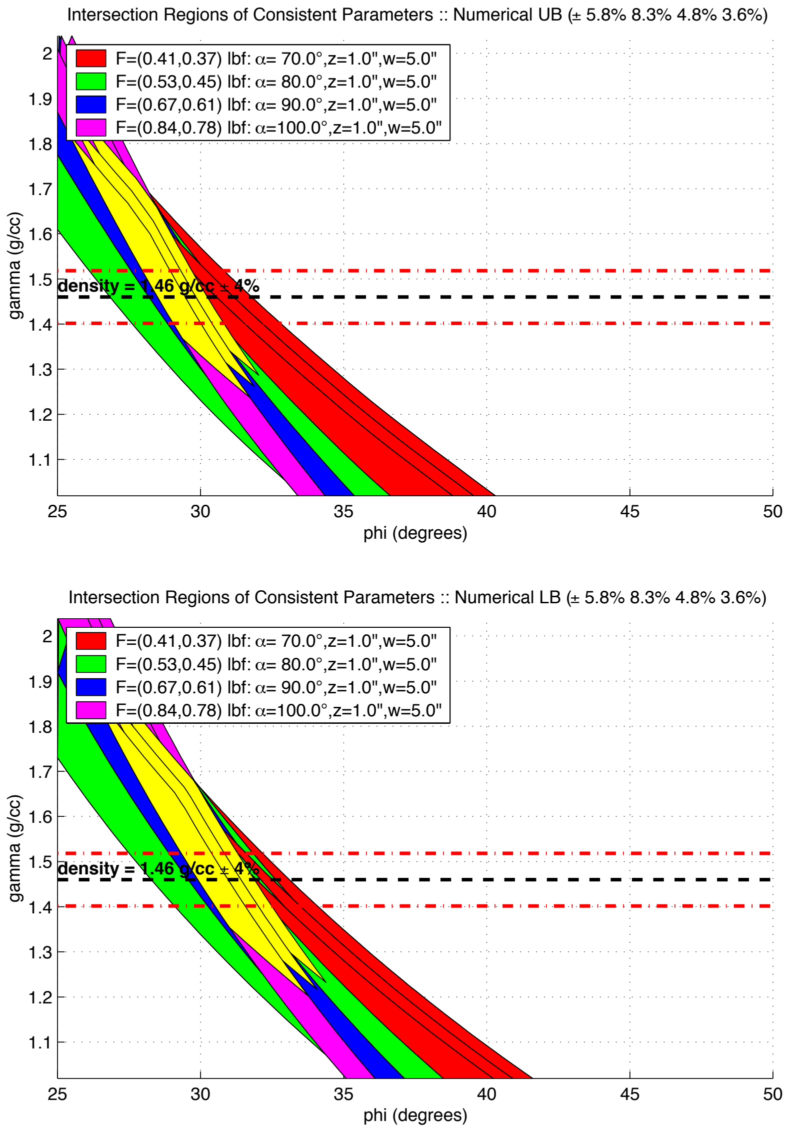

Figure 7.9: Parameter estimation for glass bead results with a 19° interface friction angle using the UB (top) and LB (bottom) models.

	Density (g/cc), γ		Internal Friction, ϕ	
	UB	LB	UB	LB
Ticino	1.33-2.10+	1.30-2.10+	$36° - 43°$	$38° - 46°$
Nevada Fine	1.20-2.10+	1.20-2.10+	$36° - 44°$	$38° - 46°$
Rained Ticino	1.20-1.90	1.15-1.81	$41° - 45°$	$43° - 48°$
Glass Beads	1.25-1.88	1.20-1.90	$26° - 32°$	$27° - 34°$

Table 7.1: Full range of possible density and friction angle values for the experimental data using the UB and LB models. These values represent the complete range spanned by the intersection of the contour bands. They do not use the independently measured density values (the horizontal dashed lines) to narrow down the estimated friction angle ranges.

	UB	LB	Chen	Caquot
Ticino	$41.4° - 44.4°$	$43.0° - 46.8°$	no int.	$40.8° - 42.9°$
Nevada Fine	$40.9° - 44.0°$	$42.7° - 46.1°$	$39.9° - 42.2°$	$39.7° - 42.8°$
Rained Ticino	$41.4° - 43.8°$	$43.6° - 46.1°$	$40.8° - 43.2°$	$41.2° - 43.6°$
Glass Beads	$28.0° - 30.8°$	$29.3° - 32.5°$	$26.5° - 29.8°$	$28.0° - 30.7°$

Table 7.2: Table of parameter estimation results from experimental data utilizing the measured densities with ±4% uncertainty. The Chen and Caquot and Kerisel models are included for comparison.

they are very near to the tips of the consistent region. This highlights another benefit of the graphical parameter estimation technique, it can be used to assess the consistency of the measured data.

7.5.1 Accounting for High Tool Angle Effects

The above parameter estimation was run on unmodified measurement data. However, it is known that the 90° and 100° tool angle measurements for the loose Ticino and for the Nevada Fine sand were affected by a combination of the progressive failure effect and the lower friction angles exhibited at higher stresses. While exact correction for the progressive failure is not possible, using the guideline of a motion of 20% of the tool height for full mobilization of friction gives a very rough correction of 10%. In order to present more complete parameter estimation results, the technique has been computed for the loose Ticino and Nevada Fine cases using adjusted measurements for the high tool

			$z = 1/2$”	$z = 2/3$”
	UB	LB	$\sigma_{U,90} - \sigma_L$	$\sigma_{U,90} - \sigma_L$
Ticino	$41.1^\circ - 44.4^\circ$	$43.0^\circ - 46.8^\circ$	$42.3^\circ - 45.4^\circ$	$41.6^\circ - 44.7^\circ$
Nevada Fine	$40.9^\circ - 44.0^\circ$	$42.7^\circ - 46.1^\circ$	$38.9^\circ - 43.3^\circ$	$38.1^\circ - 42.5^\circ$
Rained Ticino	$41.4^\circ - 43.8^\circ$	$43.6^\circ - 46.1^\circ$	$47.1^\circ - 51.2^\circ$	$46.4^\circ - 50.3^\circ$
Glass Beads	$28.0^\circ - 30.8^\circ$	$29.3^\circ - 32.5^\circ$	$31.0^\circ - 33.2^\circ$	$30.4^\circ - 32.6^\circ$

Table 7.3: Table of UB/LB parameter estimation and direct shear results. The extreme bounds of the UB/LB predictions vary from $\pm 2.25^\circ$ to $\pm 2.85^\circ$. The UB/LB bounds are found to overlap the direct shear ranges, except for the rained Ticino case.

angles.

Figures 7.10 and 7.11 show the UB and LB results for the adjusted cases. The correction acts to widen and marginally increase the estimated friction angles. For the unrained Ticino, the ranges become UB: $41.1^\circ - 44.4^\circ$ and LB: $43.0^\circ - 46.8^\circ$. For the Nevada Fine, the ranges become UB: $40.9^\circ - 44.0^\circ$ and LB: $42.7^\circ - 46.1^\circ$. It is interesting that although the bands are thickened, the UB/LB friction angle estimation ranges (using the measured density) are essentially unaffected.

7.5.2 Comparison with Direct Shear Results

Table 7.3 and Figure 7.12 compare the UB/LB friction angle estimation bounds with the direct shear friction angles computed in Section 6.6.2. The extreme bounds of the UB/LB predictions vary from $\pm 2.25^\circ$ to $\pm 2.85^\circ$. The direct shear bounds, computed from equivalent pressures at depths of z=1/2” and z=2/3”, are found to overlap the UB/LB bounds, except in the case of the dense rained Ticino. This discrepancy has been discussed in detail at the end of the previous chapter.

For the other soils, the agreement is good. The separation between the center of the UB/LB ranges and the center of the direct shear bounds vary from 0.1°-2.4° (using $z = 1/2$”), or 0.8°-3.2° (using $z = 2/3$”). The Nevada Fine sand shows the largest discrepancy. The cause may be related to the very fine particle size of this soil, which can allow the sand to compact more easily during stroking, effectively increasing the measured friction angle. While the glass beads have an even finer particle size, the particles are predominantly round, and the effect of the compaction would be less significant.

Overall, it is concluded that the parameter estimation technique has produced estimates of the internal friction angle with an average uncer-

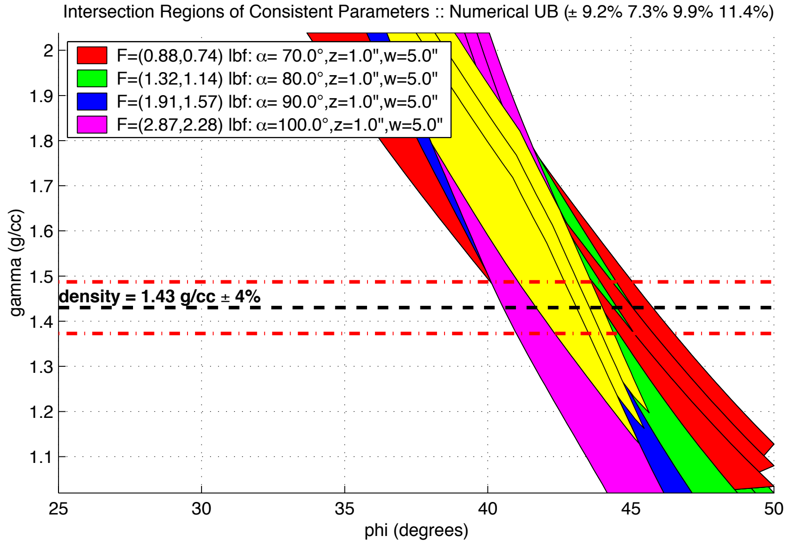

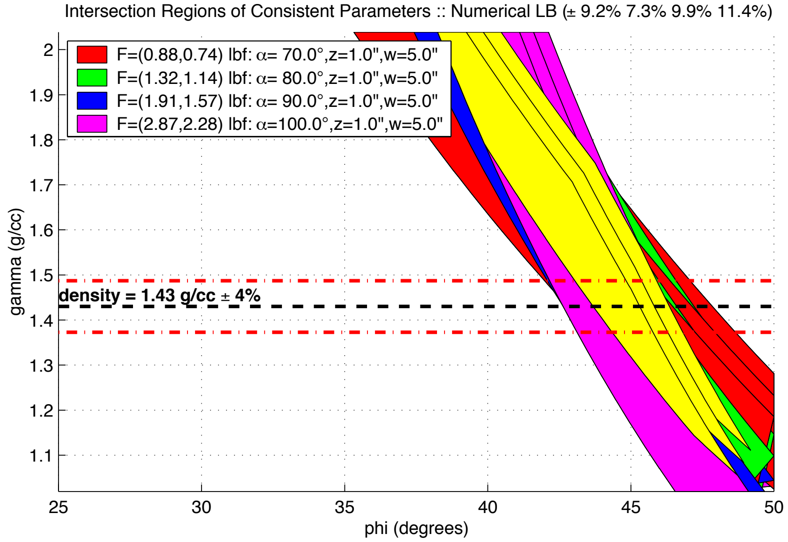

Figure 7.10: Parameter estimation for adjusted unrained Ticino measurements using the UB (top) and LB (bottom) models.

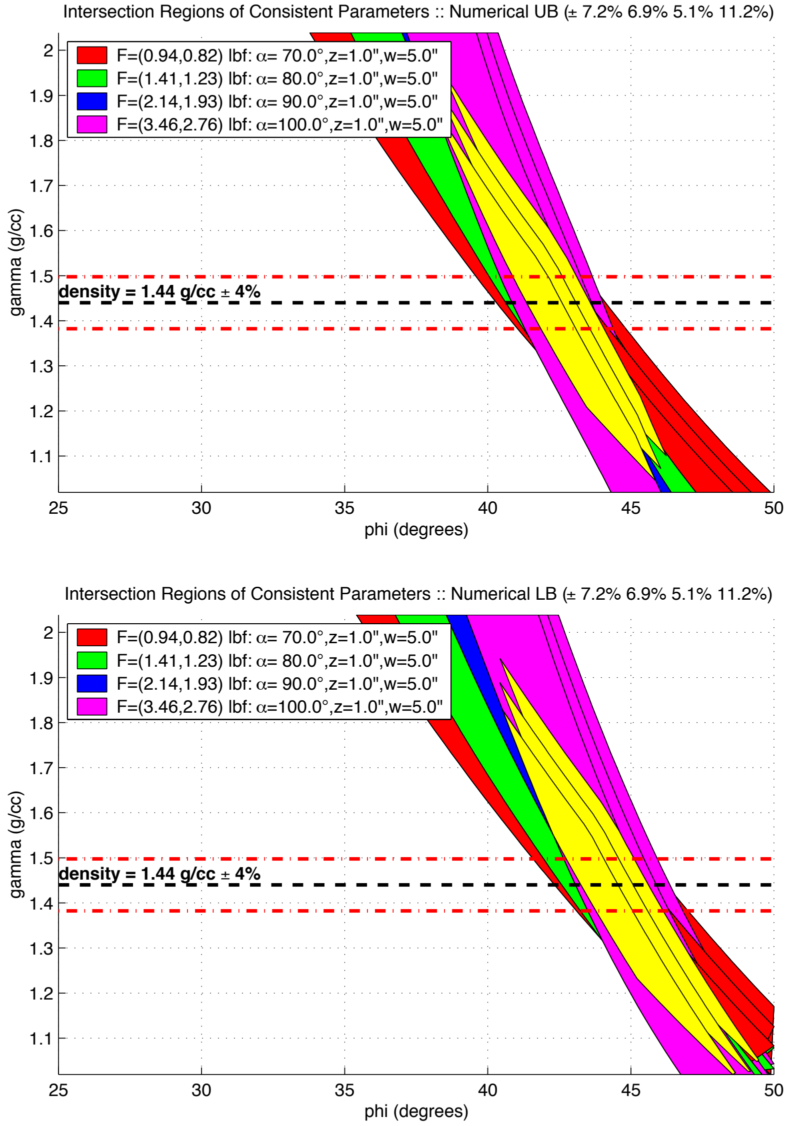

Figure 7.11: Parameter estimation for adjusted Nevada Fine measurements using the UB (top) and LB (bottom) models.

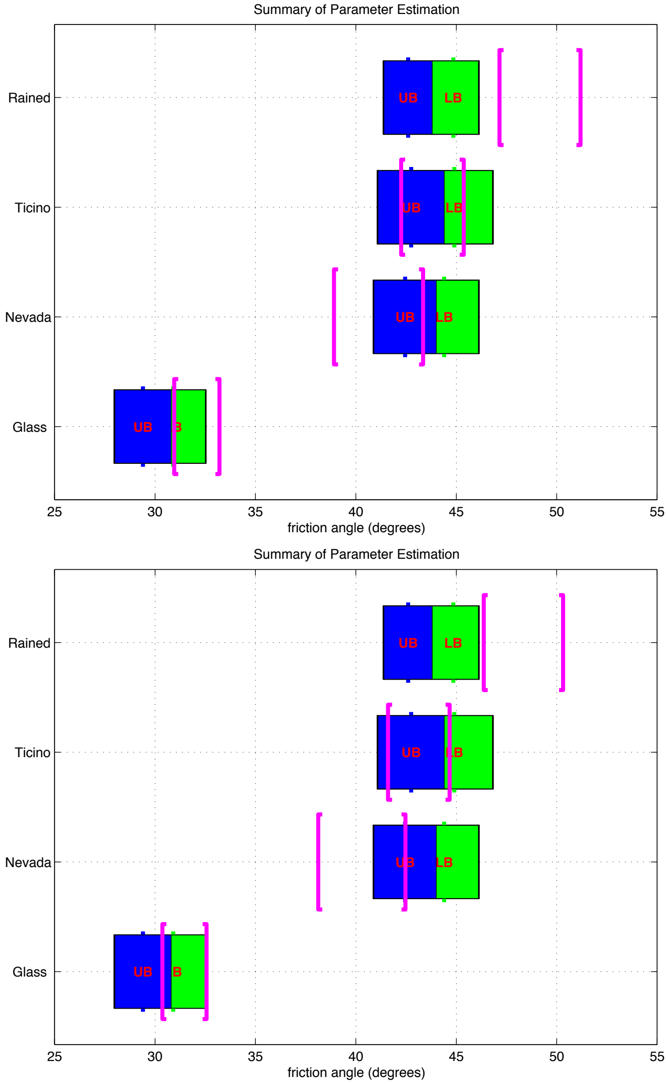

computed at $z = 1/2$"

computed at $z = 2/3$"

Figure 7.12: Graphical comparison of the full UB/LB friction angle estimates and the equivalent direct shear friction angles, computed from equivalent pressure ranges at $z = 1/2$" (upper) and $z = 2/3$" (lower). The blocks represent UB and LB parameter ranges and the brackets represent the $[\sigma_{U,90}, \sigma_L]$ direct shear ranges.

tainty of ±2.5° for these soils. The estimated values are in agreement with the direct shear results to within approximately 3°.

7.6 Discussion

An intuitive graphical parameter space intersection method for model inversion has been developed in this section that has been shown to produce more rich information than a standard nonlinear optimization method. It accomplishes this by using knowledge of the available uncertainty in the measurements to segment the parameter space into consistent and inconsistent regions. If a single "best" parameter estimate is required, as might be provided by a standard nonlinear optimization technique, then, we can compute an error measure over a smaller set of candidates (the consistent region of parameter space) and obtain comparable solutions to an exhaustive search. While a nonlinear optimization would only provide a single point solution, the intersection method essentially converts uncertainty bounds in the measurement data to uncertainty bounds in the parameter estimates.

In addition, the intersection method has allowed us to gain key insights about the estimation problem. It has been shown that good parameter estimates cannot be obtained using failure force measurements alone. For measurements with an uncertainty of only ±5%, it was shown that the consistent region of parameter space remained quite large. It was concluded that additional independent measurements were required to reduce the estimation problem. These independent measurements were provided by the interface friction estimation technique discussed in Section 5.4.

The intersection method also allowed us to clearly visualize the impact of additional measurements on the resulting consistent set of parameter estimates. This can be used to guide future interactions. For instance, it has been shown that higher tool angles provide better friction angle discrimination and lower tool angles provide better density estimation. In this chapter, since the manipulator end-effector was not able to reach lower than a 70° tool angle, we have used independent density measurements to complete the parameter estimation. However, it can be shown that strokes at 40° tool angles can be used in place of the density measurements, so that it would indeed be possible to obtain complete parameter estimation results using data collected by the manipulator alone. Figure 7.13 shows an example where we have added an additional simulated stroke at 40° to a typical collection of contour bands from $70° - 100°$ strokes. The resulting consistent

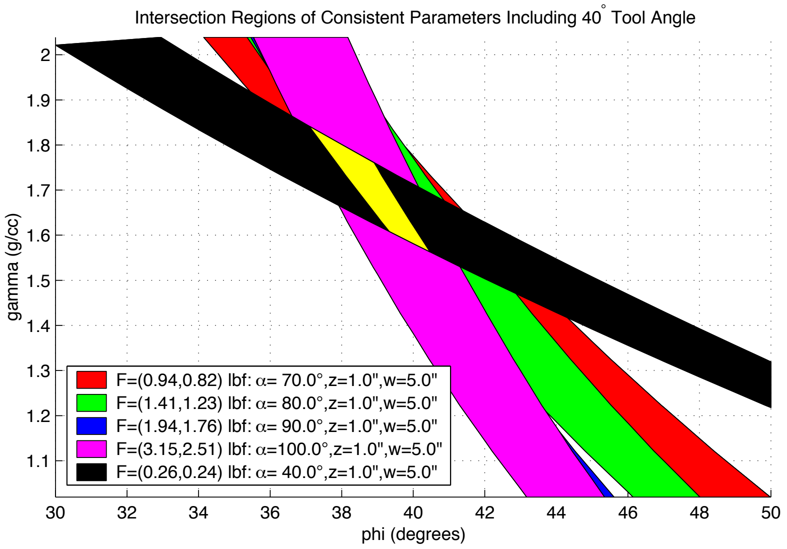

Figure 7.13: The above plot shows the results of the addition of a stroke at a 40° tool angle on the final parameter region, showing better density discrimination.

parameter region spans roughly ±1.3° in ϕ and ±1.1 g/cc in γ.

Finally, assuming that the measurement uncertainty information and the underlying soil model are correct, then the actual solution is *guaranteed* to lie within the final consistent intersection region. If no valid region is produced, then this is an indication that we must reevaluate the choice of soil model or the accuracy of the measurements and/or assumptions.

Chapter 8

Ideas for Future Work

This chapter begins with a discussion of ideas for the future that are immediate extensions of this work. Afterwards, more distant applications and possibilities are discussed. Finally, possible applications of this work to the exploration of Mars are presented.

8.1 Related Unexplored Areas

The system in this work is a first generation system, however, it shows great promise for future generations. A number of enhancements to the hardware and techniques will provide greater reliability and utility for studying a variety of the interesting issues raised in the course of this work.

The manipulator design can be improved to have greater freedom in tool angle orientation for greater discrimination of soil density (e.g. using a 40° tool angle) as discovered by the parameter estimation technique. It should also be possible to achieve greater strength and insertion depths so that a wider range of applied stress can be tested in order to map dependencies of friction angle on the applied stress. The addition of comprehensive sensing of the arm compliance would enable the modeling of the progressive failure effect and enable the closer examination of the mobilization of friction along the failure surface.

A number of items related to soil modeling provide additional interesting avenues of research. All testing done here assumes horizontal cohesionless soil, but the models can support both inclined surfaces and cohesion. In addition, no use of the shape of the failure surface predicted from models has been made. This could be tested experimentally and then used as an added measurement for model inversion and would prove useful for soil simulation. Application of the numerical limit analysis techniques can be extended to non-flat tools, such as curved bulldozer blades or piece-wise linear surfaces (buckets). In addition, the models can be extended to account for increased forces due to buried obstacles, which could be used for non-contact buried obstacle detection.

Closer examination of the stress level dependence of the friction angle should be studied. Multiple strokes can be conducted at a greater variety of depths, providing data at a variety of stress levels. Thus the stress dependence over a wider range can be studied. Our depth verification tests in this work could not span a wide range of depths, however, the data typically showed higher forces at the lower insertion depths. This was attributed to insertion depth uncertainty, but this could also indicate higher friction angles at very low confining stresses.

Another topic which may be of interest to future researchers would be to verify the force versus inclination angle "friction-cone" predictions as in Figure 5.13. The exact nature of the safe force magnitudes below the case of a perfectly rough interface ($\delta = \phi$) could be explored. The resulting detailed force versus inclination curve could then be used to plan optimal digging trajectories. For instance, if the arm motors have an optimal operating force, the desired path of the end-effector can be planned to dig with as large an inclination as possible using the optimal operating force value.

One final idea would be to combine our system with a terrain mapping mechanism (e.g. laser range scanning or stereo vision). This would enable the examination of the extent of the failure region and the resulting accumulation of soil ahead of the plate after failure. This information could be used to validate the extent of the failure wedges predicted from the soil models. It could also be used to aid in the construction of a realistic virtual physically-based simulation of soil behavior.

8.2 Virtual Reality Simulation

One of the initial goals of this research was the development of a virtual reality simulation populated with the soil models from this work, using the soil properties determined by the manipulator. After the development of the graphical 3-D rendering of the manipulator, which was used primarily for debugging during system development, the idea of enhancing the system to become a full virtual reality system with haptic feedback came to mind. Due to time constraints, this topic was

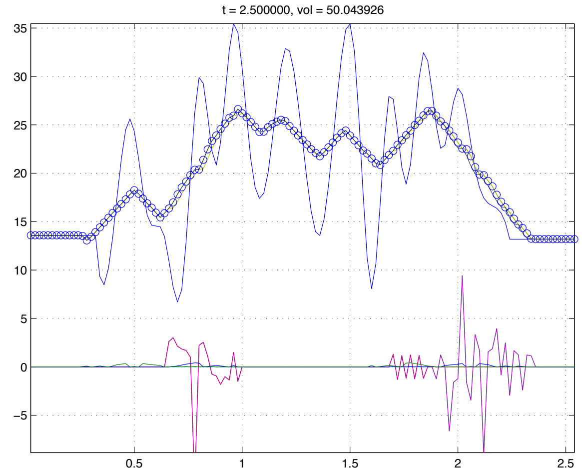

Figure 8.1: Results from a 2-D simulation of constant volume dynamic soil settling. The smooth solid line represents an initial state of the soil. The circles represent the evolving state of the soil surface. The jagged line near the bottom represents the activity, where larger magnitudes represent larger masses of soil moving at this location.

not explored.

There are a number of components which would need to be developed in order to create such a system. An accurate physically-based simulation of soil settling and deformation behavior would be required. A more complete manipulator model with dynamics and collision detection would need to be developed. And models for soil-manipulator interaction forces would need to be integrated with the control of a force-feedback device. A few references related to this type of work are [4, 15, 25, 40, 76, 125].

Currently, there appears to be very little research in the area of physically-based soil simulations. There is work in computer graphics to visually simulate soil deformation [110], but these are not intended to be physically accurate. Looking specifically at physical soil simulation, only papers from Li and Moshell [66, 67] are found. They develop a real-time physically-based model of soil being operated upon (digging, cutting, piling) and settling under gravity. They present two- and three-dimensional models. The three-dimensional (3-D) version is essentially a lattice of two-dimensional (2-D) versions arranged to cover a 3-D

Figure 8.2: OpenGL model of the manipulator arm and soil surface. The model is capable of receiving manipulator position information over the network and displaying this information in real-time.

area. Figure 8.1 shows an example of the 2-D dynamic soil settling behavior. The solid line is an initial soil profile. The circles represent the soil surface after settling under the influence of gravity. How this work scales with increased number of nodes needs to be examined. A new 3-D model, which is more advanced than a combination of multiple 2-D models, should also be developed. We have only briefly played with the idea of using gradient fields instead of a lattice of 2-D models.

Assuming that a suitable real-time model for soil settling is available, a complete dynamic model for the manipulator arm is required. A basic model of our manipulator has been constructed, which accounts for the geometry of the arm, but not the dynamics (such as mass, inertia, friction, etc). Figure 8.2 shows a rendering of the arm resting on a block over a flat ground. Development of a graphical model is fairly simple; the difficulty lies in adding the dynamics, collision detection, and force interaction with the environment.

Once the dynamics of the arm and the capability to interact with the soil is implemented, a haptic device can be coupled to the simulation to provide real-time force feedback. This would enable users to interact with the soil, experiencing realistic forces generated from soil models, using soil parameter estimates determined by the manipulator for the specific soil of interest.

8.3 Applications of Work to Mars Exploration

Soil parameter estimates alone are interesting in the context of geological discovery. However, in addition, the estimates from this research can be used for making predictions for various interactions with soil, taking care to use appropriate friction angles for each loading condition. Most of these interactions are the standard applications of physical soil properties for stability calculations.

For instance, for a rover moving up an inclined slope, calculations can be done to see if the slope is stable or near failure. Calculations can be done to discover the maximum inclination slope that would be able to maintain the weight of the rover. Similar calculations can be done for the stability of a lander on an inclined slope.

Measurements of stratification of the soil can be made if deeper depths of soil can be uncovered. For instance, with a lander-based manipulator conducting the gross excavation, a rover-based manipulator can conduct finer estimation as new layers are uncovered. Using this dual arm approach, the lander-based manipulator can be highly geared, with minimal precise sensing capabilities, and the rover-based manipulator can be designed for precise sensing without requiring large force capability.

One final possible application is the study of geographic variation of soil properties. Sampling of soil properties can be conducted at many different locations. If there are significant physical property variations, independent of composition, perhaps deductions can be made about the historical cause of such variations.

Chapter 9

Conclusion

This thesis documented work to develop methods to enable a robot manipulator to estimate soil properties from interactions. In the course of this work, various topics were examined.

In the area of soil modeling, this thesis presented the application of numerical limit analysis to the modeling of earth pressure. The predictions from this technique were shown to be in good agreement with currently accepted models. In addition, this technique provides greater versatility than the existing models. It provides both upper and lower bounds and can easily accommodate a variety of loading and boundary conditions. No assumptions on the failure surface are made, allowing for arbitrary elements to be added to the meshes. For instance, different tool shapes, such as curved blades of bulldozers or the piecewise linear buckets of excavators can be modeled. Also, buried obstacles can easily be incorporated into the meshes. The benefits of this aspect of this work is not limited to robot interactions with soil. This portion also has the potential to benefit all researchers working on earth pressure problems by demonstrating and verifying a widely applicable modeling technique.

The design of a robotic manipulator arm for interactions with soil was documented. A flat plate was used to more accurately model interactions and to enable the application of the wealth of research in the area of earth pressure theory. From the experience gained in this work, a few design recommendations can be made for future researchers. Use a flat plate if possible, with a large width to depth ratio, near 5:1 or greater. The end-effector design should be carefully thought out to assure a suitable range of motion for plate orientation and it should not be backdriveable. For the other joints, design them to be backdriveable if you intend to use motors to obtain force measurements. Have end-point position sensing accuracy to less than one percent of typical insertion depths, or use external feedback to verify insertion depths. If there is compliance, make sure it is fully sensable, so that the actual displacement of the soil is easily separable from the measured displacement. This will enable study of the progressive failure of soils. If good force sensing is available, control the angle of the applied force on the plate during stroking. If not tracked well, it can result in widely varied measurements. The control of the angle of force has been shown to enable the *in situ* estimation of soil-tool interface friction. This was shown to be key in the property estimation technique.

This work also represents the first set of experimental results of its kind. The experimental results in this work have highlighted a few issues in soil modeling which must be considered by any researcher working on a similar problem. Common assumptions are made in soil modeling about the behavior of soils. Most notably, the assumption of the Mohr-Coulomb failure law and the perfectly plastic behavior of soils. The results of this work were in wide disagreement with direct shear tests conducted at high normal stresses (> 7 psi). Upon closer examination, a study of friction angle dependence on stress at low stresses was conducted, showing a significant change in measured friction angle (up to 10° from a normal stress of 7 psi down to 0.2 psi). This has ramifications for any study of friction angles and cohesion done at low stresses. If these elevated values are applied to stability calculations under higher stresses, drastic over-estimation of the shear strength of the soil will result. The soil models have also assumed perfectly plastic failure of soils. For a large fraction of the failures at vertical tools and tools inclined away from the direction of motion, the failure was gradual. It is clear that progressive failure occurred. This complicated the estimation of failure force for these strokes. Unfortunately, a detailed study of this effect was not possible using the manipulator in this thesis and must be left for future researchers.

Finally, this thesis has presented a parameter space intersection technique for model inversion that operates on tabulated model predictions. This method utilized the associated uncertainties of the measurements to produce a set of parameters which were consistent with the observations. The main conclusion from the graphical technique was that independent measurements of one or more of the variables were *required* for doing parameter estimation. The problem was shown to be very difficult since a large region of parameter space was found to be consistent with measurements with only ±5% error. To narrow down the set of consistent parameters, independent measurements must be utilized. Fortunately, the development of manipulator stroke control techniques provided a method for estimating the soil-tool interface friction independently. This reduced the region of consistent parameters considerably; however, precise parameter estimates of both density and internal friction were still not quite achievable. A final conclusion from the graphical technique has shown that strokes at lower tool angles can discriminate densities better (and narrow down internal friction angle estimates at the same time). Higher tool angles are typically better for discriminating internal friction angle. Since higher tool angles are prone to gradual failure which introduces additional complications, and lower tool angles have more drastic, easily discernible failures, future researchers should use a range of tool angles from $40° - 80°$. This would provide better density discrimination, good friction angle discrimination, and definite failure force estimates. Strokes at lower tool angles, combined with the independent interface friction estimation technique, provide a basis for enabling precise estimation of density and internal friction using interaction force measurements.

In conclusion, this thesis has presented the development of a complete system for studying robot-soil interactions. The ultimate goal of this work was to enable a manipulator arm to estimate soil properties *in situ*. This thesis has successfully shown that it is indeed possible to estimate physical properties of cohesionless soils using the manipulator alone. This thesis has documented the hardware, software, soil modeling, and estimation techniques involved in reaching this goal. Experimental results in multiple soils have been conducted to validate the methods described. Finally, recommendations have been made for future researchers, to enable them to develop systems that build upon this work. This hopefully will lead to systems which can estimate soil properties with greater precision and further explore the interesting issues raised by this work.

Appendix A

Arm Flexibility Compensation

A.1 Nature of the Problem

Although we have mounted external encoders to account for the backlash in the motor gearheads, there is still some imprecision in the measurement of the end-point of the manipulator resulting primarily from cable stretch and to a small extent link flexion and motor gearhead compliance. The external encoder on the shoulder is mounted directly to the shoulder joint, so that measurement is independent of cable stretch. On the other hand, the elbow joint has external encoders mounted to motor output shafts since we could not mount them on the elbow due to the differential. In addition, there are very long runs of cable with minimal distance for pre-tensioning those cables properly. Therefore, we will experience a significant flexion in the elbow joint from the cable stretch during high loads.

A.2 Flexion Estimation

In order to estimate the arm flexion, we immobilized the end of the manipulator and drove the motors to a specified position within the obstruction. We know that the actual manipulator end-point has not changed significantly but the manipulator end-point derived from the external encoder measurements will reflect some motion. We repeat this at different locations and we can back out the approximate stiffness of each of the joints.

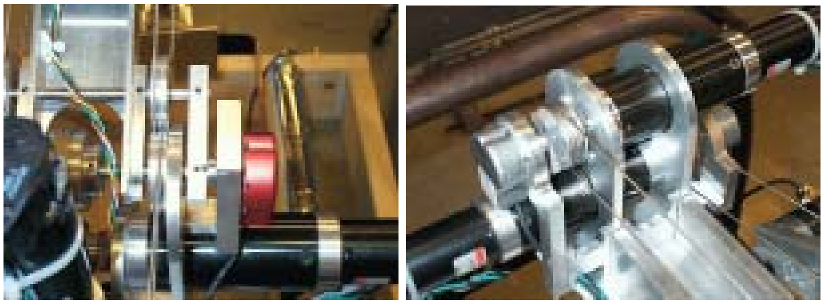

Figure A.1: External encoders for the shoulder and elbow motors. The shoulder encoder is mounted directly on the joint, whereas the elbow encoders are at the motor output shafts.

Figure A.2: In order to estimate arm flexion, the end of the arm is immobilized while the motors drive the arm into the obstruction.

So we can relate the measured force, $\mathbf{F}_{meas}$, and the measured apparent displacement, $\Delta\mathbf{x}_{meas}$

$$\mathbf{F}_{meas} = \mathbf{J}^{-T}\mathbf{K}_{stiff}\mathbf{J}^{-1}\Delta\mathbf{x}_{meas} \tag{A.1}$$

and convert this into torque and joint displacements, replacing the stiffness matrix with individual matrix elements, and using $\boldsymbol{\tau} = \mathbf{J}^T F$ and $\Delta\mathbf{x} \approx \mathbf{J}\Delta\theta$

$$\boldsymbol{\tau}_{meas} = \left[\begin{array}{cc} k_1 & k_2 \\ k_3 & k_4 \end{array} \right] \Delta\boldsymbol{\theta}_{meas} \tag{A.2}$$

A.3 Flexion Compensation

We compensate for the flexion in the elbow joint only since the shoulder joint is much more stiff in comparison. We do the compensation by estimating the amount of stretch in the cable for a given torque at the elbow. The torque at the elbow is computed using the force from the F/T sensor and orientation of the wrist to compute the tangential force and distance from the elbow joint. As mentioned before, we make a very simple assumption of a linear stiffness. Therefore we can compute the adjustment to the elbow measurement by simply dividing the estimated torque at the elbow by the estimated elbow stiffness.

$$\theta_{2_{offset}} = \frac{|\mathbf{F}| r \cos(\theta_4 - \delta)}{k_{elbow}} \tag{A.3}$$

where $|\mathbf{F}|$ is the magnitude and δ is the angle of the force as measured by the F/T sensor. The point of application of the force on the plate, at distance r from the elbow joint, is computed from the F/T sensor data. The stiffness value k_{elbow} is k_4 from equation A.2. The shoulder is known to be stiff with sensing located directly on the joint axis. In our tests, we found that the contribution to $\theta_{2_{offset}}$ from the shoulder torque was minimal, and thus, we use $k_{elbow} = k_4$.

In practice, we have found that this compensation can overpredict and underpredict depending upon the arm configuration. We have made assumptions that the stiffness of the elbow is configuration independent and also linear. Both of these assumptions are probably inaccurate to some degree. But nevertheless, the resulting compensation, which can be up to 1-2 degrees during a stroke, places us closer to the true elbow joint value than if we ignored the flexibility.

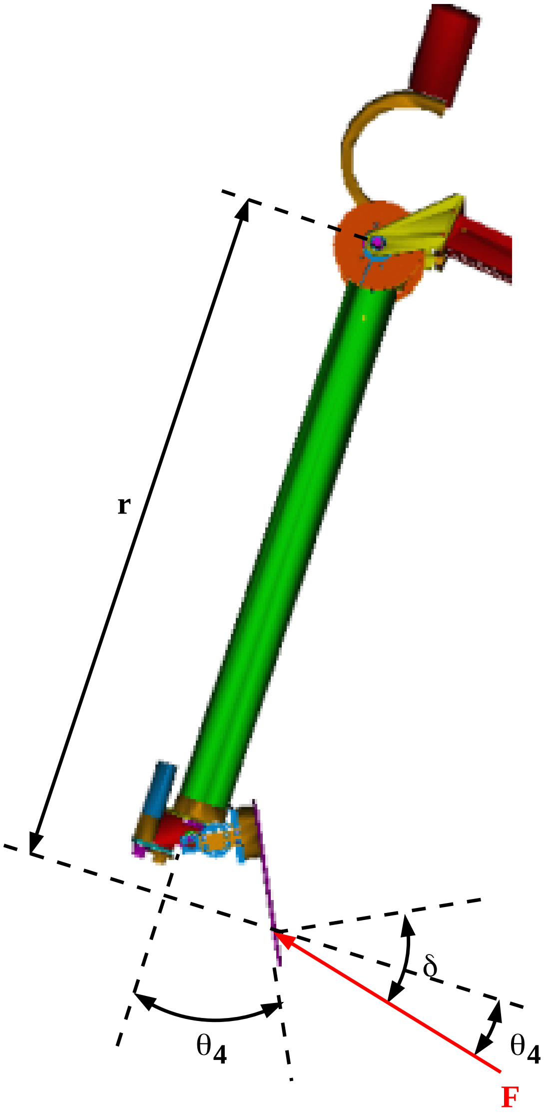

Figure A.3: To compensate for the elbow flexion, we compute the tangential end-point force to find the torque at the elbow.

Appendix B

Arm Kinematics

This section documents the derivation of the full 5-DOF forward kinematics, Jacobian, inverse kinematics, and joint to motor transformations for the manipulator arm. The joint angles are labeled from θ_0 to θ_4 and corresponding link lengths are l_0 to l_4.

B.1 Forward Kinematics

Let the end point of the base 3-DOF of the arm be labeled $\mathbf{X}_A$. This is the point just before the end-effector links. The coordinates of point $\mathbf{X}_A$ are then given by

$$\mathbf{X}_A = \begin{bmatrix} (l_1 \sin\theta_1 + l_2 \sin(\theta_1 + \theta_2) \cos\theta_0 \\ (l_1 \sin\theta_1 + l_2 \sin(\theta_1 + \theta_2) \sin\theta_0 \\ l_0 + l_1 \cos\theta_1 + l_2 \cos(\theta_1 + \theta_2) \end{bmatrix} \tag{B.1}$$

The last 2-DOF (forearm and end-effector wrist) results in a unit vector along the following orientation

$$\mathbf{u}_e = \begin{bmatrix} (\sin\theta_4 \cos\theta_3 \cos(\theta_1 + \theta_2) + \cos\theta_4 \sin(\theta_1 + \theta_2)) \cos\theta_0 - \\ \hfill (\sin\theta_4 \sin\theta_3) \sin\theta_0 \\ (\sin\theta_4 \cos\theta_3 \cos(\theta_1 + \theta_2) + \cos\theta_4 \sin(\theta_1 + \theta_2)) \sin\theta_0 + \\ \hfill (\sin\theta_4 \sin\theta_3) \cos\theta_0 \\ -\sin\theta_4 \cos\theta_3 \sin(\theta_1 + \theta_2) + \cos\theta_4 \sin(\theta_1 + \theta_2) \end{bmatrix} \tag{B.2}$$

The Cartesian position of the end-point can then be computed from

$$\mathbf{X}_E = \mathbf{X}_A + l_4 \mathbf{u}_e \tag{B.3}$$

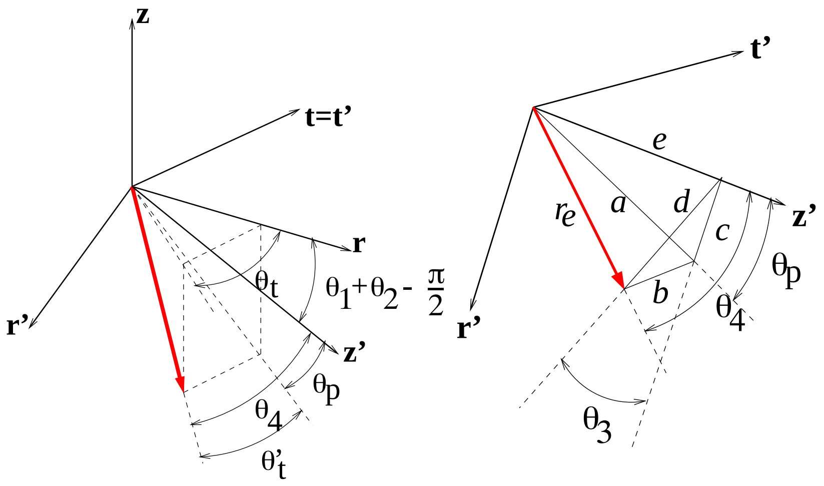

Figure B.1: Geometry for determination of transformation of end-effector orientation vector angles.

Two additional orientation variables are available for specifying the Cartesian orientation. These variables need to be sufficient to determine $\mathbf{u}_e$ without knowledge of the joint angles for the inverse kinematics to solvable. Figure B.1 shows a diagram of the end-effector orientation vector and associated joint angles. The following trigonometric relations can be defined.

$$\begin{array}{llll} \cos\theta_3 = \frac{c}{d} & \cos\theta_4 = \frac{e}{r_e} & \cos\theta_p = \frac{e}{a} & \cos\theta_t' = \frac{a}{r_e} \\ \sin\theta_3 = \frac{b}{d} & \sin\theta_4 = \frac{d}{r_e} & \sin\theta_p = \frac{c}{a} & \sin\theta_t' = \frac{b}{r_e} \\ \tan\theta_3 = \frac{b}{c} & \tan\theta_4 = \frac{d}{e} & \tan\theta_p = \frac{c}{e} & \tan\theta_t' = \frac{b}{a} \end{array} \tag{B.4}$$

Combining a select few of the above equations leads to the following two relations

$$\tan\theta_p = \tan\theta_4 \cos\theta_3 \tag{B.5}$$

$$\sin\theta_t' = \sin\theta_4 \sin\theta_3 \tag{B.6}$$

This gives us a means for specifying the last two orientation variables which are sufficient for solving the inverse kinematics problem.

$$n_1 = \theta_1 + \theta_2 + \tan^{-1}(\tan\theta_4 \cos\theta_3) \tag{B.7}$$

$$n_2 = \sin^{-1}(\sin\theta_4 \sin\theta_3) \tag{B.8}$$

This gives the 5-DOF Cartesian position vector, the first three are x, y, z and the last two components, n_1 and n_2, represent the angle of the end-effector with respect to vertical and the angle "out-of-plane" relative to θ_0. In typical operation, n_2 is usually zero, otherwise, the lower edge of the end-effector plate would be inclined relative to horizontal in the world frame.

B.2 Jacobian

We obtain the Jacobian matrix by computing

$$\mathbf{J} = \begin{bmatrix} \frac{\partial x}{\partial \theta_0} & \frac{\partial x}{\partial \theta_1} & \frac{\partial x}{\partial \theta_2} & \frac{\partial x}{\partial \theta_3} & \frac{\partial x}{\partial \theta_4} \\ \frac{\partial y}{\partial \theta_0} & \frac{\partial y}{\partial \theta_1} & \frac{\partial y}{\partial \theta_2} & \frac{\partial y}{\partial \theta_3} & \frac{\partial y}{\partial \theta_4} \\ \frac{\partial z}{\partial \theta_0} & \frac{\partial z}{\partial \theta_1} & \frac{\partial z}{\partial \theta_2} & \frac{\partial z}{\partial \theta_3} & \frac{\partial z}{\partial \theta_4} \\ \frac{\partial n_1}{\partial \theta_0} & \frac{\partial n_1}{\partial \theta_1} & \frac{\partial n_1}{\partial \theta_2} & \frac{\partial n_1}{\partial \theta_3} & \frac{\partial n_1}{\partial \theta_4} \\ \frac{\partial n_2}{\partial \theta_0} & \frac{\partial n_2}{\partial \theta_1} & \frac{\partial n_2}{\partial \theta_2} & \frac{\partial n_2}{\partial \theta_3} & \frac{\partial n_2}{\partial \theta_4} \end{bmatrix} \tag{B.9}$$

The first row of partial derivatives of x are

$$\frac{\partial x}{\partial \theta_0} = -\left(l_1 s_1 + l_2 s_{12}\right) s_0 + l_4 \left(-\left(s_4 c_3 c_{12} + c_4 s_{12}\right) s_0 - \left(s_4 s_3\right) c_0\right) \tag{B.10}$$

$$\frac{\partial x}{\partial \theta_1} = \left(l_1 c_1 + l_2 c_{12}\right) c_0 + l_4 \left(-\left(s_4 c_3 s_{12} - c_4 c_{12}\right) c_0\right) \tag{B.11}$$

$$\frac{\partial x}{\partial \theta_2} = \left(l_2 c_{12}\right) c_0 + l_4 \left(-\left(s_4 c_3 s_{12} - c_4 c_{12}\right) c_0\right) \tag{B.12}$$

$$\frac{\partial x}{\partial \theta_3} = l_4 \left(-\left(s_4 s_3 c_{12}\right) c_0 - \left(s_4 c_3\right) s_0\right) \tag{B.13}$$

$$\frac{\partial x}{\partial \theta_4} = l_4 \left(\left(c_4 c_3 c_{12} - s_4 s_{12}\right) c_0 - \left(c_4 s_3\right) s_0\right) \tag{B.14}$$

where $s_0 = \sin\theta_0$, $c_0 = \cos\theta_0$, and $s_{12} = \sin(\theta_1 + \theta_2)$ and so on. The second row of partial derivatives of y are

$$\frac{\partial y}{\partial \theta_0} = \left(l_1 s_1 + l_2 s_{12}\right) c_0 + l_4 \left(\left(s_4 c_3 c_{12} + c_4 s_{12}\right) c_0 - \left(s_4 s_3\right) s_0\right) \tag{B.15}$$

$$\frac{\partial y}{\partial \theta_1} = \left(l_1 c_1 + l_2 c_{12}\right) s_0 + l_4 \left(-\left(s_4 c_3 s_{12} - c_4 c_{12}\right) s_0\right) \tag{B.16}$$

$$\frac{\partial y}{\partial \theta_2} = \left(l_2 c_{12}\right) s_0 + l_4 \left(-\left(s_4 c_3 s_{12} - c_4 c_{12}\right) s_0\right) \tag{B.17}$$

$$\frac{\partial y}{\partial \theta_3} = l_4\left(-\left(s_4 s_3 c_{12}\right)s_0 + \left(s_4 c_3\right)c_0\right) \tag{B.18}$$

$$\frac{\partial y}{\partial \theta_4} = l_4\left(\left(c_4 c_3 c_{12} - s_4 s_{12}\right)s_0 + \left(c_4 s_3\right)c_0\right) \tag{B.19}$$

The third row of partial derivatives of z are

$$\frac{\partial z}{\partial \theta_0} = 0 \tag{B.20}$$

$$\frac{\partial z}{\partial \theta_1} = -\left(l_1 s_1 + l_2 s_{12}\right) + l_4\left(-s_4 c_3 c_{12} - c_4 s_{12}\right) \tag{B.21}$$

$$\frac{\partial z}{\partial \theta_2} = -\left(l_2 s_{12}\right) + l_4\left(-s_4 c_3 c_{12} - c_4 s_{12}\right) \tag{B.22}$$

$$\frac{\partial z}{\partial \theta_3} = l_4\left(s_4 s_3 s_{12}\right) \tag{B.23}$$

$$\frac{\partial z}{\partial \theta_4} = l_4\left(-c_4 c_3 s_{12} - s_4 c_{12}\right) \tag{B.24}$$

The fourth row of partial derivatives of n_1 are

$$\frac{\partial n_1}{\partial \theta_0} = 0 \tag{B.25}$$

$$\frac{\partial n_1}{\partial \theta_1} = 1 \tag{B.26}$$

$$\frac{\partial n_1}{\partial \theta_2} = 1 \tag{B.27}$$

$$\frac{\partial n_1}{\partial \theta_3} = \frac{-s_3}{1 + t_4^2 c_3^2} \quad \text{or zero if } c_4 = 0 \tag{B.28}$$

$$\frac{\partial n_1}{\partial \theta_4} = \frac{1}{c_4^2 + s_4^2 c_3^2} \quad \text{or zero if } c_3 = 0 \text{ or one if } c_4 = 0 \tag{B.29}$$

where $t_4 = \tan\theta_4$. The last row of partial derivatives of n_2 are

$$\frac{\partial n_2}{\partial \theta_0} = 0 \tag{B.30}$$

$$\frac{\partial n_2}{\partial \theta_1} = 0 \tag{B.31}$$

$$\frac{\partial n_2}{\partial \theta_2} = 0 \tag{B.32}$$

$$\frac{\partial n_2}{\partial \theta_3} = \frac{c_3}{\sqrt{1 - s_4^2 s_3^2}} \tag{B.33}$$

$$\frac{\partial n_2}{\partial \theta_4} = \frac{c_4}{\sqrt{1 - s_4^2 s_3^2}} \quad \text{or zero if } s_3 = 0 \tag{B.34}$$

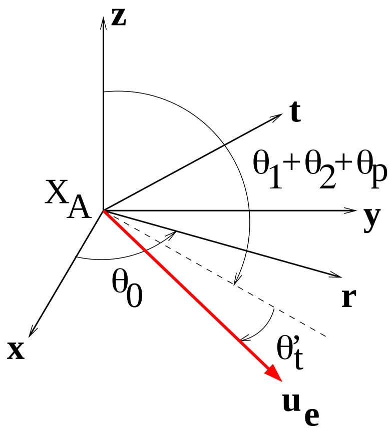

Figure B.2: The orientation of the end effector can be found from $n_1 = \theta_1 + \theta_2 + \theta_p$ and $n_2 = \theta'_t$.

B.3 Inverse Kinematics

First, we need to determine $\mathbf{u}_e$ in the world frame so that we can find $\mathbf{X}_A$ from $\mathbf{X}_E$. In order to do this, we first need to compute the base joint angle θ_0. This follows a couple steps, first we find $\mathbf{u}'_e$, the end-point vector in the base-rotated frame.

$$\mathbf{u}'_e = \begin{bmatrix} c_{n_2} s_{n_1} \\ s_{n_2} \\ c_{n_2} c_{n_1} \end{bmatrix} \tag{B.35}$$

where $c_{n_1} = \cos n_1$ and $s_{n_1} = \sin n_1$, etc.. Next, we need the length and angle to the end-point $\mathbf{X}_A$, and the length of the end-point vector in the xy plane.

$$r_{X_A} = \sqrt{x^2 + y^2} \qquad \theta_{X_A} = \tan^{-1} \frac{y}{x} \tag{B.36}$$

$$r'_e = l_4 \sqrt{c_{n_2}^2 s_{n_1}^2 + s_{n_2}^2} \tag{B.37}$$

Finally, we project n_2 into the xy plane and use the law of sines to ultimately find the base angle θ_0.

$$\theta'_{n_2} = \tan^{-1} \left| \frac{t_{n_2}}{s_{n_1}} \right| \tag{B.38}$$

$$\theta_{off} = \sin^{-1} \left(\frac{r'_e}{r_{X_A}} \sin \theta'_{n_2} \right) \tag{B.39}$$

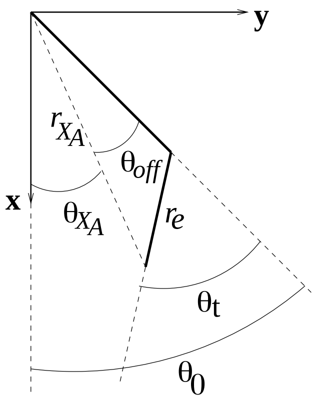

Figure B.3: Given the values for r_{X_A}, θ_{X_A}, and r_e, the value of θ_{off} can be found using the law of sines.

then we have $\theta_0 = \theta_{X_A} + \theta_{off}$. From this, we compute the end-point vector in the world frame as

$$\mathbf{u}_e = \begin{bmatrix} c_{n_2} s_{n_1} c_0 - s_{n_2} s_0 \\ c_{n_2} s_{n_1} s_0 + s_{n_2} c_0 \\ c_{n_2} c_{n_1} \end{bmatrix} \tag{B.40}$$

Thus we can find the coordinates of $\mathbf{X}_A$ in the world frame.

The problem then reduces to a simple 3-DOF manipulator with a given end-point position. Let us label the coordinates of $\mathbf{X}_A$ as x_A, y_A, and z_A and let $r_A = \sqrt{x_A^2 + y_A^2}$ and $u_A = \sqrt{r_A^2 + z_A^2}$. The solution for the joint angles is then

$$\theta_2 = \cos^{-1}\left(\frac{u_A^2 - l_1^2 - l_2^2}{2 l_1 l_2}\right) \tag{B.41}$$

$$\theta_1 = \frac{\pi}{2} - \tan^{-1}\left(\frac{z_A}{r_A}\right) - \sin^{-1}\left(\frac{l_2 \sin\theta_2}{u_A}\right) \tag{B.42}$$

$$\theta_0 = \tan^{-1}\left(\frac{y_A}{x_A}\right) \tag{B.43}$$

Now that we know the first three joint values, we can compute the last two orientation joint values from $\theta_p = n_1 - \theta_1 - \theta_2$ and $\theta_t' = n_2$.

$$\theta_3 = \tan^{-1}\left(\frac{\sin\theta_t'}{\cos\theta_t' \sin\theta_p}\right) \tag{B.44}$$

$$\theta_4 = \tan^{-1}\left(\frac{\sqrt{\sin^2\theta_t' + \cos^2\theta_t' \sin^2\theta_p}}{\cos\theta_t' \cos\theta_p}\right) \tag{B.45}$$

Additional range and sign checks need to be done. If $\theta_p < 0$ then $\theta_4 = -\theta_4$ and if $\theta_p < 0$ and $\theta_3 > 0$ then $\theta_3 = \theta_3 - \pi$ otherwise $\theta_3 = \theta_3 - \pi$.

B.4 Arm Transformations

Transformation matrices must be used to convert from joint space to motor space and vice versa. These matrices account for joint signs, the elbow differential, and the coupling between the elbow and shoulder joint as a result of the routing of the elbow coupling through the shoulder pulleys. The transformation from joint to motor values is

$$\mathbf{T}_{mtr}^{jnt} = \begin{bmatrix} s_0 & 0 & 0 & 0 & 0 \\ 0 & s_1 & 0 & 0 & 0 \\ 0 & -s_2 r_c & s_2 & \frac{1}{2} r_d s_3 & 0 \\ 0 & s_2 r_c & -s_2 & -\frac{1}{2} r_d s_3 & 0 \\ 0 & 0 & 0 & 0 & s_4 \end{bmatrix} \tag{B.46}$$

and the inverse transformation from motor to joint values is

$$\mathbf{T}_{jnt}^{mtr} = \begin{bmatrix} s_0 & 0 & 0 & 0 & 0 \\ 0 & s_1 & 0 & 0 & 0 \\ 0 & s_2 r_c & \frac{1}{2} s_2 & -\frac{1}{2} s_3 & 0 \\ 0 & 0 & -\frac{s_2}{r_d} & -\frac{s_3}{r_d} & 0 \\ 0 & 0 & 0 & 0 & s_4 \end{bmatrix} \tag{B.47}$$

The s_0 through s_4 are either +1 or -1 and represent the joint sign for each, r_c is the coupling ratio between the elbow and shoulder, and r_d is the gear ratio of the differential. For the final arm configuration, $r_c = 0.58$ and $r_d = 2.0$.

Appendix C

Model Prediction Tables

In this Appendix, we provide a listing of the predictions from the various models we have used. They are tabulated for the discrete values at which the numerical UB/LB solutions were computed. All predictions are computed directly, with the exception of the model from Caquot and Kerisel, which was interpolated from their tabulated values. A reminder of the notation used here:

α	tool angle
ϕ	internal friction angle
δ	interface friction angle

Tabulated values are passive - active earth pressure coefficients,

$$K_P - K_A = \frac{2}{\gamma L^2} \left(F_P - F_A\right) \tag{C.1}$$

The logarithmic spiral model does not have an explicit active earth pressure counterparts, therefore we have used the active from Caquot and Kerisel since it is likely closest in form. The choice of active model is somewhat minor. The contribution of the active portion is can reach up to around 15%, typically much lower.

Table C.1: Earth Pressure Coefficient Predictions for $\boldsymbol{\alpha} = \mathbf{70^\circ}$

ϕ	δ	Coulomb	Log Spiral	Chen UB	Caquot	Num. UB	Num. LB
25°	0°	1.504	1.552	1.502	1.333	1.677	1.450
	5°	1.697	1.702	1.693	1.600	1.842	1.652
	10°	1.908	1.891	1.900	1.870	2.021	1.854
	15°	2.147	2.137	2.132	2.162	2.217	2.075
	20°	2.425	2.456	2.377	2.428	2.460	2.292
	25°	2.759	2.876	2.624	2.557	2.692	2.520
30°	0°	1.821	1.895	1.820	1.568	2.027	1.760
	5°	2.055	2.077	2.054	1.912	2.225	2.009
	10°	2.321	2.311	2.316	2.262	2.441	2.258
	15°	2.633	2.619	2.623	2.645	2.703	2.552
	20°	3.007	3.038	2.970	3.066	3.048	2.868
	25°	3.469	3.593	3.346	3.427	3.431	3.191
	30°	4.055	4.231	3.737	3.610	3.792	3.544
35°	0°	2.171	2.283	2.172	1.796	2.404	2.101
	5°	2.462	2.509	2.463	2.229	2.636	2.414
	10°	2.804	2.804	2.801	2.691	2.911	2.727
	15°	3.214	3.200	3.208	3.210	3.275	3.117
	20°	3.722	3.749	3.692	3.784	3.772	3.558
	25°	4.368	4.505	4.245	4.418	4.363	4.021
	30°	5.214	5.393	4.863	4.979	4.945	4.569
40°	0°	2.571	2.737	2.573	2.012	2.799	2.485
	5°	2.939	3.024	2.943	2.570	3.086	2.885
	10°	3.383	3.403	3.384	3.187	3.466	3.285
	15°	3.933	3.920	3.928	3.890	3.985	3.816
	20°	4.633	4.658	4.607	4.685	4.726	4.425
	25°	5.552	5.705	5.419	5.618	5.615	5.106
	30°	6.802	6.977	6.372	6.644	6.519	5.861
45°	0°	3.041	3.285	3.044	2.227	3.222	2.930
	5°	3.514	3.654	3.520	2.929	3.615	3.449
	10°	4.101	4.151	4.105	3.761	4.152	3.969
	15°	4.850	4.842	4.847	4.739	4.920	4.690
	20°	5.834	5.858	5.812	5.905	6.051	5.548
	25°	7.175	7.351	7.019	7.270	7.339	6.552
	30°	9.083	9.238	8.505	8.896	8.763	7.712
50°	0°	3.608	3.972	3.612	2.413	3.728	3.447
	5°	4.228	4.457	4.237	3.281	4.274	4.139
	10°	5.019	5.120	5.027	4.415	5.063	4.830
	15°	6.060	6.066	6.060	5.789	6.268	5.820
	20°	7.482	7.506	7.464	7.501	7.923	7.056
	25°	9.509	9.719	9.308	9.574	9.857	8.564
	30°	12.563	12.640	11.698	12.153	12.146	10.388

Table C.2: Earth Pressure Coefficient Predictions for $\boldsymbol{\alpha = 75^\circ}$

ϕ	δ	Coulomb	Log Spiral	Chen UB	Caquot	Num. UB	Num. LB
25°	0°	1.626	1.661	1.626	1.502	1.818	1.587
	5°	1.857	1.852	1.853	1.803	2.015	1.828
	10°	2.113	2.099	2.106	2.107	2.234	2.069
	15°	2.410	2.427	2.383	2.436	2.496	2.327
	20°	2.763	2.853	2.676	2.736	2.782	2.590
	25°	3.195	3.334	2.971	2.881	3.053	2.851
30°	0°	2.000	2.054	2.000	1.800	2.222	1.959
	5°	2.285	2.291	2.283	2.195	2.460	2.264
	10°	2.616	2.602	2.611	2.597	2.749	2.569
	15°	3.011	3.024	2.990	3.037	3.121	2.920
	20°	3.496	3.596	3.411	3.522	3.549	3.298
	25°	4.110	4.254	3.871	3.937	3.994	3.700
	30°	4.912	4.989	4.350	4.147	4.431	4.118
35°	0°	2.424	2.507	2.426	2.125	2.652	2.382
	5°	2.786	2.807	2.786	2.637	2.960	2.775
	10°	3.218	3.207	3.214	3.184	3.358	3.167
	15°	3.751	3.763	3.734	3.798	3.894	3.648
	20°	4.427	4.537	4.339	4.479	4.522	4.179
	25°	5.312	5.462	5.032	5.228	5.213	4.777
	30°	6.512	6.525	5.806	5.893	5.947	5.460
40°	0°	2.921	3.046	2.924	2.458	3.136	2.875
	5°	3.387	3.431	3.390	3.139	3.551	3.390
	10°	3.964	3.957	3.961	3.894	4.132	3.906
	15°	4.696	4.707	4.681	4.753	4.914	4.576
	20°	5.656	5.781	5.555	5.726	5.839	5.340
	25°	6.961	7.109	6.602	6.866	6.900	6.211
	30°	8.816	8.695	7.833	8.121	8.079	7.244
45°	0°	3.519	3.707	3.524	2.815	3.706	3.469
	5°	4.133	4.213	4.138	3.703	4.307	4.159
	10°	4.915	4.919	4.914	4.755	5.187	4.849
	15°	5.943	5.955	5.930	5.992	6.306	5.792
	20°	7.343	7.493	7.220	7.466	7.714	6.908
	25°	9.337	9.465	8.833	9.193	9.348	8.223
	30°	12.337	11.920	10.824	11.251	11.286	9.750
50°	0°	4.261	4.547	4.268	3.202	4.437	4.197
	5°	5.087	5.226	5.096	4.355	5.352	5.144
	10°	6.174	6.195	6.176	5.859	6.646	6.092
	15°	7.658	7.670	7.647	7.684	8.326	7.432
	20°	9.774	9.958	9.608	9.956	10.470	9.115
	25°	12.966	13.022	12.185	12.709	13.094	11.182
	30°	18.149	17.016	15.532	16.134	16.417	13.785

Table C.3: Earth Pressure Coefficient Predictions for $\boldsymbol{\alpha = 80^\circ}$

ϕ	δ	Coulomb	Log Spiral	Chen UB	Caquot	Num. UB	Num. LB
25°	0°	1.757	1.778	1.757	1.673	1.937	1.707
	5°	2.031	2.022	2.028	2.007	2.166	1.986
	10°	2.343	2.347	2.332	2.345	2.425	2.265
	15°	2.711	2.780	2.658	2.711	2.754	2.559
	20°	3.160	3.272	3.004	3.044	3.082	2.867
	25°	3.725	3.812	3.355	3.204	3.391	3.158
30°	0°	2.197	2.229	2.198	2.061	2.393	2.141
	5°	2.544	2.538	2.542	2.512	2.671	2.500
	10°	2.955	2.957	2.945	2.971	3.035	2.860
	15°	3.457	3.531	3.403	3.474	3.520	3.268
	20°	4.091	4.212	3.914	4.028	4.030	3.706
	25°	4.918	4.976	4.472	4.503	4.535	4.187
	30°	6.035	5.825	5.054	4.743	5.047	4.668
35°	0°	2.709	2.758	2.711	2.498	2.874	2.644
	5°	3.159	3.157	3.157	3.100	3.257	3.117
	10°	3.710	3.712	3.702	3.743	3.783	3.590
	15°	4.407	4.491	4.347	4.465	4.497	4.160
	20°	5.318	5.442	5.099	5.266	5.259	4.781
	25°	6.554	6.555	5.962	6.147	6.045	5.515
	30°	8.305	7.827	6.926	6.929	6.933	6.332
40°	0°	3.325	3.401	3.329	2.988	3.446	3.247
	5°	3.920	3.927	3.920	3.816	3.994	3.880
	10°	4.675	4.677	4.668	4.734	4.784	4.513
	15°	5.662	5.763	5.590	5.777	5.839	5.322
	20°	7.005	7.128	6.710	6.959	6.949	6.242
	25°	8.913	8.788	8.055	8.345	8.178	7.305
	30°	11.781	10.757	9.636	9.870	9.635	8.624
45°	0°	4.088	4.204	4.094	3.573	4.165	3.993
	5°	4.894	4.912	4.895	4.700	4.983	4.857
	10°	5.950	5.953	5.944	6.035	6.222	5.722
	15°	7.390	7.514	7.296	7.605	7.705	6.890
	20°	9.440	9.546	9.008	9.477	9.391	8.269
	25°	12.527	12.114	11.158	11.669	11.372	9.900
	30°	17.535	15.294	13.812	14.281	13.840	11.800
50°	0°	5.064	5.246	5.073	4.252	5.130	4.939
	5°	6.182	6.223	6.185	5.783	6.432	6.149
	10°	7.706	7.709	7.701	7.781	8.257	7.359
	15°	9.882	10.040	9.748	10.204	10.425	9.058
	20°	13.166	13.205	12.470	13.222	13.065	11.201
	25°	18.504	17.392	16.061	16.878	16.396	13.841
	30°	28.137	22.826	20.732	21.426	20.790	17.250

Table C.4: Earth Pressure Coefficient Predictions for $\boldsymbol{\alpha = 85^\circ}$

ϕ	δ	Coulomb	Log Spiral	Chen UB	Caquot	Num. UB	Num. LB
25°	0°	1.900	1.906	1.900	1.861	2.078	1.805
	5°	2.226	2.222	2.223	2.231	2.361	2.151
	10°	2.606	2.650	2.577	2.606	2.700	2.497
	15°	3.066	3.155	2.961	3.011	3.080	2.847
	20°	3.641	3.712	3.368	3.380	3.457	3.206
	25°	4.387	4.317	3.782	3.558	3.818	3.547
30°	0°	2.416	2.427	2.417	2.349	2.605	2.289
	5°	2.840	2.837	2.837	2.862	2.987	2.747
	10°	3.354	3.405	3.322	3.384	3.477	3.205
	15°	3.999	4.093	3.872	3.956	4.040	3.707
	20°	4.838	4.887	4.487	4.586	4.627	4.243
	25°	5.972	5.773	5.161	5.125	5.241	4.819
	30°	7.573	6.753	5.864	5.397	5.840	5.389
35°	0°	3.036	3.053	3.037	2.930	3.215	2.863
	5°	3.599	3.596	3.597	3.633	3.775	3.477
	10°	4.308	4.370	4.270	4.386	4.486	4.091
	15°	5.232	5.332	5.065	5.231	5.309	4.817
	20°	6.485	6.477	5.996	6.168	6.208	5.612
	25°	8.259	7.812	7.066	7.200	7.202	6.525
	30°	10.920	9.332	8.261	8.115	8.270	7.520
40°	0°	3.803	3.829	3.805	3.613	3.994	3.563
	5°	4.569	4.567	4.567	4.613	4.828	4.400
	10°	5.571	5.650	5.522	5.721	5.856	5.237
	15°	6.932	7.033	6.695	6.982	7.086	6.300
	20°	8.865	8.738	8.126	8.410	8.468	7.509
	25°	11.771	10.801	9.846	10.084	10.095	8.920
	30°	16.476	13.241	11.868	11.927	11.955	10.581
45°	0°	4.783	4.824	4.786	4.503	5.076	4.443
	5°	5.854	5.852	5.853	5.922	6.287	5.609
	10°	7.312	7.414	7.243	7.603	7.828	6.774
	15°	9.388	9.476	9.026	9.580	9.678	8.360
	20°	12.517	12.118	11.296	11.937	11.897	10.232
	25°	17.596	15.445	14.150	14.698	14.640	12.498
	30°	26.750	19.550	17.674	17.986	18.056	15.202
50°	0°	6.082	6.150	6.087	5.637	6.613	5.577
	5°	7.625	7.624	7.624	7.664	8.403	7.251
	10°	9.828	9.963	9.724	10.310	10.739	8.924
	15°	13.155	13.182	12.546	13.520	13.653	11.348
	20°	18.568	17.498	16.320	17.518	17.409	14.351
	25°	28.351	23.194	21.314	22.360	22.372	18.160
	30°	49.094	30.564	27.807	28.384	28.038	23.015

Table C.5: Earth Pressure Coefficient Predictions for $\boldsymbol{\alpha = 90^\circ}$

ϕ	δ	Coulomb	Log Spiral	Chen UB	Caquot	Num. UB	Num. LB
25°	0°	2.058	2.058	2.058	2.056	2.190	1.876
	5°	2.447	2.472	2.434	2.464	2.525	2.286
	10°	2.913	2.977	2.846	2.875	2.941	2.696
	15°	3.492	3.549	3.294	3.321	3.367	3.099
	20°	4.239	4.177	3.771	3.727	3.790	3.504
	25°	5.244	4.857	4.258	3.923	4.197	3.892
30°	0°	2.667	2.667	2.667	2.665	2.782	2.405
	5°	3.186	3.219	3.170	3.245	3.265	2.957
	10°	3.835	3.906	3.748	3.835	3.878	3.509
	15°	4.675	4.709	4.405	4.481	4.512	4.100
	20°	5.808	5.631	5.144	5.193	5.169	4.729
	25°	7.408	6.658	5.953	5.804	5.886	5.394
	30°	9.798	7.793	6.800	6.112	6.565	6.047
35°	0°	3.419	3.419	3.419	3.421	3.516	3.042
	5°	4.131	4.175	4.109	4.241	4.249	3.793
	10°	5.056	5.135	4.933	5.118	5.141	4.543
	15°	6.307	6.292	5.912	6.102	6.062	5.419
	20°	8.079	7.665	7.059	7.193	7.088	6.379
	25°	10.735	9.261	8.380	8.395	8.281	7.463
	30°	15.027	11.077	9.855	9.462	9.517	8.625
40°	0°	4.381	4.382	4.381	4.368	4.495	3.832
	5°	5.383	5.443	5.352	5.574	5.612	4.866
	10°	6.742	6.825	6.557	6.911	6.867	5.900
	15°	8.671	8.548	8.047	8.432	8.260	7.210
	20°	11.572	10.667	9.869	10.154	9.901	8.696
	25°	16.273	13.223	12.061	12.174	11.911	10.444
	30°	24.731	16.241	14.636	14.397	14.159	12.432
45°	0°	5.657	5.656	5.657	5.657	5.934	4.837
	5°	7.112	7.193	7.064	7.438	7.532	6.294
	10°	9.183	9.256	8.886	9.546	9.360	7.751
	15°	12.306	11.931	11.235	12.026	11.559	9.744
	20°	17.379	15.350	14.237	14.983	14.293	12.095
	25°	26.536	19.646	18.017	18.447	17.777	14.980
	30°	45.925	24.933	22.678	22.572	22.119	18.469
50°	0°	7.416	7.416	7.416	7.446	8.038	6.148
	5°	9.613	9.726	9.535	10.121	10.303	8.272
	10°	12.933	12.951	12.410	13.613	13.129	10.397
	15°	18.340	17.329	16.303	17.849	16.766	13.529
	20°	28.124	23.196	21.532	23.125	21.613	17.371
	25°	48.899	30.923	28.458	29.515	28.180	22.326
	30°	107.223	40.891	37.456	37.465	35.068	28.596

Table C.6: Earth Pressure Coefficient Predictions for $\boldsymbol{\alpha = 95^\circ}$

ϕ	δ	Coulomb	Log Spiral	Chen UB	Caquot	Num. UB	Num. LB
25°	0°	2.237	2.249	2.233	2.271	2.423	2.023
	5°	2.704	2.749	2.665	2.718	2.826	2.495
	10°	3.280	3.320	3.142	3.170	3.281	2.968
	15°	4.019	3.966	3.663	3.659	3.758	3.431
	20°	5.010	4.672	4.219	4.105	4.240	3.900
	25°	6.401	5.436	4.790	4.319	4.703	4.360
30°	0°	2.958	2.978	2.952	3.020	3.174	2.636
	5°	3.602	3.655	3.546	3.673	3.752	3.292
	10°	4.432	4.455	4.231	4.339	4.428	3.949
	15°	5.548	5.387	5.016	5.067	5.159	4.643
	20°	7.123	6.455	5.899	5.871	5.946	5.388
	25°	9.475	7.643	6.868	6.559	6.790	6.173
	30°	13.262	8.956	7.881	6.906	7.626	6.949
35°	0°	3.880	3.910	3.870	4.004	4.152	3.398
	5°	4.793	4.855	4.707	4.959	5.009	4.322
	10°	6.025	6.007	5.713	5.981	6.012	5.246
	15°	7.768	7.393	6.913	7.129	7.133	6.298
	20°	10.381	9.035	8.325	8.400	8.410	7.466
	25°	14.605	10.940	9.950	9.802	9.891	8.783
	30°	22.186	13.107	11.763	11.046	11.445	10.184
40°	0°	5.103	5.146	5.086	5.278	5.481	4.379
	5°	6.440	6.507	6.301	6.732	6.770	5.698
	10°	8.337	8.224	7.821	8.343	8.273	7.017
	15°	11.190	10.362	9.709	10.177	10.066	8.642
	20°	15.817	12.986	12.023	12.252	12.205	10.508
	25°	24.150	16.146	14.808	14.687	14.821	12.700
	30°	41.763	19.873	18.076	17.368	17.775	14.585
45°	0°	6.794	6.857	6.763	7.123	7.411	5.678
	5°	8.830	8.891	8.592	9.360	9.349	7.610
	10°	11.900	11.556	10.978	12.009	11.701	9.541
	15°	16.892	15.012	14.072	15.125	14.704	12.117
	20°	25.911	19.425	18.035	18.841	18.513	15.195
	25°	45.039	24.956	23.025	23.192	23.346	18.949
	30°	98.658	31.752	29.171	28.376	29.233	23.223
50°	0°	9.243	9.336	9.188	9.855	10.315	7.467
	5°	12.506	12.519	12.068	13.391	13.318	10.395
	10°	17.826	16.890	16.012	18.006	17.240	13.323
	15°	27.462	22.832	21.385	23.603	22.638	17.554
	20°	47.956	30.790	28.618	30.576	30.191	22.846
	25°	105.584	41.246	38.200	39.021	40.433	29.061
	30°	411.594	54.700	50.633	49.528	53.257	36.024

Table C.7: Earth Pressure Coefficient Predictions for $\boldsymbol{\alpha = 100^\circ}$

ϕ	δ	Coulomb	Log Spiral	Chen UB	Caquot	Num. UB	Num. LB
25°	0°	2.443	2.474	2.425	2.501	2.612	2.133
	5°	3.010	3.038	2.919	2.988	3.076	2.660
	10°	3.731	3.681	3.469	3.481	3.560	3.186
	15°	4.695	4.406	4.072	4.015	4.079	3.700
	20°	6.045	5.199	4.720	4.503	4.611	4.225
	25°	8.052	6.059	5.385	4.737	5.121	4.747
30°	0°	3.305	3.345	3.273	3.417	3.507	2.819
	5°	4.115	4.130	3.972	4.153	4.167	3.567
	10°	5.200	5.057	4.783	4.901	4.894	4.314
	15°	6.726	6.135	5.716	5.721	5.708	5.098
	20°	9.006	7.369	6.769	6.625	6.608	5.944
	25°	12.678	8.742	7.924	7.400	7.563	6.833
	30°	19.247	10.264	9.133	7.792	8.539	7.718
35°	0°	4.450	4.499	4.394	4.660	4.706	3.692
	5°	5.646	5.629	5.409	5.766	5.670	4.770
	10°	7.336	7.005	6.636	6.950	6.765	5.848
	15°	9.868	8.660	8.104	8.279	8.064	7.054
	20°	13.962	10.617	9.834	9.753	9.564	8.406
	25°	21.317	12.887	11.827	11.378	11.302	9.929
	30°	36.826	15.470	14.048	12.821	13.139	11.539
40°	0°	6.035	6.091	5.936	6.399	6.353	4.841
	5°	7.873	7.773	7.459	8.155	7.789	6.417
	10°	10.637	9.897	9.375	10.101	9.510	7.993
	15°	15.120	12.542	11.762	12.316	11.664	9.898
	20°	23.203	15.783	14.694	14.824	14.254	12.104
	25°	40.313	19.680	18.222	17.765	17.415	14.692
	30°	88.186	24.275	22.356	21.004	21.010	16.451
45°	0°	8.338	8.388	8.156	8.970	8.729	6.407
	5°	11.311	11.003	10.537	11.780	10.967	8.769
	10°	16.148	14.440	13.664	15.108	13.793	11.131
	15°	24.896	18.896	17.734	19.023	17.529	14.233
	20°	43.475	24.578	22.954	23.691	22.322	17.969
	25°	95.645	31.685	29.525	29.158	28.389	22.508
	30°	372.252	40.405	37.605	35.671	35.685	27.478
50°	0°	11.887	11.897	11.530	13.068	12.366	8.632
	5°	17.040	16.191	15.459	17.747	16.038	12.295
	10°	26.386	22.112	20.880	23.857	20.962	15.957
	15°	46.291	30.170	28.291	31.266	27.986	21.190
	20°	102.360	40.946	38.281	40.496	38.047	27.805
	25°	400.660	55.068	51.506	51.675	51.698	35.147
	30°			68.639	65.584	70.082	42.676

Appendix D

Direct Shear Results

In this Appendix, we include the results from our low stress direct shear tests and a few tests at higher, more typical loads. For each soil we have tested at 0.4473, 0.921, 2.921, and 5.891 kg using the low stress assembly and at 17.545, 27.545, and 47.545 kg at high stress. The area over which these loads are applied is 35.6 cm^2 (5.5 in^2). The load cell has a sensing range of 0-500 lbs and a small bias which was removed. At low readings, there is some noise present in the measurements. For the low stress cases, a windowed average over three data points is used to filter out the noise. The displacement is generated via a motor, maintaining a constant strain rate of 0.0021 cm/sec.

There is some friction inherent in the system. Typically, the small contribution to measured shear force is negligible when using large loads. For the low stress measurements, this friction becomes more significant. The system is run without any soil in the shear box in both the forward and reverse direction to obtain a friction hysteresis loop. Figure D.1 shows the measured force versus displacement. Half of the magnitude of this loop is subtracted from the subsequent experimental data. This typically results in a reduction of the estimated friction angle of roughly half to a full degree in the lowest stress case.

In the following figures, the estimated friction angle and the dilation of the soil are plotted against the horizontal displacement. The peak angle for each test is used as the measured friction angle. Four tests are conducted for each of the low stress cases and the closest three are kept and plotted. For the higher loads, only a single run is done for each. The average densities and standard deviations in g/cc for the samples tested were: loose Ticino - 1.450, 0.026, Nevada Fine - 1.456, 0.022, dense Ticino - 1.521, 0.012, and glass beads - 1.451, 0.013. The dense

Figure D.1: Direct shear results with no sand, showing the friction hysteresis loop of the test assembly. Half the magnitude is subtracted from subsequent tests.

Ticino was prepared using simple tamping, since no other means was readily available. For denser samples, we would expect the measured friction angles to be higher.

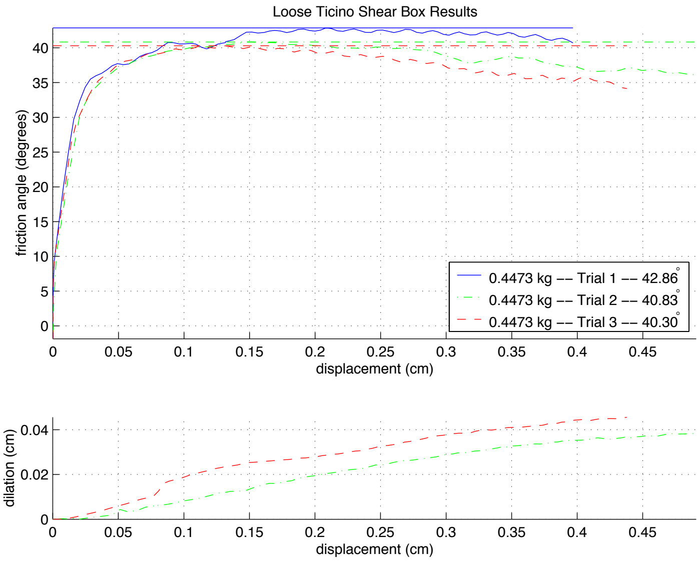

Figure D.2: Direct shear results for three trials of loose Ticino with 0.4473 kg load.

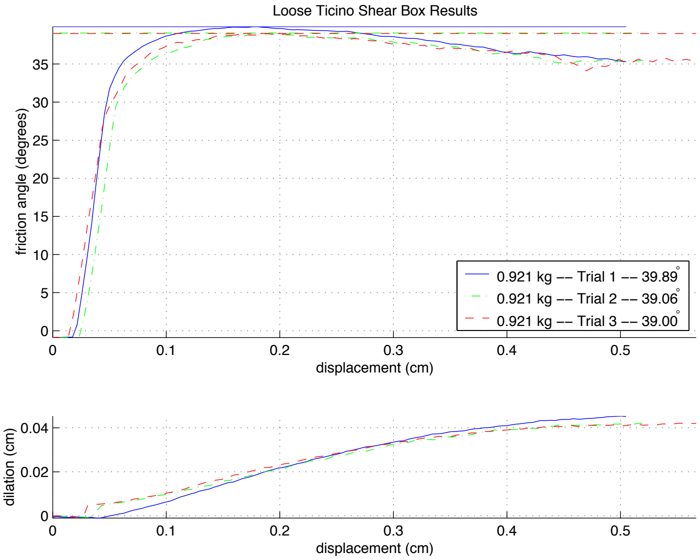

Figure D.3: Direct shear results for three trials of loose Ticino with 0.921 kg load.

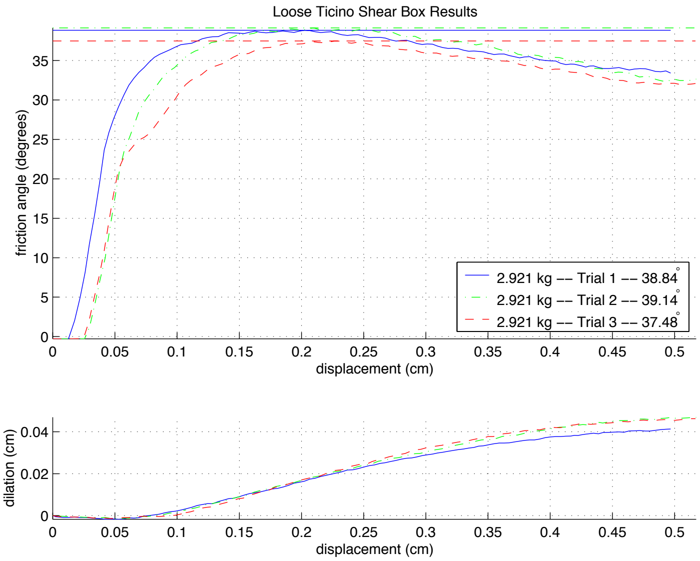

Figure D.4: Direct shear results for three trials of loose Ticino with 2.921 kg load.

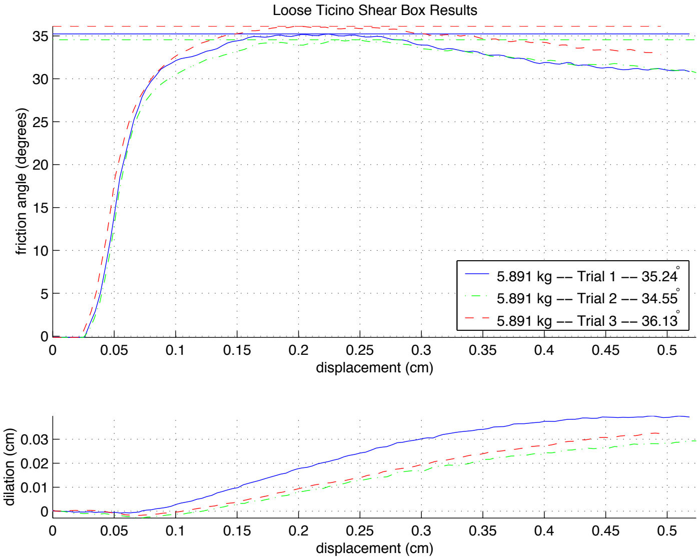

Figure D.5: Direct shear results for three trials of loose Ticino with 5.891 kg load.

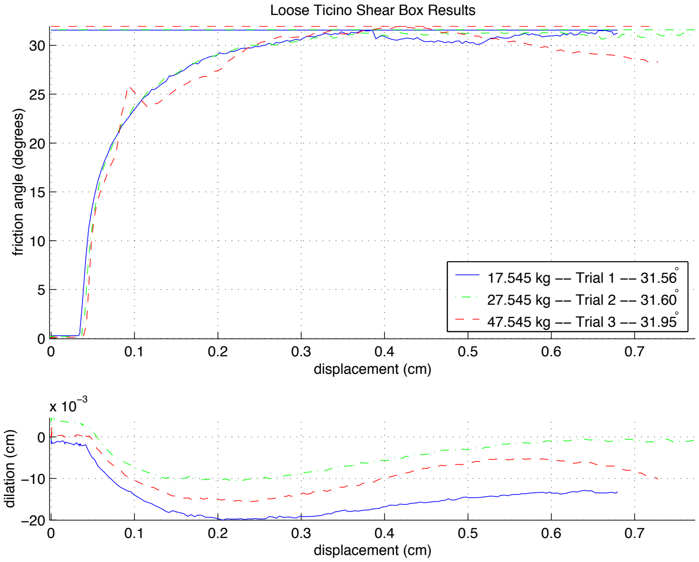

Figure D.6: Direct shear results for three trials of loose Ticino with high loads.

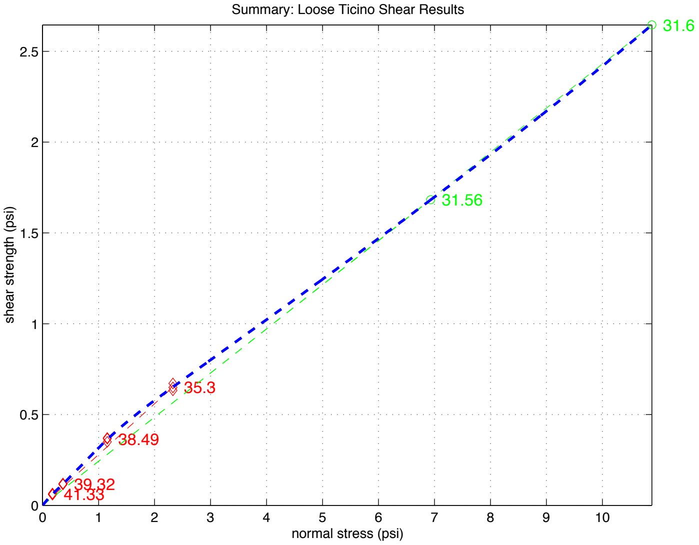

Figure D.7: Compiled friction angle measurements for loose Ticino sand.

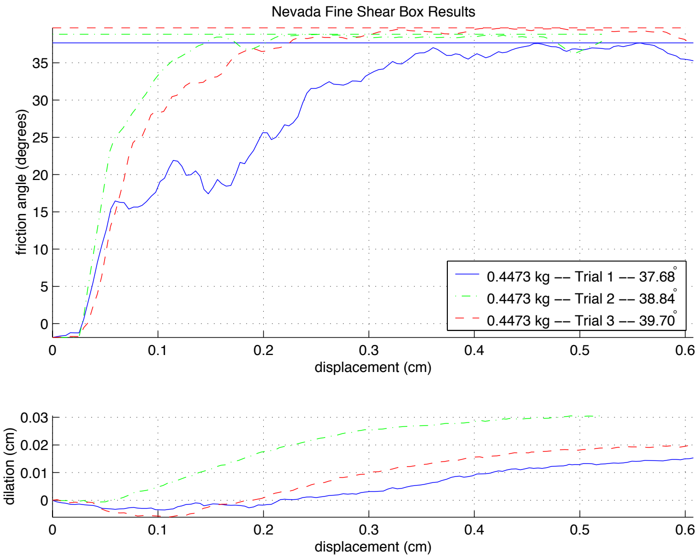

Figure D.8: Direct shear results for three trials of loose Nevada with 0.4473 kg load.

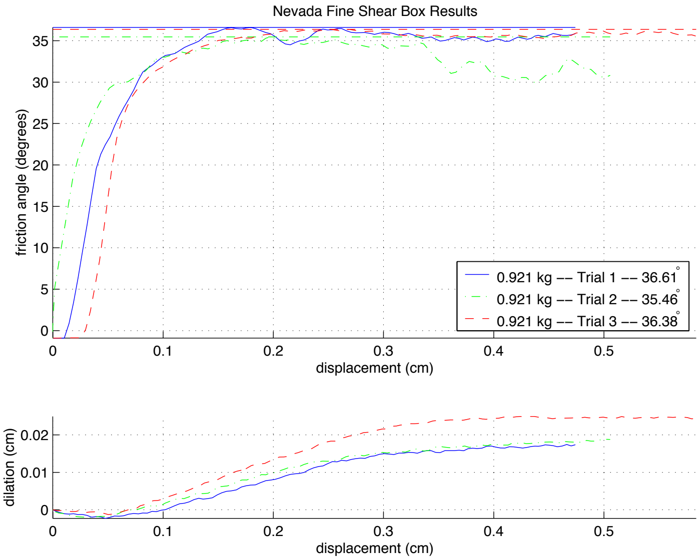

Figure D.9: Direct shear results for three trials of loose Nevada with 0.921 kg load.

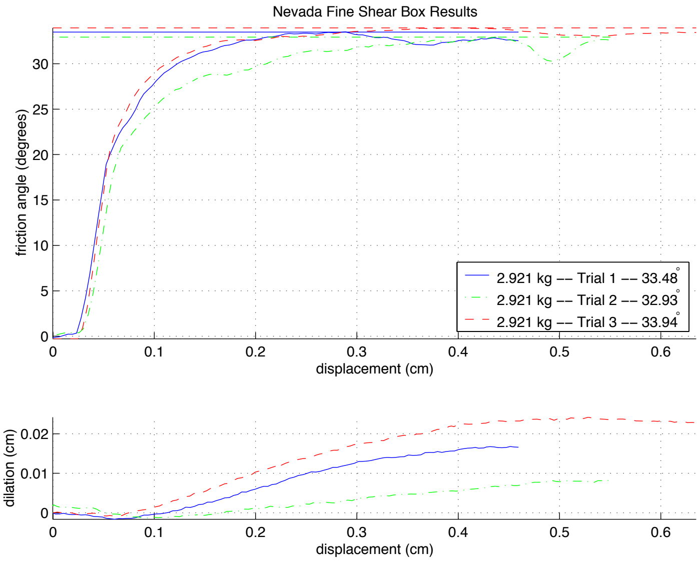

Figure D.10: Direct shear results for three trials of loose Nevada with 2.921 kg load.

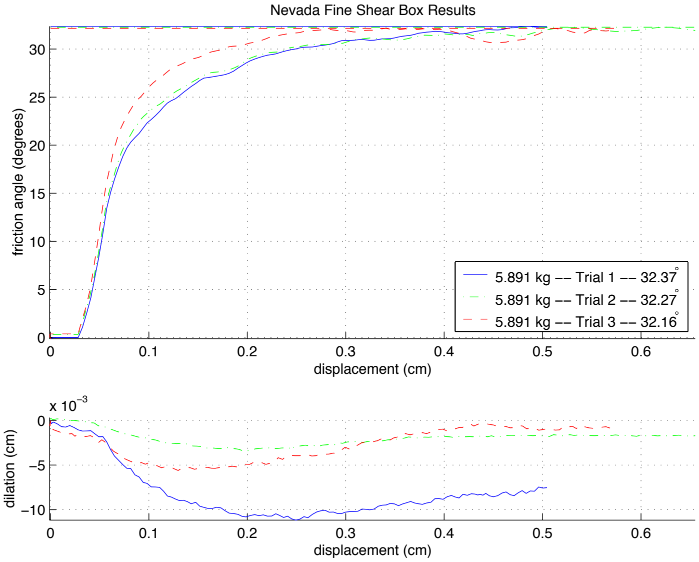

Figure D.11: Direct shear results for three trials of loose Nevada with 5.891 kg load.

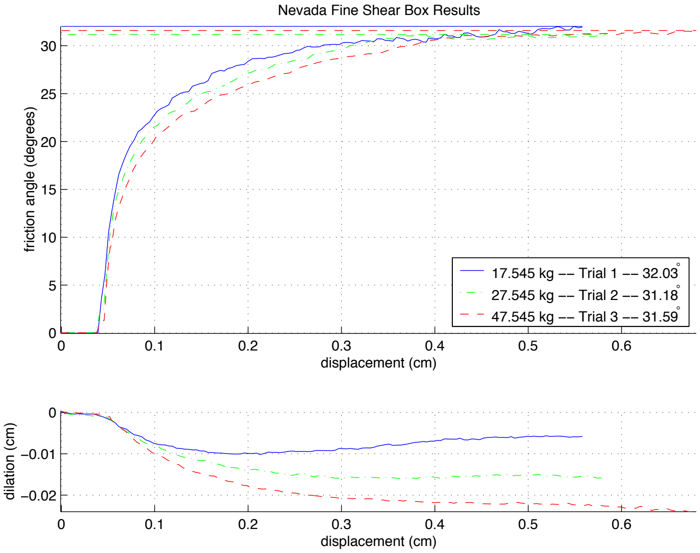

Figure D.12: Direct shear results for three trials of loose Nevada with high loads.

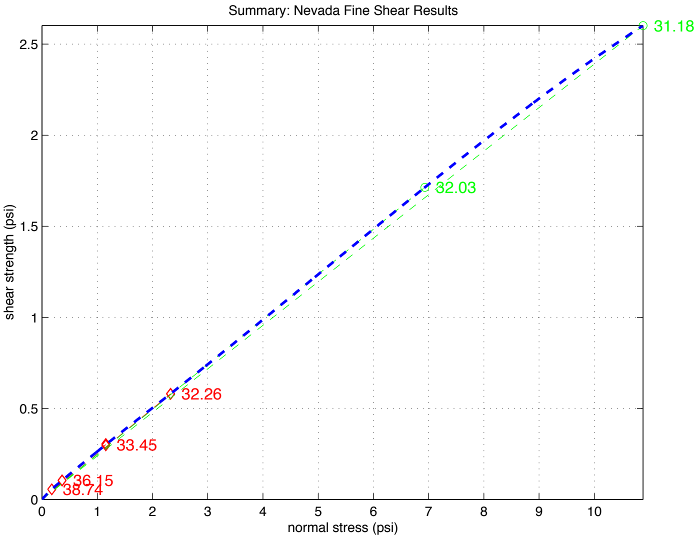

Figure D.13: Compiled friction angle measurements for loose Nevada Fine sand.

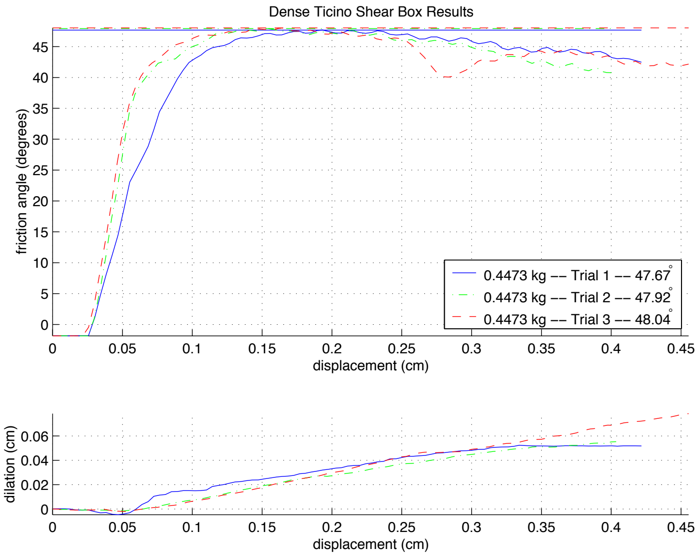

Figure D.14: Direct shear results for three trials of dense Ticino with 0.4473 kg load.

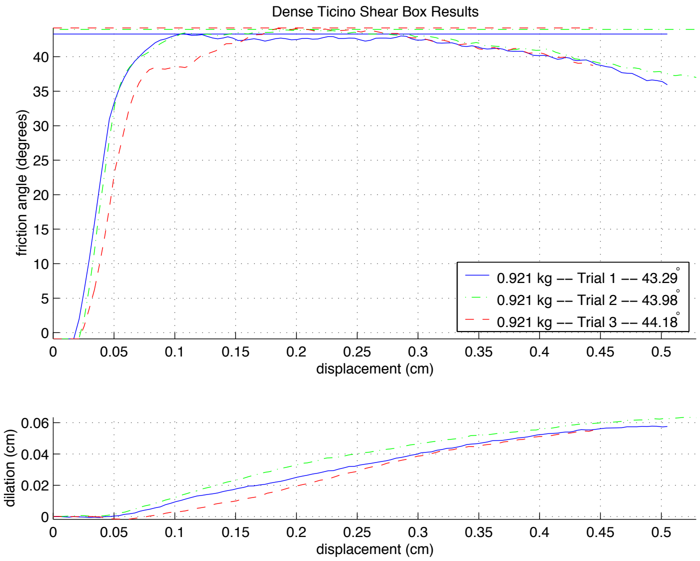

Figure D.15: Direct shear results for three trials of dense Ticino with 0.921 kg load.

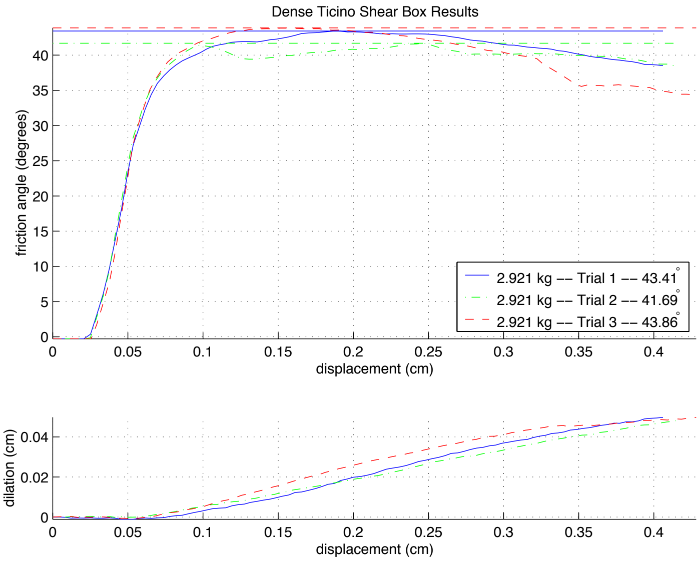

Figure D.16: Direct shear results for three trials of dense Ticino with 2.921 kg load.

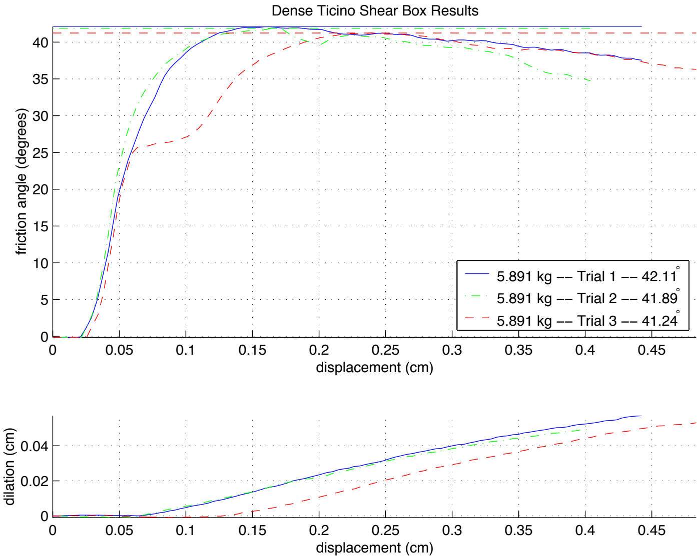

Figure D.17: Direct shear results for three trials of dense Ticino with 5.891 kg load.

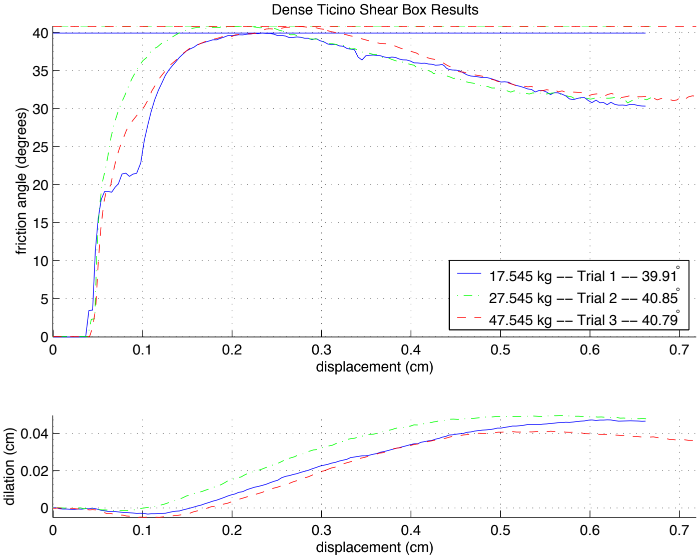

Figure D.18: Direct shear results for three trials of dense Ticino sand at high loads.

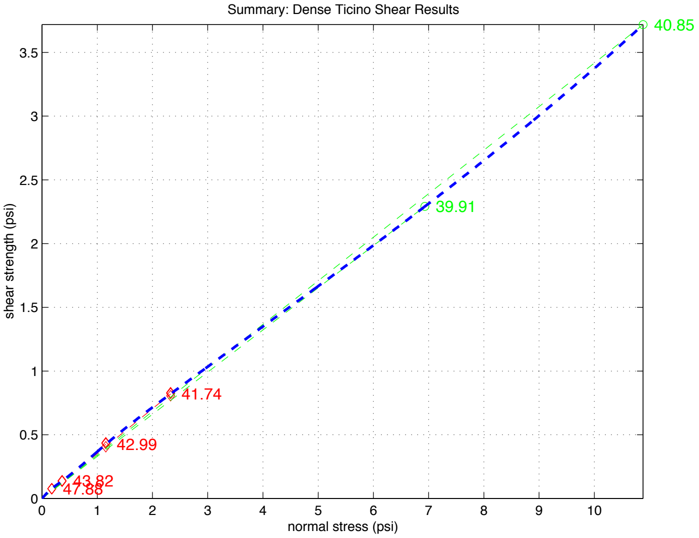

Figure D.19: Compiled friction angle measurements for dense Ticino sand.

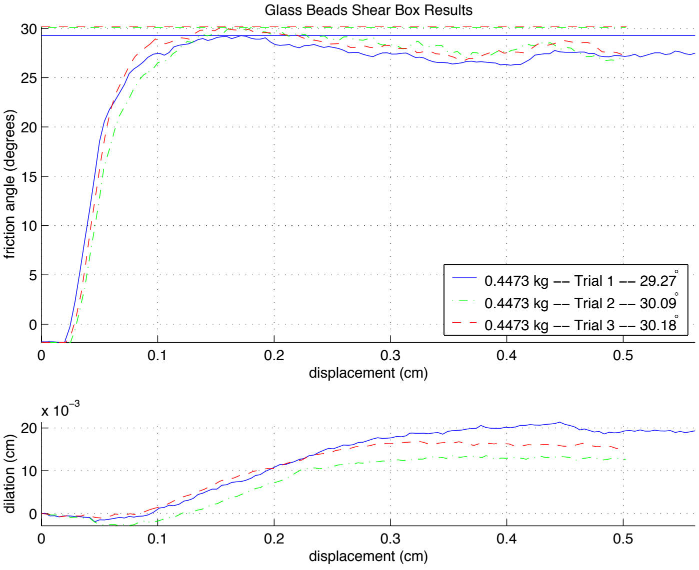

Figure D.20: Direct shear results for three trials of dense Ticino with 0.4473 kg load.

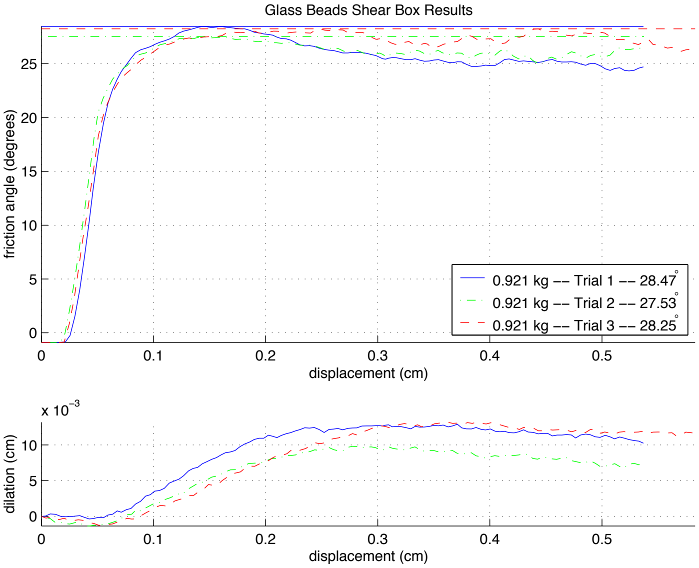

Figure D.21: Direct shear results for three trials of dense Ticino with 0.921 kg load.

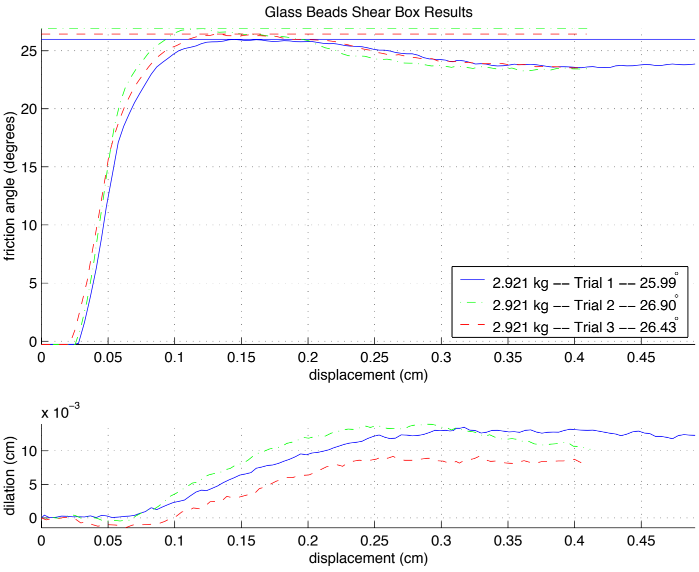

Figure D.22: Direct shear results for three trials of dense Ticino with 2.921 kg load.

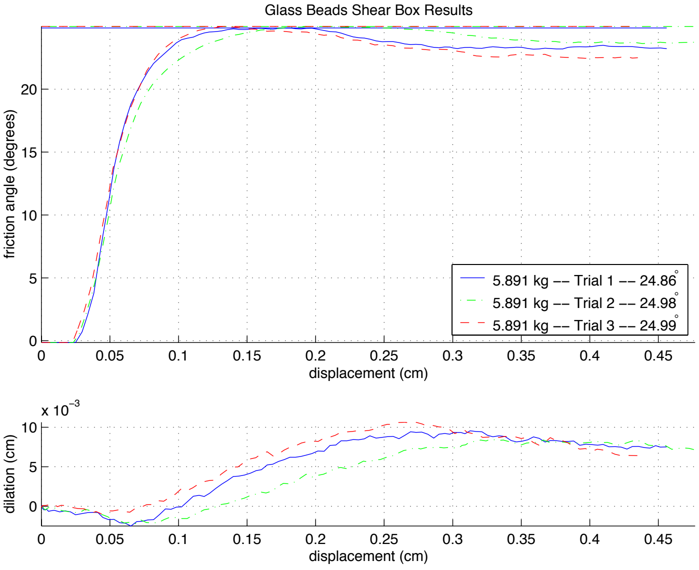

Figure D.23: Direct shear results for three trials of dense Ticino with 5.891 kg load.

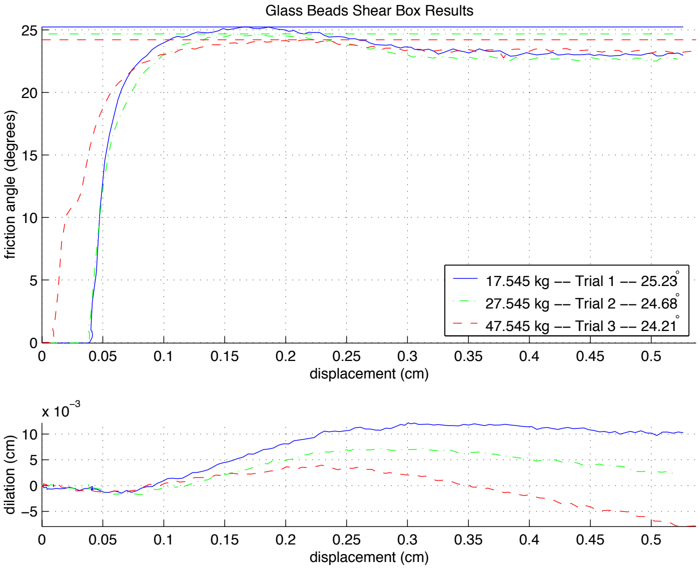

Figure D.24: Direct shear results for three trials of loose glass beads at high loads.

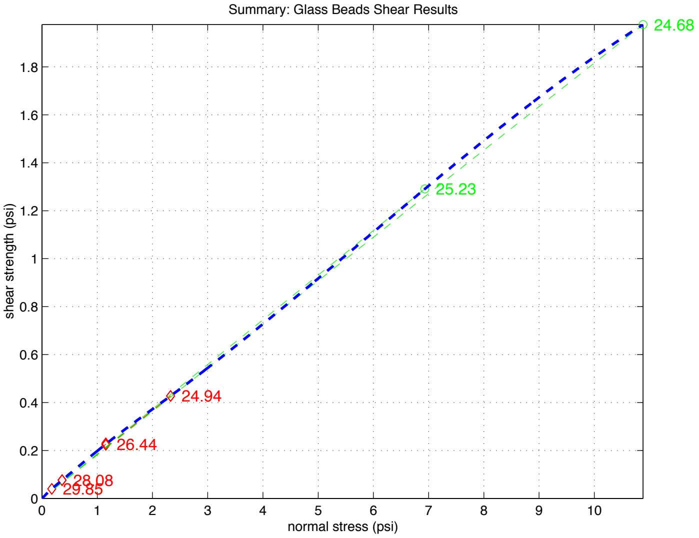

Figure D.25: Compiled friction angle measurements for loose glass beads.

Bibliography

[1] T. V. Alekseeva, K. A. Artem'ev, A. A. Bromberg, R. I. Voitsekhovskii, and N. A. Ul'yanov. *Machines for Earthmoving Work, Theory and Calculations.* Amerind Publishing Co. Pvt. Ltd., New Delhi, 1985.

[2] S. M. Apte and I. J. Oppenheim. Planning intricate robot motions to remove natural materials. In *ASCE Specialty Conf. on Robotics for Challenging Environments*, pp. 106–114, Albuquerque, NM, Feb. 26 - Mar. 2 1994.

[3] J. H. Atkinson. *Foundations and Slopes: An introduction to applications of critical state soil mechanics.* McGraw-Hill Book Company Limited, London, 1981.

[4] J. Ballantyne and E. Wong. A virtual environment display for teleoperated excavation. In *Proc. of the 1998 IEEE/RSJ Intl. Conf. on Intelligent Robots and Systems*, pp. 1894–1899, Victoria, B.C., Canada, October 1998.

[5] M. Barbanov and V. Yodaiken. Real-time linux. *Linux Journal*, February 1997.

[6] L. E. Bernold. Principles of control for robotic excavation. In *Proc. of the 3rd Intl. Conf. on Engineering, Construction, and Operations in Space, SPACE '92*, pp. 1401–1412, Denver, CO, May 31-Jun. 4 1992.

[7] L. E. Bernold. Motion and path control for robotic excavation. *Journal of Aerospace Engineering*, 6(1):1–18, Jan. 1993.

[8] M. Bodur, H. Zontul, A. Ersak, A. J. Koivo, H. Ö. Yurtseven, E. Kocaoğlan, and G. Paşamehmetoğlu. Dynamic cognitive force control for an automatic land excavation robot. In *MELECON,*

Proc. of the 7th Mediterranean Electrotechnical Conf., v. 2, pp. 703–706, Apr. 12-14 1994.

[9] R. H. Bracewell, D. A. Bradley, R. V. Chaplin, and D. W. Seward. Control systems design for robotic backhoe. In *7th Intl. Symposium on Robotics in Construction*, pp. 222–229, Bristol, Jun. 1990.

[10] D. A. Bradley and D. W. Seward. Developing real-time autonomous excavation - the LUCIE story. In *Proc. of the 34th Conf. on Decision and Control*, v. 3, pp. 3028–3033, New Orleans, LA, Dec. 1995.

[11] D. A. Bradley, D. W. Seward, J. E. Mann, and M. R. Goodwin. Artificial intelligence in the control and operation of construction plant-the autonomous robot excavator. *Automation in Construction*, 2(3):217–228, Dec. 1993.

[12] D. M. Bullock, S. M. Apte, and I. J. Oppenheim. Force and geometry constraints in robot excavation. In *Engineering, Construction, and Operations in Space II: Proc. of Space '90*, pp. 960–969, Albuquerque, NM, Apr. 22-26 1990.

[13] D. M. Bullock and I. J. Oppenheim. A laboratory study of force-cognitive excavation. In *Proc. of the Sixth Intl. Symposium on Automation and Robotics In Construction*, Jun. 1989.

[14] D. M. Bullock and I. J. Oppenheim. Object-oriented programming in robotics research for excavation. *Journal of Computing in Civil Engineering*, 6(3):370–385, Jul. 1992.

[15] B. L. Burks, S. M. Killough, and D. H. Thompson. Remote excavation using telerobotic small emplacement excavator. In *Winter Meeting, Intl. Conf. on Fifty Years of Controlled Nuclear Chain Reaction: Past, Present and Future*, pp. 559–60, Nov. 1992.

[16] H. Cannon and S. Singh. Models for automated earthmoving. In *Proceedings, Intl. Symposium on Experimental Robotics (ISER)*, Sydney, Australia, March 1999.

[17] A. Caquot and J. Kerisel. *Tables for the Calculation of Passive Pressure, Active Pressure, and Bearing Capacity of Foundations.* Paris - Imprimerie Gauthier-Villars, 1948.

[18] W. F. Chen and X. L. Liu. *Limit Analysis in Soil Mechanics.* Elsevier, Amsterdam, 1990.

[19] L. Chi and R. L. Kushwaha. A non-linear 3-d finite element anaylsis of soil failure with tillage tools. *Journal of Terramechanics*, 27(4):343–366, 1990.

[20] K. M. Chua and S. W. Johnson. Martian and lunar cold region soil mechanics considerations. *Journal of Aerospace Engineering*, 11(4):138–147, Oct. 1998.

[21] C. A. Coulomb. Essai sur une application des règles des maximis et minimis à quelques problèmes de statique relatifs à l'architecture. *Mém. acad. roy. preés. divers savants*, 7, 1776.

[22] J. J. Craig. *Introduction to Robotics: Mechanics and Control.* Addison-Wesley, 2nd edition, 1989.

[23] D. S. Crouch. Mars Viking surface sampler subsystem. In *Proceedings of the 25th Conference on Remote Systems Technology*, pp. 141–152, San Francisco, CA, 1977. American Nuclear Society.

[24] A. Curtis. *A Nonlinearly Compliant Transmission Element for Force Sensing and Control.* M.S. Thesis, Department of Mechanical Engineering, Massachusetts Institute of Technology, January 2000.

[25] S. P. DiMaio, S. E. Salcudean, C. Reboulet, S. Tafazoli, and K. Hashtrudi-Zaad. A virtual excavator for controller development and evaluation. In *Proc. of the 1998 Intl. Conf. on Robotics and Automation*, Leuven, Belgium, May 16-20 1998.

[26] D. C. Drucker. Limit analysis of two- and three-dimensional soil mechanics problems. *Journal of the Mechanics and Physics of Solids*, 1:217–226, 1953.

[27] D. C. Drucker, H. J. Greenberg, and W. Prager. Extended limit design theorems for continuous media. *Quarterly of Applied Mathematics*, 9:381–389, 1952.

[28] D. C. Drucker and W. Prager. Soil mechanics and plastic analysis or limit design. *Quarterly of Applied Mathematics*, 10:157–165, 1952.

[29] J. M. Duncan and C. Chin-Yung. Nonlinear analysis of stress and strain in soils. *Journal of the Soil Mechanics and Foundations Division*, ASCE 89 (SM5):1629–1653, 1970.

[30] J. M. Duncan and R. L. Mokwa. Passive earth pressure: Theories and tests. *Journal of Geotechnical and Geoenvironmental Engineering*, 127(3):248–257, March 2001.

[31] P. Feng, Y. Yang, Z. Qi, and S. Sun. Research on control method of planning level for excavation robot. In *Proceedings 9th Intl. Symposium on Automation and Robotics in Construction*, Tokyo, 1992.

[32] R. J. Godwin and G. Spoor. Soil failure with narrow tines. *Journal of Agricultural Engineering Research*, 22(3):213–228, 1977.

[33] P. Green, D. W. Seward, and D. A. Bradley. Knowledge acquisition for a robot excavator. In *7th Intl. Symposium on Robotics in Construction*, pp. 351–357, Bristol, Jun. 1990.

[34] K. Habibagahi and A. Ghahramani. Zero extension line theory of earth pressure. *Journal of the Geotechnical Engineering Division, ASCE*, 105(GT7):881–896, July 1979.

[35] A. Haldemann. Mars soil white paper.
http://mvacs.ess.ucla.edu/mvacs/envi/soil/wht-ppr.html, 1996.

[36] A. Hemami. An approximation of the weight of the loaded material during the scooping operation of a mechanical loader. *Transactions of the Canadian Society for Mechanical Engineering*, 18(3):191–205, 1994.

[37] A. Hemami. Modelling, analysis and preliminary studies for automatic scooping. *Advanced Robotics*, 8(5):511–529, 1994.

[38] H. Herman and S. Singh. First results in the autonomous retrieval of buried objects. In *Proc. of the Intl. Conf. on Robotics and Automation*, San Diego, May 1994.

[39] D. P. Hettiaratchi and A. R. Reece. Symmetrical three-dimensional soil failure. *Journal of Terramechanics*, 4(3):45–67, 1967.

[40] R. Hoffman and R. Simmons. Simulation of autonomous robotic excavation. In *ASCE Specialty Conf. on Robotics for Challenging Environments*, pp. 115–122, Albuquerque, NM, Feb. 26 - Mar. 2 1994.

[41] W. Hong. *Robotic Catching and Manipulation Using Active Vision.* M.S. Thesis, Department of Mechanical Engineering, Massachusetts Institute of Technology, September 1995.

[42] W. J. Hong and J. K. Salisbury. Obstacle negotiation in robotic excavation. In *IASTED Intl. Conf. on Robotics and Applications*, Santa Barbara, CA, Oct. 28-30 1999.

[43] X. Huang and L. E. Bernold. Toward an adaptive control model for robotic backhoe excavation. *Transportation Research Record*, 11(1406):20–24, May 1993.

[44] X. Huang and L. E. Bernold. Control model for robotic backhoe excavation and obstacle handling. In *ASCE Specialty Conf. on Robotics for Challenging Environments*, pp. 123–130, Albuquerque, NM, Feb. 26-Mar. 2 1994.

[45] X. Huang, L. E. Bernold, and G. Lee. An adaptive feedforward neural network learning controller for robotic manipulators. In *Proc. of the ISCA Intl. Conf.*, pp. 114–117, 1994.

[46] X. D. Huang and L. E. Bernold. Robotic rock handling during backhoe excavation. In *Automation and Robotics in Construction X*, 1993.

[47] R. G. James and P. L. Bransby. Experimental and theoretical investigations of a passive earth pressure problem. *Géotechnique*, 20(1):17–37, 1970.

[48] Q. Ji and R. L. Sanford. Autonomous excavation of fragmented rock using machine vision. In *Symposium on Emerging Computer Techniques for the Minerals Industry*, pp. 221–228, Tuscaloosa, AL, Feb. 1993.

[49] A. R. Jumikis. *Active and Passive Earth Pressure Coefficient Tables.* Number 43 in Engineering Research Publication. Rutgers, College of Engineering, Bureau of Engineering Research, 1962.

[50] A. R. Jumikis. *Soil Mechanics.* Robert E. Krieger Publishing Company, Inc., 1984.

[51] A. Katz. *The Design and Application of a Nonlinear Series Compliance Actuator for Use in Robotic Arms.* M.S. Thesis, Department of Mechanical Engineering, Massachusetts Institute of Technology, September 1999.

[52] A. J. Koivo. Controlling an intelligent excavator for autonomous digging in difficult ground. In *Proceedings 9th Intl. Symposium on Automation and Robotics in Construction*, Tokyo, Japan, Jun. 1992.

[53] A. J. Koivo. Planning for automatic excavation operations. In *Proceedings 9th Intl. Symposium on Automation and Robotics in Construction*, Tokyo, Japan, Jun. 1992.

[54] A. J. Koivo. Kinematics of excavators (backhoes) for transferring surface material. *Journal of Aerospace Engineering*, 7(1):17–32, Jan. 1994.

[55] A. J. Koivo, M. C. Ramos, and et al. Development of motion equations for excavators and backhoes. *Intl. Journal of Intelligent Mechatronics*, 1(1):46–55, Sep. 1994.

[56] A. J. Koivo, M. Thoma, E. Kocaoglan, and J. Andrade-Cetto. Modeling and control of excavator dynamics during digging operation. *Journal of Aerospace Engineering*, 9(1):10–18, Jan. 1996.

[57] R. L. Kondner and J. S. Zelasko. A hyperbolic stress-strain response: cohesive soil. *Journal of the Soil Mechanics and Foundations Division*, ASCE 89 (SM1):115–143, 1963.

[58] R. L. Kushwaha and J. Shen. Finite element analysis of the dynamic interaction between soil and tillage tool. *Transactions of the ASAE*, 37(5):1315–1319, 1995.

[59] R. L. Kushwaha and J. Shen. Numeric simulation of friction phenomenon at soil-tool interface. *Tribology Transactions*, 38(2):424–430, 1995.

[60] R. L. Kushwaha and Z. X. Zhang. Artificial neural networks modeling of soil-tool interaction. In *Proc. of the 1997 ASAE Annual Intl. Meeting*, v. 1, Minneapolis, MN, Aug. 10-14 1997.

[61] P. V. Lade. Elasto-plastic stress-strain theory for cohesionless soil with curved yield surface. *Intl. Journal of Solids Structure*, 13:1019–1035, 1977.

[62] T. W. Lambe and R. V. Whitman. *Soil Mechanics.* John Wiley & Sons, Inc., New York, 1969.

[63] D. G. Larson. *A Laboratory Investigation of Load Transfer in Reinforced Soil.* Ph.D. Thesis, Department of Civil and Environmental Engineering, Massachusetts Institute of Technology, August 1992.

[64] K. L. Lee and H. B. Seed. Drained strength characteristics of sands. *Journal of the Soil Mechanics and Foundations Division, ASCE*, 93(SM6):117–141, November 1967.

[65] P. J. A. Lever, F.-Y. Wang, and D. Chen. Intelligent excavator control for a lunar mining system. In *Proc. of the ASCE Conf. on Robotics for Challenging Environments*, pp. 97–105, Albuquerque, NM, Feb. 26-Mar. 2 1994.

[66] X. Li and J. M. Moshell. Modeling soil: Realtime dynamic models for soil slippage and manipulation. In *Proc. of SIGGRAPH93*, 1993.

[67] X. Li and J. M. Moshell. Real-time graphical simulation of soil slippage. *Transactions of the Society for Computer Simulation*, 11(2):63–91, 1994.

[68] O. Luengo, S. Singh, and H. Cannon. Modeling and identification of soil-tool interaction in automated excavation. In *Proc. of the 1998 IEEE/RSJ Intl. Conf. on Intelligent Robots and Systems*, v. 3, pp. 1900–1906, Victoria, Canada, Oct. 13-17 1998.

[69] E. McKyes and O. S. Ali. The cutting of soil by narrow blades. *Journal of Terramechanics*, 14(2):43–58, 1977.

[70] H. J. Moore, G. D. Clow, and R. E. Hutton. A summary of Viking sample trench analyses for angles of internal friction and cohesion. *Journal of Geophysical Research*, 87:10,043–10,050, 1982.

[71] H. J. Moore, G. D. Clow, R. E. Hutton, and C. R. Spitzer. Physical properties of the surface materials at the Viking landing sites on Mars. *U.S. Geological Survey Professional Paper 1389*, 1987.

[72] G. Niemeyer and J. J. E. Slotine. Performance in adaptive manipulator control. *Intl. Journal of Robotics Research*, Dec. 1988.

[73] J. R. O'Callaghan and P. J. McCullen. Soil mechanics in relation to earth-moving machinery. In *Proceedings Institution of Mechanical Engineers*, v. 179 Pt 3F, pp. 23–29, 1964-65.

[74] J. Ohde. Zur theorie des erddruckes unter besonderer berücksichtigung der erddruck verteilung. *Die Bautechnik*, 16, 1938.

[75] M. S. Osman. The mechanics of soil cutting blades. *Journal of Agricultural Engineering Research*, 9(4):313–328, 1964.

[76] M. Ostoja-Starzewski and M. Skibniewski. A master-slave manipulator for excavation and construction tasks. *Robotics and Autonomous Systems*, 4:333–337, 1988/89.

[77] P. C. J. Payne, D. W. Tanner, and G. Spoor. A review of the relevance of soil mechanics in earth-moving. In *Proceedings Institution of Mechanical Engineers*, v. 179 Pt 3F, pp. 9–15, 1964-65.

[78] J. V. Perumpral, R. D. Grisso, and C. S. Desai. A soil-tool model based on limit equilibrium analysis. *Transactions of the ASAE*, 26(4):991–995, 1983.

[79] M. A. Peshkin. Programmed compliance for error-corrective assembly. *IEEE Transactions on Robotics and Automation*, 6(4):473–482, August 1990.

[80] G. A. Pratt, M. M. Williamson, P. Dillworth, J. Pratt, K. Ulland, and A. Wright. Stiffness isn't everything. In *Proceedings of the Fourth International Symposium on Experimental Robotics, ISER '95*, Stanford, California, June 30-July 2 1995.

[81] W. H. Press, S. A. Teukolsky, W. T. Vetterling, and B. P. Flannery. *Numerical Recipes in C.* Cambridge University Press, 2nd edition, 1992.

[82] W. J. M. Rankine. On the stability of loose earth. *Phil. Trans. Roy. Soc. London*, 147, 1857.

[83] A. R. Reece. The fundamental equation of earth-moving mechanics. In *Proceedings Institution of Mechanical Engineers*, v. 179 Pt 3F, pp. 16–22, 1964-65.

[84] D. J. Rocke. Control system for automatically controlling a work implement of an earthmoving machine to capture material. U.S. Patent 5528843, 1994.

[85] P. W. Rowe. The stress-dilatancy relation for static equilibrium of an assembly of particles in contact. In *Proceedings of the Royal Society of London. Series A, Mathematical and Physical Sciences*, v. 269, pp. 500–527, 9 October 1962.

[86] P. W. Rowe. The relation between the shear strength of sands in triaxial compression, plane strain and direct shear. *Géotechnique*, 19(1):75–86, 1969.

[87] P. W. Rowe and K. Peaker. Passive earth pressure measurements. *Géotechnique*, 15(1):57–78, 1965.

[88] S. E. Salcudean, S. Tafazoli, P. D. Lawrence, and I. Chau. Impedance control of a teleoperated mini excavator. In *Proc. of the 1997 8th Intl. Conf. on Advanced Robotics, ICAR '97*, pp. 19–25, Monterey, CA, Jul. 7-9 1997.

[89] J. K. Salisbury. Active stiffness control of a manipulator in cartesian coordinates. In *Proc. of the IEEE Conf. on Decision and Control*, pp. 95–100, 1980.

[90] D. Seward, D. Bradley, J. Mann, and M. Goodwin. Controlling an intelligent excavator for autonomous digging in difficult ground. In *Proc. of the 9th Intl. Symposium on Automation and Construction*, Tokyo, Jun. 1992.

[91] D. Seward and F. Margrave. LUCIE the robot excavator - design for system safety. In *Proc. of the 1996 IEEE Intl. Conf. on Robotics and Automation*, pp. 963–968, Minneapolis, Minnesota, Apr. 1996.

[92] D. W. Seward, D. A. Bradley, and R. H. Bracewell. The development of research models for automatic excavation. In *Proceedings 5th Intl. Symposium on Robotics in Construction*, pp. 703–706. Intl. Association for Automation of Robotics in Construction, 1988.

[93] J. Shen and R. L. Kushwaha. *Soil-Machine Interactions: A Finite Element Perspective.* Marcel Dekker, Inc., 1998.

[94] X. Shi, P. J. A. Lever, and F.-Y. Wang. Experimental robotic excavation with fuzzy logic and neural networks. In *Proc. of the 13th IEEE Intl. Conf. on Robotics and Automation*, v. 1, pp. 957–962, Minneapolis, MN, Apr. 22-28 1996.

[95] X. Shi, P. J. A. Lever, and F.-Y. Wang. Fuzzy behavior integration and action fusion for robotic excavation. *IEEE Transactions on Industrial Engineering*, 43(3):395–402, Jun. 1996.

[96] X. Shi, P. J. A. Lever, and F.-Y. Wang. *Autonomous Rock Excavation: Intelligent Control Techniques and Experimentation.* World Scientific, Singapore, 1998.

[97] X. Shi, F.-Y. Wang, and P. J. A. Lever. Task and behavior formulations for robotic rock excavation. In *Proc. of the 10th IEEE Intl. Symposium on Intelligent Control*, pp. 248–253, Monterey, CA, Aug. 27-29 1995.

[98] X. Shi, F.-Y. Wang, and P. J. A. Lever. Experimental results of robotic excavation using fuzzy behavior control. *Control Engineering Practice*, 4(2):145–152, Feb. 1996.

[99] S. Singh. Developing plans for robotic excavators. In *Proc. of the ASCE Conf. on Robotics for Challenging Environments*, pp. 88–96, Albuquerque, NM, Feb. 26-Mar. 2 1994.

[100] S. Singh. Learning to predict resistive forces during robotic excavation. In *IEEE Intl. Conf. on Robotics and Automation*, v. 2, pp. 2102–2107, 1995.

[101] S. Singh. *Synthesizing Plans for Tactical Robotic Excavation.* Ph.D. Thesis, Carnegie Mellon University, Jan. 1995.

[102] S. Singh. State of the art in automation of earthmoving. *Journal of Aerospace Engineering*, 10(4), Oct. 1997.

[103] S. Singh. Multi-resolution planning for earthmoving. In *Proceedings Intl. Conf. on Robotics and Automation (ICRA)*, Lueven, May 1998.

[104] S. W. Sloan. Lower bound limit analysis using finite elements and linear programming. *Intl. Journal for Numerical and Analytical Methods in Geomechanics*, 12:61–77, 1988.

[105] S. W. Sloan. A steepest edge active set algorithm for solving sparse linear programming problems. *Intl. Journal for Numerical Methods in Engineering*, 26:2671–2685, 1988.

[106] S. W. Sloan. Upper bound limit analysis using finite elements and linear programming. *Intl. Journal for Numerical and Analytical Methods in Geomechanics*, 13:263–282, 1989.

[107] S. W. Sloan. Limit analysis in geotechnical engineering. In C. Haberfield, editor, *Ian Boyd Donald Symposium on Modern Developments in Geomechanics*, Monash University, June 7 1995.

[108] V. V. Sokolovskii. *Statics of Granular Media.* Pergamom Press, Oxford, 1965.

[109] A. Stentz, J. Bares, S. Singh, and P. Rowe. A robotic excavator for autonomous truck loading. In *Proc. of the 1998 IEEE/RSJ Intl. Conf. on Intelligent Robots and Systems*, pp. 1885–1893, Victoria, B.C., Canada, Oct. 1998.

[110] R. Sumner, J. F. O'Brien, and J. K. Hodgins. Animating sand, mud, and snow. *Computer Graphics Forum*, 18(1):17–26, 1999.

[111] W. C. Swick and J. V. Perumpral. A model for predicting soil-tool interaction. *Journal of Terramechanics*, 25(1):43–56, 1988.

[112] K. Terzaghi. *Theoretical Soil Mechanics.* John Wiley and Sons, Inc., New York, 1943.

[113] The Rover Team. Characterization of the Martian surface deposits by the Mars Pathfinder Rover, Sojourner. *Science*, 278:1765–1768, 5 December 1997.

[114] The Rover Team. The Pathfinder Microrover. *Science*, 278:1765–1768, 5 December 1997.

[115] D. A. Theobald, W. J. Hong, A. Madhani, B. Hoffman, G. Niemeyer, L. Cadapan, J.-J. E. Slotine, and J. K. Salisbury. Autonomous rock acquisition. In *Proc. of the AIAA Forum on Advanced Development in Space Robotics*, Madison, Wisconsin, Aug. 1-2 1996.

[116] B. Ukritchon. *Evaluation of numerical limit analyses by finite elements and linear programming.* M.S. Thesis, Department of Civil and Environmental Engineering, Massachusetts Institute of Technology, 1996.

[117] B. Ukritchon. *Application of numerical limit analyses for undrained stability problems in clay.* Sc.D. Thesis, Department of Civil and Environmental Engineering, Massachusetts Institute of Technology, 1998.

[118] B. Ukritchon, A. J. Whittle, and S. W. Sloan. Undrained limit analyses for combined loading of strip footings in clay. *Journal of Geotechnical and Geoenvironmental Engineering*, 124(3):265–276, March 1998.

[119] P. K. Vähä and M. J. Skibniewski. Cognitive force control of excavators. *Journal of Aerospace Engineering*, 6(2), Apr. 1993.

[120] P. K. Vähä and M. J. Skibniewski. Dynamic model of excavator. *Journal of Aerospace Engineering*, 6(2):148–158, 1993.

[121] P. K. Vähä, M. J. Skibniewski, and A. J. Koivo. Kinematics and trajectory planning for robotic excavation. In *Preparing for Construction in the 21st Century, Construction Congress '91*, pp. 787–793, Cambridge, MA, Apr. 13-16 1991.

[122] F.-Y. Wang and P. J. A. Lever. On-line trajectory planning for autonomous robotic excavation based on force/torque sensor measurements. In *Proc. of the 1994 IEEE Intl. Conf. on Multisensor Fusion and Integration for Intelligent Systems (MFI '94)*, pp. 371–378, Las Vegas, NV, Oct. 2-5 1994.

[123] B. M. Willman and W. W. Boles. Soil-tool interaction theories as they apply to lunar soil simulant. *Journal of Aerospace Engineering*, 8(2):88–99, Apr. 1995.

[124] B. M. Willman, W. W. Boles, D. S. McKay, and C. C. Allen. Properties of lunar soil simulant JSC-1. *Journal of Aerospace Engineering*, 8(2):88–99, Apr. 1995.

[125] W. P. Wohlford, B. D. Bode, and F. D. Griswold. New capability for remotely controlled excavation. In *Proc. of 1990 Winter Meeting of the American Nuclear Society*, pp. 628–9, Nov. 1990.

[126] R. N. Yong and A. W. Hanna. Finite element analysis of plane soil cutting. *Journal of Terramechanics*, 14(3):103–125, 1977.

[127] A. N. Zelenin, V. I. Balovnev, and I. P. Kerov. *Machines for Moving the Earth.* A. A. Balkema, Rotterdam, 1986.